N° d'ordre: 40192

Université Lille 1
Sciences et Technologies

Discipline: Sciences of Matter, Radiation and Environment

Dissertation

High sensitivity detection of Polycyclic Aromatic Hydrocarbons desorbed from soot particles using Laser Desorption/Laser Ionisation/Time-Of-Flight Mass Spectrometry. An approach for studying the soot growth process in flames

by

Alessandro FACCINETTO

Reviewers:	Barbara APICELLA, Senior Scientist, CNR Napoli
	Nabiha CHAUMEIX, Directrice de Recherche CNRS, Université dOrléans
Examiners:	Kevin THOMSON, Research Officer, NRC Ottawa
	Thomas PINO, Chargé de Recherche CNRS, Université Paris Sud Orsay
	Jean-François PAUWELS, Professor, Université Lille 1
	Cristian FOCSA, Professor, Université Lille 1
Supervisors:	Pascale DESGROUX, Directrice de Recherche CNRS, Université Lille 1
	Michael ZISKIND, Maître de Conférences, Université Lille 1

14th December 2009

Discipline: Sciences of Matter, Radiation and Environment

Dissertation

High sensitivity detection of Polycyclic Aromatic Hydrocarbons desorbed from soot particles using Laser Desorption/Laser Ionisation/Time-Of-Flight Mass Spectrometry. An approach for studying the soot growth process in flames

by

Alessandro FACCINETTO

Reviewers: Barbara APICELLA, Senior Scientist, CNR Napoli

Nabiha CHAUMEIX, Directrice de Recherche CNRS, Université dOrléans

Examiners: Kevin THOMSON, Research Officer, NRC Ottawa

Thomas PINO, Chargé de Recherche CNRS, Université Paris Sud Orsay

Jean-François PAUWELS, Professor, Université Lille 1

Cristian FOCSA, Professor, Université Lille 1

Supervisors: Pascale DESGROUX, Directrice de Recherche CNRS, Université Lille 1

Michael ZISKIND, Maître de Conférences, Université Lille 1

14th December 2009

If we knew what we were doing it wouldn't be called research, would it?
Albert Einstein

Abstract

Soot is constituted by carbonaceous particles formed during the incomplete combustion of hydrocarbons. Soot formation in flames is a complex and not yet fully understood process involving both physical and chemical transformations. Polycyclic Aromatic Hydrocarbons (PAH), are generally considered as the main precursors of soot particles and as important species participating to the soot growth process.

PAH are formed in the early combustion steps from the reaction of the still hydrogen-rich fuel components, and they are found adsorbed on soot particles surface. The presence of PAH adsorbed on soot is correlated to the amount and the morphology of the soot released in the environment during the combustion. Therefore, there is a scientific interest in the characterisation and quantification of the PAH adsorbed on soot particles with the aim of understanding the mechanism of formation of the soot particles as well as their impact on the environment and human health.

In this work, an experimental setup dedicated to such investigation has been developed. This setup relies on the coupling of three different experimental techniques, laser desorption, laser ionisation and time-of-flight mass spectrometry (LD/LI/TOF-MS). Soot is extracted from flames using a vacuum probe and deposed on the surface of porous borosilicate glass filters. The samples obtained this way are then introduced in the ion source of the mass spectrometer where they are irradiated by a laser pulse at 532 nm wavelength. The energy delivered to the sample causes the desorption of neutral molecules from the sample, which form a plume expanding in the high-vacuum of the mass spectrometer. This plume is irradiated by a second laser pulse at 266 nm wavelength which promotes the ionisation of the neutral molecules, and the so-produced ions are detected via time-of-flight mass spectrometry.

The early mass spectra obtained via LD/LI/TOF-MS were complex and difficult to interpret. Therefore, a strategy of systematic investigations has been adopted, starting from the study of less complex systems constituted by pure PAH only, and then growing in complexity up to natural soot. In the context of this analytical approach, important intermediate systems which have been extensively characterised are the so called model soot, made adsorbing a known concentration of pure PAH on a substrate similar to natural soot (carbon black). Their characterisation allowed a good understanding of the analytical response of PAH to the desorption and ionisation processes when adsorbed on a carbonaceous matrix. Further, they

allowed the definition of the optimal experimental conditions and the acquisition of the overall skills required to master the LD/LI/TOF-MS diagnostic.

The ensemble of the above mentioned optimisations increased the system sensitivity and selectivity, leading to original analytical methods. For instance, the determination of the analytical conditions under which the mass spectra of pure PAH are fragment free made easier the interpretation of the mass spectra obtained from real soot, allowing the unambiguous attribution of the detected peak signals to precursor ions.. Analogously, the investigations on model soot demonstrated the possibility of achieving a soft desorption without destroying the underlying carbonaceous matrix or causing the apparition of measurement artifacts. Further, it demonstrated the ability of producing homogeneous samples, having a known concentration of PAH adsorbed on the substrate, which allowed the determination of the amount of desorbed substance, estimated in the order of the tenth of fmol per laser pulse. In principle that could lead to quantitative analyses using series of samples to build up a calibration curve signal vs. concentration. From a more fundamental point of view, insights on the coupling occurring between the desorption and ionisation processes have been given as well.

The LD/LI/TOF-MS has then been used to analyse soot samples collected from different flames. These are: a premixed atmospheric ethylene flame, a low-pressure premixed methane flame and jet-diffusion Diesel/Diesel surrogate flame.

The analysis of the phase adsorbed on soot collected from the premixed atmospheric ethylene flame was already available in the literature. The measurements performed on this flame allowed the determination of the limits and potentialities of the LD/LI/TOF-MS diagnostic and the calibration of the sampling procedure as well. The low-pressure premixed flame is characterised by an expanded reaction zone and a soot concentration gradient weak enough to allow the investigation of the early steps of soot formation by microprobe sampling. The analysis of the jet-diffusion flame allows investigations on commercial Diesel fuels nebulised as an aerosol and simulating the injection process. All the measurements concerning those flames and reported in this work span the most representative regions of the investigated flames, which have been identified using in-situ laser diagnostics like Laser Induced Incandescence (LII) and Laser Induced Fluorescence (LIF).

The obtained mass spectra are reproducible, fragment-free, well-resolved in the analysed m/z range and they are characterised by an excellent signal-to-noise ratio. They all feature regular peak sequences, where each signal peak has been attributed to the most stable high-temperature formed PAH. The richest mass spectrum has been obtained from the premixed flames. Generally, the structure of the mass spectra depends on the sampling height into the flame, i.e. on the reaction time. On the other hand, the PAH soot content depends on the nature of fuel as well, as demonstrated by the comparative investigations on the soot produced by a Diesel fuel and its two-component model fuel.

A contribution to the data interpretation comes from the development of a new sampling method allowing the separation of soot and gaseous PAH present in the gas phase. This method highlights the presence of high-mass PAH in the soot nucleation zone, suggesting the importance of the heterogeneous reactions occurring between gaseous PAH and soot particles.

Table of contents

Glossary

The terms used in this work are those recommanded by IUPAC in the last revision (done on 2006) to the standard definitions of terms relating to mass spectrometry. This glossary contains the recommendations for nomenclature, definitions of terms, and acronyms to be used in mass spectrometry.

Accelerating voltage. Electrical potential used to impart translational energy to ions in a mass spectrometer.

Accurate mass. Experimentally determined mass of an ion that is used to determine an elemental formula. Note: *accurate mass* and *exact mass* are not synonymous. The former refers to a measured mass and the latter to a calculated mass.

Average mass. Mass of an ion or molecule calculated using the average mass of each element weighted for its natural isotopic abundance.

Base peak (BP). Peak in a mass spectrum that has the greatest intensity.

Charge numbe (z). Total charge on an ion, regardless of sign, divided by the magnitude of the electron charge e.

Cluster ion. Ion formed by a multi-component atomic or molecular assembly of one or more ions with atoms or molecules, such as $[(H_2O)_nH]^+$, $[(NaCl)_nNa]^+$ or $[(H_3PO_3)_nH_2PO_3]^-$.

Delayed extraction (DE). Application of the accelerating voltage pulse after a time delay in desorption/ionisation from a surface. The extraction delay can produce energy focusing in a Time-Of-Flight mass spectrometer.

Diagnostic ion. Product ion whose formation reveals structural or compositional information of its precursor. For instance, the phenyl cation in an electron ionisation mass spectrum is a diagnostic ion for benzene and derivatives.

Dimeric ion. An ion formed by ionisation of a dimer or by the association of an ion with its neutral counterpart such as $[M_2]^{+\bullet}$ or $[M-H-M]^+$.

Desorption Ionisation (DI). Formation of ions from a solid or liquid material by the rapid vaporisation of that sample.

Dissociative ionisation. Reaction of a gas-phase molecule that results in its decomposition to form products, one of which is an ion.

Einzel lens. Three-element charged particle lens in which the first and third elements are held at the same voltage. Such a lens produces focusing without changing the translational energy of the particle.

Electron affinity (*EA*). Electron affinity of a species M is the minimum energy required for the process $M^{-\bullet} \rightarrow M + e$ where $M^{-\bullet}$ and M are in their ground rotational, vibrational and electronic states and the electron has zero translational energy.

Electron energy. Magnitude of the electron charge multiplied by the potential difference through which electrons are accelerated in order to effect electron ionisation.

Electron ionisation. Ionisation of an atom or molecule by electrons that are typically accelerated to energies between 10 and 150 eV in order to remove one or more electrons from the molecule.

Electron volt (eV). Non-SI unit of energy defined as the energy acquired by a particle containing one unit of charge through a potential difference of one volt. $1 eV = 1.60217733 \cdot 10^{-19} J$.

Exact mass. Calculated mass of an ion or molecule containing a single isotope of each atom, most frequently the lightest isotope of each element, calculated from the masses of these isotopes using an appropriate degree of accuracy.

Fragment ion. A product ion that results from the dissociation of a *precursor ion*.

Hard ionisation. Formation of gas-phase ions accompanied by extensive dissociation.

Heterolytic cleavage. Dissociation of a molecule or ion in which both electrons forming the single bond that is broken remain on one of the atoms that were originally bonded.

Homolytic cleavage. Dissociation of an ion or molecule in which the electrons forming the single bond that is broken are shared between the two atoms that were originally bonded. For an odd electron ion, dissociation results from one of a pair of electrons that form a bond between two atoms moving to form a pair with the odd electron on the atom at the apparent charge site. Dissociation results in the formation of an even electron ion and a radical. This reaction involves the movement of a single electron and is represented by a single-barbed arrow.

Ionic dissociation. The dissociation of an ion into another ion of lower mass and one or more neutral species or ions with a lower charge.

Ionisation cross section. A measure of the probability that a given ionisation process will occur when an atom or molecule interacts with a photon, electron, atom or molecule.

Ionisation efficiency. Ratio of the number of ions formed to the number of molecules consumed in the ion source.

Ionising collision. Reaction of an ion with a neutral species in which one or more electrons are removed from either the ion or neutral.

Ion source. Region in a mass spectrometer where ions are produced.

Isotope dilution mass spectrometry. A quantitative mass spectrometry technique in which an isotopically enriched compound is used as an internal standard.

Isotopologue ions. Ions that differs only in the isotopic composition of one or more of the constituent atoms. For example, CH_4^+ and CH_3D^+ or $^{10}BF_3$ and $^{11}BF_3$ or the ions forming an isotope cluster. The term isotopologue is a shortening of isotopic homologue.

Isotopomeric ions. Isomeric ion having the same numbers of each isotopic atom but differing in their positions. Isotopomeric ions can be either configurational isomers in which two atomic isotopes exchange positions or isotopic stereoisomers. The term isotopomer is a shortening of isotopic isomer.

Laser Desorption (LD). Formation of gas-phase neutral species by the interaction of photons from a pulsed laser beam with a solid or liquid material.

Laser Desorption/Ionisation (LDI). Formation of gas-phase ions by the interaction of photons from a pulsed laser beam with a solid or liquid material.

Laser Ionisation (LI). Formation of ions through the interaction of photons from a laser with a material or with gasphase ions or molecules.

Laser Microprobe Mass Spectrometry (LMMS). *Laser desorption/ionisation* mass spectrometry, particularly emphasizing spatially resolved composition information.

Mass calibration. A means of determining *m/z* values from their times of detection relative to initiation of acquisition of a mass spectrum. Most commonly this is accomplished using a computer-based data system

and a calibration file obtained from a mass spectrum of a compound that produces ions whose *m/z* values are known.

Mass gate. A set of plates or grid of wires in a Time-Of-Flight mass spectrometer that is used to apply a pulsed electric field with the purpose of deflecting charged particles in a given *m/z* range.

Mass limit. The *m/z* value above which ions cannot be detected in a mass spectrometer.

Mass number (A). Sum of the number of protons and neutrons in an atom, molecule or ion.

Mass range. Range of *m/z* over which a mass spectrometer can detect ions or is operated to record a mass spectrum.

Mass resolution. Smallest mass difference Δm between two equal magnitude peaks so that the valley between them is a specified fraction of the peak height.

Mass resolving power. In a mass spectrum, the observed mass divided by the difference between two masses that can be separated: $m/\Delta m$. The procedure by which Δm was obtained and the mass at which the measurement was made should be reported.

Mass spectrum. A plot of the relative abundances of ions forming a beam or other collection as a function of their *m/z* values.

Matrix-Assisted Laser Desorption/Ionisation (MALDI). Formation of gas-phase ions from molecules that are present in a solid or liquid matrix that is irradiated with a pulsed laser.

Metastable ion. An ion that is formed with internal energy higher than the threshold for dissociation but with a lifetime great enough to allow it to exit the ion source and enter the mass analyzer where it dissociates before detection.

Microchannel plate (MCP). A thin plate that contains a closely spaced array of channels that each act as a continuous dynode particle multiplier. A charged particle, fast neutral particle, or photon striking the plate causes a cascade of secondary electrons that ultimately exits the opposite side of the plate.

Molar mass (m). Mass of one mole ($6.0221215 \cdot 10^{-23}$ atoms or molecules) of a compound.

Molecular beam mass spectrometry. A mass spectrometry technique in which the sample is introduced into the ion source of the mass spectrometer as a collimated beam of molecules with a narrow velocity distribution.

Molecular ion. An ion formed by the removal of one or more electrons to form a positive ion or the addition of one or more electrons to form a negative ion.

Monoisotopic mass. Exact mass of an ion or molecule calculated using the mass of the most abundant isotope of each element.

Multiphoton Ionisation (MPI). Photoionisation of an atom or molecule in which two or more photons are absorbed.

***m/z*.** The three-character symbol *m/z* is used to denote the dimensionless quantity formed by dividing the mass of an ion in unified atomic mass units by its charge number (regardless of sign). The symbol is written in italicised lower case letters with no spaces

Nominal mass. Mass of an ion or molecule calculated using the mass of the most abundant isotope of each element rounded to the nearest integer value and equivalent to the sum of the *mass numbers* of all constituent atoms.

Peak (in mass spectrometry). Localised region of relatively large ion signal in a mass spectrum. Although peaks are *often* associated with particular ions, the terms peak and ion should not be used interchangeably.

Peak intensity. Height or area of a peak in a mass spectrum.

Photodissociation. Process wherein the reactant ion is dissociated as a result of absorption of one or more photons.

Photoionisation. Ionisation of an atom or molecule by a photon, written $M + \hbar\omega \rightarrow M^{\cdot +} + e$.

Precursor ion. Ion that reacts to form particular product ions. The reaction can be unimolecular dissociation, ion/molecule reaction, isomerisation, or change in charge state.

Principal ion. Most abundant ion of an isotope cluster. The term principal ion has also been used to describe ions that have been artificially isotopically enriched in one or more positions.

Product ion. An ion formed as the product of a reaction involving a particular precursor ion. The reaction can be unimolecular dissociation to form fragment ions, an ion/molecule reaction, or simply involve a change in the number of charges.

Product ion spectrum. Mass spectrum recorded from any spectrometer in which the appropriate *m/z* separation scan function is set to record the product ion or ions of selected precursor ions.

Progeny fragment ions. Charged product of a series of consecutive reactions that includes product ions, 1st generation product ions, 2nd generation product ions, etc. Given the sequential dissociation scheme:

$$M_1^+ \rightarrow M_2^+ \rightarrow M_3^+ \rightarrow M_4^+ \rightarrow M_5^+$$
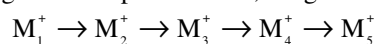
M_4^+ is the precursor ion of M_5^+, a 1st generation product ion of M_3^+, a 2nd generation product ionof M_2^+ and a 3rd generation product ion of M_1^+.

Quadratic field reflectron. A reflectron in which the electric field varies with the square of the distance from the entrance and compensates for translational kinetic energy spread to all orders.

Radical ion. An ion, either a cation or anion, containing unpaired electrons in its ground state. The unpaired electron is denoted by a superscript dot alongside the superscript symbol for charge, such as for the molecular ion of a molecule M, that is, $M^{+\bullet}$. Radical ions with more than one charge and/or more than one unpaired electron are denoted such as $M^{(2+)(2\bullet)}$. Unless the positions of the unpaired electron and charge can be associated with specific atoms, superscript charge designation should be placed before the superscript dot designation.

Reference ion. Stable ion whose structure is known with certainty. These ions are usually formed by direct ionisation of a molecule of known structure, and are used to verify by comparison the structure of an unknown ion.

Reflectron. Constituent of a time-of-flight mass spectrometer that uses a static electric field to reverse the direction of travel of the ions entering it. A reflectron improves mass resolution by assuring that ions of the same *m/z* but different translational kinetic energy arrive at the detector at the same time.

Relative molecular mass (M$_r$). Mass of one molecule of a compound, with specified isotopic composition, relative to one-twelfth of the mass of one atom of ^{12}C.

Resonance-Enhanced Multiphoton Ionisation (REMPI). Multiphoton ionisation in which the ionisation cross section is significantly enhanced because the energy of the incident photons is resonant with an intermediate excited state of the neutral species.

Soft ionisation. Formation of gas-phase ions without extensive dissociation.

Stable ion. Ion with internal energy sufficiently low that it does not rearrange or dissociate prior to detection in a mass spectrometer.

Time lag focusing. Energy focusing in a Time-Of-Flight mass spectrometer that is accomplished by introducing a time delay between the formation of the ions and the application of the accelerating voltage pulse. Ion formation may be in the gas phase or at a sample surface.

Unified atomic mass unit (u). A non-SI unit of mass defined as one twelfth of the mass of one atom of ^{12}C in its ground state and equal to $1.6605402 \cdot 10^{-27} kg$. Note: The term *atomic mass unit* (*amu*) is ambiguous as it has been used to denote atomic masses measured relative to a single atom of ^{16}O, or to the isotope-averaged mass of an oxygen atom, or to a single atom of ^{12}C.

Unimolecular dissociation. Dissociation reaction in which the molecularity is treated as one, irrespective of whether the dissociative state is that of a metastable ion produced in the ion source or results from collisional excitation of a stable ion.

Unstable ion. Ion with sufficient energy to dissociate within the ion source.

Vertical ionisation. Process in which an electron is removed from or added to a molecule without a change in the positions of the atoms. The resulting ion is typically in an excited vibrational state.

Chapter 1.

Introduction

Incomplete combustion may result in the emission of a complex mixture of pollutants in the atmosphere. The term *combustion* implicitly describes a number of processes, and under such a variety of practical conditions a potentially huge range of pollutants is produced, playing a lead role on the impact on human health and environment. Typically, these combustion by-products include carbon monoxide (CO), nitrogen oxides (NO_x), Polycyclic Aromatic Hydrocarbons (PAH), dioxins, metals and particulate matter. Each one of these pollutants has been associated with adverse impacts on human health. Furthermore, combustion sources are widespread, and many by-products have potential for wide-ranging impacts, not only on human health but on entire ecosystems and the global climate. For instance, the aerosol particles formed from soot behave like a grey body, absorbing a fraction of the solar power, and ultimately heating the atmosphere.

Particulate matter constitutes one of the major pollutants identified by the Environment Protection Agency (EPA) since 2004. Especially, the environmental and health impact of particles is determined by both their size and chemical composition.

The particle size covers many orders of magnitude spanning from a few nanometers up to tenth of micrometers. The fine particles ($PM_{2.5}$) are mainly produced directly from combustion processes, and those in the approximate size range of 0.2–0.5 μm can be transported for long distances from the source site. The smallest particles are the most dangerous, since they can readily penetrate indoors resulting in ubiquitous exposure, and they can be breathed deeply into the lungs. Moreover, as a result of the complex network of physico-chemical interactions leading to their formation, fine particles have a large surface area and are able to adsorb other chemicals produced during the combustion, such as PAH, partially oxidised hydrocarbons including oxy-PAH, and other heteroatom-containing species such as dioxins. Fine particles are also able to stabilise organic radicals biologically active, which can induce oxidative stress and DNA damage.

For the above mentioned reasons, the emission of particulate is limited by international laws which are becoming stricter and stricter. For instance, the currently valid standard imposed by the European Community (Euro V) limits the emissions of particulate produced by car diesel engines at 5 mg/km, value which represents a reduction of the 80% with respect to the value valid until 2006 (Euro IV). The new Euro VI beginning on 2012 will further reduce this value down to 2.5 mg/km. This same value was 140 mg/km in 1992.

In this work, our primary concern is to study the formation of particles produced during combustion processes. There is a growing scientific attention on the formation of soot particles from their gaseous precursors (soot inception). This crucial step leads from a molecular system mainly located in the gas phase and evolving through homogeneous reactions up to primary particles and later to macroscopic aggregates where a fundamental role is played by the heterogeneous reactions at the particle surface.

The mechanisms leading to the soot inception are not yet fully understood and the quantitative detection using the available commercial equipment is difficult. Investigations performed along decades only identified some of the fundamental steps of the soot particles formation process. Particularly, the role of most likely precursors of the soot particles has been attributed to a specific class of molecules, the PAH.

Aiming to get information on those processes and to improve the overall knowledge on the soot formation and growth, the strategy usually adopted by the scientific community is to identify and quantify the species formed into the flame at different levels of their evolution, i.e. in different locations into the flame. A second strategy follows the opposite approach. The young soot particles are disassembled in order to determine the fundamental constituents which are responsible of their formation. This second method has been initially developed by Dobbins, and then adopted by a few other teams (Öktem, Mathieu, Grotheer, see Chapter 3). This approach takes advantage of a preliminary laser induced desorption at the particle surface followed by the laser ionisation of the ejected molecules and their detection via time-of-flight mass spectrometry. The chemical composition of the desorbed phase can be deduced from the structure of the mass spectra.

Such an experimental setup has been developed in Lille in the context of a years-long research project, thanks to the collaboration of the combustion group from the *Physicochimie des Processus de Combustion et de l'Atmosphère* (PC2A) laboratory, and the ANATRAC group from the *Physique des Lasers, Atomes et Molécules* (PhLAM) laboratory in the framework of the CNRS Research Federation CERLA (*Centre d'Etudes et de Recherches Lasers et Applications*) of the University of Lille 1. The last mentioned group, specialised in the trace analysis of the adsorbed phase on various substrates (ice, graphite) has developed an experimental set-up allowing the analyses of the adsorbed phase on substrate by a complex technique combining Laser Desorption, Laser Ionisation and Time-Of-Flight Mass Spectrometry (LD/LI/TOF-MS).

This dissertation has been realised as the continuation of the work of Claudia Mihesan (Section 5.1), during which the characterisation of the desorption step and the feasibility of the application of the LD/LI/TOF-MS diagnostic on pure PAH and mixture of pure PAH has been tested. At the time of this early work, some analyses of PAH adsorbed on a graphite substrate (model soot) and soot sampled from atmospheric laminar flames had been performed, highlighting the analytical potentiality of the diagnostic as well as the aspects to be improved.

Several goals have been pursued during this work. The first one concerns the improvement of the performances of the LD/LI/TOF-MS diagnostic. The functional dependences of mass selectivity, sensitivity and data reproducibility have all been subject of extended investigations.

The response of pure PAH and PAH adsorbed on model soot have been studied aiming to fully characterise the response of those molecules to the LD/LI/TOF-MS analyses. Particularly, the characterisation of the desorption, the ionisation steps and their coupling have been completed. A way allowing semi-quantitative measurements of concentration of PAH on soot is also proposed.

We have then switched to the analysis of three flames. First, we investigated an atmospheric premixed ethylene/oxygen flame which has been the object of a number of studies of the group of

Ciajolo, Apicella and Tregrossi of Naples (Section 6.2). This flame has been ranked as our reference flame allowing us to test the potentialities and limits of the LD/LI/TOF-MS diagnostic with respect to the literature.

The second analysed flame was a low-pressure methane/oxygen/nitrogen flame. This flame is the current object of investigations at PC2A laboratory, aiming to understand the mechanisms of formation of soot in low-pressure flames. The knowledge of the chemical composition of the species adsorbed on soot particles as a function of the flame reaction time is an important complement for the forthcoming kinetic modelling. Finally the analytical potential of the LD/LI/TOF-MS diagnostic has been verified in a jet turbulent diesel flame.

A flame sampling method based on the extraction of the soot from the flame using a quartz microprobe has been developed. Soot particles are deposed on the surface of porous borosilicate glass filters, and the complementary analysis of the gas phase has been performed by gas condensation on adsorbing substrates. The discrimination between the particles and the gas phase has been obtained via comparison of the mass spectra of samples obtained depositing gases and soot on adsorbing and non-adsorbing substrates. Finally, the last goal is the analysis of the sampled soot and the interpretation of the results leading to the improvement of the understanding of nucleation and growth processes of soot into the studied flames.

This work is composed of five chapters. Chapter 2 briefly reviews the fundamental research in combustion paying particular attention to the synthesis and growth of the polyaromatic systems in flames and their role in the soot particle formation. The first part describes the gas phase reactions, while the second one focuses on the particulate phase. Chapter 3 proposes a review of the most important aspects related to detection of PAH on soot using laser methods coupled with Time-Of-Flight mass spectrometry, first introducing the LD/LI/TOF-MS and discussing its potentialities and limits of applicability. Chapter 4 describes the LD/LI/TOF-MS diagnostic setup used in this work, as well as the adopted flame configuration. In this chapter all the experimental details needed in order to set a LD/LI/TOF-MS experiment are reported, from the laser optical path, to the description of the sampling line used to collect the soot from flames. Chapter 5 describes the first part of experimental results, treating the setup optimisation aiming to characterise the desorption and ionisation processes and their coupling. Finally, Chapter 6 describes the results obtained from the analyses of the three flames described above.

Chapter 2.

Soot formation in flames

Soot formation in flames is a complex process involving several physical and chemical steps. In the flame reaction zone the oxidation of the molecules of fuel leads to a large number of species including small hydrocarbon radicals, acetylene and both atomic and molecular hydrogen. This zone is typically blue-coloured due to the chemiluminescence of radicals, among which CH and C_2 dominate under rich combustion conditions. As the combustion progresses, the small radicals produced during the fuel oxidation quickly recombine, producing larger and larger hydrogen-rich structures, and finally polymerising in soot precursors and soot. This last stage is referred to as soot inception, and it represents the key-step to get knowledge about the overall soot formation and growth. Once the soot particles are formed, they can undergo a variety of physical interactions, and a potentially huge number of heterogeneous reactions may occur at their surface. The gas-solid phase transition is evident even at macroscopic level, since in this region the flame colour shifts from the typical blue of the reaction zone to the characteristic yellow-orange due to the incandescence of soot particles. During the last combustion stages the hydrogen content of soot progressively decreases, and the soot itself becomes more and more carbonaceous. Whether the soot is completely oxidised to CO and CO_2 a non-smoking combustion occurs. Otherwise the soot particles can leave the flame environment.

Many of the steps occurring during combustions are not yet completely understood, despite the effort devoted to this topic. At the present moment, the kinetic model of soot formation is constituted by two main parts.

The first part only deals with the gas-phase chemistry, explaining the reaction pathway leading from the fuel oxidation up to the formation of large molecular species. Indeed, a central issue in the understanding of soot formation path is the identification of the most important molecular precursors. During the last fifty years a certain number of proposals have been presented, among which the most noteworthy included polyacetylenes [1], ionic species [2] and Polycyclic Aromatic Hydrocarbons (PAH) [3]. However, at the present moment most opinions, sustained by several experimental and modelling studies [4-10], support PAH as the most probable soot precursors.

The second part of the model treats the physical-chemistry involving the particulate phase, studying the formation processes of the very first solid particles, their growth, the surface processes, and all the modifications leading to the mature soot found in the exhausts. Once the soot molecular precursors are available into the combustion environment a nucleation process occurs, during which the very first solid particles are formed. From this point onward a number of important physical-chemical processes actively participate to the growth process, shaping the

particles in what is usually referred as *primary soot particles*. Particle coagulation and surface growth cause the particles to gain mass and increase their size, while oxidation phenomena tend to counterbalance the growth removing carbon as CO and CO_2. Eventually the primary particles stop their growth and approach a steady state. There, agglomeration processes cause the mature primary particle to stick each other, forming the macroscopic chain-like aggregates.

This Section is structured as follows. The first part, Section 2.1, deals with the soot molecular precursors, briefly introducing the most studied reaction pathways leading to the formation of the first aromatic rings, the high temperature stability of hydrocarbons and the aromatic growth in the gas phase. The second part, Section 2.2, focus on the soot inception and on the physical-chemical reaction involving the growing soot particles, there including the aromatic growth at the soot surface, the surface reactions and the soot aging.

2.1. Soot molecular precursors

The mechanism of formation of soot precursors consists of several interconnected steps. No single reaction pathway directly produces the first aromatics in all flames, and most reaction pathways vary with the flame conditions and particularly with the fuel composition. For instance, during the combustion of aliphatics the fuel molecules first form small aliphatic fragments, hydrocarbon molecules and radicals via oxidation reactions. The species formed this way undergo a large number of chemical reactions, among which the formation of the first aromatics links the homogeneous processes occurring in the early combustion steps with the heterogeneous physical-chemistry typical of the later soot particle evolution [7,11]. For this reason the high temperature chemistry of aromatics received great attention in the last decades. A detailed discussion of this subject is reported in Section 2.1.1.

2.1.1. First aromatic ring formation

In flame combustion the first aromatic ring formation appears to be the key process leading to the successive aromatic growth [12-17]. Particular attention has been devoted to the formation of the first aromatics from small aliphatic radicals, because this is the step perceived to be the rate-limiting in the chain of reactions leading from the fuel pyrolysis up to the mature soot [12,14,17,18].

The reactions introduced in this Paragraph mainly involve resonantly-stabilised radicals that can accumulate in relatively high concentrations, and therefore at the present moment they are considered the most important pathways leading to the first and the second aromatic rings in flames of aliphatic fuels.

One of the first radical pathways has been proposed by Weissman and Benson [19] and by Cole and co-workers [20], and it involves the addition of acetylene to the even-carbon radicals $n-C_4H_3$ and $n-C_4H_5$ leading to phenyl (⬡) and benzene (⬡):

$$n-C_4H_3 + C_2H_2 \rightarrow C_6H_5 \tag{2.1}$$

$$n-C_4H_5 + C_2H_2 \rightarrow C_6H_6 + H \tag{2.2}$$

These reactions are favourable because they do not require intra-molecular hydrogen transfer. On the other hand they involve two non-resonant radicals ($n-C_4H_3$ and $n-C_4H_5$)[1] having resonant-stabilised counterparts ($i-C_4H_3$ and $i-C_4H_5$)[2] they can readily be converted to. For this reason, Miller and Melius proposed an alternative odd-carbon atom pathway based on the reactions of propargyl radicals C_3H_3 [21]. The global reaction is:

$$C_3H_3 + C_3H_3 \rightarrow C_6H_6 \tag{2.3}$$

$$C_3H_3 + C_3H_5 \rightarrow C_6H_6 + 2H \tag{2.4}$$

These reactions form benzene from the combination of two propargyls or from one propargyl and one allyl radicals, passing through the formation of fulvene (⬠=CH₂) as demonstrated by Marinov and co-workers [14,23]. Because of its stability, for a long time propargyl has been assumed to be one of the most abundant intermediates in aromatics formation in many flames [22,24]. Quantum-mechanical calculations show that the chemical activation of the adduct is sufficient to overcome the cyclisation energy barrier to aromatic [13].

A radical suspected of playing an important role during aromatic formation is the cyclopentadienyl $c-C_5H_5$ (⬠˙), which can act as a primary intermediate in pathways leading to one- and two-cycles aromatics.

$$c\text{-}C_5H_5 + CH_3 \rightarrow C_6H_6 + 2H \tag{2.5}$$

$$c\text{-}C_5H_5 + C_5H_5 \rightarrow C_{10}H_8 + 2H \tag{2.6}$$

The first reaction represents the enlargement of the cyclopentadienyl ring to form benzene. As McEnally and co-workers pointed out [25], this reaction is potentially important because of the abundance of the methyl radical in fuel-rich flames, and Melius and co-workers suggested a detailed mechanism of benzene formation through fulvene [14]. The second one, occurring whether the cyclopentadienyl concentration is high enough, is the direct reaction of two radicals to form naphthalene bypassing the benzene step [26].

The synthesis pathway of cyclopentadienyl beginning from propargyl and acetylene is well known [27]:

$$C_3H_3 + C_2H_2 \rightarrow c\text{-}C_5H_5 \tag{2.7}$$

This reaction has been proposed as an important cyclisation step because propargyl and acetylene are very common species existing in high concentrations in fuel-rich flame environments.
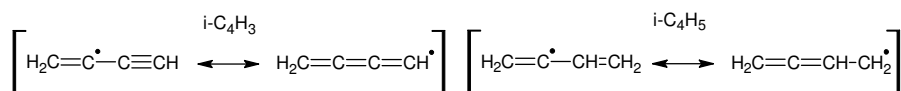
2.1.2. High-temperature stability of hydrocarbons

One of the most relevant works in the theoretical prediction of the high-temperature stability of hydrocarbons has been published by Stein and Fahr [28]. They considered a large number of structures having molecular formula $C_{2n}H_{2m}$ as potentially involved in the carbon polymerisation mechanism leading from small molecular units up to graphitic-like structures. The possible structural formulae consistent with such a general molecular formula belong to classes of molecules potentially completely different under the chemical and thermodynamic profile, and

---

[1]

n-C₄H₃

HC⁼CH–C≡CH

n-C₄H₅

HC⁼CH–CH=CH₂

[2]

i-C₄H₃

[H₂C=C˙–C≡CH ⟷ H₂C=C=C=CH˙]

i-C₄H₅

[H₂C=C˙–CH=CH₂ ⟷ H₂C=C=CH–CH₂˙]

therefore very different polymerisation mechanism may be involved. For instance two major candidates are polyacetylenes and Polycyclic Aromatic Hydrocarbons (PAH).

In their interpretation Stein and Fahr began from strict chemical thermodynamic considerations to predict the most stable isomers (*stabilomers*) of the most stable classes of hydrocarbons under typical flame conditions of pressure and temperature. They stated that, since under those conditions acetylene and hydrogen are among the dominant non-oxygen-containing molecules [29,30], it is possible to discuss the thermodynamic stability of $C_{2n}H_{2m}$ structures in terms of equilibrium concentrations of the reaction:

$$nC_2H_2 \rightleftharpoons C_{2n}H_{2m} + (n-m)H_2 \tag{2.8}$$

Stein and Fahr estimated the equilibrium constant of the above mentioned reaction using the method of group additivity, where a thermodynamic property is calculated by summing the contributions of each of the structural groups that compose the molecule itself. The equilibrium constants obtained this way are conveniently reported in the form of $n \times m$ grids over a range of temperatures and hydrogen and acetylene partial pressures. This representation evidences a diagonal path of high values equilibrium constants corresponding to the thermodynamic most stable structures.

Within the considered temperature range (between 1500 and 3000 K) calculations lead to two different behaviours depending on the relative ratio of hydrogen and acetylene. When $p_{H_2} \geq p_{C_2H_2}$, most species in the stability path are benzenoid PAH with occasionally five-atom rings around the edge. Conversely, when $p_{H_2} < p_{C_2H_2}$ acyclic species like polyacetylenes prevail. In Figure 2.1 the Stein and Fahr's grid containing an example of the proposed structural formulae is reported.
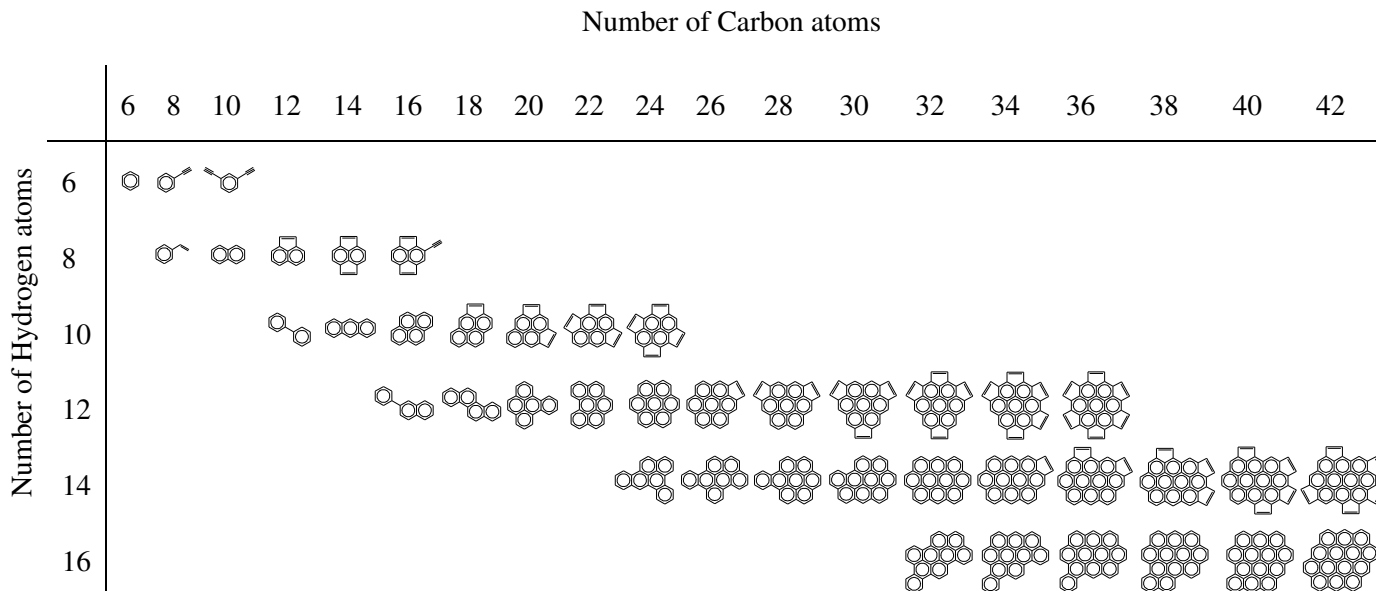

Figure 2.1. Stein and Fahr's stabilomers grid [28].

These results have at least one important consequence. The Authors suggested that PAH are involved as primary intermediates in the molecular growth process occurring in flames, *de facto* predicting a reaction pathway leading from small molecules up to graphite-like structures, which evolves through a logical series of steps involving the species lying in the stability path. These results gave the incipit and a theoretic basis for the development of the HACA growth model which

will be discussed in Paragraph 2.1.3. From there the interest of the H/C diagrams as a representation of the sequence of the PAH detected in flame soot comes as well.

In their original work Stein and Fahr examined only closed-shell hydrocarbons up to forty-two carbon atoms. Molecules having odd number of carbon atoms have not been considered, since they cannot be completely conjugated and therefore they are generally less stable than molecules of comparable structure containing even number of carbon atoms. However Authors noted that the most thermodynamically stable radicals at high temperature generally have both odd H-number and C-number [30].

2.1.3. Growth of PAH via HACA pathway

The HACA mechanism is a repetitive reaction pathway first introduced by Frenklach and Wang [31] and then expanded [32] to describe the PAH growth from the first aromatic up to large molecules and some soot surface reactions. HACA is an acronym standing for "H-abstraction-C_2H_2-addition", and as the name itself suggests that it is a reaction chain involving two different steps. The first step is the activation of a pre-existing aromatic molecule occurring via homolytic cleavage of a C-H bond and following loss of an aromatic hydrogen atom (H-abstraction). The second step is a bonding reaction of acetylene from the gas phase to the radical site created during the fist step (C_2H_2-addition). Following the Frenklach and Wang's notation, the pathway can be described by the two equations:
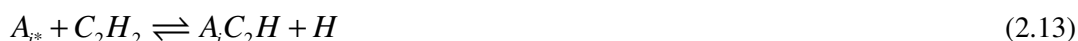
$$A_i + H \rightleftharpoons A_{i*} + H_2 \qquad\qquad (2.9)$$

$$A_{i*} + C_2H_2 \rightarrow products \qquad\qquad (2.10)$$

where A_i represents an aromatic molecule with i peri-condensed aromatic rings and A_{i*} its radical.

The hydrogen abstraction is a highly reversible step which creates the reaction site by converting the molecule to a radical. Many different activators are allowed, but under the conditions of typical shock-tubes and flame experiments the H-abstraction by a gaseous hydrogen atom dominates [26].

On the other hand the reversibility of the acetylene addition determines whether the overall reaction will contribute to the molecular growth. In many cases this second step is reversible, for instance the simple acetylene addition reaction follows the equation:

$$A_{i*} + C_2H_2 \rightleftharpoons A_iC_2H + H \qquad\qquad (2.11)$$

In such a situation, when the second step is reversible, it does not contribute to the molecular growth. Other times the acetylene addition leads to particularly stable products, for which the variation of Gibbs energy following the creation of an extended aromatic layer is large enough to make the acetylene addition practically irreversible. Therefore the overall reaction can be written into the form:

$$A_i + H \rightleftharpoons A_{i*} + H_2 \qquad\qquad (2.12)$$

$$A_{i*} + C_2H_2 \rightleftharpoons A_iC_2H + H \qquad\qquad (2.13)$$

$$A_iC_2H + C_2H_2 \rightarrow A_{i+1*} + H \qquad\qquad (2.14)$$

where the last acetylene addition is now highly irreversible. This is particularly true when the specie A_{i+1*} is a radical associated to one of the stabilomers predicted by Stein and Fahr. The irreversibility of the last step of the reaction chain represents the driving force pulling the above mentioned reactions towards the formation of larger and larger PAH, hopping from one island of stability to another. As Frenklach himself stated, this way the chain of reactions can follow the

smallest thermodynamic resistance. The consequent thermodynamics-kinetics coupling explains [17] the reason for the overcoming of the energy barrier [28] to PAH growth and the appearance of stabilomer sequences during the molecular growth. An example of HACA pathway is reported in Figure 2.2.
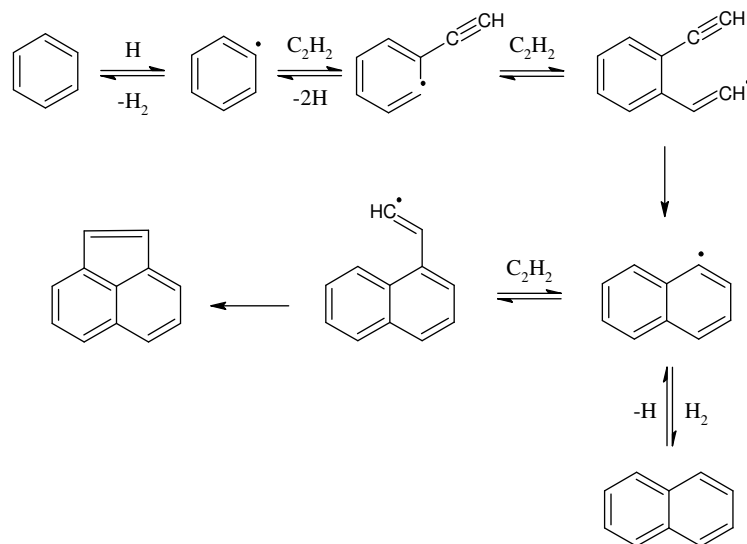

Figure 2.2. Example of HACA pathway leading from benzene to naphthalene and acenaphthylene. The first reaction step is the formation of phenylacetylene (C_8H_6) from benzene. From phenylacetylene a second HACA reaction form 1-naphtyl radical ($C_{10}H_7$). H addition though reaction of H_2 with 1-naphtyl radical leads to naphthalene ($C_{10}H_8$), and a further acetylene addition leads to acenaphthylene ($C_{12}H_8$).

2.1.4. Growth of PAH via other pathways

The HACA mechanism is not the only possible growth reaction pathway occurring in flames. Particularly Frenklach showed that the very first reaction steps are usually fuel-specific [33], like during the combustion of benzene where the aromatic growth is initiated by the formation of biphenyl. However it is interesting to note that the further growth quickly converts to acetylene addition:
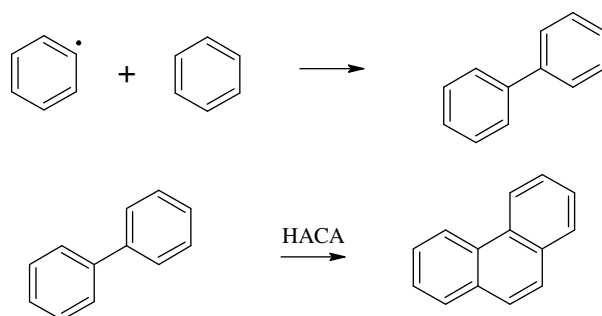
During the formation of two-ring aromatics, an important role is played by resonantly stabilised radicals [25]. Specifically, as already mentioned in Section 2.1.1, the naphthalene can be formed from the combination of cyclopentadienyl radicals, or alternatively via benzyl-propargyl reaction:
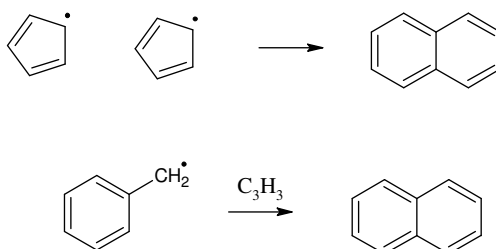
An interesting alternative reaction pathway cooperating with or assisting the HACA growth occurs through the edge migration reactions. This conclusion is the result of an extended theoretical study performed by Frenklach and co-workers [34] on several reaction pathways assisted by hydrogen atom migration. Those reactions include the formation of five- and six- member aromatic rings, the interconversion between them, and the migration of the five-member rings along zigzag aromatic edges [35]. Furthermore, Authors studied the five-member ring migration along a graphene edge, concluding that five-member rings are constantly being formed on the PAH growing edge, but they do not accumulate, being rather converted to six-member rings [36].

2.1.5. Gas phase oxidation of aromatics

The aromatic oxidation occurring in the gas phase is the most important concurrent process of the aromatic growth. The oxidation process is mostly associated to the presence of radicals able to interfere with the aromatic growth, the most important among which has been identified by Frenklach in the molecular oxygen [26]. High concentration of molecular oxygen destroys the radicals needed for the HACA activation step, for instance removing most of the hydrogen atoms from the flame environment. For the same reason the soot inception appears in an environment rich in hydrogen atoms but poor in oxygen molecules. Furthermore, while a small amount of free oxidisers promotes the formation of soot generating radicals capable of sustaining the HACA growth, high concentrations at early stages of the combustion process lowers the amount of carbon available for the soot growth [37].

The oxidation of aromatics removes carbon mass from further growth, but even more important is the removal of mass previous to the PAH formation. This effect is particularly evident when considering the region before the formation of the first aromatic ring, because of the still very high concentration of molecular oxygen. Recurring to numerical simulations performed on sooting acetylene low-pressure flames, the oxidation of C_2H_3 has been found the critical branching point between carbon growth and carbon oxidation [18,38].

2.2. Particle formation

The reactions leading to the formation of soot from the molecular precursors are schematically illustrated in Figure 2.3 and described in the following Paragraphs 2.2.3 to 2.2.6. These pathways include nucleation, surface reactions, coagulation and soot aging.
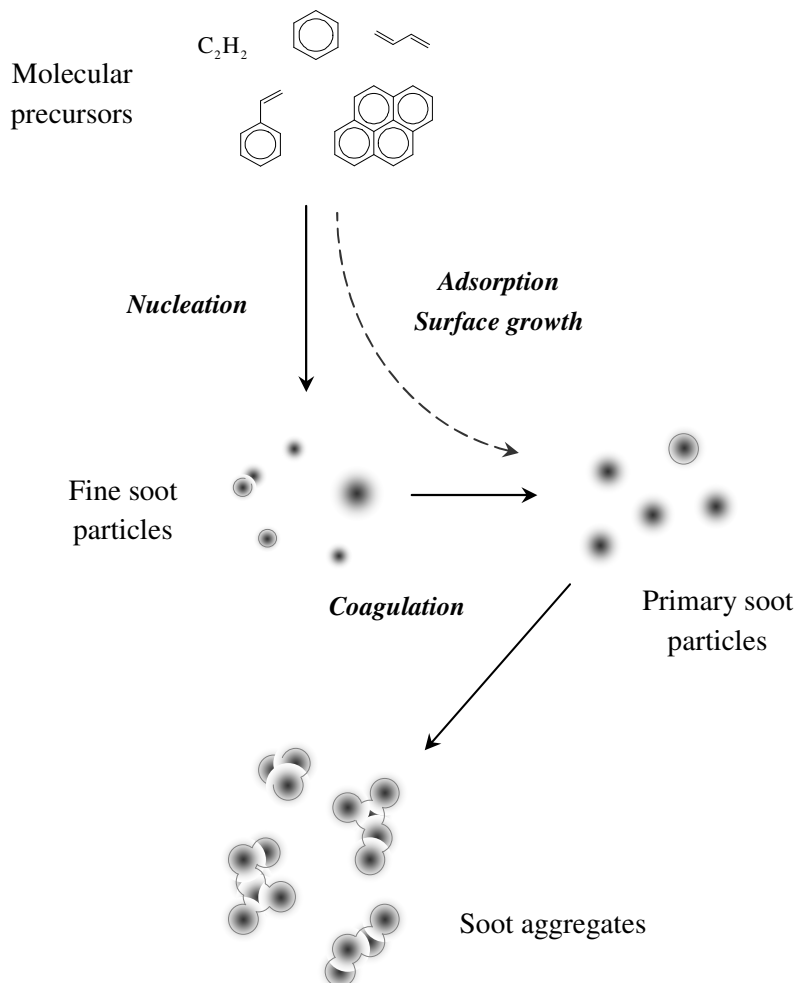

Figure 2.3. Soot particle formation diagram.

During the nucleation or soot inception the very first solid particles are formed from molecular precursors. These particles, named *primary soot particles*, have diameter of the order of few nanometers. The chemical details regarding the formation of nascent soot particles and their direct precursors are still poorly understood, mostly because of experimental difficulties.

Surface reactions include the heterogeneous processes occurring at the particles surface which do not affect the number of soot particles but only their mass. They are usually labelled as surface growth and oxidation: the former increases the particle mass by addition of gas-phase species, while the latter removes carbon mass converting it into CO and CO_2.

The coagulation via reactive particle-particle collisions significantly increases the particle size and decreases the particle number without changing the total mass of soot.

The soot aging describes all the processes taking place in the final stage of the soot growth, thus when the surface growth occurs at negligible rate. These processes shape the primary soot particles into the mature soot.

2.2.1. Structure of soot particles

A detailed analysis of the structure of primary soot particles collected from a diesel engine has been accomplished by Ishiguro and co-workers using High-Resolution Transmission Electron Microscopy [39]. Under transmission electron microscopy soot appears as a collection of necklace-like agglomerates constituted by up to thousands of nearly spherical particles, most of them having diameter between 15 and 50 nm (primary soot particles).

As depicted in Figure 2.4, primary soot particles reveal two different levels of structure, an inner core and an outer shell. The inner core has about 10 nm of diameter, and contains several fine particles having diameter of 3-4 nm each. The fine particles observed in the core are likely related to the very first particles produced during soot nucleation, even if their identity is partly hidden in electron microscopy images because of particle-particle collisions [26]. The outer shell is composed of graphitised layers of carbon, called crystallites, oriented perpendicularly to the radius of the primary particle [39,40]. The thickness of crystallites is around 12 nm, and there are up to 10^3 of them per soot primary particle. Each crystallite is constituted by 2-5 layers of carbon atoms called platelets. The spacing between platelets is 0.35-0.40 nm, only slightly larger than that of graphite. X-ray analysis [41] demonstrated that the carbon atoms platelets are arranged into hexagonal face-centred arrays (*graphene-like* structure).

Soot particles first formed in flames are roughly spherical in shape and have H/C ~ 0.5. During the further growth more processes take place and the very early particles are converted up to the mature soot. Particle coagulation, surface reactions and oxidation transform the nascent particle in the soot found in the exhausts, characterised by an underlying graphitic-like structure and H/C ~ 0.1 [17].
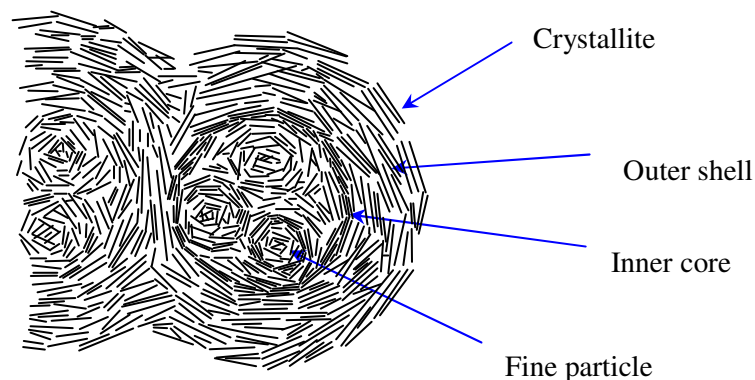

Figure 2.4. Structure of Diesel soot particles obtained by Ishiguro and co-workers via High Resolution Transmission Electron Microscopy [39].

A recent advance supporting and completing the analyses of Ishiguro and co-workers on the structure of the early soot particles have been carried on by Maricq [42] and Sgro and-co-workers [43,44]. In these works ex-situ Differential Mobility Analyses (DMA) and Atomic Force Microscopy (AFM) have been performed on soot sampled from premixed diffusion flames, and the results compared with in-situ optical measurements. These techniques have been chosen because of their sensitivity in detecting particles smaller than 5 nm diameter.

The measurments generally revealed bimodal distribution of soot. The upper mode is constituted by the heaviest particles having diameter from 5 up to 50 nm. They show the typical features consistent with the conventional measurements, like light scattering and TEM, which evolve as a function of the reaction time. Their number decreases due to coagulation, but the volume fraction increases because of the surface growth. On the other hand, the lower mode is constituted by light particles having less than 5 nm diameter, and it has been detected in most, but not all flames. Interesting enough, this behaviour seems not to be dependent on the Height Above the Burner (HAB), thus these fine particles survive even in the later stages of the combustion process, suggesting that coagulation process may persist high in the flame. This mode has been first revealed by Sgro and co-workers [45], and the co-existence of different kinds of soot particles has been recently corroborated by photoionisation mass spectrometry analyses on low pressure flames by Grotheer and co-workers [46].

2.2.2. Particle nucleation

The nucleation or soot inception is the transition process leading from a molecular to a particulate system. This is by far the less understood step of soot formation, and because of the difficulty of collecting experimental data a comprehensive model explaining the soot nucleation is still lacking.

A central issue in the understanding of the nucleation is the definition of the molecular mass range in which the soot inception takes place, and thus where the concept of "soot particle" becomes physically meaningful. During the last twenty years this investigation has been the subject of several works, the most prominent of which set the soot inception in the region of 300-700 u [47], 700 u [46], 1600 u [48] and 2000 u [49].

Several hypotheses have been proposed to model the soot inception, among which the most widely discussed and accepted by the scientific community is based on the HACA reaction mechanism and it has been first proposed by Frenklach and Wang in 1991 [31]. During the two last decades this hypothesis has been expanded and modified to take into account the ongoing experimental measurements [50-52]. The core idea is that at some size the PAH begin to stick together during collisions essentially because of Van der Waals interactions [53,54], forming PAH dimers which are *assumed* to be the very first solid particles. PAH dimers undergo further growth by collision with other similar species (thus forming multimers), while individual PAH keep increasing in size via molecular chemical growth reactions. Thus the core idea of the model is that the growth of the surface (formation of new C-C and C-H bonds) and the collisional growth (inter-planar interactions) go along simultaneously. In order to perform numerical simulations the pyrene (202 u) is often arbitrarily considered as the lightest PAH capable to give a dimerisation reaction [55].

Recently [26] Frenklach observed that two limit situations may occur. If the chemical growth is limited by high reaction reversibility then the aromatic growth is possible only if the system

switches to an acetylene-based HACA. This way the growing PAH are dominated by the Stein's compact stabilomers while other species decompose. Once formed, the stabilomers may create physically-bound clusters when colliding. Otherwise, in presence of very low reaction reversibility there is no thermodynamic limitation on the structural form the growing molecule may assume, because the inverse reactions are too slow to counterbalance the direct reactions. This leads to the formation of a variety of chemical structures as a result of collisions with different gaseous species, for instance complex networks of aromatic-aliphatic-linked structures.

As a concluding remark, an interesting alternative proposal about the transition from 2D to 3D structure comes from a work of Zhang [56] whose interest has been recently renewed following the discovery of the high mobility of 5-atoms rings [35]. Zhang observed that in an extended benzenoid structure, i.e. a large PAH constituted only by 6-atoms rings, the presence of 5-atoms rings cause the structure to fold up like in fullerene-like molecules, thus generating a 3D structure.

2.2.3. Particle coagulation

During the soot coagulation several fine particles produced during the nucleation step stick together and form aggregates that are quickly covered by an outer shell generated by material deposition from the gas phase. The coagulation increases the particle size and decreases the particle number without changing the total mass of soot.

Particle coagulation is typical of early combustion stages, where the surface growth is fast enough to generate a spherical outer shell [57]. This point is easy to realise when considering the quasi-spherical shape of the primary particles due to the smoothing effect of the surface growth, which literally buries the smaller colliding particles. Whether the colliding particles are too large or the matter deposition too slow, the surface growth is not efficient enough to cover the underlying structure, and the spherical shape of particles is lost. Small colliding particles and fast surface growth are typical of early combustion steps, thus the particle coagulation rate quickly decreases as the combustion progresses. This argument is further supported by numerical simulations [58], and the mathematical treatment needed to describe this regime is borrowed from the field of aerosol dynamics [26].

2.2.4. Surface reactions

The nascent particles produced during the nucleation step can undergo a certain number of chemical modifications. These are heterogeneous processes where the surface of the particle plays an active role, and where adsorption and desorption have to be considered. For this reason assumptions on the structure of the soot surface become critical.

Frenklach [26] invoked the principle of chemical similarity to describe the soot surface similarly to that of large PAH. In other words, the surface of soot particles is assumed to be covered with terminal C–H bonds like the edge of PAH. The main advantage of this assumption is the possibility of treating the surface reactions in terms of elementary chemical reactions analogously to the case of gaseous PAH growth/oxidation. The abstraction of surface hydrogen atoms forms surface radicals. The sites activated this way can react with incoming gaseous species, both hydrocarbons that propagate the growth and oxidizing agents that remove the carbon from the surface. The main

reactants are assumed to be acetylene/PAH [26] in the case of soot growth, and O_2/OH radicals in the case of soot oxidation.

The surface growth causes the particles to increase their mass without changing their total number. Furthermore, a high rate of surface growth is responsible of the spherical shape of the primary soot particles. This process determines the amount of carbon mass accumulated on soot via gas-surface deposition. Because of the lack of precise data, a phenomenological approach describing the soot volume fraction is usually adopted. The soot volume fraction f_v is defined as the soot volume per unit volume:

$$f_v = \frac{V_{soot}}{V}$$ (2.15)

In premixed flames, its time evolution is usually described by a first order differential equation:

$$\frac{df_v}{dt} = k_{sg} \left(f_v^\infty - f_v \right)$$ (2.16)

where k_{sg} is the temperature-dependent surface growth rate coefficient only depending on the flame experimental conditions [59]. f_v^∞ is a fitted parameter representing the total volume fraction of formed soot. It should be noted that the mass growth rises to an asymptotic value, i.e. the soot growth approaches a final steady state. Due to its very phenomenological nature, the former Equation (2.16) do not contain any dependence on gas-phase species concentrations.

An example of the ongoing debate on the nature of the surface growth process is the role of acetylene and PAH as the main responsible of the surface growth. Because the surface growth occurs in environments of acetylene abundance, an extension of the HACA model to surface reactions seems straightforward. The hypothesis on which the surface HACA is based is the chemical similarity, which postulates that the chemical reactions occurring on the soot surface are analogous to those of large PAH [26,32]. Once assumed that the surface of soot particles behave similarly to the edge of a PAH (i.e. it is covered by C-H terminal bonds), it is possible to make hypotheses on the specific nature of the surface active sites and then on the elementary chemical reactions taking place on the particle surface. Particularly, the abstraction of hydrogen atoms activates the sites generating surface radicals which can then react with gas-phase species, both hydrocarbons that propagate the growth and oxidisers that remove carbon from the surface. This mechanism was originally assumed to take place via a single irreversible step in which an additional phenomenological parameter quantifyied the changing morphology of the soot particle surface. The so-defined surface HACA is consistent with the analysis of Harris and Weiner [60], who proposed a simplified model describing the soot volume fraction growth for a premixed ethylene/air flame in which the soot mass growth rate is only proportional to acetylene gas phase concentration:

$$\frac{df_v}{dt} = k_{C_2H_2} p_{C_2H_2} S$$ (2.17)

where f_v is the soot volume fraction, $p_{C_2H_2}$ is the partial pressure of acetylene in gas phase and S is the soot total surface area. However, fourteen years later Benish and co-workers [61] reproduced the particular flames investigated by Harris and Weiner, and identifying twenty-six small PAH via High Performance Liquid Chromatography (HPLC). They assumed that PAH growth was the net effect of acetylene addition to PAH and PAH addition to soot, while soot growth resulted from addition of acetylene and PAH.

Soot particles oxidation is the heterogeneous process in direct competition with the surface growth. Oxidation reactions take place on the surface of soot particles, decreasing their mass

without changing their total number and converting the removed carbon to CO and CO_2. Unlike the soot surface growth, which occurs in a well delimited combustion stage, soot oxidation extends over the entire course of soot formation. The main oxidation reactants are OH, O and O_2. Particularly, Neoh and co-workers [62] and Lucht and co-workers [63] noted the soot volume fraction decreases when increasing the gas-phase OH concentration, and concluded that OH is the limiting oxidative reactant under fuel-rich condition.

2.2.5. Soot aging

Soot aging is a term naming all the physical-chemical changes responsible for the conversion of the young soot to the mature particulate found in the exhausts. During this step the surface growth rate decreases and the primary particles tend to aggregate [64,65]. The aggregates formed during this step are chemically and morphologically very different compared to earlier growth steps, since the surface growth occurs at negligible rate. Particles do not coagulate any more, but rather stick together forming chain-like aggregates and open structures characterised by fractal geometry [26].

The most relevant phenomenon occurring during soot aging is the progressive soot graphitisation, that is, from a chemical point of view, the reduction of the number of active sites capable of sustaining the overall growth process. Functional group elimination, cyclisation, ring condensation, decrease of the H/C ratio, growth and alignment of the polyaromatic layers are all processes occurring during this final growth step. Particularly, the decrease of hydrogen atoms available in the gas phase reduces the kinetic driving force of the HACA as the system moves toward equilibrium.

2.3. Concluding remarks

In this Section the main reaction pathways responsible of the soot growth have been presented. These pathways have been implemented in several numerical tools devoted to the modelling of the soot growth process under different combustion conditions, like flames, jet-stirred reactors and shock tubes [26,66].

The description of the detailed models is beyond the goals of the present work. However, the validation of a model ultimately lies on the comparison between the predicted values and the experimental data, and therefore a large number of information on the soot size distribution, on the soot profiles, and on the detailed structure of PAH is required. Particularly, the idea that the PAH actively contribute to the soot growth and participate to the gas phase/particle surface heterogeneous mass transfer moves the attention to the chemical analysis of the adsorbed phase on soot particles. When the soot is sampled from the combustion environment, the stable PAH persisting in the phase adsorbed on its surface are related to those formed during the combustion process, and therefore they give information about the islands of thermodynamic stability [28], through which the PAH and soot grow.

Chapter 3.

Detection of PAH adsorbed on soot: laser techniques/mass spectrometry

The inception of soot from large molecular precursors is the less explored area of the whole soot formation path. This transition regime is difficult to follow essentially because of the lack of diagnostics able to efficiently detect *large* molecular species or *small* solid particles. The situation is particularly complex since the exact definition of the border running between a large molecular system and a small solid structure still represents an unresolved epistemological problem. The ongoing scientific research produced an impressive amount of documents during the last fifty years, and currently the answer to this issue is thought to be hidden in the mass distribution function of the combustion-formed species detected along the whole soot formation pathway. The mass of the involved species, both molecular and solid, is the easiest accessible physical quantity to measure during the transition, and therefore it is assumed to be one of the keys for understanding the soot nucleation process.

The determination of the mass of the combustion-formed species can provide two levels of information. The first one is about the thermodynamic stable molecules adsorbed on soot, which are strictly related to those involved in the soot formation, and which participate to the very carbonaceous structure of the particles themselves. The second level of information concerns the range of masses detected in the transition regime, which has been narrowed down to the mass interval going from 300 up to 2000 u during the last twenty years of investigation [46-49]. Carbon-rich particles having mass in that range have molecular structures consistent with aggregates having 1.0-1.5 nm of diameter [8].

The soot inception mass regime is usually explored using *ex-situ* chromatographic techniques like High Performance Liquid Chromatography (HPLC) and Gas Chromatography coupled with quadrupolar Mass Spectrometry (GC-MS), which give information on the masses up to 300-400 u. Also, *in-situ* laser-based diagnostics like Laser Induced Incandescence (LII) are commonly used, which allows the detection of particles having size down to the nanometer scale. However, while HPLC and GC-MS are well suited for detecting molecular species below 300-400 u mass, they completely fail when higher masses are sought [67,68]. Analogously the black-body emission on which LII is built only occurs when a laser beam encounters and heats solid particulate matter, thus the LII can only provide information after the nucleation has begun. The diagnostic gap occurring

between chromatography and LII has been filled by Fourier Transform Mass Spectrometry (FT-MS) [69] and by Time-Of-Flight Mass Spectrometry (TOF-MS) subject of the present work, which are able to give information on a large mass range going from the molecular regime up to the mesoscale. The main advantage of the TOF-MS is its virtually unlimited mass range, allowing in principle the simultaneous detection of masses ranging from the small molecules characteristic of the fuel oxidation regime up to the carbonaceous solid particles typical of the later soot growth. Particularly, when the ions are produced via photoionisation instead of the traditional electron impact, a smooth energy transfer to the analytes into the gas phase can be provided, thus completely avoiding the parasite phenomena, like photo-dissociation, which affected the earlier analyses. As a consequence, in the above mentioned mass range, going from 300 up to 2000 u, the number of signals detected via photoionisation mass spectrometry is still reasonably small. Therefore once the classes of molecules involved in the soot formation are known from thermodynamic or kinetic calculations [28] it is possible to assign a molecular formula to each signal peak.

The fundamental arrangements of the photoionisation mass spectrometry are schematically illustrated in Figure 3.1. They basically consist in a first analysis step required to bring the analytes into the gas phase followed by a laser ionisation which produces the ions to be mass-analysed.

In order to get the analytes into the gas phase two major methods are currently being used: desorption-based and molecular beam-based. In the former the transition of the analyte to the gas phase is induced via thermal effect or via direct energy transfer with an optical field (Figure 3.1a). The laser desorption is particularly suitable for detecting the molecules weakly bounded to the soot surface (adsorbed and condensed), but the attainable mass range is upper limited by the very low vapour pressure of the high-mass analytes. Alternatively the sample, including both gaseous species and solid particles, can be sent as a molecular beam directly into the mass spectrometer as detailed below (Figure 3.1b). In this case all the components of the molecular beam, there included the large particles, can be ionised and thus detected, but it is not possible to distinguish between the particles and the adsorbed/condensed matter.

The coupling of the photoionisation mass spectrometry with the desorption step or alternatively the molecular beam technique is obtained at the level of the analysis chamber of the mass spectrometer (Chapter 4). As shown in Figure 3.1, in the general case each one of the three axial dimensions is dedicated to one specific process, where the origin of the Cartesian coordinate system represents the analysis chamber of the mass spectrometer. This 3D configuration is not only an attractive way to couple different techniques, but, as discussed in Section 4.1, it brings specific advantages to the mass analysis.

During the last decade laser photoionisation coupled to the time-of-flight mass spectrometry has been used as a method for the analysis of high molecular mass species involved in combustion processes. However, a number of different experimental configurations have been reviewed. All the versions of the photoionisation mass spectrometry share a laser-induced ionisation step to produce ion packets which are detected via time-of-flight mass spectrometry. And there the common features end. The ways in which the analytes are brought into the gas phase before the ionisation and the ionisation step itself are subject to important variations, and new methods are currently being tested. For instance, a fairly common version of the desorption-based photoionisation mass spectrometry uses a single laser pulse to perform one-step desorption/ionisation of the analytes.
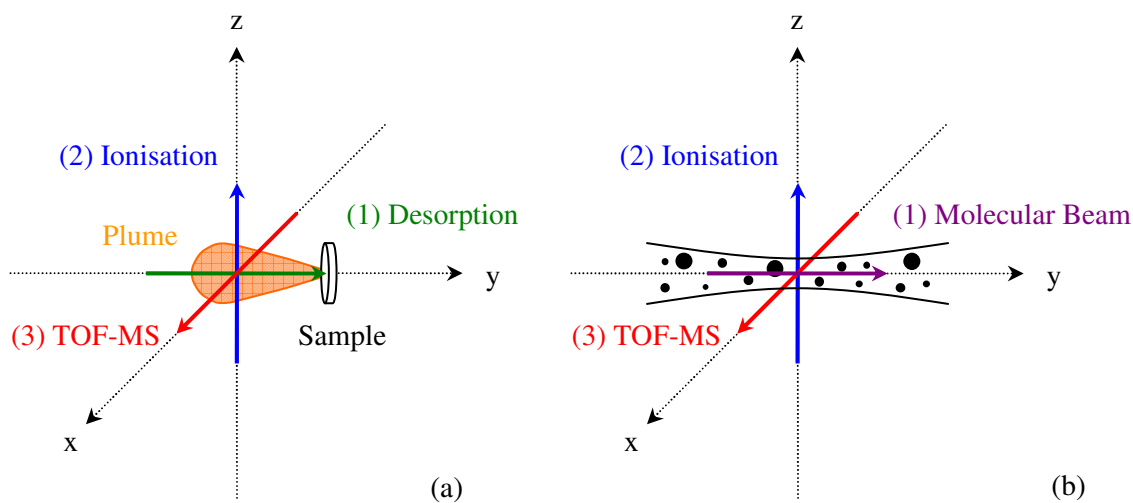
Figure 3.1. Coupling of the three techniques in the photoionisation mass spectrometry experimental setup and analysis dynamic. (1a) The desorption laser pulse irradiates the sample surface / (1b) the molecular beam is sent into the ionisation chamber of the mass spectrometer. (2) The plume of neutral desorbed molecules / the molecular beam is irradiated by the ionisation laser pulse, which produces the ions finally analysed via (3) Time-Of-Flight Mass Spectrometry.

Each research group carries out a particular experimental solution depending on the results aimed to, or on the availability of the specific laboratory equipment. As a result, the scientific literature does not contain two series of measurements performed under the same experimental conditions, and therefore the critical analysis of the published results becomes crucially important for understanding the physical meaning of the measurements themselves.

This Section aims to give to the Reader a general overview of the photoionisation mass spectrometry-based methods applied to the analysis of the phase adsorbed on soot particles. Section 3.1 focuses on the desorption-based version, while Section 3.2 on the molecular beam-based version. Paragraph 3.1.6 describes the most relevant experimental solutions implemented by different research groups. This discussion does not claim to be exhaustive, but rather aims to discuss some particularly relevant published results in the context of both the data interpretation they suggest and the specific experimental modifications introduced in the setup.

3.1. Desorption photoionisation mass spectrometry

In the present work a Laser Desorption (LD) method has been developed. In such a setup the surface of a solid sample is first irradiated by a nanosecond laser pulse. As a consequence of the energy transfer, thermal desorption of neutral species occurs from the sample, and the desorbed analytes form a plume of gases expanding in the high-vacuum of the mass spectrometer. The independent control of almost all the parameters associated to the measure, particularly the possibility of changing independently the lasers wavelength, irradiance, and timing of the pulses is likely the main advantage of this setup.

Before proceeding any further into the discussion, a brief note on the quantification is required. As Zenobi and Zare pointed out [70], the nature of the recorded mass spectra (intensity and occurrence of the signals) strongly depends on several experimental parameters (beam geometry, laser wavelengths, desorption/ionisation delay and so on). Therefore the quantitative analysis via laser desorption photoionisation mass spectrometry still remains very difficult. Semi-quantitative analyses are usually performed by comparing the ratio of signal intensities of an analyte to an internal standard. Some Authors reported evidences about the ways these ratios are influenced by a certain number of experimental parameters. Particularly the ionisation laser setup is found to be the most difficult parameter to control, and the one giving the most practical limitations [71].

3.1.1. Soot sampling

The first issue to be faced when analysing soot is how to collect it, and some major methods which have been successfully performed are discussed. For instance, when dealing with flames or shock tubes, the simplest solution is the deposition of the combustion products (both gases and particles) on a solid support suitable for subsequent mass analysis. This Paragraph lists the most common ex-situ sampling methods. They all need to be coupled with a desorption step in order to bring back in the gas phase the combustion products to be mass-analysed. The discussed methods are: thermophoretic sampling, chemical extraction using organic solvents, online deposition, direct deposition on a metal target behind a shock wave, and extractive probing followed by deposition on a glass filter.

Dobbins and co-workers (Laser Microprobe Mass Spectrometry, LMMS) perform thermophoretic sampling on atmospheric flames [72,73]. This method takes advantage of a temperature gradient created by introducing a cold metal slab into the hot flame environment to cause small particles to stick on the surface of the slab. In fact, because of the temperature gradient generated by the cold slab, small enough particles acquire a linear momentum directed towards the surface of the slab, where the particles stick after the collision [74,75]. If the slab is small enough, it can be pneumatically driven into the flame (generally radially with respect to the flame flow) reaching ±0.5 mm spatial resolution and minimising any flow perturbation. In their analysis, Dobbins and co-workers use an electron microscope grid as a collecting slab. The main advantage of the thermophoretic sampling is the small occurrence of gas condensation phenomena at the slab surface. On the other hand, the collected amount of matter is potentially as small as 10^{-12} g [72], thus the same slab must be introduced several times into the flame in order to get detectable signals.

While Dobbins aimed to extract a small amount of matter minimising the flame perturbations, Apicella and co-workers (Laser Desorption Ionisation Time Of Flight Mass Spectrometry,

LDI/TOF-MS) chose the opposite approach, recovering a massive amount of soot and condensed gases [76,77]. In their setup, the combustion products are collected from the flame using a stainless steel water-cooled probe, having a 2 mm-orifice and introduced axially into the atmospheric flame. This collecting procedure allows recovering mg of soot and condensed gases from both the probe walls, and from a Teflon filter and an ice-cooled trap placed downstream in the sampling line. The combustion products are extracted with dichloromethane until no detectable UV-fluorescence signal in the washings indicates that the exhaust carbonaceous soot is clean. The TOF-MS target is then prepared by deposition of the extract solution on the surface of an aluminium slab, which is then moved to the ion source of the mass spectrometer once the solvent is removed. Currently Apicella and co-workers perform a full collection of all the combustion products deposed along the whole sampling line.

Öktem and co-workers (Photo-Ionisation Aerosol Mass Spectrometry, PIAMS) take advantage of an original compromise between online and offline sampling [5,78]. In their setup the combustion products are directly sent into the mass spectrometer, and there deposed on the surface of a metal target located in the ion source. The deposed substance is then desorbed using a Near Infrared pulsed laser source, and the plume of neutral gases ionised with a second UV pulsed laser.

Mathieu and co-workers (Laser Desorption Ionisation Time of Flight Mass Spectrometry, LDIToFMS) study the pyrolysis phenomena in shock tubes [6,79]. In their setup the sample is a slab of metal inserted at the end of the shock tube, which got covered by the combustion products once the shock wave passes away. The slab is inserted in the ion source of the mass spectrometer without further treatment.

Finally, in this work (Laser Desorption Laser Ionisation Time-Of-Flight Mass Spectrometry, LD/LI/TOF-MS) the sampling is accomplished via a quartz extractive probe. From the probe, the collected gases enter a short sampling line and then pass through a borosilicate glass filter on which the soot particles deposit. The collected mass amount varies from hundreds of ng when sampling low pressure flames up to tenth of µg when sampling atmospheric flames. The glass filters covered by soot are cooled down to -160 °C to avoid the spontaneous desorption of the most volatile species, and introduced into the ion source of the mass spectrometer without further preparation. It is important to point out that this *modus operandi* cannot avoid the condensation phenomena of the gaseous PAH on the soot deposed on the filter.

Removing the combustion products perturbs all the equilibriums they were involved in the flame environment. A big concern when sampling soot and semi-volatile organics is that heterogeneous particles/gas phase equilibriums are involved as well. Particularly the gas-phase PAH can adsorb on the surface of particles. Thus *a priori* it is difficult to distinguish the PAH initially adsorbed on soot from those in the gas phase which condensed during the sampling procedure.

Öktem and co-workers [5] demonstrated that under high sampling dilution conditions $(1:10^3 – 1:10^5)$ the soot morphology is not affected by the dilution ratio, and shape and distribution function of the particles do not change any longer varying the dilution ratio. They finally concluded that this way the condensation phenomena are completely avoided.

3.1.2. Laser desorption

The absorption of laser light on a solid target can induce four different phenomena as a function of the peak irradiance at the sample surface. These situations are usually referred as desorption, phase explosion, hydrodynamic sputtering and photomechanical spallation [80,81]. The laser desorption is the only low-energy process which involves a molecular ejection without causing the destruction of the sample surface. It has no bottom irradiance limit. Phase explosion, hydrodynamic sputtering and photomechanical spallation are known under the collective name of laser ablation, being more dramatic processes involving the sample's bulk properties and often causing the partial or total destruction of its surface. Ablation phenomena are used in specific analytical techniques, most notable example is the phase explosion which is the basis of the MALDI (Matrix Assisted Laser Desorption Ionisation) techniques [82].

The role of the desorption step in photionisation mass spectrometry is twofold. First, the desorption is the process generating the gas plume containing the analytes to be mass-analysed. Second, whether the energy transferred to the sample is small enough, it is possible to produce a thermal desorption of the weakly-bounded species without affecting the underlying carbon matrix (Section 5.2). In other words, it is possible to induce the transition to the gas phase of the molecular species adsorbed and condensed on the soot particles without breaking the much stronger chemical bonds responsible for the structure of the particulate themselves. Furthermore a low-irradiance regime is a required condition to avoid the direct ionisation of the ejected molecules. This issue becomes particularly important if a selective ionisation of the ejecta is sought (see also Paragraph 3.1.3).

In the present work the desorption step is a *soft* energy transfer from the optical field to the soot carbonaceous matrix induced in the nanosecond time regime by 532 nm wavelength laser pulses. The following energy transfer between the matrix and the species adsorbed and condensed on it ultimately causes the desorption of neutral molecules. In the low-irradiance regime the ejection of matter from a surface can be described by a molecular desorption process, where an Arrhenius-type expression is well suited for predicting the number of molecules N ejected from the sample surface, following the equation [83]:

$$N = A \exp\left(-\frac{E_s^*}{k_B \left(T_0 + B I_{des}\right)}\right) \tag{3.1}$$

where A is the pre-exponential factor, E_s^* is the activation energy, k_B the Boltzmann's constant, T_0 the initial temperature of the surface, I_{des} the desorption irradiance and B the thermal conversion efficiency. Such a model only works when I_{des} is smaller than a threshold value. Above this threshold, which reflects the qualitative change in the ejection mechanism, the thermal model is valid no longer and a different description must be used.

Since in the present work the desorption is ultimately a thermal process, there is an upper limit of the molecular mass beyond which the vapour pressure is totally negligible, i.e. the analytes are not enough volatile for being desorbed. In this case raising the laser power to switch to the high energy ablation regime does not solve the problem, because the important amount of energy delivered to the sample often induces dissociation phenomena on the vaporised matter as well (*hard* laser desorption). Since the analytes detectable in this experimental configuration all belong to the same class of molecules (PAH), they would all produce the same dissociation pattern, and thus it would not be possible to distinguish the precursor ions.

The desorption step can be performed simultaneously with the ionisation, i.e. a single laser pulse is delivered to the sample surface (Dobbins' LMMS [72,73], Apicella's LDI/TOF-MS [76,77] and Mathieu's LDIToFMS [6,79]), or otherwise as a two step procedure where a plume of gases is generated by a first laser pulse, while the ions are produced by a second different laser pulse (Öktem's PIAMS [5,78] and this work LD/LI/TOF-MS, see Chapter 4).

3.1.3. The ionisation step

The ionisation is likely the most critical step of the whole analytical procedure dedicated to PAH analysis. In order to set the Reader comfortable with the energy involved in the ionisation of PAH, Figure 3.2 reports the ionisation energies of 132 benzenoid PAH and some substituted low-mass PAH carrying a short side chain ($-CH_3$, $-CH = CH_2$, $-C \equiv CH$). The values are plotted as a function of the number of carbon atoms contained in the molecule. As the carbon number rises and the aromatic layer increases its size, the ionisation energy falls from above 9 eV down to 6.5-7.0 eV [84].
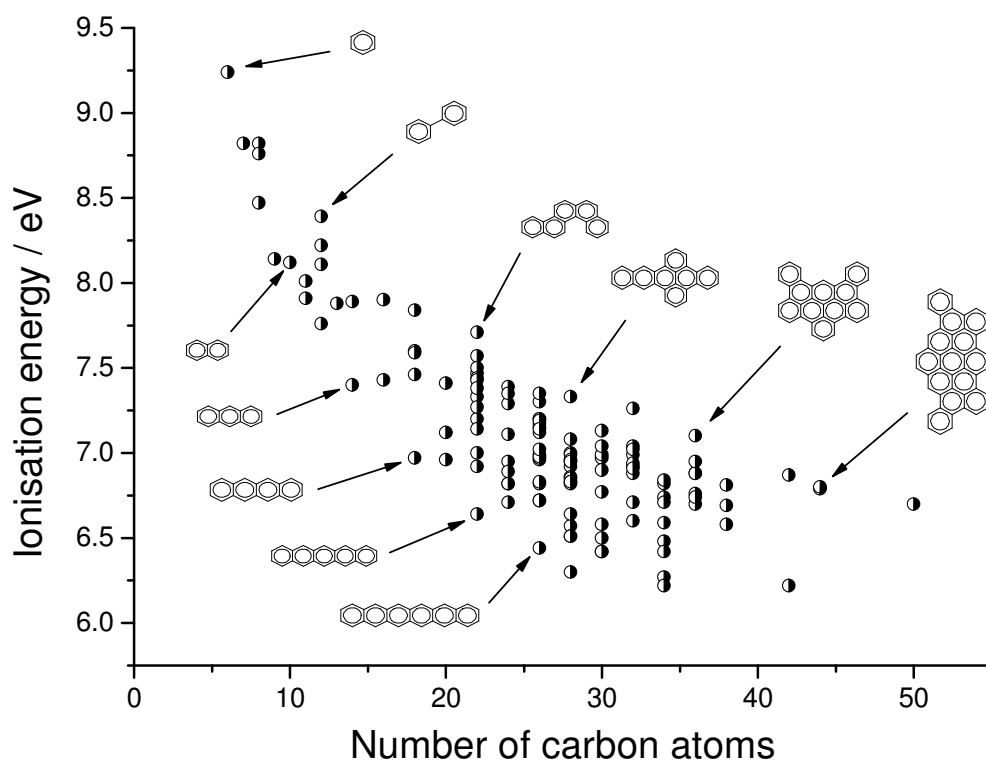
Figure 3.2. Ionisation energies for 132 benzenoid PAH and some substituted PAH carrying a short side chain (–CH₃, –CH=CH₂, –C≡CH) as a function of the number of carbon atoms contained in the molecule. Data have been collected from the NIST database [84]. Benzene is not properly a PAH, but it has been reported as a reference since it has the highest ionisation energy of the series (IE = 9.24 eV). No data are available for PAH larger than 626 u (50 carbon atoms).

In this energy range (6-9 eV) a single-photon ionisation method is difficult to get experimentally since it would require a laser input wavelength in the vacuum UV (<180 nm). On the other hand, when a powerful enough laser source is available, a multi-photon absorption-based method can be performed.

During a multi-photon absorption an atomic or molecular system makes a transition from its ground state up to an excited state absorbing simultaneously more than one laser photon. Such a transition only involves virtual states, while the real states of the excited atomic or molecular system are not necessarily concerned during the process. If the energy of the final state exceeds the ionisation energy of the system, one electron is permanently removed and therefore the overall process is referred as Multi-Photon Ionisation (MPI). The main advantage of using a multi-photon ionisation is that levels not connected to the molecular ground state by one-photon transitions become readily accessible.

The near UV is usually a good choice for the ionisation wavelength, since most PAH have large absorption cross sections in this spectral region [85]. Furthermore in the near UV ionisation energies up to 9 eV can be easily reached via a two-photon absorption process. The order of the MPI (i.e. the number of simultaneously absorbed photons) is crucial since gaining access to nonlinear processes requires higher and higher input power density. Whenever a too long excitation wavelength is used, high laser irradiance must be set to promote a multi-photon absorption up to the ionisation threshold, and this usually leads to unwanted ion dissociation phenomena as well. Therefore the order of the MPI should be kept as lower as possible.
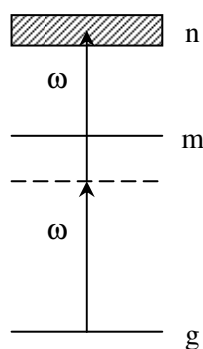
The simplified scheme of the two-photon ionisation process is depicted on side: ω is the frequency of the optical field, g is the atomic/molecular ground state, n the final state which is possibly spread into a density of states $\rho_f(\omega_{ng})$, and m one of the intermediate states of the system (not concerned in the process and thus spectrally far from ω). In this case a time-independent transition rate for the process $R_{ng}^{(2)}$ can be defined as follows [86]:

$$R_{ng}^{(2)} = \sigma_{ng}^{(2)}(\omega) I^2 \qquad (3.2)$$

where $\sigma_{ng}^{(2)}$ is the two-photon absorption cross-section, defined to be only dependent on molecular properties like the electric dipole transition moments, the resonance frequencies and the density of final states. I is the irradiance of the input laser beam.

A fairly common choice for this kind of analyses, including this work, is the two-photon ionisation at 266 nm (4.66 eV), which is easily attainable being the Nd:YAG fourth harmonic. Of course the two-photon ionisation at 266 nm is not the only possible choice for the photoionisation of PAH, and different research groups performed their own custom solution following specific purposes which will be discussed in Section 3.1.6, or simply the equipment available in the laboratory. A brief summary of these solutions is reported in Figure 3.3, where the gray points represent the ionisation energies of several PAH (the same as in Figure 3.2), while the arrows represent the ionisation methods chosen by different groups. These experimental solutions cover a spectral region going from the one-photon at 118 nm chosen by Öktem and co-workers [5,78], down to the two- or three-photon ionisation at 337 nm chosen by Apicella and co-workers [76,77].
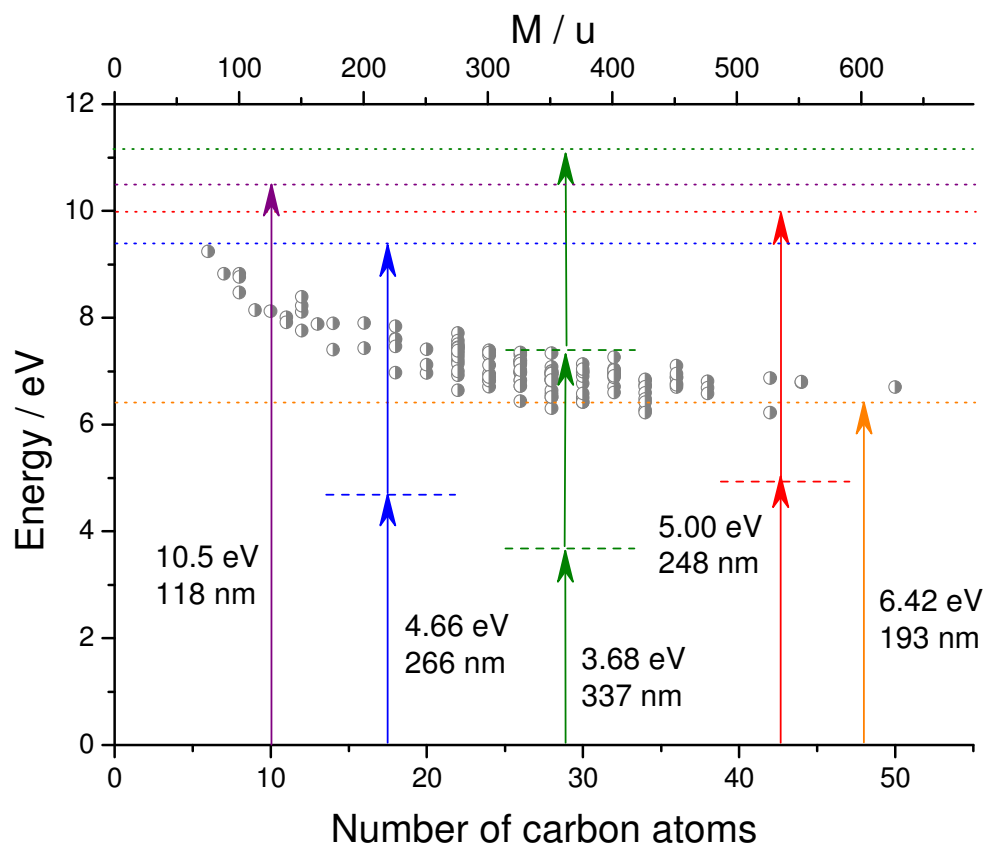
Figure 3.3. Experimental solutions adopted for the ionisation step. The gray dots represent the ionisation energies of PAH, the same as in Figure 3.2. The purple arrow represents one-photon ionisation at 118 nm (Öktem [5,78]), the blue arrows two-photon ionisation at 266 nm (Dobbins [72,73], Mathieu [6,79] and the present work), the green arrow two- and three-photon ionisation at 337 nm (Apicella [76,77]), and finally red and orange arrows represent respectively two-photon ionisation at 248 nm and one-photon ionisation at 193 nm (Grotheer [46,87]).

REMPI

Resonance Enhanced Multi-Photon Ionisation (REMPI) is a special case of the multi-photon ionisation. REMPI occurs when a real state of the molecule (intermediate state, m) is spectrally

very close to one of the virtual states generated by the optical field (ω). Under these circumstances, the absorption of the first photon becomes a real spectroscopic transition depending on the level structure of the excited molecule, and thus subject to resonance conditions. When the first photon absorption is resonant, a selective excitation can take place from the intermediate level, leading to the high-efficient overall ionisation. The most favourable case of one-colour (one laser wavelength) two-photon ionisation, (1+1) REMPI, is illustrated in the side scheme.
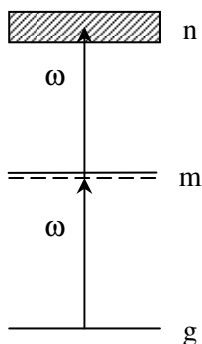
Actually two situations potentially limiting the ionisation efficiency have to be considered [88]. Since the real state m is involved in the transition, the absorption of the two photons is not

necessarily simultaneous, and therefore the properties of the intermediate state play a role on the efficiency of the REMPI transition. Particularly, large Franck-Condon factors, i.e. a sufficient overlap between the wavefunctions of the intermediate state and the ground and arrival state are required in order to get a high transition rate. This situation is illustrated in the scheme (a) below. Furthermore the intermediate state must not relax too quickly, leading for instance to Inter-System Crossing (ISC) or dissociation, as depicted in the scheme (b) below. In other words the lifetime of the intermediate state has to be long enough to allow the absorption of the second photon. If all these conditions are fulfilled, the REMPI overall efficiency is large.

(a)   (b)
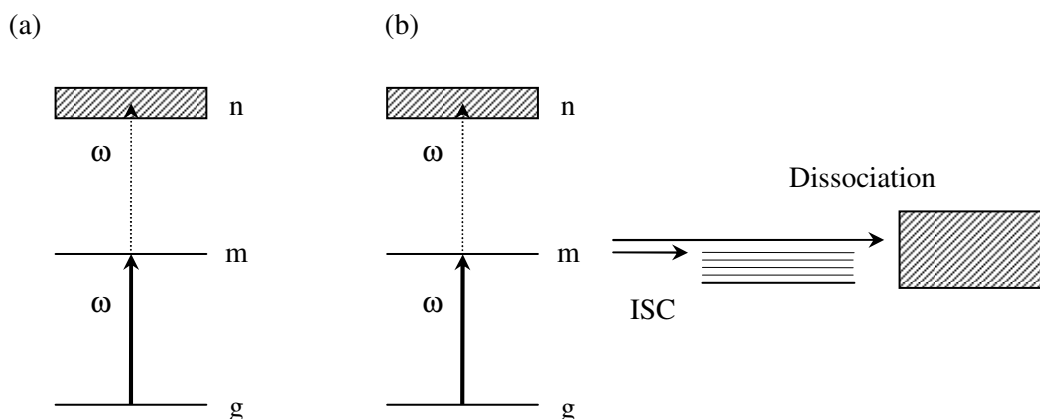
In principle the REMPI analysis is a powerful analytical tool when coupled with other experimental techniques allowing ready ion detection like the mass spectrometry. When a complex mixture is REMPI-analysed, only the resonant species are efficiently ionised, thus resulting in a potentially selective detection. However the temperature of the molecules in the ground state represents an analytical limitation to the selectivity of the REMPI technique [89]. The first photon is absorbed into an excited electronic state. At room temperature many rotational and a few lower vibrational levels of the electronic ground state are partially occupied, and the consequent broadening of the absorption bands causes the loss of the fine structure of the spectrum, and thus of the selectivity of the technique. This is particularly true in the case of large molecules such as high-mass PAH. More than ever this problem is present when working with a plume of desorbed, hot gases, where the potential selectivity of the (1+1) REMPI is completely frustrated. A way proposed to overcome this limitation is the molecular cooling, which lowers the temperature down to few K and so depopulates almost all the rotational and vibrational levels except the one at lowest energy, and consequently originating a spectral band narrowing. However, it must be pointed out that if only a semi-selective analysis is wanted, the broadening of the absorption bands can actually be an advantage, since it allows the ionisation of PAH which normally would not absorb at the selected wavelength.

Ion dissociation

An unwanted process often occurring as a consequence of the ionisation is the breakdown of the precursor molecular ion into both smaller ionic and neutral species, a process referred as primary dissociation. Ions and neutral molecules obtained this way are named *primary fragments*. When the analysis conditions are particularly unfavourable, the primary fragments may break down again, producing a huge variety of ionic species and therefore mass spectra potentially very rich of

low-mass peaks. The unambiguous identification of the precursor ion under heavy dissociation becomes very tough. To this purpose, the most common procedure is to compare the experimental mass spectrum with a database of known standard ions, and look for known dissociation pattern. However, the dissociation becomes a particularly difficult issue to deal with when analysing complex mixtures containing more analytes having similar dissociation paths. In this situation it is possible to identify the molecular class the analytes belong to, but not the mass of the precursor ions.

An example is given in Figure 3.4, reporting two mass spectra obtained for pure pyrene in the same analytical conditions except the ionisation irradiance. When the ionisation irradiance is low a two-photon ionisation occurs, the pyrene is efficiently ionised and it appears as a single peak at m/z = 202. By the way, the detection of the dissociation is obviously strictly related to the electronic structure of the precursor ion, and PAH ions have a lifetime long enough to be detected as molecular ions. On the other hand when high ionisation irradiance is delivered to the analyte, a multi-photon absorption leading to dissociative states occurs, and the largest part of molecular ions breaks down generating the complex mass spectrum reported in Figure 3.4 (a). This subject will be discussed in more details in Section 5.3, particularly in the context of the ladder switching model [90].
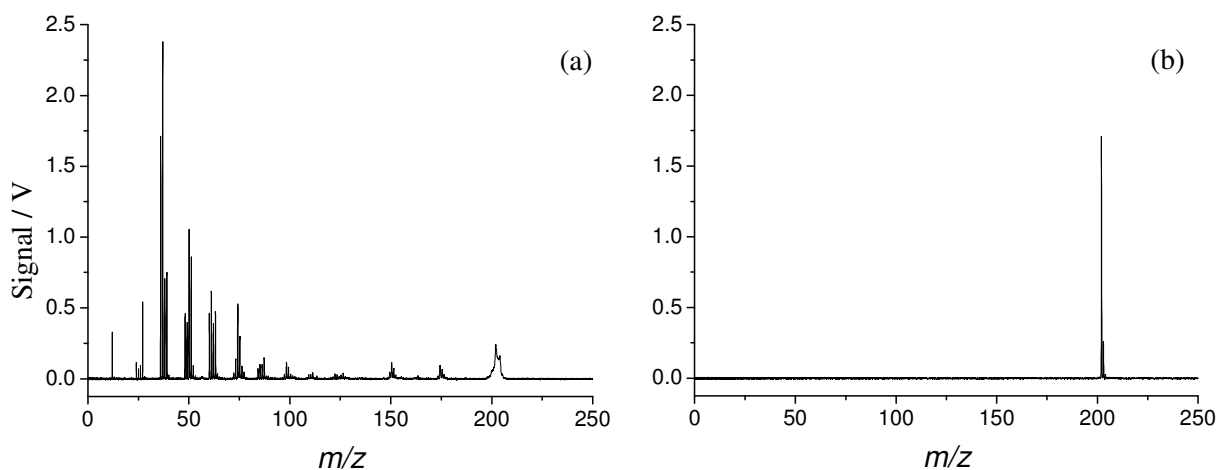
Figure 3.4. LD/LI/TOF-MS mass spectra obtained for a standard sample made of pure pyrene under the same experimental conditions except the ionisation power density. (a) Heavy dissociation and peak broadening occurring at $I_{ion} = 61$ MW cm^{-2}. (b) Fragment-free spectrum at $I_{ion} = 3.3$ MW cm^{-2}.

3.1.4. TOF-MS

Time-Of-Flight is a method in Mass Spectrometry where the mass separation is obtained creating ion having approximately all the same potential energy, and allowing them to travel in a field-free region. Since the ion velocity is acquired according to their mass-to-charge ratio m/z, whether a sufficient time of flight is supplied the ions separate into individual packets, thus they can be detected sequentially in time.

The main advantage of the TOF with respect to other Mass Spectrometry techniques is its virtually unlimited mass range. While quadrupoles and magnetic sectors are fundamentally limited in the higher mass they can detect, TOF-MS only requires the supply of microsecond quantities of time to extend the mass range. This feature represents the key to get knowledge about the

chemistry of high-mass PAH, detected far beyond the intrinsic limits of gas chromatography-based techniques for example.

In the ion source the ions are accelerated by a static or pulsed electric field, therefore all ions having the same charge acquire the same potential energy. Because of the potential-kinetic energy conversion, ions acquire a velocity depending on *m/z*, i.e. the heavier the ion and the smaller is the velocity at which it travels. The ions accelerated this way enter a field-free drift region where the time they need to reach the detector is measured. Once all the experimental parameters are set, this time only depends on *m/z*.

A TOF-MS is a device ruled by fundamentally simple physical principles. In the limit of the non-relativistic energy all the TOF-MS equations are well described by the classical Newtonian mechanics:

- $qV = \dfrac{1}{2}mv^2$ potential-kinetic energy conversion   (3.3)

- $qE = ma$ force on a charge in a static electric field   (3.4)

where q and m are the charge and the mass of the ion, V and E are the acceleration potential and electric field, v and a the velocity and the acceleration experienced by the ion. Typically a TOF-MS experiment requires the detection of the mass spectrum on the microsecond timescale.

The Reader wishing of going further into details will find a complete review and the derivation of the motion equations in the review articles of Guilhaus and co-workers [91,92] and Mamyrin [93].

3.1.5. Interpreting the mass spectra

A time-of-flight mass spectrum is a pattern constituted by a series of peak signals corresponding to the impacts on the detector of ions having different masses. The impacts are revealed as a function of the time that the ions need to cover the distance from the ions source to the detector. Since a quadratic relationship occurs between the time of flight and m/z ($t^2 \propto m/z$), once the masses corresponding to at least a couple of peaks are known it is possible to build a calibration curve and identify the *m/z* for all the detected peaks. In the mass spectra obtained this way, the x-axis brings the *m/z*, while the y-axis the intensities of the detected signals. An example is reported in Figure 3.5. In the present work soft ionisation condition have been employed, therefore all the detected ions have charge +1, and then the x-axis is *numerically* equal to the mass of the ions impacting the detector.
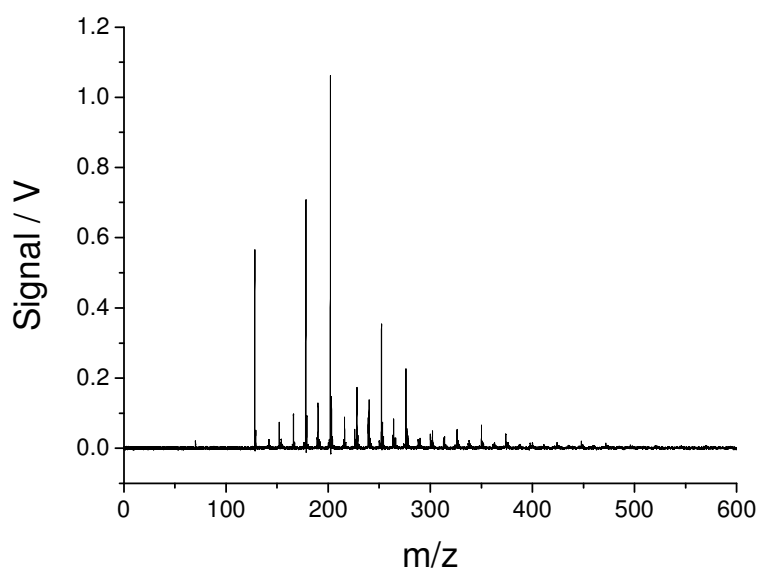
Figure 3.5. LD/LI/TOF-MS mass spectrum obtained from soot collected from an ethylene atmospheric flame, sampling at 14 mm HAB, $I_{des} = 5.3$ MW cm^{-2}, $I_{ion} = 1.9$ MW cm^{-2}.

PAH or carbon clusters?

The unambiguous attribution of a molecular formula $C_nH_m^+$ to a signal peak is not possible if only the mass is known. The molecular formulae $C_{n+1}H_{m-12}^+$, $C_nH_m^+$ and $C_{n-1}H_{m+12}^+$ have all the same nominal mass $12n+m$, and they are indistinguishable unless an extraordinary mass resolution is available. In mass spectra collected from soot, two interpretations subject of discussion were the $C_nH_m^+$ and the hydrogen poor C_n^+, where the former is consistent with the PAH structure, and the latter with the carbon clusters hypothesis. For instance the relative mass difference of the molecular ions (only containing ^{12}C) $C_{19}H_{12}^+$ (PAH) and C_{20}^+ (carbon cluster) is $\Delta m/m = 3.91 \cdot 10^{-4}$, i.e. a mass resolution of $\Delta m/m^{-1} \sim 2600$ is required to distinguish the two peaks. If such mass resolution is not experimentally available, an alternative way is needed.

The choice between PAH and carbon clusters is actually an easy-to-solve problem if the detailed structure of the mass spectra is available, with no needing of ultra-high mass resolution. As shown in Figure 3.6 each signal group in a PAH mass spectra typically occurs as a very intense signal peak corresponding to the mass of the molecular ion M, surrounded by a certain number of satellites at masses M±1, M±2 and M±3. While the peaks M+1, M+2 and M+3 are due to the isotopic occurrence of carbon, the presence of the satellite peaks M-1, M-2 and M-3 is attributed to the homolytic cleavage of one or more C-H bonds, and to the following elimination of hydrogen atoms:

$$C_nH_m^+ \rightarrow C_nH_{m-x}^+ + xH \text{ , with } x = 1,2,3 \tag{3.5}$$
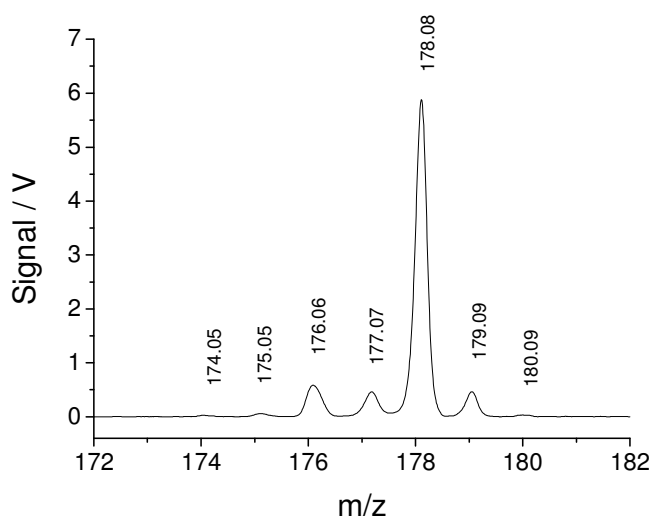
Figure 3.6. Mass spectrum obtained in this work from the LD/LI/TOF-MS analysis of a pure phenanthrene sample, zoom on the peak region. The mass of the most intense signal peak, corresponding to the all ^{12}C molecular ion is 178.08 u. I_{des}= 35.7 MW cm^{-2}, I_{ion}= 3.2 MW cm^{-2}.

Dobbins and co-workers [94] definitively attributed the detected masses to PAH via replacement of the fuel with its deuterated version. They observed that the soot produced burning a deuterated version of the fuel would necessarily contain only deuterated PAH, whose masses are expected to increase with respect to the hydrogenated fuel of a value equal to the number of hydrogen atoms contained in the molecule. This stated, they compared the masses obtained from the combustion of ethylene C_2H_4 with those obtained from the combustion of deuterated ethylene C_2D_4. They tracked the incremental change of the two series of masses, observing that the shift towards heavier masses measured in the deuterated soot was consistent with the molecular formulae of PAH, thus definitely discarding the two hypotheses of H-rich and H-poor structures. These results eventually fixed the number of hydrogen atoms contained in each detected mass.

Isomers identification

Several PAH isomeric structures are possible for each C_nH_m molecular formula. The number of possible isomers quickly increases as a function of the number of carbon atoms, giving rise in principle to all the possible permutations of the aromatic rings consistent with a certain molecular formula. For instance, while the molecular formula $C_{10}H_8$ gives rise to only one *benzenoid* structure (naphthalene), $C_{26}H_{16}$ gives 37 possible structures, and more than 1489 structural formulae have been theoretically predicted for the $C_{38}H_{22}$ [95]. The physical-chemical properties of a very small number of isomers are known, and even a smaller number has been synthesised. The situation becomes even more complicated when 5-atoms rings or side-substituted PAH are considered.

The optical response of irradiated PAH depends on a number of factors, and since the molecular symmetry plays an important role on the electronic transitions, in principle it can be very different for isomeric structures. When only one-photon transitions occur, the optical response is only dependent on the properties of the electronic ground state. On the other hand the situation grows more complicated when multi-photon transitions are involved, because all the properties of the

intermediate state(s), like the lifetimes, the Franck-Condon factors and so on play a role. For instance pyrene and fluoranthene have both 202 u mass, and the absorption cross section of pyrene is about twice that of fluoranthene at 266 nm wavelength [85]. Additionally, the lifetime of the intermediate state involved in the REMPI is ten times longer for pyrene than fluoranthene, and therefore the overall ionisation is far more efficient in the case of pyrene than fluoranthene [89]. This also implies that the most important contributions to the peak signals in a photoionisation mass spectrum are due to the PAH having the best combination of their concentration on soot and ionisation efficiency.

3.1.6. Laser desorption/photoionisation TOF-MS in combustion

Laser desorption/photoionisation TOF-MS analyses provide useful information on the combustion processes making it possible to follow the PAH growth process. Especially valuable is the knowledge of the mass sequence of PAH adsorbed on soot, which is related to the soot growth process as discussed in Section 2.1. As described below, a pioneer work on diffusion flames has been performed by Dobbins and co-workers in 1998 [72,73], who first recognised the role of Stein and Fahr's stabilomers in the PAH growth process. Some topical and still discussed subjects are the detection of aliphatic species in flame soot as reported by Öktem and co-workers [5]. The evolution of the mass sequence as a function of the flame reaction time is a most investigated subject as well, as reported by Apicella and co-workers [77]. Finally, the soot produced by fuel pyrolysis has been recently investigated by Mathieu and co-workers [79].

The role of Stein and Fahr's stabilomers

The correlation between the PAH adsorbed on soot surface detectable via laser desorption/ionisation techniques and the stability of PAH at high temperature was first proposed by Dobbins and co-workers [72]. The striking observation that gave rise to the research around this specific subject was the detection of benzenoid PAH as intermediate combustion products in soot collected from a large number of different flames. The remarkably little effect of the flame conditions (pressure, nature of the burnt fuel and so on) on the presence of those PAH suggested that their growth might have been favoured in the formation process of carbonaceous soot rather than other classes of PAH.

Dobbins and co-workers performed their analyses on an atmospheric ethylene diffusion flame [72,73], whose conditions are reported in Table 3.1. The soot was analysed via Laser Microprobe Mass Spectrometry (LMMS), where desorption and ionisation were performed in a single step using an UV laser beam. The samples were irradiated with a 10 ns laser pulses at 266 nm wavelength (irradiance range going from 10 up to 20 MW cm^{-2}). A twenty-four standard PAH sample has been used to calibrate the mass spectrometer.

	Feeding	Q_{fuel} / slpm	Q_{air} / slpm
Diffusion atmospheric flame	C_2H_4:air	3.85	715
Sampling: thermophoretic sampling performed on electron microscope grid (see Paragraph 3.1.1)			

Table 3.1. Experimental conditions of the LMMS [72, 73]. Q_{fuel} and Q_{oxi} are the flows of fuel and oxidiser.

The early LMMS study allowed the detection of 252, 276 and 300 u as prominent masses in a soot-rich region of the test flame [73]. The successive and more detailed study [72] revealed a full series of masses ranging from 202 u up to 472 u. The published mass spectra are reproduced in Figure 3.7.
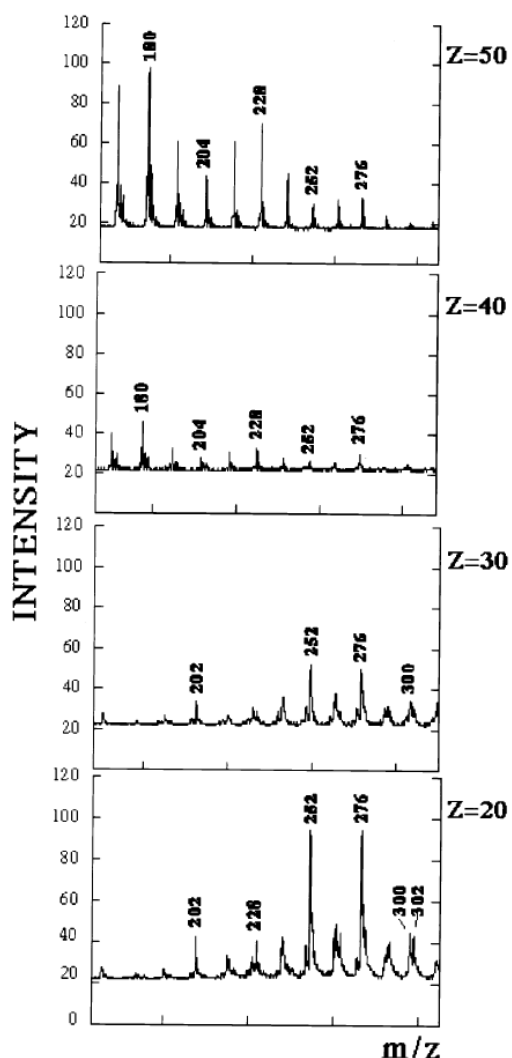
This latter work revealed a number of interesting features. The most intense signals of the mass sequence span the range 202<m/z<472, and they all correspond to PAH masses found within Stein's stabilomer grid (detailed in Section 2.1.2), i.e. benzenoid PAH. Reasonably, each signal is given by the contribution of a large number of different isomers. The masses detected between two even C-number peaks correspond to PAH having odd C-number, and even if they do not belong to the stabilomers grid, they are all well consistent with variations of the structure of stabilomers, for instance when a CH_2 group bridges a bay site. Dobbins concluded that the strong correlation between the stabilomers detected early in the flame (gas phase) and those on the soot surface (mature soot) indicated that the composition of the young particles was somehow controlled by the gas-phase PAH molecules. He suggested as well that the growth of the gas-phase PAH should occur via a species present at high concentration in the flame, and he indicated acetylene as probable candidate. The evidences of the growth process and the presence of acetylene as one of the major gaseous species in the flame supports the HACA mechanism developed by Frenklach (see Section 2.1.3).

Figure 3.7. Mass spectra published by Dobbins and co-workers [72], obtained from an atmospheric diffusion flame (see text) as a function of the sampling HAB. The regularity of the observed mass sequence and the correspondence of the even C-numbered masses with Stein's stabilomers founded the first attempt to give a thermodynamic basis to the PAH growth process in flames.

Detection of aliphatics

The ability of detecting aliphatic molecules represents an interesting and natural extension of the potentialities of the photoionisation mass spectrometry.

The optical response of aliphatic molecules (only containing σ electrons) is very different from that of molecules containing heteroatoms (n electrons) and conjugated/ aromatic bonds (π electrons), essentially because π electrons tend to be delocalised in space. The delocalisation in

space causes π electrons to be less tightly bond to the nuclear backbone, and therefore to interact more easily with an applied optical field. Aliphatic molecules only contain σ bonds, thus only the transition $\sigma^* \leftarrow \sigma$ is possible, which typically requires high-energy vacuum UV radiation (λ<150 nm, $\hbar\omega$ >8.27 eV). On the other hand the presence of conjugated electrons thus the availability of π molecular orbitals makes the transition $\pi^* \leftarrow \pi$ possible. This transition can be typically initiated by light whose wavelength is 150<λ<250 nm (7.95<$\hbar\omega$<8.27 eV). If one or more heteroatoms are present, then even the transitions $\sigma^* \leftarrow n$ and $\pi^* \leftarrow n$ are allowed, as illustrated in the scheme reported in Figure 3.8.
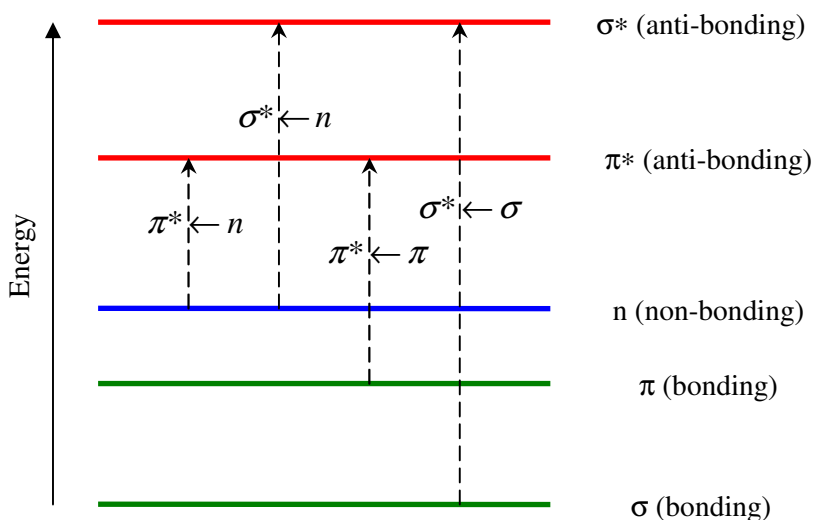
Figure 3.8. Different types of electronic transitions. Green lines represent bonding electrons, the blue line non-bonding electrons, and the red lines anti-bonding electrons.

The ionisation energy of most small aliphatics is far too high (from 10 eV upward) to be reached via one-photon or two-photon transitions with 266 nm wavelength radiation unless higher order nonlinear absorption was induced. Therefore aliphatics molecules are invisible under this analysis conditions. However the detection of aliphatics via photoionisation mass spectrometry is possible at shorter ionisation wavelength, as it has been demonstrated by Öktem and co-workers [78]. They took advantage of 118 nm (10.5 eV) ionisation wavelength, which is energetic enough to promote the $\sigma^* \leftarrow \sigma$ transition.

	Feeding	ϕ	Q_T / slpm	v_0 / cm s^{-1}
Premixed atmospheric flame	C_2H_4:O_2:Ar = 0.141:0.170:0.689	2.50	14.57	8.0

Sampling: water-cooled stainless steel tube inserted horizontally into the flame, having a side 0.2 mm orifice allowing a flow from the flame, while a 29.5 slpm nitrogen flow running into the tube provide the dilution.

Table 3.2. Experimental conditions of the PIAMS experimental [5,78]. ϕ, is the flame equivalence ratio, Q_T and v_0 are the total unburned flow and velocity of the unburned gases.

Öktem and co-workers studied an ethylene flame whose conditions are reported in Table 3.2. The sampled particles have been deposited on a metal target in the ion source of the mass spectrometer, where a desorption laser pulse at 1064 nm wavelength generates a plume of gases irradiated 30 ms later by a 118 nm wavelength pulse for ionisation. Mass analyses have been performed with a desorption irradiance of 40 MW cm^{-2}, while the ionisation irradiance, not measured, was expected to be equivalent to 1-2 μJ/pulse on the basis of the previous work [78]. The published mass spectra obtained sampling the flame are reported in Figure 3.9.

Since the ionisation of aliphatic molecules necessarily implies a σ bond cleavage, the dissociation of the precursor ion cannot be avoided. The consequent rearrangement of the fragments produces both neutral-charged molecules and ions, where the latter create typical patterns from which the structure of the precursor ion has to be derived.

Authors tested the system on pure pyrene to verify that mass spectra were completely fragment-free [78]. According to the obtained results, two different sequences of peaks have been identified. The prominent masses in the first peak sequence (m/z<150) are: 15, 29, 42, 54, 69, 83, and 99 u. To the best of our knowledge, this paper is the only one mentioning the certain presence of aliphatics, and indeed the masses 15 and 29 u undoubtedly correspond to the $C_nH_{n+1}^+$ aliphatic fragments associated to methyl (CH_3^+) and ethyl ($C_2H_5^+$) positive ions. This finding might be observable because of their one-photon ionisation scheme (Figure 3.3). Nevertheless the interpretation of the other masses might be subject of discussion. Indeed the mass spectrum of pure pyrene obtained by the same Authors in a previous paper [78] clearly shows the presence of a background of peaks which has been attributed to dissociation. However, when analysing flame soot [5], the Authors claim that the low-mass side of the mass spectra comes from fragments of aliphatics.
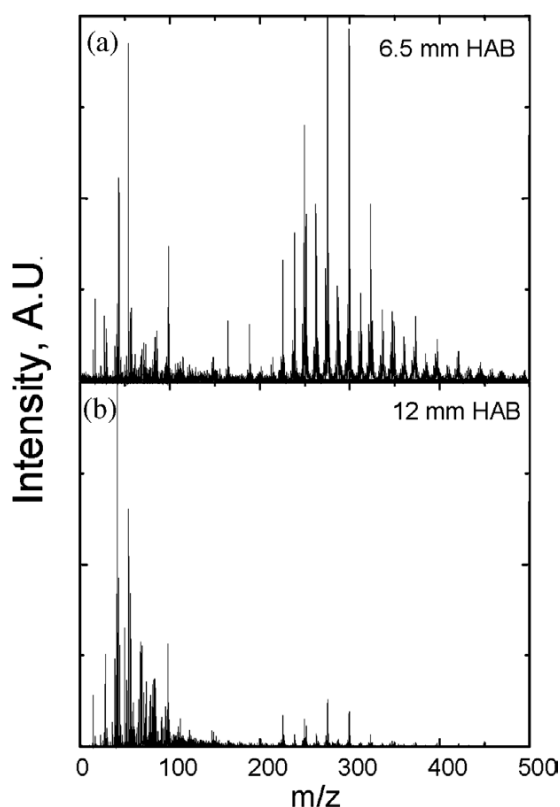
In the second peak sequence (150<m/z<500) it is prominent a series of strong peaks corresponding to PAH having an even C-number consistent with Stein and Fahr's stabilomers (202, 226/228, 250/252, 276, 300 and 324 u). A second series of weaker signals, corresponding to PAH containing an odd C-number (239/240 and 264 u, and for extension 216, 288 and 314 u), has been detected.

Figure 3.9. Photoionisation aerosol mass spectra published by Öktem and co-workers [5], obtained from an atmospheric ethylene premixed flame (see text) at (a) 6.5 mm and (b) 12 mm HAB. This is currently the only analysis clearly showing the presence of aliphatic fragment.

Signals intensities have the same order of magnitude in the two main sequences of peaks, but while the PAH signals almost disappear higher in the flame, the aliphatic signals seems to be little dependent on the HAB.

Effect of the reaction time

The evolution of the mass spectra as a function of the Height Above the Burner (representative of the reaction time) have been studied by Apicella and co-workers, who published two major works on this subject. The first one contains the experimental system calibration [77], while the second one deals with a more detailed analysis of the same flame as a function of the HAB [76]. The flame studied in the above mentioned works is the atmospheric premixed ethylene flame described in Table 3.3. In Apicella's ex-situ experimental setup, the surface desorption and the ionisation occur in one step, via a nitrogen laser emitting at 337 nm wavelength and delivering 3 ns pulses. Neither the peak irradiance nor the energy delivered per laser pulse is known.

	Feeding	ϕ	Q_T / slpm	v_0 / cm s^{-1}
Premixed atmospheric flame	C_2H_4:O_2 = 0.503:0.497	3.03	6.786	4.0

Sampling: full collection of all the combustion products deposed along the sampling line. The collected materials have been extracted using dicholoromethane, and the obtained solution used to prepare the mass-spectrometry target via deposition and solvent evaporation

Table 3.3. Experimental conditions of the LDI/TOF-MS experimental [76,77]. ϕ, is the flame equivalence ratio, Q_T and v_0 are the total unburned flow and velocity of the unburned gases.

Three different HAB have been sampled, in flame regions corresponding to the soot inception zone (6 mm), to the maximum of the soot formation rate (8 mm) and to the end of soot formation region (14 mm). The structure of the flame was known from previous analyses [96]. The published mass spectra are reproduced in Figure 3.10.

The mass spectra extend over 300<m/z<1200. However, for m/z > 1000 the signal-to-noise ratio is too poor to allow a clear mass attribution to the signal peaks. In all the mass spectra two different series of peaks can be easily identified. The first one contains the most intense signals, corresponding to PAH having an even C-number and once again consistent with Stein and Fahr's stabilomers. The mass difference between two consecutive terms has been identified as 24 u, and this observation is consistent with the growth HACA model. The second series contains weaker signals, which correspond to odd C-numbered PAH. Authors suggested that PAH containing cyclopenta-fused rings may constitute a large fraction of the odd C-numbered PAH.

The mass sequence does not show any dependence on the sampling HAB. The low-HAB mass spectrum is the less rich in signal peaks, and raising the HAB the spectra become richer and richer in signals. The peak signals appearing higher in the flame are always consistent with those detected lower, thus they belong to the same PAH series. On the other hand the signal intensities of the high-mass side of the spectrum progressively increase with respect to the low-mass side. Particularly the mass spectrum obtained at 14 mm show signal peaks up to m/z ~ 1000, while at 6 mm the upper mass limit was located for m/z ~ 800. This progression of signal intensities from 6 to 14 mm HAB has been interpreted as evidence that a growing phenomenon is occurring.

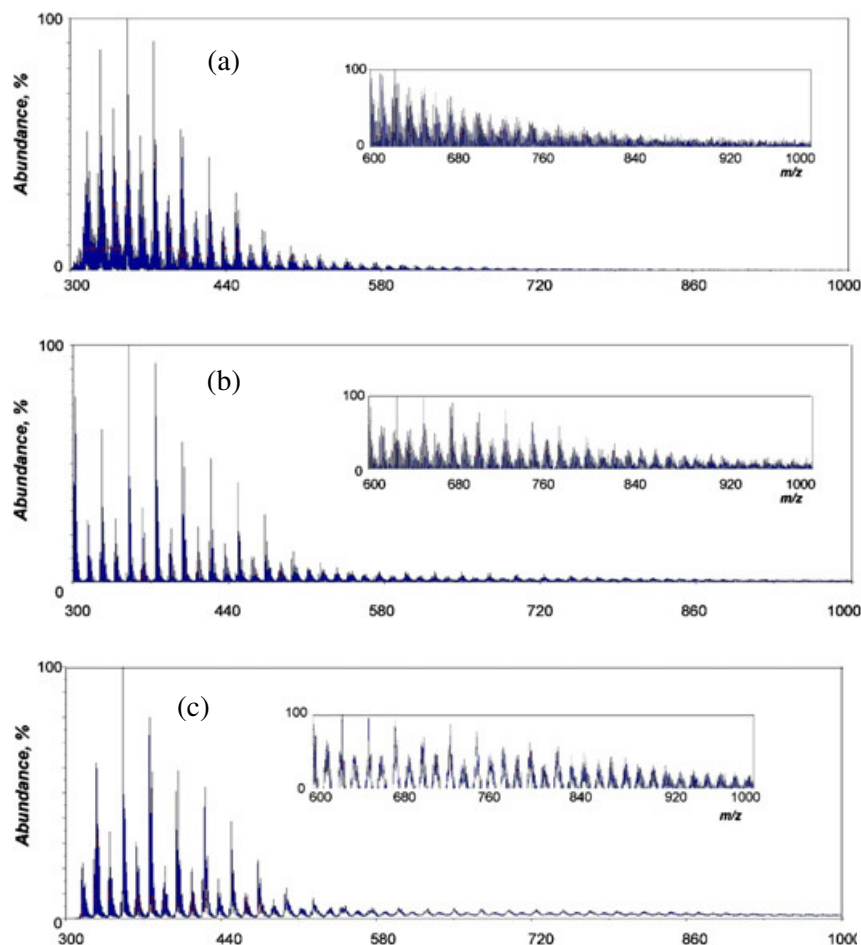**Figure 3.10.** LDI/TOF-MS analyses [76] of soot extract sampled at (a) 6 mm, (b) 8 mm, and (c) 14 mm HAB in the range 300<m/z<1000 (top) with zoom in the range 600<m/z<1000 (inset).

Effect of the fuel pyrolysis

Photoionisation mass spectrometry analyses have been performed on soot obtained from a pyrolysis process by Mathieu and co-workers [6,79]. The soot analysed in these works has been obtained via the pyrolysis of different fuels (toluene C_7H_8 and tiophene C_4H_4S) induced by a shockwave. The experimental conditions are reported in Table 3.4. The sample consists in a metal slab fixed on the inner wall of the shock tube's end with a strong magnet, which is covered by soot after the passage of the shock wave. The slab is then introduced into the mass spectrometer without any further treatment.

The first work [6] discusses the pyrolysis of toluene highly diluted in argon (10^{18} carbon atoms/cm^3). The published mass spectra are very similar to those obtained from flame experiences in terms of the detected PAH mass sequence. As shown in Figure 3.11, the sequence of masses is well evident, as it is the alternation of strong peaks and weak peaks, where the former correspond to even C-number PAH and to Stein's stabilomers, and the latter to odd C-number PAH. The original work reports a study as a function of the temperature and the soot yield.

	Feeding	p (kPa)	T (K)
Shock tube	C_7H_8 or C_4H_4S	1135-1600	1470-2230
Sampling: metal slab located into the shock tube			

Table 3.4. Experimental conditions of the LDIToFMS experimental [6,79]. p and T are the studied intervals of pressure and temperature.
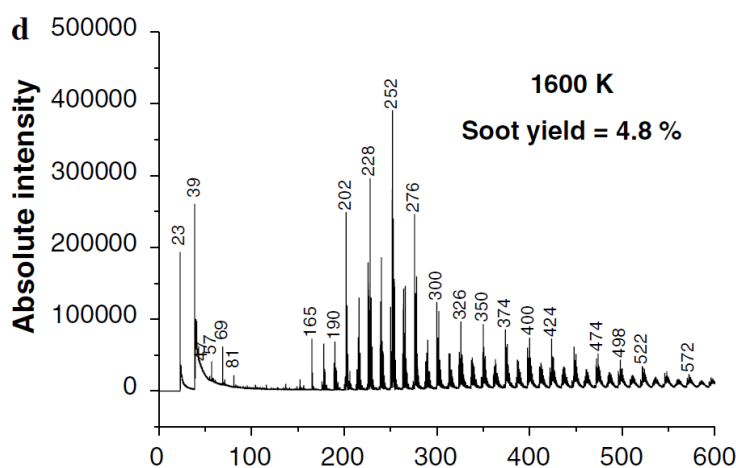
Figure 3.11. LDIToFMS mass spectra of soot obtained from toluene pyrolysis in a shock tube [6].
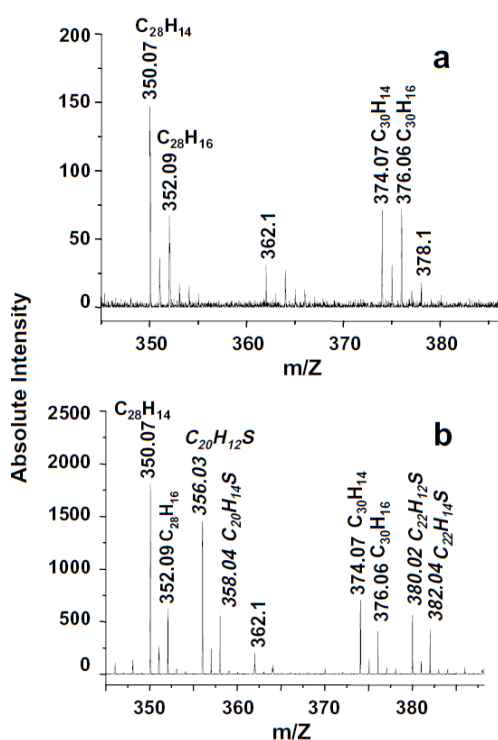
The role of the nature of the pyrolised fuel is discussed as well. In a most recent work [79], a comparison between the pyrolysis products of toluene and tiophene has been reported. In the LDIToFMS mass spectra of tiophene soot (Figure 3.12), the main sequence of PAH is still present and dominates the mass spectrum. However a series of weak peaks not observed in the toluene soot were observed, which indicates the presence of hydrocarbon species having structure analogous to PAH but containing sulphur atoms.

This work suggests that the way the soot is produced has little influence on the sequence of Stein's stabilomers adsorbed on soot, and that PAH are among the major species if a carbon containing fuel is burned. On the other hand, a trace of the chemical composition of the fuel is found on the structure of the adsorbed phase on soot, where species consistent with the presence of sulphur atoms are found.

Figure 3.12. Qualitative comparison between the LDIToFMS mass spectra of the pyrolysis products of toluene (above) and thiophene (below). Masses consistent with molecular structures containing sulphur have been identified [79].

3.2. Molecular beam photoionisation mass spectrometry

Directly ionising a molecular beam instead of performing a desorption step allows the detection of all the components of the beam itself, there included both the molecular and the particulate phase. Particularly, this technique allows the detection of masses up to 10^6 u (Paragraph 3.2.2) and gives the very first evidences of the gas-solid phase transition (Paragraph 3.2.3).

3.2.1. Online sampling

A totally different approach to the soot collecting problem has been recently proposed by Grotheer and co-workers [46,87]. In the Photo-Ionisation Mass Spectrometry (PIMS) setup the soot particles collected from the flame are sent as a molecular beam into the ion source of the mass spectrometer. A molecular beam is a collimated beam of atoms, radicals, molecules or ions all moving at approximately equal velocities, thus minimising the collisions occurring between them. It is usually produced by allowing a gas at higher pressure to expand through a small orifice into a container at lower pressure [97]. In Grotheer's setup the burner is connected to a fast flow reactor, where the discharge stream is diluted by helium. The fast flow reactor is connected via a molecular beam inlet to the mass spectrometer, as shown in Figure 3.13. The residence time of the particles into the reactor is estimated of the order of 1.5 ms, and therefore the measured spectra are assumed to be representative of the flame conditions. Such a setup simultaneously requires a differential pumping system to lower the pressure down to the very high vacuum required to operate a time of flight mass spectrometer, and very high dilution ratios of the probed flow with an inert gas to avoid the overloading of the pumping system.
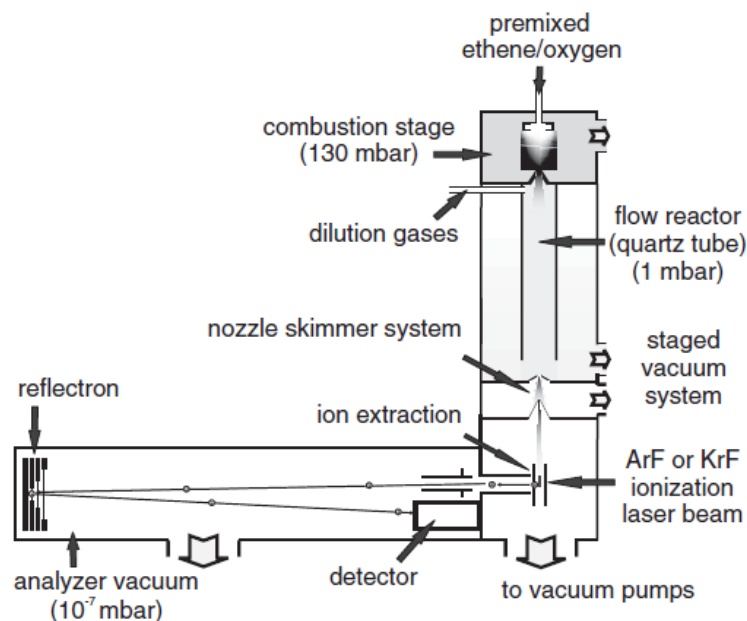
Figure 3.13. Scheme of the experimental setup adopted by Grotheer and co-workers [46]. The fast flow reactor allows the direct connection of the flame to the mass spectrometer.

This method allows the simultaneous detection of the species adsorbed on soot particles and the solid particles themselves. The selectivity is introduced at the level of the ionisation step. A drawback of the online sampling is that one of the axes of the setup (see also Figure 3.1) must be reserved for the particle beam running into the mass spectrometer, partially limiting the versatility of the technique[3].

3.2.2. Detection of very high masses

Most of the works available in the specific literature place the upper limit of detectable masses for photoionisation mass spectrometry in the range 800<m/z<2000. Grotheer and co-workers [46,87] recently demonstrated that the detection of masses up to 10^6 u is possible via direct photoionisation of the combustion products sent into the ion source as an aerosol of soot particles and gaseous PAH. The aerosol has previously been diluted with an inert gas in order to quench the still occurring chemical reactions. Using such configuration Grotheer and co-workers obtained a striking result extending the limit of the detected masses up to m/z = 1 000 000, where the mass spectra are well resolved up to m/z = 4000. The published mass spectrum is reproduced in Figure 3.14. The detected masses have been associated to soot nanoparticles having up to 11 nm diameter. Surprisingly, despite the upper mass limit is well beyond any other TOF-MS setup currently used in combustion, the main interest of these works is rather in the low-side of the mass spectra, and particularly in the transition region 600<m/z<1000. This subject is discussed in the next Paragraph 3.2.3.
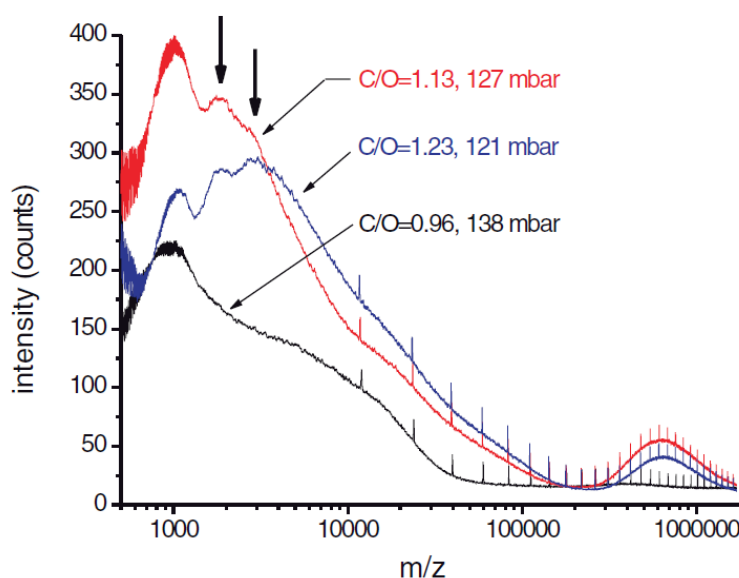
Figure 3.14. Photoionisation mass spectra up to 1 000 000 u obtained for low pressure ethylene/oxygen flames having different C/O ratios. The spikes are measure artefacts [87].

---

[3] It should be noted that in the desorption photoionisation mass spectrometry, the desorption and ionisation beam can run on the same axis.

3.2.3. Evidences of the gas-solid phase transition

In the same publication [46], Groother and co-workers proposed a way to distinguish the soot particles from the molecular species. Their idea is based on a previous work of Homann and co-workers [98], who evaluated the ionisation energy of carbon nanoparticles having mass in the range 300<m<2000 u as 5 eV or less. This value is slightly smaller than the ionisation energy of molecular PAH having the same mass, which stabilises around 6-7 eV. Therefore, the ionisation process performed with a wavelength delivering an intermediate amount of energy between those values (193 nm, 6.41 eV) allows in principle one-photon ionisation of the nanoparticles and two-photon ionisation of the molecular PAH. The distinction between the two species is then performed on the basis of the ionisation order.

	Feeding	ϕ	Q_T / slpm	v_0 /cm s^{-1}
Premixed atmospheric flame	C_2H_4:O_2 = 0.492:0.508	2.91	15.9	54.0

Sampling: soot and gases sampled from the flame are sent as a molecular beam to the ion source of the mass spectrometer. The height of the sampling above the burner was fixed at 15 mm.

Table 3.5. Experimental conditions of the flame in the PIMS experiment [46, 87]. ϕ, is the flame equivalence ratio, Q_T and v_0 are the total unburned flow and velocity of the unburned gases.

The conditions of the ethylene flame stabilised by Grotheer and co-workers are reported in Table 3.5. They sampled in the sooting region, at 15 mm HAB. The laser ionisation was performed with an ArF laser emitting at 193 nm (6.42 eV), and independently with a KrF laser emitting at 248 nm (5.00 eV), both delivering 10 ns pulses. The explored range of peak irradiances was from 0.01 up to 0.21 MW cm^{-2} for the ArF laser, and from 0.08 up to 0.6 MW cm^{-2} for the KrF laser.
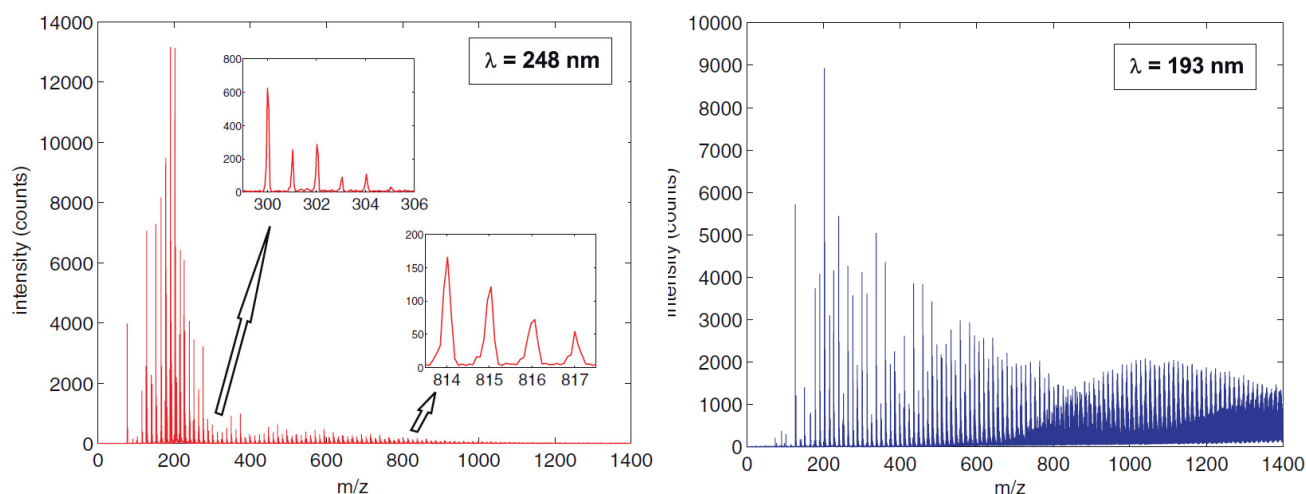
Figure 3.15. Photoionisation mass spectra obtained from the combustion products of the low-pressure ethylene/oxygen flame investigated by Grotheer and co-workers, ionisation at 248 nm (left) and at 193 nm wavelength (right) [87].

The published mass spectra are reported in Figure 3.15. When working at 248 nm the obtained mass spectra are very close to those found in the literature under 266 nm ionisation conditions [6,72]. A sequence of signals associated to molecular PAH is detected, composed of strong peaks in the range 200<m/z<300 followed by weaker signals in the range 300<m/z<1000. The alternate peak intensity sequences due to PAH containing even and odd carbon numbers are well recognisable.

When working at 193 nm the situation considerably changes. Although the low-mass side of the mass spectrum still resembles to the 248 mass spectrum, a new progression of signal appears in the high-mass side, starting around m/z = 680. The two series overlap up to m/z 1000, beyond which the new one dominates. This new signal progression does not correspond to molecular PAH masses, being shifted from the expected masses of a few m/z. A similar behaviour has been observed by Siegmann and co-workers [99].

From mass spectra collected at different ionisation irradiances, Authors measured the ionisation order for this new series of masses, finding a value of one. Since a one-photon ionisation at 193 nm is consistent with Homann's evaluation of the ionisation energy for carbon aggregates having m < 2000 u, Authors concluded that the new mass progression is due to the very first three-dimensional aggregates of large PAH, i.e. the very first soot nanoparticles. The hypotheses of very large molecular PAH and polyaryls have been discarded because of the very low concentration of the former and the too high ionisation energies of the latter. In other words the soot inception process is suggested to begin at significant rate around 700 u mass. As the Authors themselves claimed this is still a preliminary work; however, if this interpretation is verified, it will set a much narrower mass range to be explored, allowing the identification of the very first soot particles around 600<m/z<800 u.

Chapter 4.

Experimental methods

This section is intended to provide to the Reader a complete overview of the apparatus and experimental methods adopted in this work, as they have been set to perform the measurements presented in the following Chapter 5 and 6. The description of the apparatus includes the LD/LI/TOF-MS setup described in Section 4.1 as well as the burners and sampling setup described in Section 4.2.

4.1. LD/LI/TOF-MS

An experimental setup based on the coupling of Laser Desorption (LD), Laser Ionisation (LI) and Time-Of-Flight Mass Spectrometry (TOF-MS) has been developed throughout the present work and dedicated to the analysis of PAH desorbed from soot [100-103]. This setup was originally developed at PhLAM laboratory to analyse organic substances desorbed from ice. During a LD/LI/TOF-MS analysis the surface of a solid sample is irradiated by a first laser pulse (LD). As a consequence of the induced local heating, thermal desorption of neutral species occurs from the sample. After a time delay, a second laser pulse (LI) irradiates the expanding plume of gases to produce the ions to be mass-analysed (TOF-MS).

In Figure 4.1 pictures of the LD/LI/TOF-MS are reported, while in Figure 4.2 and Figure 4.3 the analysis chamber is detailed. In this work the setup is described in the context of the experimental method. It is useful to remember that in our setup the LD/LI/TOF-MS diagnostic is an ex-situ technique. Samples enter the TOF-MS via a preparation chamber separated from the analysis chamber via a gate valve. At the same time they are liquid-nitrogen cooled (down to maximum -160°C) to avoid the sublimation of the volatile compounds because of the high-vacuum (residual pressure 10^{-7} torr). Once these conditions are met, the gate valve is opened and the sample is moved into the analysis chamber (very high vacuum, residual pressure is 10^{-9} torr). A typical analysis requires 2-3 hours to be accomplished.
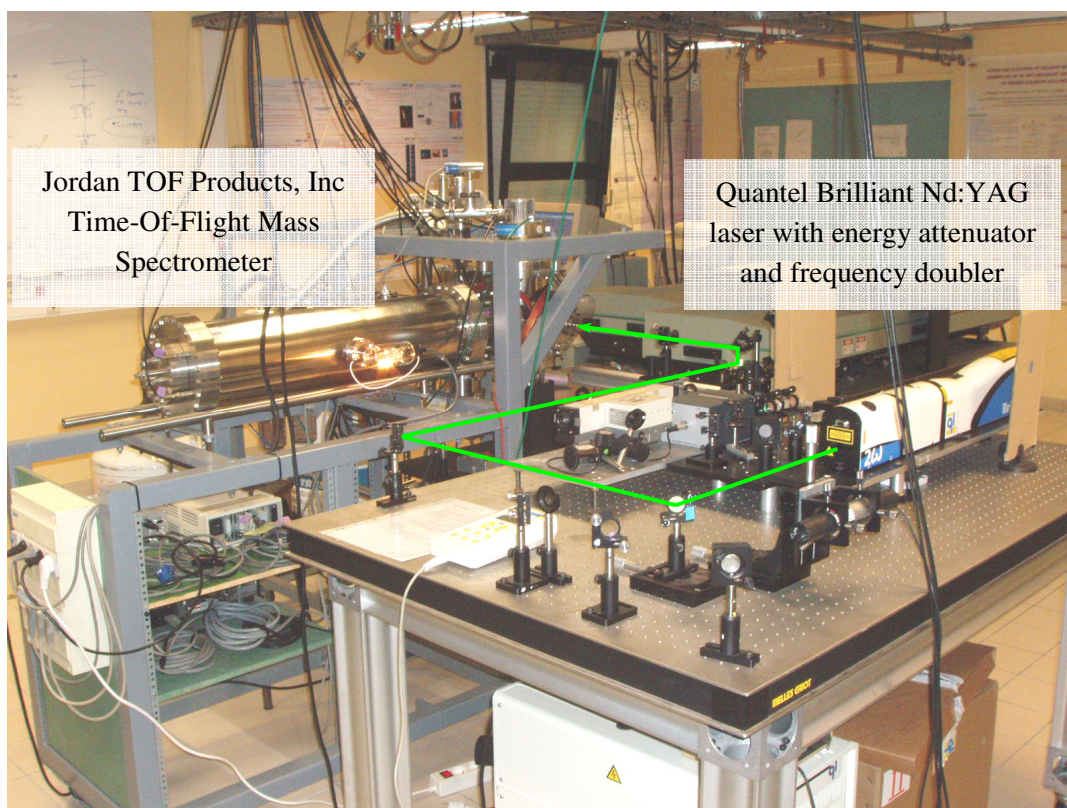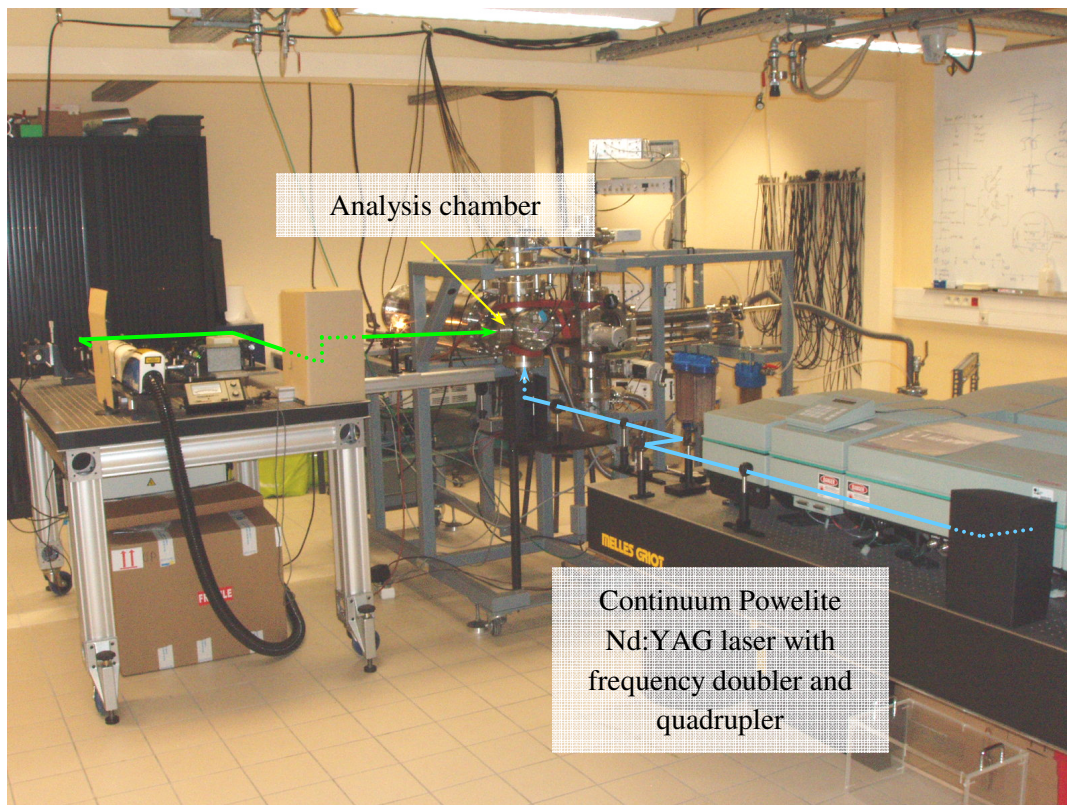
Figure 4.1. Pictures of the experimental apparatus, in which the desorption (green) and ionisation (blue) laser optical paths are highlighted.
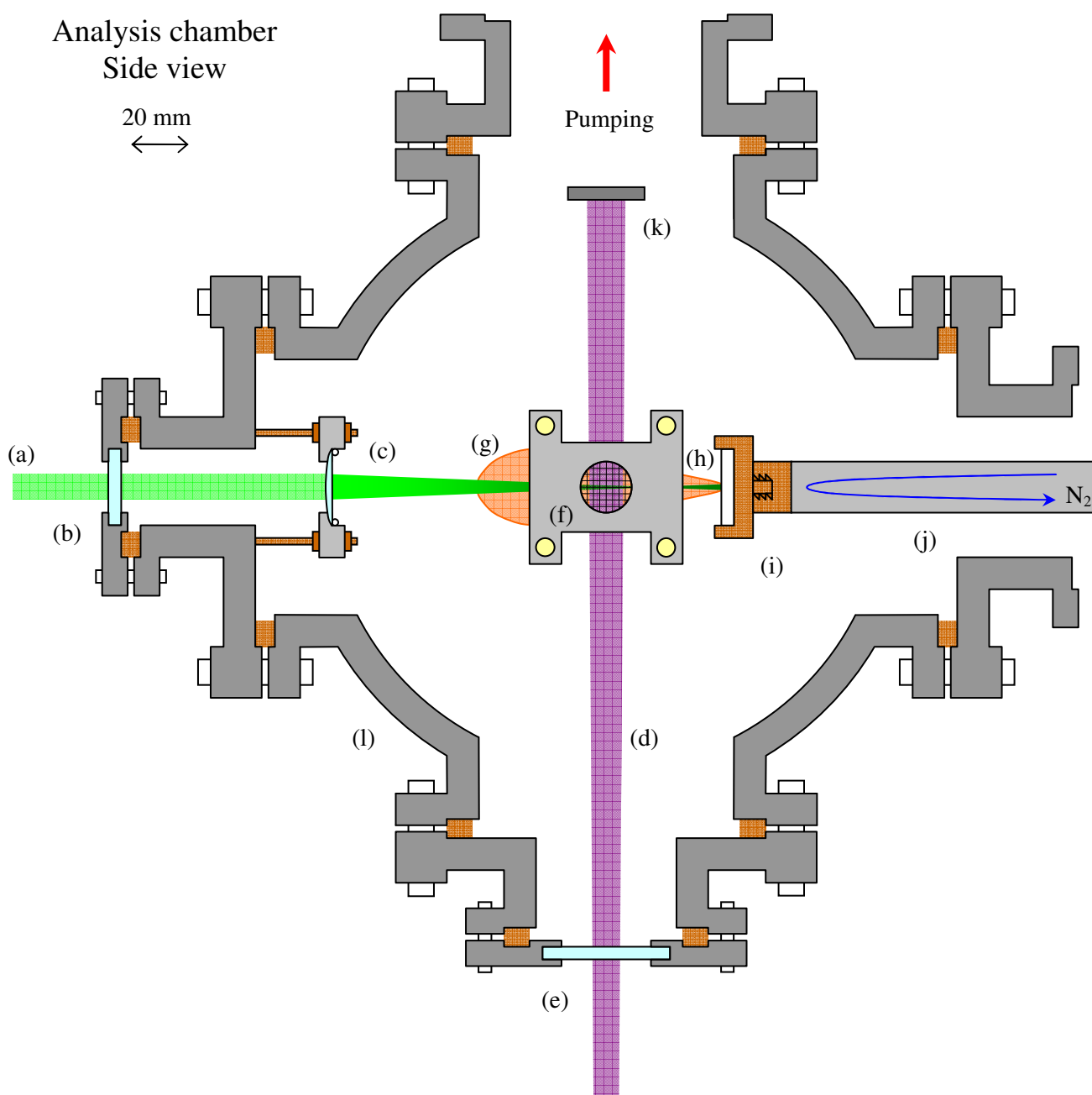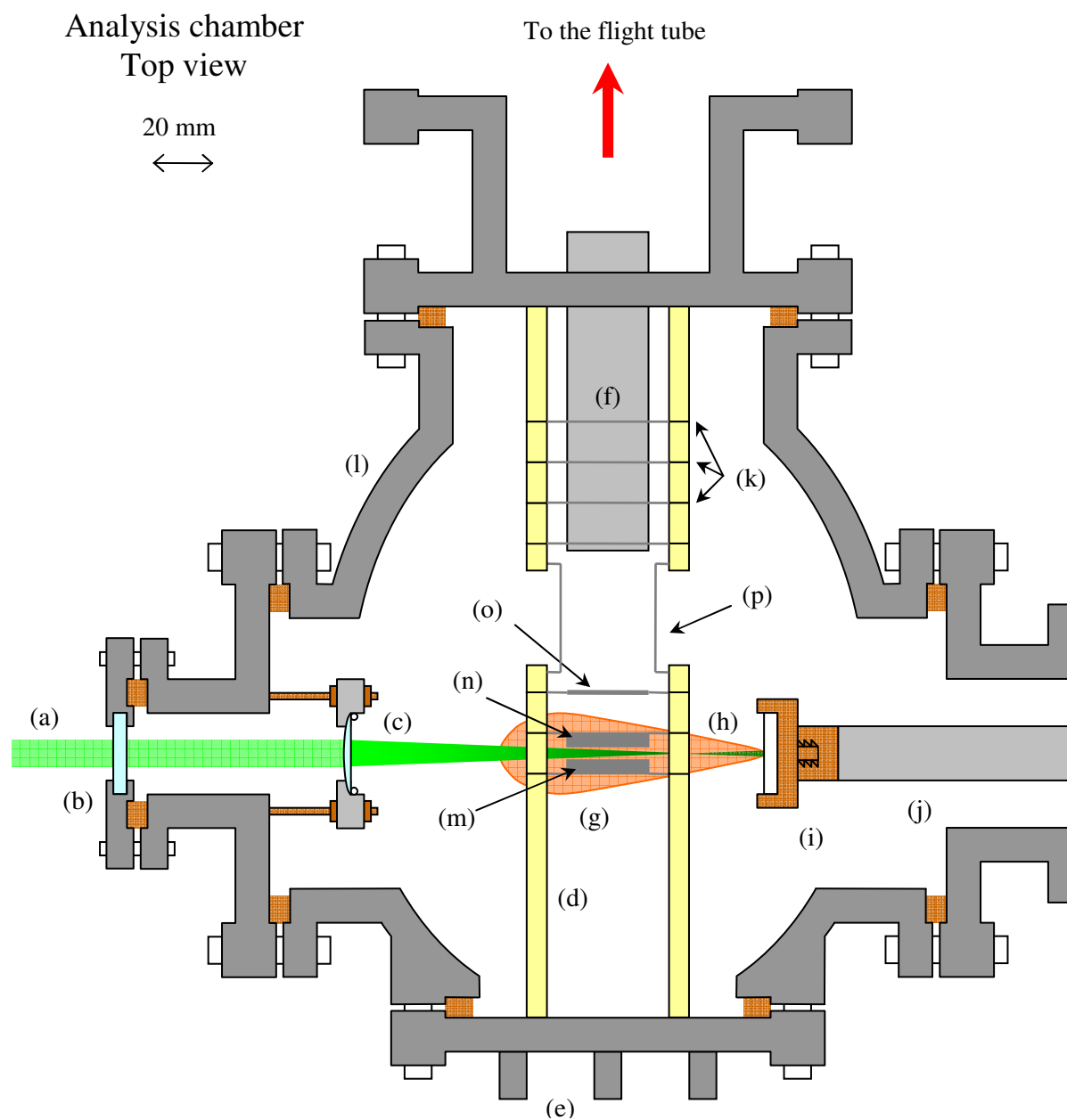
Figure 4.2. Section of the analysis chamber of the mass spectrometer, side view. (a) Laser desorption optical path end, 532 nm wavelength. (b) Desorption path CaF$_2$ viewport, it allows desorption in the visible and near infrared spectral range. (c) Desorption path CaF$_2$ lens, f = 100 mm. (d) Laser ionisation optical path end, 266 nm wavelength. (e) Ionisation path fused silica viewport, it allows ionisation in the visible and near ultraviolet spectral range. (f) Extraction grid V$_{A2}$. The repeller plate is exactly behind it, as shown in the Top View diagram on the next page. (g) Desorbed plume. (h) Sample. (i) Bronze sample holder. (j) Support rod ("cold finger"), it contains the hoses where the liquid nitrogen flows, as indicated by the arrow. (k) Beam stopper. (l) 5.0 mm thick ultra-vacuum vessel. In this scheme the ion packet flight direction is normal to the plane of the sheet.

Figure 4.3. Section of the analysis chamber of the mass spectrometer, top view. (a) Laser desorption optical path end, 532 nm wavelength. (b) Desorption path CaF_2 viewport, it allows desorption in the visible and near infrared spectral range. (c) Desorption path CaF_2 lens, f = 100 mm. (d) Insulator supporting the acceleration plates. (e) High voltage external supply. (f) Grounded tube connecting the analysis chamber with the flight tube. (g) Desorbed plume (h) Sample. (i) Bronze sample-holder. (j) Sample-holder support rod ("cold finger"). (k) Einzel lens. (l) 5.0 mm thick ultra-vacuum vessel. (m) Repeller plate V_{A1}. (n) Extraction grid V_{A2}. (o) Ground grid V_{A3}. (p) Deflection plates V_{xy}.

4.1.1. Laser Desorption

Once introduced into the analysis chamber, the sample is irradiated at normal incidence by the ns pulses produced by a doubled Nd:YAG Quantel Brilliant laser. In the case of soot analyses, the energy transfer involves both the carbonaceous matrix and the adsorbed substances, inducing the desorption of neutral species from the matrix (see Section 5.2). The desorbed molecules form a plume, which expands in the vacuum of the vessel normally to the sample surface and between the repeller and the extraction plate of the TOF-MS (see Figure 4.2 and Figure 4.3).

The desorption beam has wavelength $\lambda = 532 \text{ nm}$, temporal amplitude $\Delta\tau = 4.6 \pm 0.2 \text{ ns}$ and angular divergence $\theta = 0.409 \text{ mrad}$. The measurements are performed at the repetition rate of $\tau_{rep} = 10 \text{ Hz}$. The characterisation of the spatial beam profile is performed as a standard procedure before any campaign of measurements. The beam transverse intensity profile at the sample surface is reported in Figure 4.4.
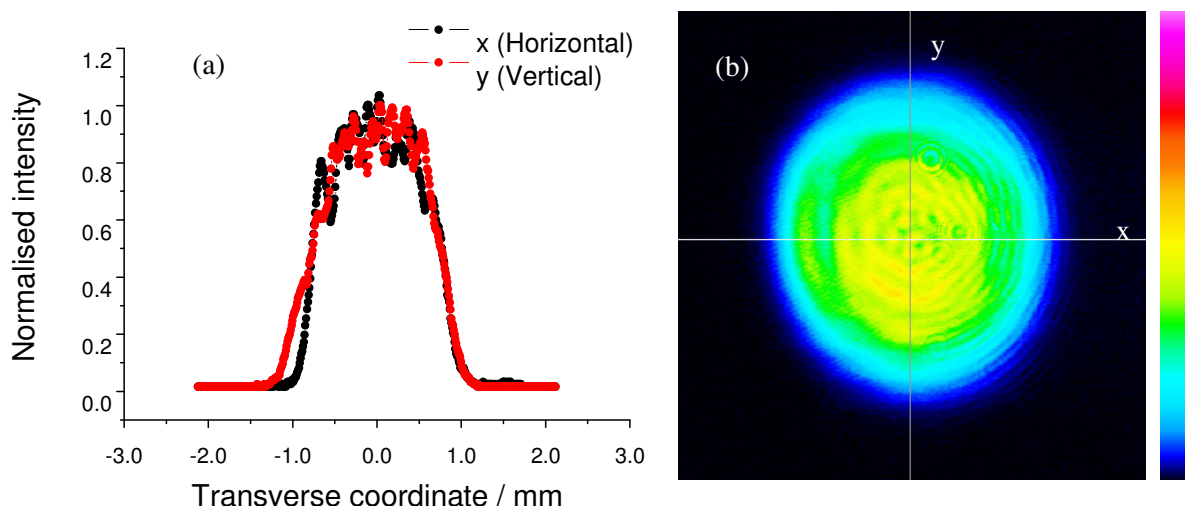
Figure 4.4. Beam profile of 532 nm desorption laser at the sample surface (1.83 mm diameter). (a) intensity as a function of the transverse coordinate, (b) beam profiler image.

The beam transverse intensity profile is a *quasi* Top-Hat (see Paragraph 5.3.1). After energy attenuation and frequency doubling the profile is slightly elliptical (e = 0.90) because of a shoulder located on the external bottom region of the beam in Figure 4.4. The average e^{-2} diameter value has been used to calculate the beam irradiance. In this configuration the beam e^{-2} diameter and section at the sample surface are respectively 1.83 ± 0.01 mm and 2.64 ± 0.03 mm^2, where the measurement error is calculated from the dispersion of 360 consecutive laser pulses. In a typical soot analysis the explored range of irradiances goes from 3 up to 18 MW cm^{-2}.

A detailed scheme of the optical path is reported in Figure 4.5 and Figure 4.6. A series of 532 nm wavelength dichroic mirrors lead the beam from the laser optical head to the analysis chamber's side viewport, and a periscope compensate for the height difference between the optical table and the mass spectrometer. Finally the beam is focused by means of a plano-convex CaF$_2$ lens

(f = 100 mm) placed in the analysis chamber, as shown in Figure 4.6. In order to further lowering the desorption irradiance, the sample surface is located 25 mm away from the focus.
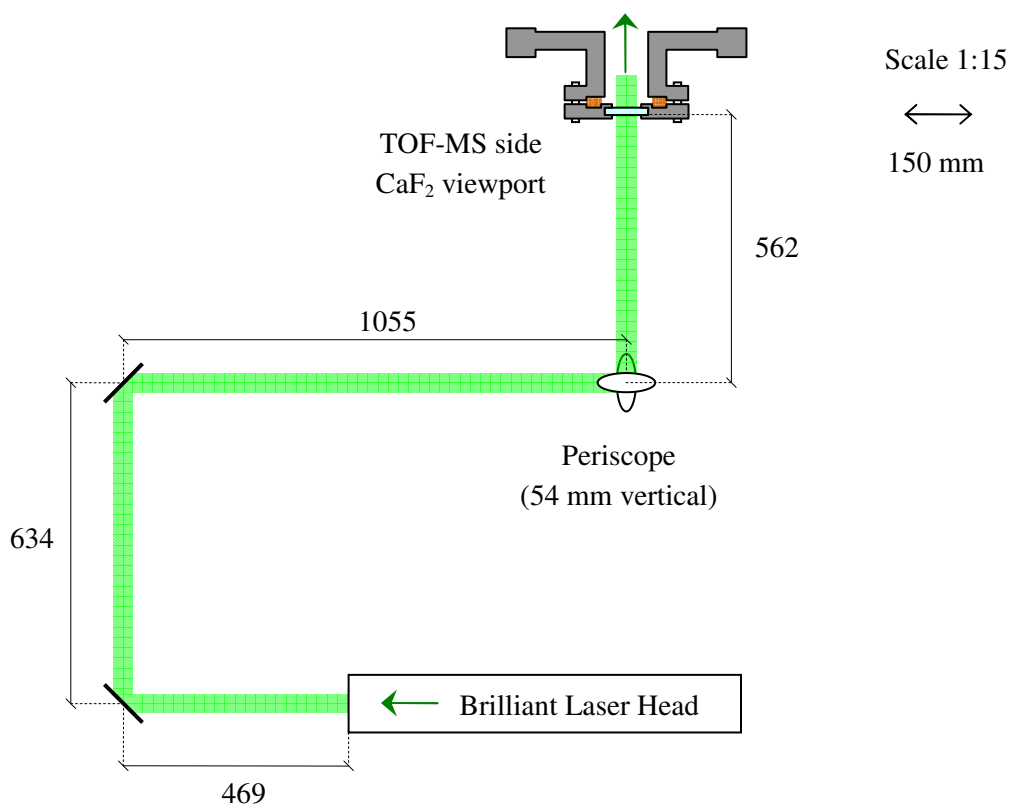
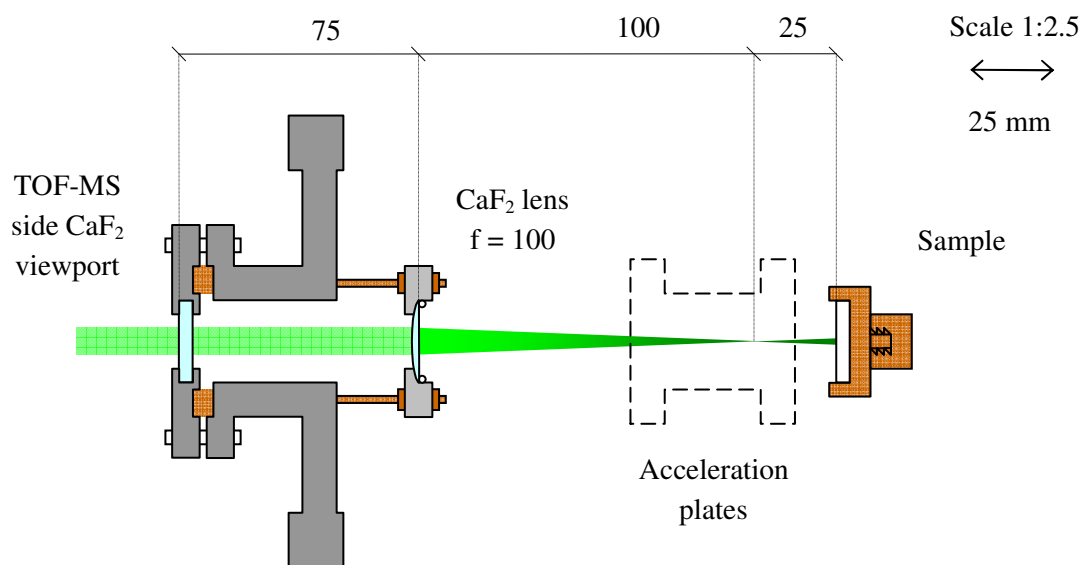**Figure 4.5.** Desorption beam external optical path, from the laser head to the TOF-MS side viewport.

Figure 4.6. Desorption beam optical path into the ionisation chamber of the TOF-MS.

4.1.2. Laser Ionisation

The desorbed plume, now propagating between the TOF-MS repeller and extraction plate, is irradiated by a quadrupled Nd:YAG Spectra Physics Continuum Powerlite Laser. In a typical soot analysis the irradiance varies in the range 1 up 2 MW cm^{-2}, and it is high enough to promote two-photon ionisation on the neutral PAH without inducing dissociation. The ions generated this way are be accelerated into the TOF-MS flight tube.

The ionisation beam has wavelength $\lambda = 266\,\text{nm}$, temporal amplitude $\Delta\tau = 6 \pm 1\,\text{ns}$ and angular divergence $\theta = 0.450\,\text{mrad}$. The measurements are performed at the repetition rate of $\tau_{rep} = 10\,\text{Hz}$. The very poor quality of the laser output required a certain degree of manipulation. A Top-Hat transverse intensity profile has been obtained using a variable diameter diaphragm for selecting the most homogeneous region of the untreated output, and then relay imaging to the centre of the extraction voltage plates by means of a fused silica plano-convex lens (f = 500 mm). A second collimation lens is not required because the imaging lens' focal length is long enough to cover the whole path between the acceleration plates.
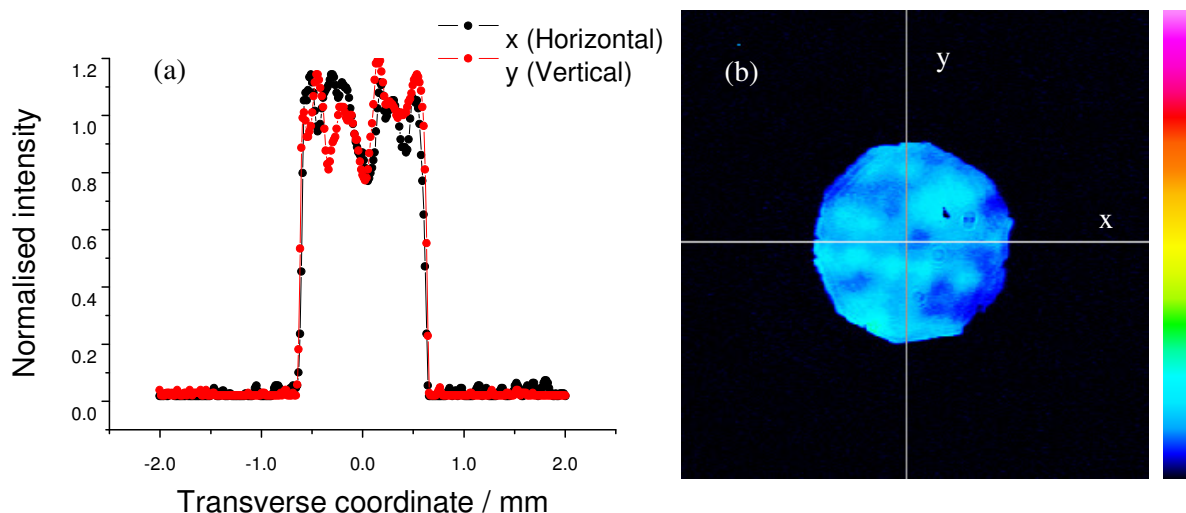
Figure 4.7. Beam profile of 266 nm ionisation laser between the acceleration plated (1.266 mm diameter). (a) intensity as a function of the transverse coordinate, (b) beam profiler image.

The beam shape is polygonal rather than circular because of the variable diameter diaphragm used to produce the image. Indeed, the advantages behind a careful diameter adjustment largely overcome this small deviation from a perfectly circular profile. The ellipticity of the beam calculated on the two axes shown in Figure 4.7 is e = 1.00, and the beam e^{-2} diameter and section are respectively 1.266 ± 0.002 mm and 1.259 ± 0.004 mm^2. The measurement error has been calculated from the average over 360 consecutive laser pulses.

The detailed description of the optical path is reported in Figure 4.8 and Figure 4.9. A series of 266 nm wavelength dichroic mirrors lead the beam from the laser side output mirror to the mass spectrometer bottom viewport. It is important to notice that the beam is unfocused to lower the ionisation irradiance between the acceleration plates. This way it is possible to lower the ionisation irradiance below the PAH dissociation threshold, and at the same time to increase the ionisation volume and therefore the sensitivity of the measure respect to the focused-beam configuration.
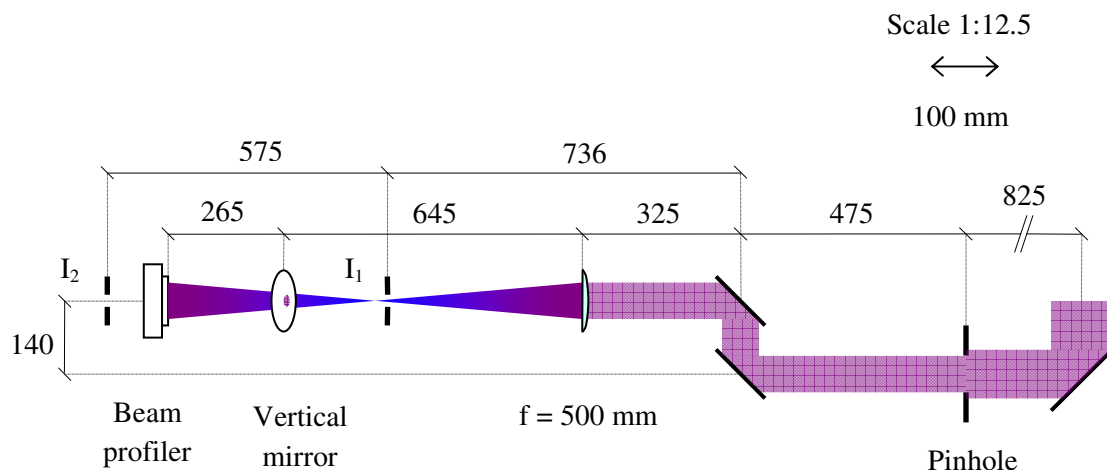
Scale 1:12.5

⟷

100 mm

575

736

265   645   325   475   825

I_2

I_1

140

Beam
profiler

Vertical
mirror

f = 500 mm

Pinhole

Figure 4.8. Ionisation beam external optical path in the configuration used during the diagnostic setup, top view. The laser head (not depicted in the Figure) is on the right of the figure. The beam passes throughout a pinhole, the f = 500 mm lens and eventually it is reflected by the vertical mirror into the analysis chamber. The distance between the beam profiler and the vertical mirror is the same than that between the vertical mirror and the ion source of the mass spectrometer.

Ion source

Scale 1:5

⟵ ⟶

50 mm

194

265

UV
Viewport

71

From the
laser

Vertical
mirror

151

Optical table
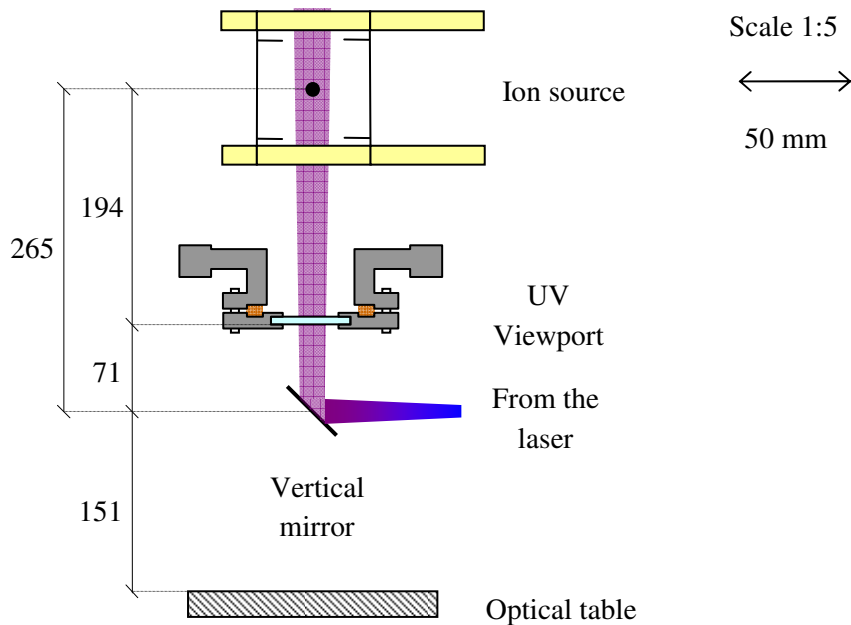
Figure 4.9. Ionisation beam optical path into the analysis chamber of the TOF-MS, side view.

The long focal length of the lens assures the depth of field, providing a slightly divergent beam in the ion source, as shown in Figure 4.10. The mean diameter of the beam varies from $d_{z = -20\ mm} =$ 1.202 mm (-5.1%) to $d_{z = +20\ mm} = 1.313$ mm (+3.6%). The depth of field is long enough to largely cover the whole acceleration plate's zone.
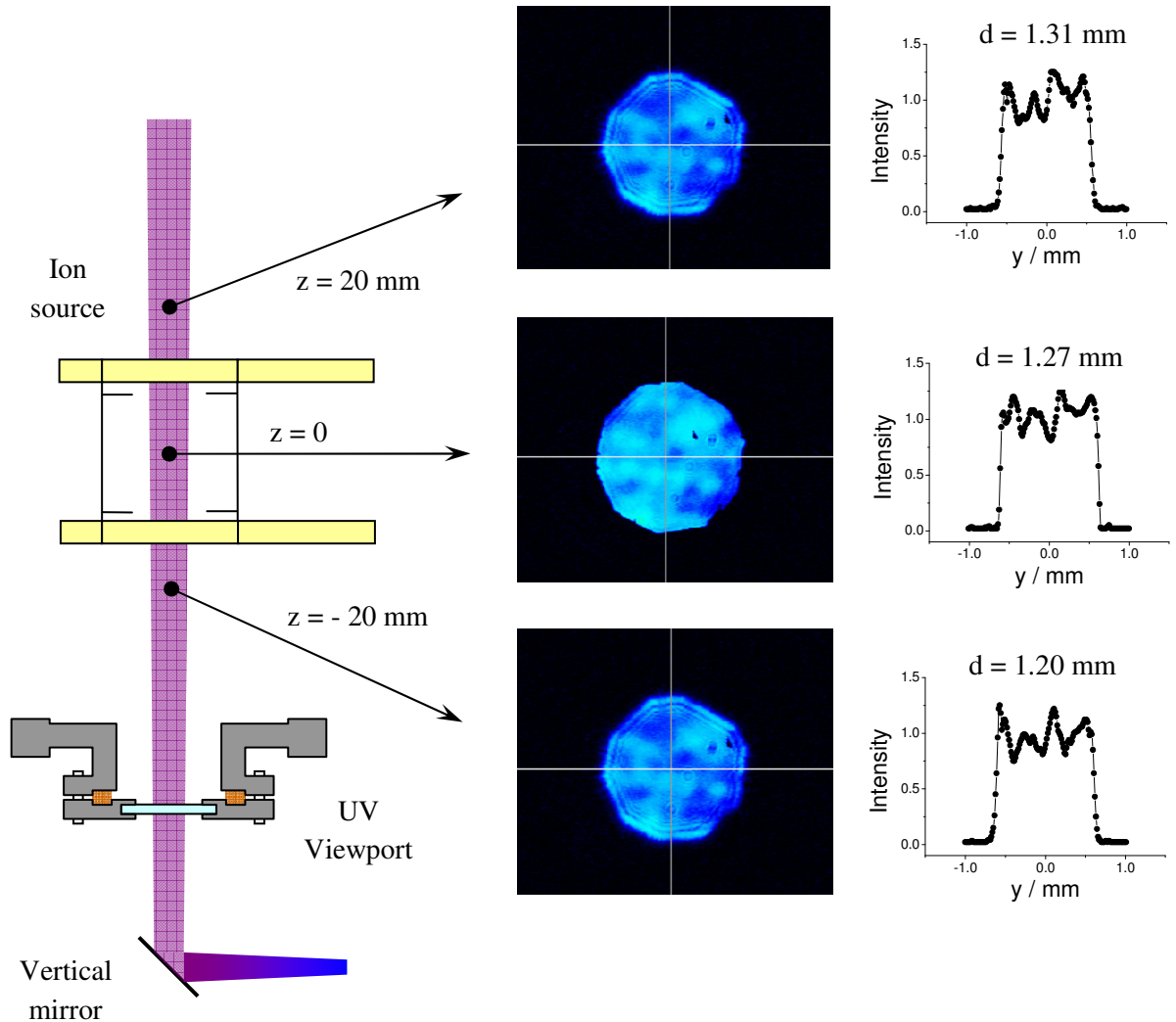
Figure 4.10. Depth of field of the Top-Hat profile. On the left, scheme of the monitored range. On the middle, single shot top views. On the right, transverse y-axis profiles.

During all the soot routine analyses the ionisation irradiance was set constant, but finding the best ionisation conditions required a certain work of system optimisation. Particularly, during the investigations on the photo-dissociation process presented in Section 5.3, a wide ionisation irradiance range has been explored.

At the time of this work a variable energy attenuator working in the UV was not available. Therefore, the final adjustment of the ionisation laser irradiance has been performed acting on the delay between the Continuum laser's flashlamp pulse and the Pockels cell cycle (Q-switch). Though this procedure is very easy to perform and does not require any additional equipment, it has two main drawbacks. First the output profile is generally not constant as a function of the

delay, and second the output is stable in time only when the Q-switch is close to the flashlamp peak emission.

It has been found that the imaging procedure described above largely overcomes the problem of the profile stability since it selects only a small section of the laser output which does not change appreciably in the delay range from 280 up to 380 μs.

Similarly the time output dispersion is less than 5% from 290 to 360 μs delay, as shown in Figure 4.11 where the overall UV output as a function of the Q-switch-flashlamp delay is reported.
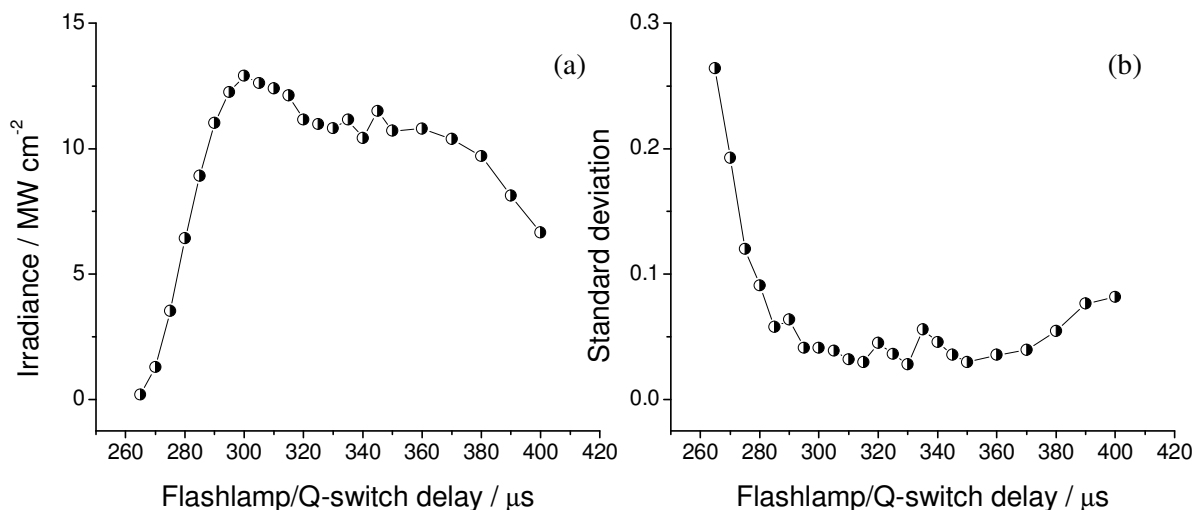
Figure 4.11. (a) Continuum laser output at 266 nm wavelength before the profile manipulation vs. the flashlamp/Q-switch delay. (b) Output reproducibility calculated as the standard deviation over the average of 100 consecutive laser pulses. 400 μs is the maximum reachable delay in the current delay configuration.

4.1.3. TOF-MS

The mass spectrometer has been purchased from Jordan TOF Products, Inc. This system has been used during several research projects including the study of desorption phenomena from ice, the formation of water clusters under sustained irradiation, the desorption of pure PAH, and finally the desorption of PAH from soot. During this time no major modifications have been done except the setting of the acceleration plates.

The scheme of the ion path in the TOF-MS is reported in Figure 4.12, from the ion source in the analysis chamber to the microchannel plate detector. Pictures of the ion source are reproduced in Figure 4.13. The ionisation pulse generates the ion packets between the repeller plate V_{A1} (1.003 kV) and the extraction grid V_{A2} (0.820 kV), which define the ionisation region. The time-of-flight direction is perpendicular to the propagation axis of the sampled plume (*orthogonal extraction*). Since $V_{A1} > V_{A2}$ the ions accelerate in the direction of V_{A2}, pass through V_{A3} (ground), the Einzel lens, between the deflection plates V_{XY} (0.064 kV) and finally enter the drift region. The mass separation is achieved by the different time-of-flight required to ions having different mass to cover the field-free tube. Once arrived at the end of the drift region, an ion mirror (*reflectron TOF-MS*) reflects the ion packets towards the microchannel detector.

Once entered the ion mirror, the ions pass through the retarding grid V_{R1} (0.680 kV) and then they are reflected back by the grid V_{R2} (1.176 kV). When the ions arrive to the detector they impact the first microchannel plate V_{D1} (-1.320 kV). This impact delivers approximately 10^4 electrons onto the face of the second microchannel plate V_{D2} (0.720 kV). Each of these secondary electrons generates another 10^4 electrons in the second plate. These electrons exit the bottom of the plate V_{D3} (0.120 kV) and accelerate the final anode which is at ground potential. The total length covered by the ions from the analysis chamber to the detector is 1.72 m. The mass resolution tipically achieved is $\Delta m/m^{-1} \sim 1000$.
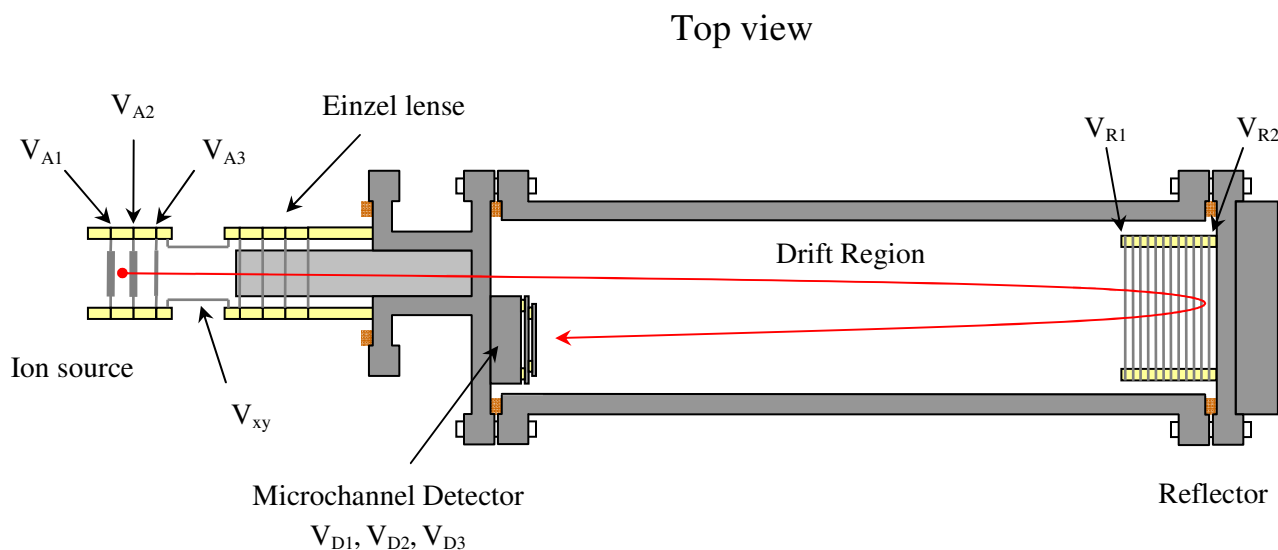
Figure 4.12. Ion path in the TOF-MS, from the generation of the ion packets in the analysis chamber to their detection by the microchannel plate detector. In the figure, the ionisation laser beam propagates normally to the sheet plane and between V_{A1} and V_{A2}.

Orthogonal acceleration TOF-MS

In the orthogonal extraction method the ions are introduced into the field-free drift tube from a direction perpendicular to the sampled beam axis. This setup avoids the problems related to the initial kinetic energy distribution in the axis of propagation of the sampled beam. Such a method improves the sensitivity and it is capable of achieving mass resolutions up to ten-times than conventional TOF-MS [91].

The classical configuration of the orthogonal acceleration requires an ion source producing a continuous collimated ion beam. The beam is usually allowed to propagate between acceleration plates located in such a way to apply a force strictly perpendicular to the propagation coordinate of the beam itself, i.e. parallel to the ion flight direction. The advantage of this configuration is, since the ion beam is collimated, the ions have zero average velocity and minimal velocity dispersion in any direction orthogonal to the propagation direction of the beam. In other words the dispersion of energy is much less important in the directions orthogonal to the ion beam propagation than in the propagation direction itself. Therefore any transverse section of ions is characterised by narrower energy distribution with respect to the packets propagating in the same direction of the beam.
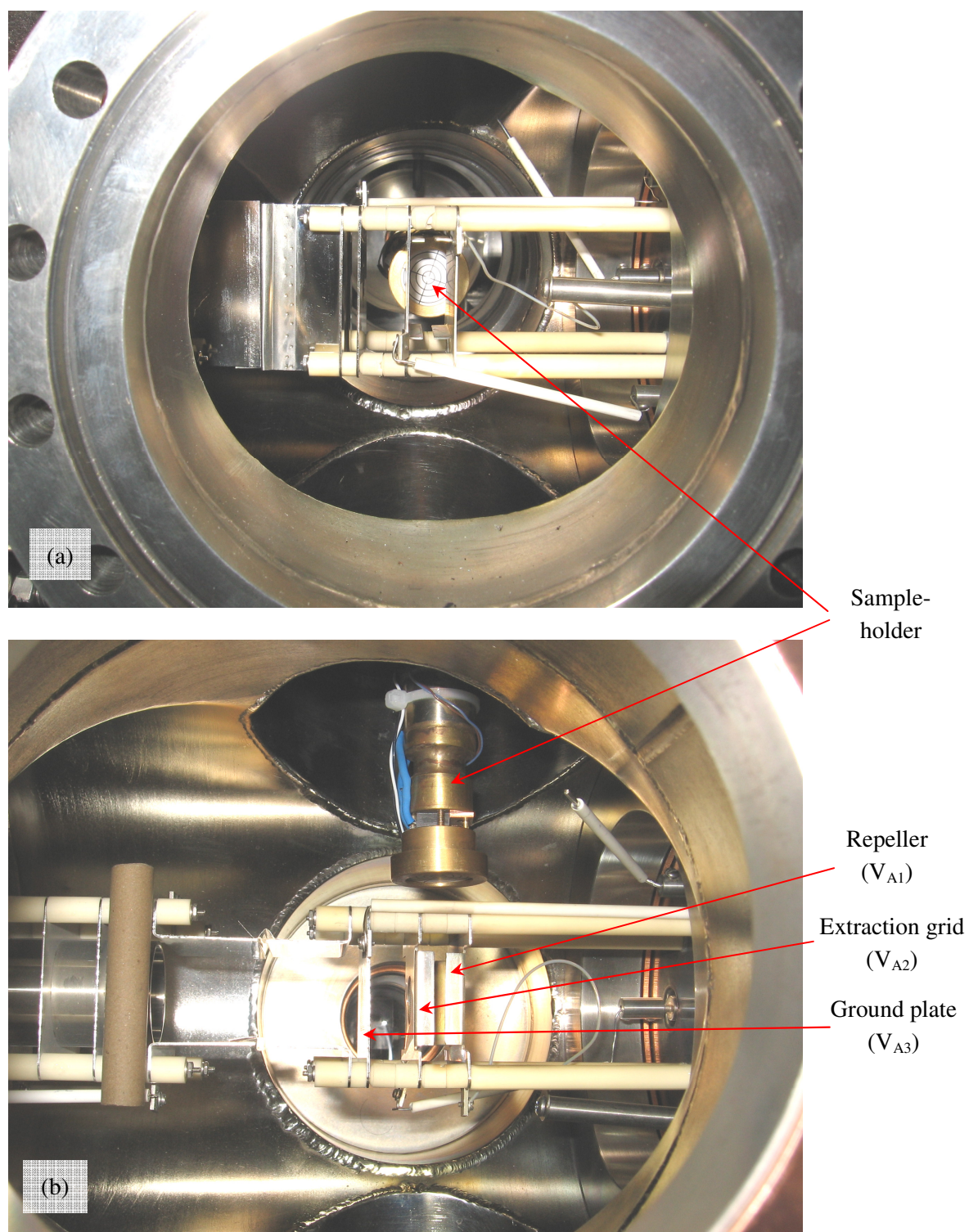
Sample-
holder

Repeller
(V_{A1})

Extraction grid
(V_{A2})

Ground plate
(V_{A3})

Figure 4.13. TOF-MS ion source. View into the analysis chamber of the mass spectrometer through the side desorption-laser port (a), and through the top vacuum-pump port (b). It is well visible the series of three acceleration plates, repeller, extraction grid and ground plate.

Though highly suited to continuous ionisation, orthogonal acceleration is a convenient way to couple TOF-MS with other experimental methods techniques in a more-than-one axis setup. Particularly in the present work this goal has been achieved through the already discussed two pulsed lasers setup.

Orthogonal acceleration has particular interest in MALDI-based techniques [104].

Reflectron TOF-MS

The ion mirror (reflector) is an elegant device which takes advantage of a static field to reverse the velocity vector of ions entering it, and to refocus them on the detector [105]. A picture of the device is reported in Figure 4.14.

The ion packets created between the repeller plate and the extraction grid immediately move toward and through the extraction grid. The ions closed to the extraction grid and far from the repeller plate leave soon the ionisation region, but their speed is low. Conversely, the ions far from the extraction grid and closed to the repeller plate leave later the ionisation region, but their velocity is bigger. This distribution of energy of the ions is due to the finite spatial width of the ionisation pulse, and it implies that the ion beam converges after the extraction plate in a point which is known as *primary focus*. Here the best mass resolution is achieved since the width of the ion packet is on its narrowest point. The Einzel ionic lens may be used for further focusing the ion packet [106]. Unfortunately the primary focus is usually too closed to the extraction plate (typically around 100 mm) to guarantee a sufficient peak separation. After the primary focus the ions beam diverges causing the important loss of mass resolution which represents the limit of the linear TOF-MS.
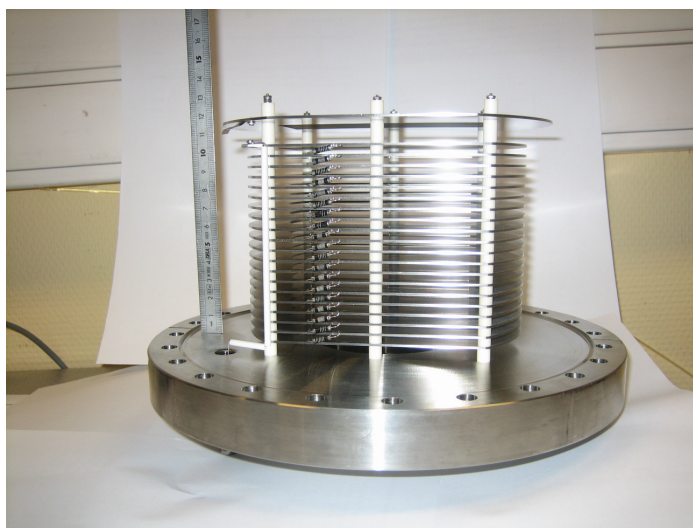
Figure 4.14. Ion mirror (reflector). Picture taken before building up the TOF-MS.

The reflectron is a convenient way to overcome this limitation. The ions are reflected and make converge to a *secondary focus* where the detector is placed. Ion packets arriving to the reflector are spread out because of the ion beam divergence occurring after the primary focus. They enter passing through a series of charged grids which generate a decelerating static field that causes them to slow down, inverse the velocity vector, and finally to accelerate back out of the reflector. When ions with the same mass enter the reflector, the ones having higher kinetic energy penetrate deeper

into the static field. The less energetic ions enter later, but do not penetrate as deep before turning around. Therefore the slower ions leave soon the reflector, while the faster ions leave later because of their longer path length in the static field. At the exit of the reflector the situation is similar to the ion source, with the more energetic ions moving faster but leaving later. The ion packets converge again on the secondary focus, and placing the detector at this point has the same benefit to resolution as it did at the primary focus.

A relatively recent alternative is the dual-focus reflectron. In such a device two field regions are generated, where the first one is significantly stronger than the second one [107]. The second field provides a second-order energy focusing, while the first stronger field reduces the overall size of the device.

Ion detection

The ion detection is performed via a microchannel plate detector (MCP). It consists of a regular array of glass capillaries fused together into a thin plate [108]. Each of these microchannels has approximately 10 μm diameter, and works as an independent secondary-electron multiplier, in which the multiplication takes place under the presence of a strong electric field. The ions entering the device hit the wall of the channels because of the small angle occurring between the channel axis and the normal to the plate. The impact starts a cascade of electrons that propagates through the channel, amplifying the original signal by several orders of magnitude depending on the electric field strength and the geometry of the microchannel plate.

After the first plate a second one rotated of 180° is placed, in the so-called *chevron* (v-like) shape. In a chevron MCP the electrons that exit the first plate start the cascade in the next, allowing a significantly more gain at a given supply voltage. The detector used in the present work gives overall signal gain around 10^6.

The MCP shows high detection efficiency to electrons and ions. They are also sensitive to a wide range of other radiation including UV, VUV, soft X-ray photons and neutrons. A picture of the device is reported in Figure 4.15.
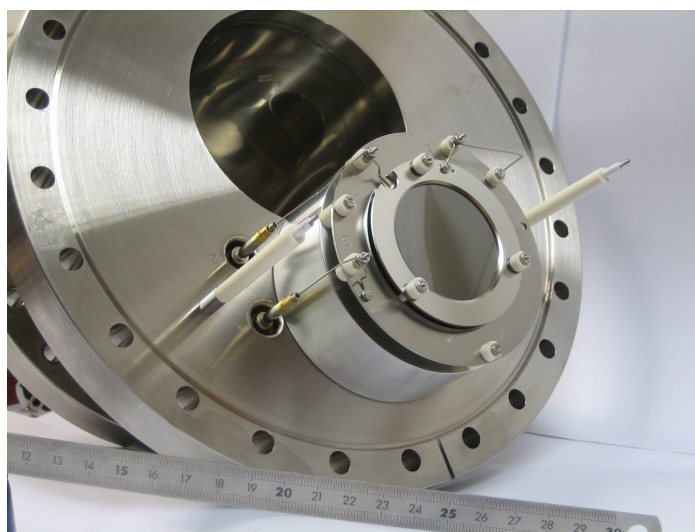

Figure 4.15. Microchannel plate detector Galileo MCP-18P. Picture taken before building up the TOF-MS.

4.1.4. Signal acquisition

Ion detector signals are recorded using a 2 GHz digital oscilloscope LeCroy Waverunner 6200A, at a time resolution of 4 ns/point. The acquisition frequency is fast enough to avoid a loss of resolution on the mass spectra. An EGG Ortec VT120 fast pre-amplifier is also available.

The time-of-flight data were externally calibrated for each desorption and ionisation condition, plate voltage and different sample preparations. To this purpose, a two-point calibration algorithm has been developped in LabVIEW (National Instruments) platform.

4.1.5. Delay desorption-ionisation. Timing setup

When setting the delay between the desorption and ionisation pulses, the time needed by the plume to expand from the sample surface up to the ionisation beam must be considered. Changing the delay time between the desorption and ionisation pulses is equivalent to sample the plume of desorbed molecules at different locations. The peak signal of a standard pyrene sample has been recorded as a function of the time delay for different desorption irradiance, as shown in Figure 4.16. The shift of the maximum of the curve towards a shorter time delay when increasing the desorption irradiance is consistent with the expected higher temperature of the ejecta, hence with the higher velocity of propagation of the plume of neutrals. The time delay has been set to 50 μs in order to get the maximum of signal, and all the analyses have been performed with this configuration.
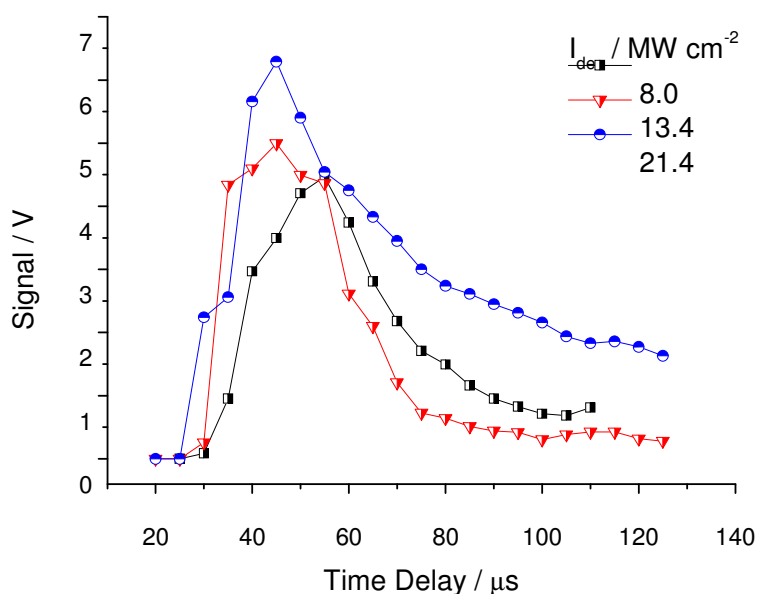
Figure 4.16. Evolution of the signal as a function of the time delay. Measurment performed on a pure pyrene sample, $I_{ion} = 0.67$ MW cm^{-2}. The curves represent three different I_{des}.

The timing of the desorption and ionisation pulses is controlled using a digital four channel delay/pulse generator, Stanford Research System, Inc (model DG-535). The currently used delay scheme is reported in Figure 24. D-B is the delay between the Q-switches corresponding to the emission of the two laser pulses.

t_0 100 μs   A   240 μs   B   50 μs   D

C   320 μs
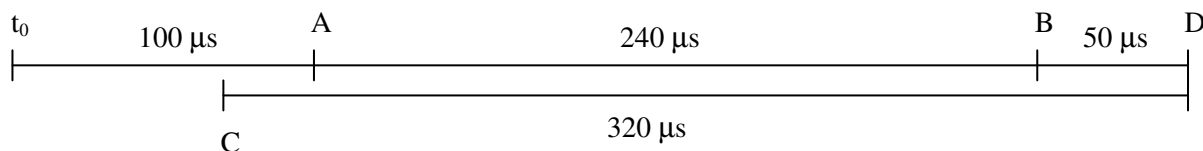
Figure 4.17. Adopted timing setup. t_0: reference time. A: Quantel Brilliant flashlamp. B: Quantel Brilliant Q-switch. C: Continuum Powerlite Flashlamp. D: Continuum Powerlite Q-switch. The delay between the two laser pulses is the D-B delay.

4.2. Flames and sampling

This Section presents an overview of the setup concerning the different flames which have been stabilised in order to sampling the soot and gases produced during the combustion process, as well as the methods used in order to produce the samples. The Section is organised as follows. Paragraph 4.2.1 presents a general description of the various version of the burner. Paragraph 4.2.2, 4.2.3 and 4.2.4 describe the setups of each one of the studied flames, respectively an ethylene premixed atmospheric flame, a methane premixed low-pressure flame and a diesel jet diffusion flame. Paragraph 4.2.5 describes the probes used during the sampling, and finally Paragraph 4.2.6 deals with the system of collection and deposition of the collected substance into a sample suitable for the LD/LI/TOF-MS analysis.

4.2.1. Burner

In this work burners have been used in order to study a premixed atmospheric ethylene flame, a premixed low-pressure methane flame, and a diffusion jet diesel flame.

The McKenna burner used for the two premixed flames is the basic unmodified commercial version. This is constituted by a central circular plug, fed with the premixed fuel/oxidant mixture, enclosed by an outer ring which can be independently fed with an inert gas, typically nitrogen, to create a protection shield around the flame. The central plug has diameter d_{in} = 60 mm. Both the central plug and the outer ring are made in porous bronze, which allows the fuel, fed by the bottom, to reach the top burner surface where ignition is caused. The burner supply is controlled by Mass Flow Controllers (MFC) conveniently located in the feeding line. The burner used in the study of the diesel jet flame consists of a modified McKenna equipped with a Direct Injection High-Efficiency Nebuliser (DIHEN-170-AA) for the atomisation of liquid fuels. The nebuliser is inserted in the centre of the bronze plug throughout a 6.35 mm diameter tube.

All the burners are water cooled. The temperature is kept constant at 50°C via a water cooling recirculation or using city water in the case of the jet flame.

4.2.2. Atmospheric ethylene premixed flame

An ethylene/oxygen premixed laminar flame, having equivalence ratio $\phi = 3.03$ and total flow $Q_T = 6.78$ slpm has been stabilised at atmospheric pressure, and used to test the LD/LI/TOF-MS diagnostic. The flame conditions have been taken from the work of Apicella and co-workers [76,77,127,128]. The velocity of the cold gases is $v_0 = 4.0$ cm s^{-1}, while the molar fractions are:

$$C_2H_4 : O_2 = 0.503 : 0.497$$

This flame has been stabilised by means of a 12 mm thick stainless steel plate located 30 mm above the surface of the burner. The characterisation of the flame via LD/LI/TOF-MS is detailed in Section 6.2. The scheme of the feeding line is detailed in Figure 4.18. The alimentation of the burner is controlled via two mass flow controllers, one for each gas of the premixed blend. The nitrogen shield has been found unnecessary in order to stabilise the flame, and therefore was not used.
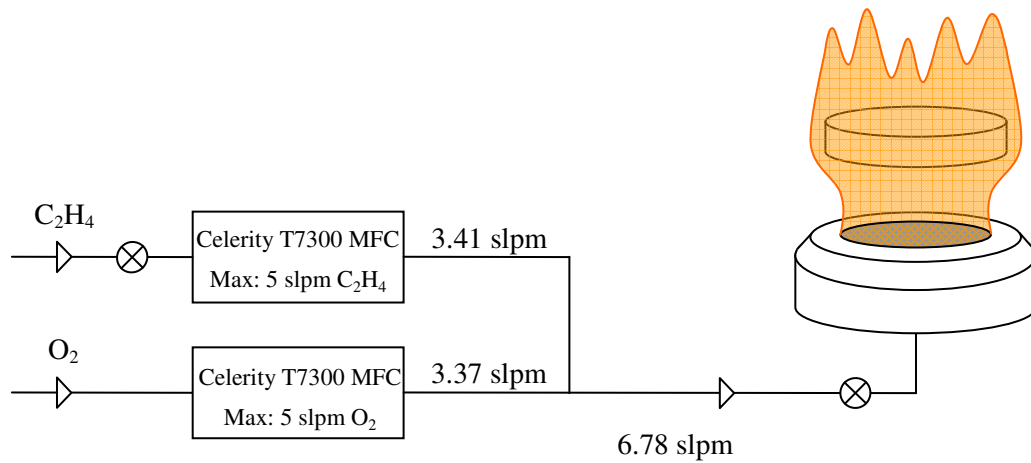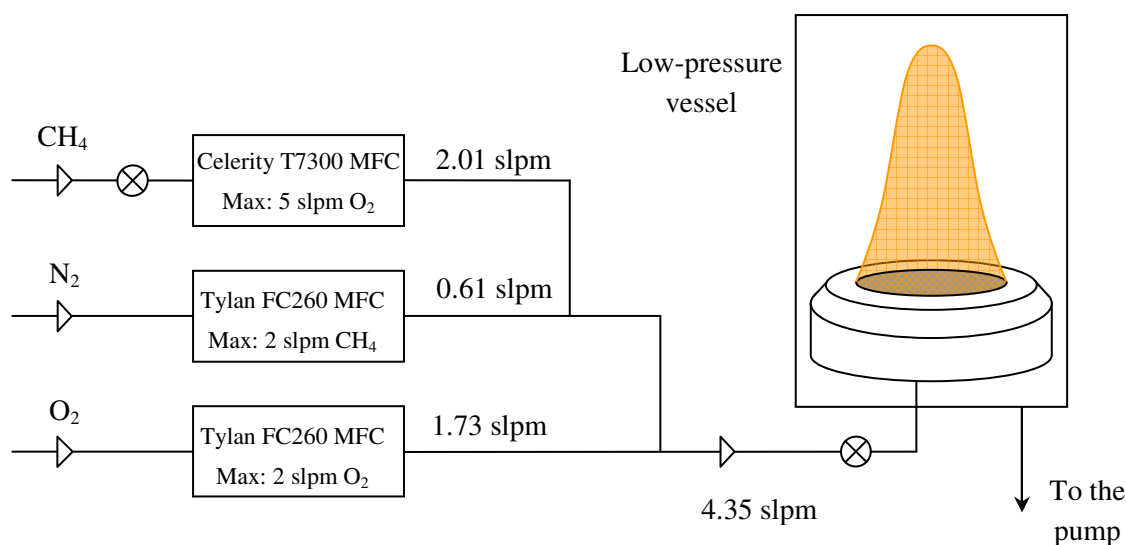

Figure 4.18. Experimental configuration of the premixed laminar ethylene flame ($\phi = 3.03$, $Q_T = 6.78$ slpm, $v_0 = 4.0$ cm s^{-1}) described in the text. The flame is stabilised at atmospheric pressure.

4.2.3. Low-pressure methane premixed flame

A methane/oxygen/nitrogen premixed laminar flame, having equivalence ratio $\phi = 2.32$ and total flow $Q_T = 4.35$ slpm has been stabilised into a stainless steel vessel at 26.66 kPa. The velocity of the cold gases is $v_0 = 25.6$ cm s^{-1}, while the molar fractions are:

$$CH_4 : O_2 : N_2 = 0.462 : 0.398 : 0.140 \tag{4.1}$$

This flame has been the subject of recent investigations [109,110]. In this work both ex-situ LD/LI/TOF-MS (Section 6.3) and in-situ LII (Appendix B) analyses have been performed.

The vessel is connected to an oil pump through a system of manual-regulation valves keeping the pressure oscillations in the range 26.66 ± 0.07 kPa (200 ± 0.5 torr). The control over the pressure is critically important since a recent work of Desgroux and co-workers performed on this same flame demonstrated a soot volume fraction vs. pressure power dependence $f_v \propto kp^{11}$ [109].

The burner is installed in the vessel on a movable support. It allows translation of the flame with respect to the probe (required for the ex-situ LD/LI/TOF-MS) and the windows the laser beam

passes through (related to the in-situ LII), which are both connected to non-movable parts of the vessel.

The scheme of the supply lines is reported in Figure 4.19. The alimentation of the burner is regulated via mass flow controllers, one for each gas of the premixed blend. A gentle flow of nitrogen (2.0 slpm) directed to the inner side of the windows has been stabilised in order to avoid the deposition of soot and keep them clean. This is particularly important when performing LII measurements (Appendix B).

A glass-insulated electrode inserted into the vessel and connected to an external power source (discharging 3.0 kV) is used to light the flame. In order to avoid the overstock of fuel in the vessel with the consequent risk of explosion the ignition is performed on a lean flame ($\phi \sim 0.8$).

Figure 4.19. Experimental configuration of the premixed laminar methane flame ($\phi = 2.32$, $Q_T = 4.35$ slpm, $v_0 = 2.56$ cm s^{-1}) described in the text. The flame is stabilised at 26.66 kPa in a stainless steel vessel.

4.2.4. Atmospheric diesel jet flame

An atmospheric diesel jet turbulent flame has been stabilised on the modified McKenna burner equipped with the nebuliser described in Section 4.2.1 [111]. The operating principle of this coaxial atomiser is based on assisted atomisation. The high velocity gas flowing in the annulus area nebulises the low velocity liquid flowing in the central 104 μm diameter capillary. This nebuliser is well suited for combustion applications since it delivers sprays of very small droplets which are quite immediately vaporised after ignition. A complete vaporisation of the liquid sprays is then obtained without fractional distillation above 15 mm HAB [111,112]. After this height, the flames behave similarly to a turbulent diffusion gas flame. Furthermore, the use of highly atomised and hence rapidly vaporising sprays generates quite comparable hydrodynamic conditions for each fuel resulting in very similar turbulent diffusion flames of around 180 mm height and 20 mm width with comparable sooting flame patterns. Flames were found to be very reproducible, leading to an accurate comparison of the characteristics of the various fuels.

In this work the nebulisation gas is nitrogen. The gas flow rate is fixed at 0.32 slpm, and the various liquid hydrocarbons are introduced in the nebuliser capillary with a constant mass flow rate of 46 g/h. The ignition of the fuel jet exiting the injector is performed by a lean premixed methane/air flat flame stabilised on the porous plug of the burner. Figure 4.20 reports the scheme of the supply lines of the burner.
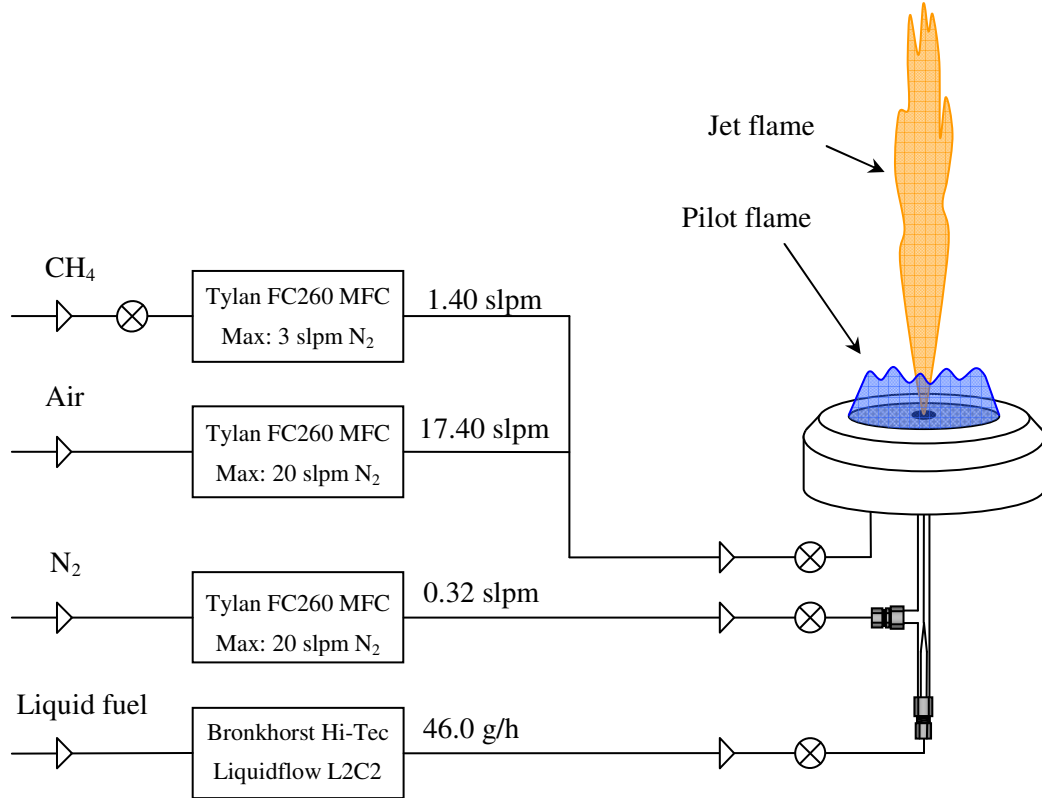

Figure 4.20. Experimental configuration of the jet turbulent flame described in the text. The flame is stabilised at atmospheric pressure. The flows of methane and air feed the pilot lean flame on the plug of the burner, while the liquid fuels arrive to the flame through the nebulised inserted in the central hole of the plug. The bottom MFC controls the nitrogen shield flow.

4.2.5. The probes

Soot and gases have been extracted from the flame by means of the two quartz extractive probes depicted in Figure 4.21.

The probe in Figure 4.21 (a) consists of a quartz tube of outside diameter 10 mm, reduced at the extremity down to 0.8 mm diameter aperture. This probe has been used to sample the two laminar premixed flames. The effect on the sampling of a 0.3 mm diameter aperture probe has been tested as well, as detailed in Paragraph 6.1.5. This probe is introduced axially in the flames, throughout the stabilisation plate in the case of the premixed ethylene flame as shown in Figure 4.22.

The probe in Figure 4.21 (b) consists of two concentric quartz tubes of outside diameter 10 and 6 mm reduced at their extremity to have a 0.9 mm diameter aperture. A nitrogen flow coming from the inner tube and controlled by a MFC allows the dilution of soot and gases in the cavity between the tubes in order to reduce the condensation phenomena and quench the chemical reactions still

occurring at the time of the sampling. This probe has only been used to sample the jet flame. Indeed, the large amount of soot produced there allows the investigation of the effect of the dilution vs. the sampling time. This is unfortunately not possible in the low pressure flame because of the insufficient amount of collected matter.The probe is introduced radially in the flame, as shown in Figure 4.22 (c).

  The thin end of the probes can be located at the desired position in the flame with high accuracy (the positioning uncertainty is less than 0.1 mm). The probed volume is estimated as twice the diameter of the probe aperture [113], and it is fine enough to target specific regions in the flame.
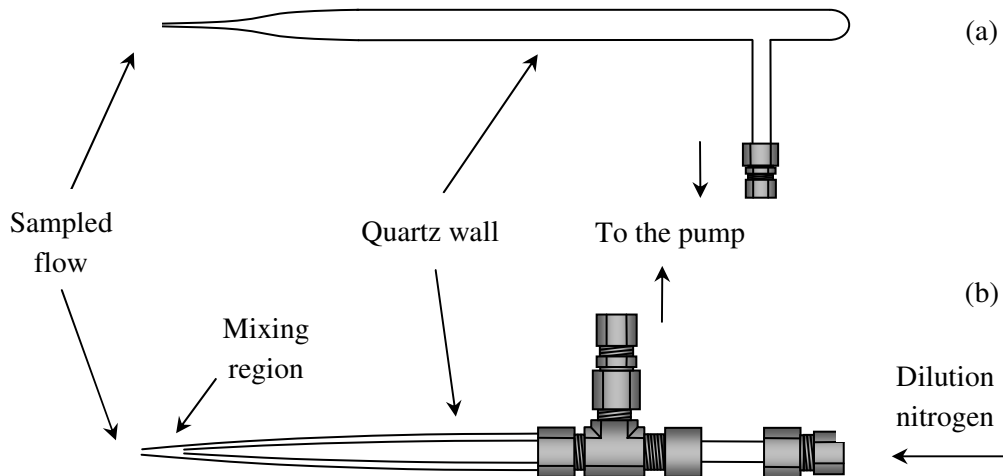
Figure 4.21. Scheme of the extractive probes. (a) probe used in the atmospheric diesel jet flame and (b) probe used in the laminar premixed low-pressure flame.
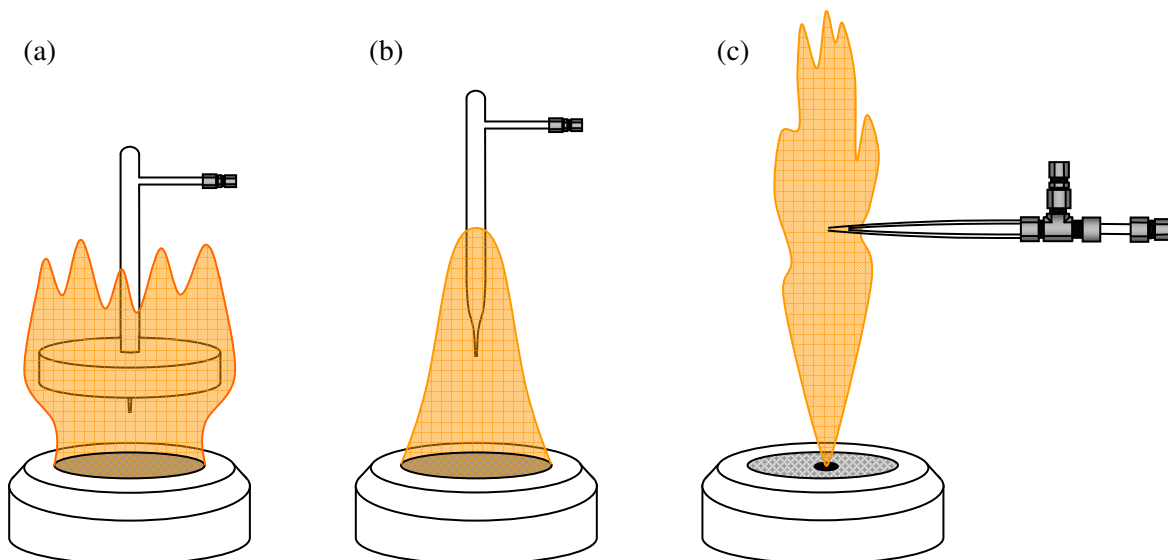
Figure 4.22. Comparison between the three extraction techniques. (a) Atmospheric ethylene premixed flame, the probe is introduced axially throughout the stabilisation plate. (b) Low-pressure methane premixed flame, the probe is introduced axially throughout the low-pressure vessels. (c) Atmospheric diesel jet flame, the probe is introduced radially.

4.2.6. The sampling line

Once extracted from the flame by means of the probes described in the previous Paragraph, soot and gases enter the sampling line. This consists of a special steel pipe connecting the probe and the sample-holder, the sample-holder itself and finally the pump.

The probe is connected to the sample-holder through a steel pipe whose inner wall is covered with a thin layer of Teflon to limit the condensation phenomena. For further reducing the condensation, the pipe is heated up to 240°C during the sampling. Measurements performed in this work and detailed in Paragraph 6.1.3 demonstrate that some light masses ($m/z<178$) result in stronger signals when heating.

The sample-holder is a home-built piece comprised of a series of ISO-KF 16/25 fittings, as depicted in Figure 4.23. The spacing between two consecutive fits well matches the size of the borosilicate filter, and therefore two centring o-rings are only needed to provide the overall sealing. A bypass line, accessible by switching a couple of three-way valves, has been set as well to provide a pre-sampling pumping along the line, in order to allow the stabilisation of pressure and temperature. The sample-holder is constituted by two parallel housing, allowing the simultaneous sampling on two different lines. This configuration is particularly useful when depositing soot and gases on different substrates. The borosilicate filters on which soot and gases are deposed are circular (20 mm diameter) and have average pore size of 10-16 μm (P4 European Standard). As detailed in Paragraph 6.1.1 , the deposition has been performed on both the surface of neat filters and on filters covered by a layer of 7-10 mg of activated carbon, in the context of a method to distinguish the condensed PAH from those adsorbed on soot.

The downstream side of the sample-holder is connected with a primary vacuum pump keeping the pressure at 2.67 kPa, thus allowing a constant flow between the flame and the sample-holder.
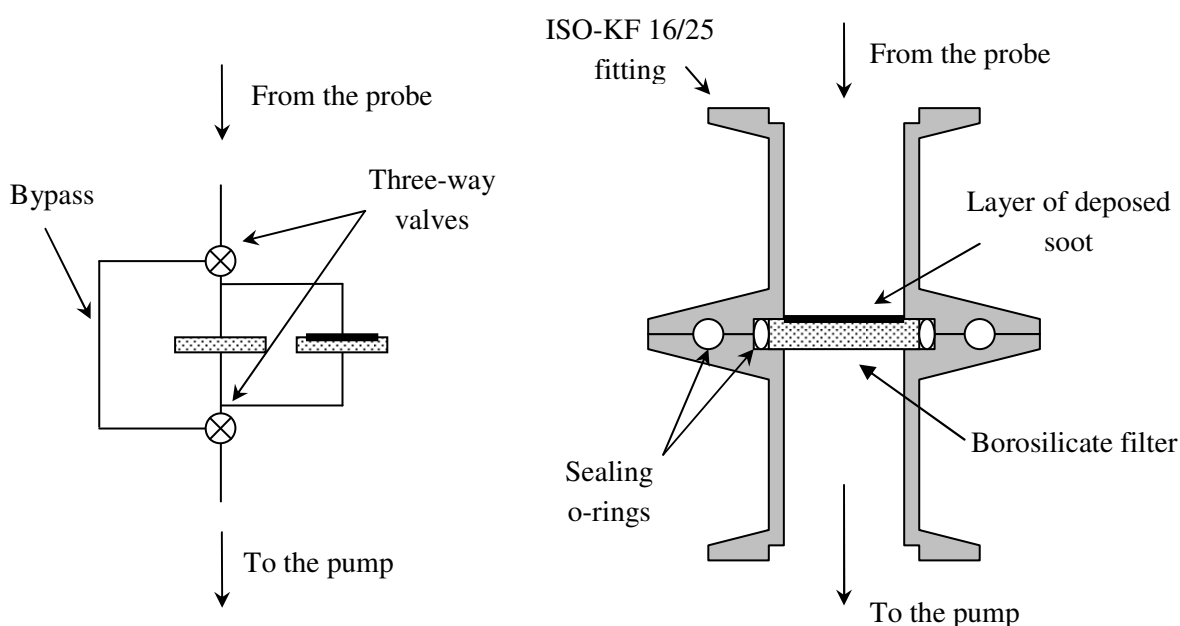
Figure 4.23. (a) working diagram of the sample-holder and (b) section of the sample-holder with the borosilicate filter in place.

Since in the atmospheric diesel jet flame a large amount of gaseous products could potentially foul the pump, additional devices to protect the pump have to be added. An ice trap cooled with a mixture of liquid nitrogen and ethanol (T ~ -60°C), a 10 μm filter and a calcium sulphate drier have been added after the sample-holder in order to protect the pump. When sampling the low-pressure methane flame (at 26.67 kPa) the amount of collected soot is much smaller, and therefore these devices are unnecessary.

The required sampling time to cover the disc surface with a more or less homogeneous layer of soot is around one minute for the atmospheric flames and not less than half an hour for the low-pressure flame. The temperature of the borosilicate discs during the sampling is 45-50°C.

The sampling has been performed at several different HAB in the same flame, to cover both the region before and after the soot inception. After each HAB change the whole sampling line between the probe and the sample-holder has been disassembled, washed and re-assembled in order to avoid contamination from soot originated at different HAB. The soot in the inner wall of the quartz probe has been removed by heating the probe using a butane camping stove.

Chapter 5.

Characterisation of the desorption and ionisation steps

This Section aims to provide to the Reader the fundamentals about the response of PAH to the desorption and ionisation processes during a LD/LI/TOF-MS analysis. A careful adjustment of the laser wavelength, irradiance and time delay between the pulses drastically affects the overall analytical response and the quality of the mass spectra, allowing for instance the optimisation of the desorption yield, or the minimisation of the parasite photo-dissociation processes.

The measurements presented in this Section have been performed on both pure PAH and PAH adsorbed on a carbonaceous substrate (*model soot*) simulating real soot, as a part of a strategy aiming to characterise the LD/LI/TOF-MS response of more and more complex systems and tending towards real soot samples. The selected standards are six low-mass PAH: naphthalene, acenaphthene, anthracene, phenanthrene, pyrene and fluoranthene. The results highlight a complex relationship between the desorption and ionisation steps, and furthermore the characterisation of the response to the ionisation leads to some insights on the photo-dissociation mechanism of PAH.

This Section contains four main parts: Section 5.1 and 5.2 deal with the characterisation of the desorption step on pure PAH and on model soot, Section 5.3 describes the photoionisation process of PAH, and finally Section 5.4 treats the coupling desorption-ionisation.

5.1. Desorption of pure PAH

This work is the following of a series of investigations aiming to make ready for use and completely characterise the LD/LI/TOF-MS setup. Several works have been dedicated to the detailed characterisation of the desorption process of pure PAH and PAH adsorbed on soot [101,112-116]. This Section briefly resumes some of the most important results of the Ph.D. thesis of C. Mihesan [116] on which the work presented in the next Section 5.2 on model soot is based. Briefly, the response to the wavelength and irradiance (I_{des}) of the desorption process has been characterised for the six pure PAH above mentioned.

5.1.1. Effect of the wavelength

The energy transfer from the optical field and the absorbing material is obviously very effective when the irradiation wavelength is resonant with one of the absorption bands of the analyte. The laser desorption response to wavelength has been studied for naphthalene, acenaphthene and phenanthrene [101] in the Mid Infra-Red (MIR), i.e. in the spectral region of the C-H stretching mode (~3300 nm). The comparison between the desorption yield and the absorption spectra is reported in Figure 5.1. The very good agreement between the desorption yield and the near infrared absorption demonstrates that it is possible to increase the efficiency of the desorption process by taking advantage on the vibrational transitions of the analysed PAH (laser resonant desorption).
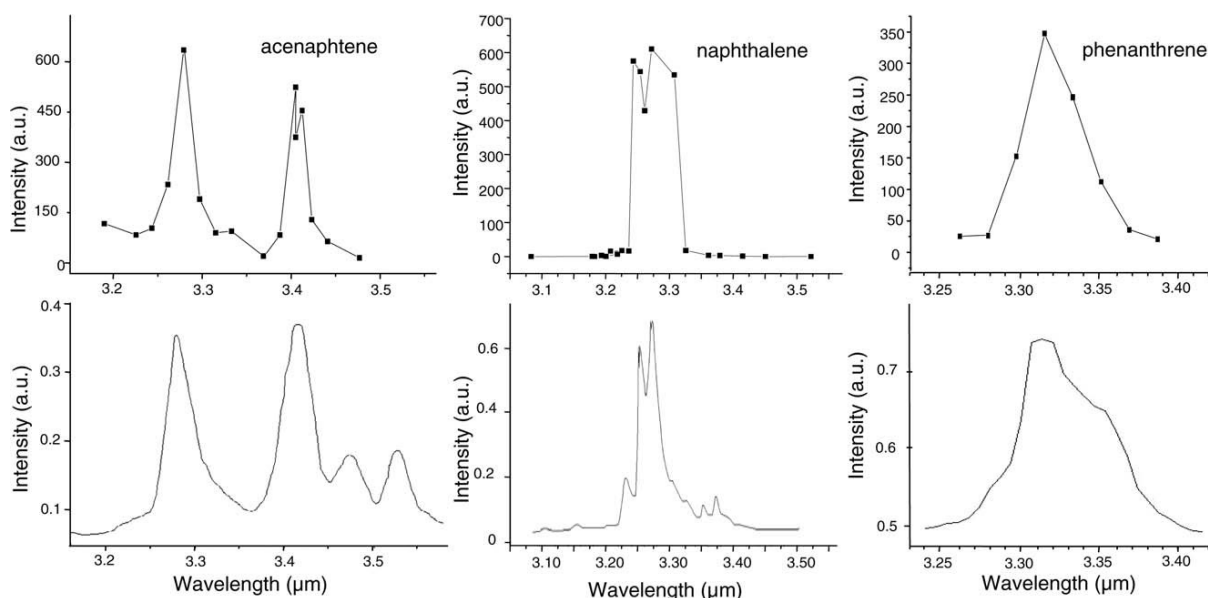
Figure 5.1. Comparison between the desorption yield (top line) and the NIR absorption spectra on acenaphthene, naphthalene and phenanthrene in the spectral region of the C-H stretching. Figure reproduced from [101].

5.1.2. Effect of the irradiance

The peak intensity vs. I_{des} dependence is reported in Figure 5.2. This study has been performed using 532 nm desorption wavelength, a convenient wavelength because of the enhanced desorption yield occurring for low-mass PAH, for which two-photon absorption (electronic resonance at 266 nm) is in principle possible (see the UV-Vis absorption spectra reported in Figure 5.3). The main advantage of working in the visible range of wavelength is the availability of a much higher laser power from the conversion in the visible rather than in the MIR, and therefore the possibility of performing wide-range signal vs. I_{des} investigations.

This study highlights a characteristic response of each tested PAH. Indeed, for each PAH it is possible to identify a specific desorption threshold, an optimum I_{des} leading to the maximum desorption yield and a working range. The difference in the response to the desorption process in principle provides the required selectivity needed to discriminate different isomeric PAH, because

the specificity is preserved in the case of mixtures of pure PAH. Furthermore the knowledge of the response to the desorption irradiance of each analyte allows the optimisation of the desorption yield in order to reach the best signal-to-noise ratio, and to avoid the dissociation reactions due to the possible excess of population in the excited rovibronic levels. Figure 5.2 reports the desorption yield as a function of the I_{des} at the wavelength of 532 nm, while Figure 5.3 reports the UV-Vis absorption spectra of the six PAH in a cycloexane solution. The analysed pure PAH feature a species-dependent desorption threshold, above which the energy transferred to the sample is sufficient to create the plume of desorbed molecules. The position of the desorption threshold depends on spectroscopic and molecular properties of the analysed PAH, like the absorption coefficient at 532 nm wavelength and the enthalpy of sublimation. In the low-irradiance limit, the number of desorbed particles increases with I_{des} leading to the sharp rise of the peak intensity above the desorption threshold. When further increasing I_{des}, the desorption yield reaches a maximum and then decreases. Because of the competition of the desorption efficiency with photo-dissociation phenomena (Section 5.3), which remove precursor ions from the plume. In the high-irradiance regime the desorption yield decreases when eventually the photo-dissociation becomes dominant.
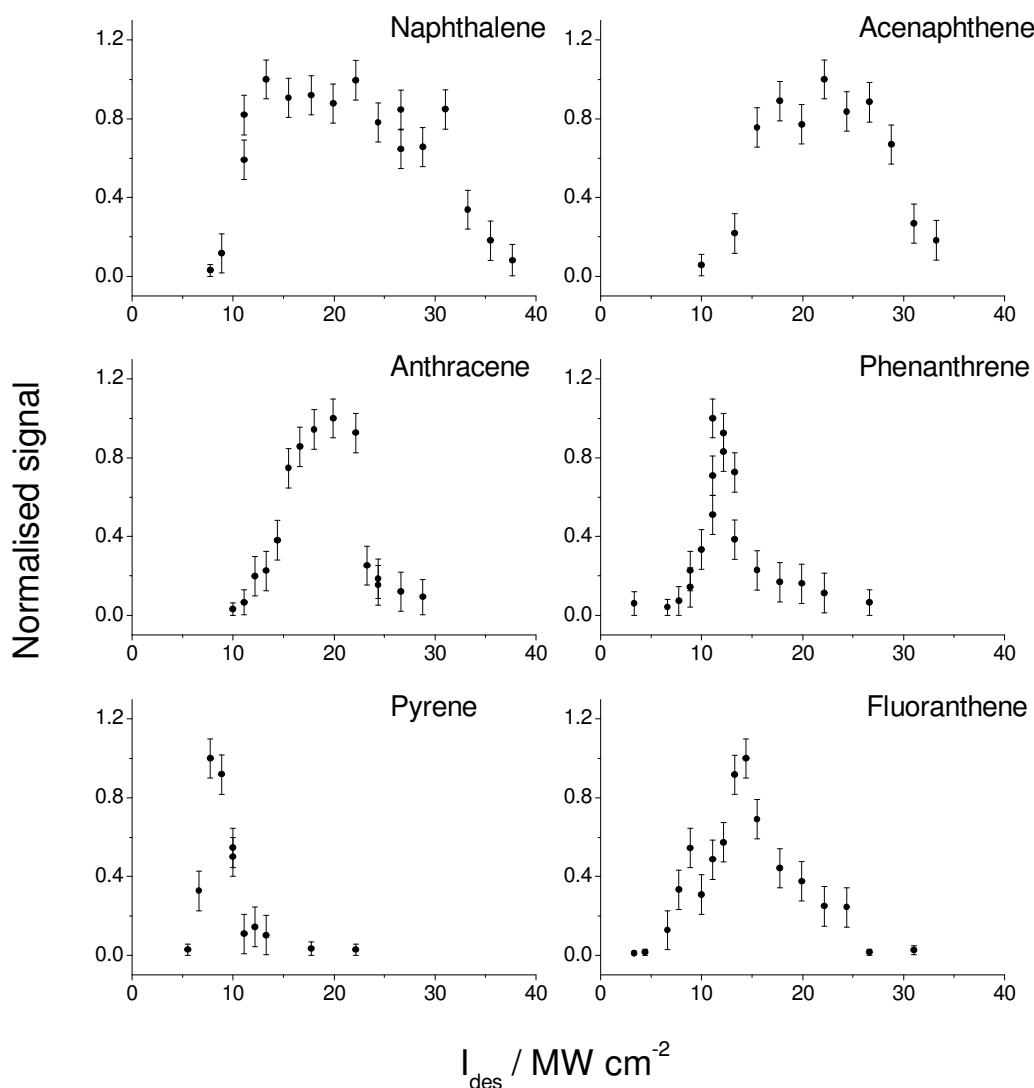
Figure 5.2. Dependence of the desorption yield on I_{des} of six PAH at the desorption wavelength of 532 nm [101].

The evolution of the precursor ions peak intensity as a function of the desorption irradiance has been described as a competition between the desorption efficiency and the photo-dissociation [100]. Higher desorption irradiance increases the internal energy of the ejected PAH, making their dissociation and ionisation possible at lower ionisation irradiance. Moreover, the number of desorbed molecules and then the number of collisions in the plume increases with the desorption irradiance, leading to an increase of the in-plume dissociation before the laser ionisation. According to the discussion so far, it is evident that the two processes (laser desorption and laser ionisation) are not independent. Their relation will be detailed in Section 5.4.
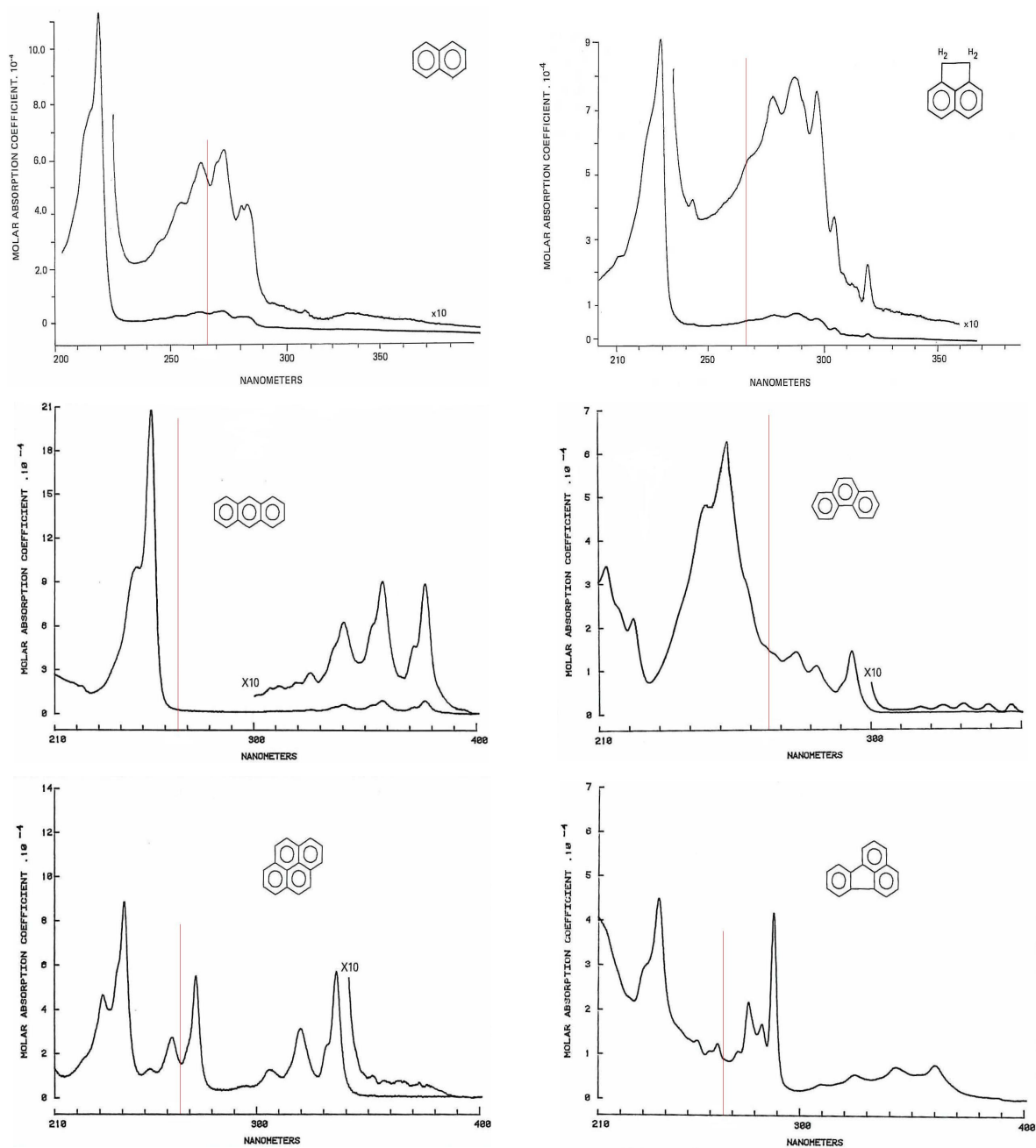
Figure 5.3. UV-Vis absorption spectra of a cycloexane solution of six PAH. The vertical red lines indicate the 266 nm wavelength [117].

5.2. Desorption of PAH from model soot

The results on pure PAH presented in previous Section 5.1 have been compared with the model soot analyses performed in this work. The comparison between the two studies give information both on the fundamentals of the desorption process and on the system optimisation required in order to analyse the natural soot.

The measurements presented in this Section investigate the LD/LI/TOF-MS response of model soot. A model soot is a simple system which simulates the natural soot, in which a known concentration of PAH is adsorbed on a carbonaceous substrate having structure similar to that of real soot. Such measurements have proven to be a convenient way to study the interaction between the adsorbed PAH and the adsorbing carbonaceous substrate, and consequently the analytical response of a system whose properties are closer to those of the natural soot than that of the pure PAH discussed in Section 5.1. Furthermore, the analyses of model soot samples allow the characterisation of the experimental setup and the definition of all the parameters involed in the response of the technique.

This Section is structured as follows. Paragraph 5.2.1 describes the response of the carbonaceous matrix alone. Paragraph 5.2.2 describes the adopted procedure for making model soot samples and discusses some important experimental parameters affecting the signal reproducibility. This procedure is then adopted for the preparation of all the samples required for the following analyses. The last two Paragraphs (5.2.3 and 5.2.4) describe new features of the LD/LI/TOF-MS response of model soot linked to the interaction of the adsorbed PAH with the substrate.

5.2.1. Response of the carbonaceous substrate

When analysing PAH adsorbed on soot particles, the first important concern is the determination of the response of the carbonaceous matrix.

In this work carbon black (Pureblack 100 Carbon, Columbian Chemicals Company) and activated carbon (high-purity Darco G60, purchased from Sigma-Aldrich) have been tested as adsorbing substrates in order to simulate the behaviour of the soot carbonaceous matrix in model soot. Carbon black and activated carbon are forms of elemental carbon obtained from the incomplete combustion of organics (typically liquid hydrocarbons for carbon black and lignin for activated carbon) under controlled conditions. The activated carbon is then processed in order to increase its specific surface. Their large specific surface (80-150 m^2/g for Pureblack Carbon and ~600 m^2/g for Darco G60) makes them very convenient adsorbing materials.

Pureblack 100 Carbon has been used to prepare the model soot since it is easily compressed into discs suitable for the mass analysis. On the other hand Darco G60 activated carbon is an impalpable powder which can be easily deposed in thin layers on the surface of the borosilicate discs used for the natural soot analyses. Furthermore, its large specific surface makes it a more suitable adsorbing substrate for the ppb amounts of PAH found in the low-pressure flame (Section 6.3).

In Figure 5.4 the desorption yield of Pureblack 100 Carbon and Darco G60 is reported. The appearance of signal peaks around $I_{des} = 25$ MW cm^{-2} indicates that the ablation process damages

the carbonaceous matrix and causes the ejection of matter, locating there the desorption threshold of the carbon. Since a priori the characteristic of the desorbed species are unknown, very high ionisation irradiance has been set during these analyses, in order to ionise the largest range of organics as possible. Particularly, the very high adopted ionisation irradiance (I_{ion} = 220 MW cm^{-2}) assures the complete dissociation of the desorbed organic species. The consequently produced C$^+$ ions can then be considered diagnostic ions indicating the desorption of any organic from the substrate.

The working range I_{des} ~ 3.5-15 MW cm^{-2} adopted for the routine soot analyses assures that the underneath carbon matrix is not destroyed. This subject will be further discussed in Paragraph 5.2.3.
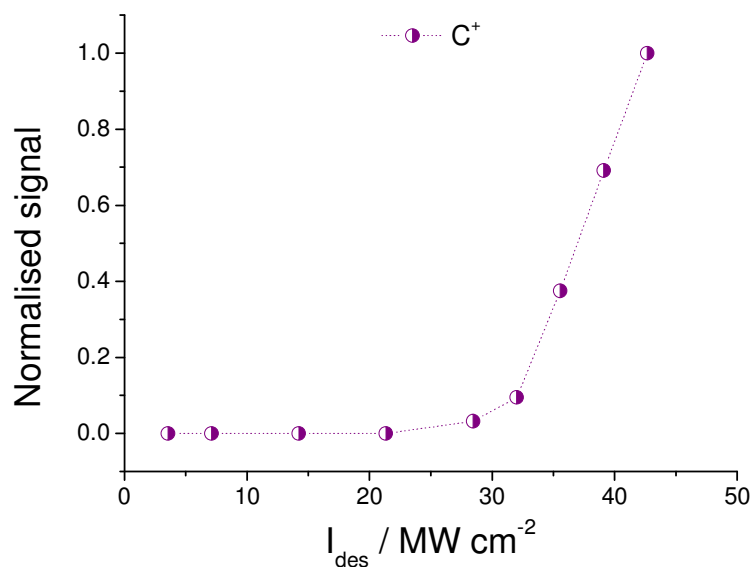
Figure 5.4. Pureblack 100 Carbon and Darco G60 activated carbon LD/LI/TOF-MS response as a function of the desorption irradiance. The destruction of the matrix with the consequent detection of C$^+$ begins around 25 MW cm^{-2} at 532 nm wavelength, which then represents the highest irradiance limit reachable during the analysis of species adsorbed on carbon-like matrixes. I_{ion} = 220 MW cm^{-2}.

5.2.2. Sample preparation and signal reproducibility

The preparation procedure of model soot samples consists in adsorbing via solution a known concentration of PAH on the powdered substrate (both Pureblack 100 Carbon and Darco G60 have been tested) and then using the treated powder to prepare a sample suitable for the LD/LI/TOF-MS analysis. Pureblack 100 Carbon and Darco G60 have been tested to be extremely low in their content of adsorbed materials like products of incomplete combustion, i.e. no signal peaks have been detected during the LD/LI/TOF-MS analyses.

The preparation procedure is detailed below. First step is the preparation of a mother-solution of the chosen PAH in dichloromethane (DCM). DCM is a convenient choice since it is a good solvent for PAH and it is volatile enough to be easily removed by vacuum filtration. Further, its absorption cross section is negligible both at 266 and 532 nm wavelength, and therefore it is invisible to both the desorption and the ionisation step. The mother solution is then diluted down to the target

concentration, and treated with ground Pureblack 100 Carbon (fifteen minutes of magnetic stirring and vacuum filtering to recover the powder). The amount of adsorbed PAH on carbon is determined from the difference between the initial amount of substance and the residual amount of substance in the exhaust solution. The residual concentration of PAH in the solution has been obtained measuring the UV-Vis extinction of the exhaust solution, and calculated using Beer-Lambert's law. In the adopted range of concentration almost the totality of the initial amount of PAH is adsorbed on carbon, as shown in Figure 5.5. The LD/LI/TOF-MS sample is finally prepared pressing 0.15 g of the model soot powder directly into the sample-holder to obtain a compact disc.
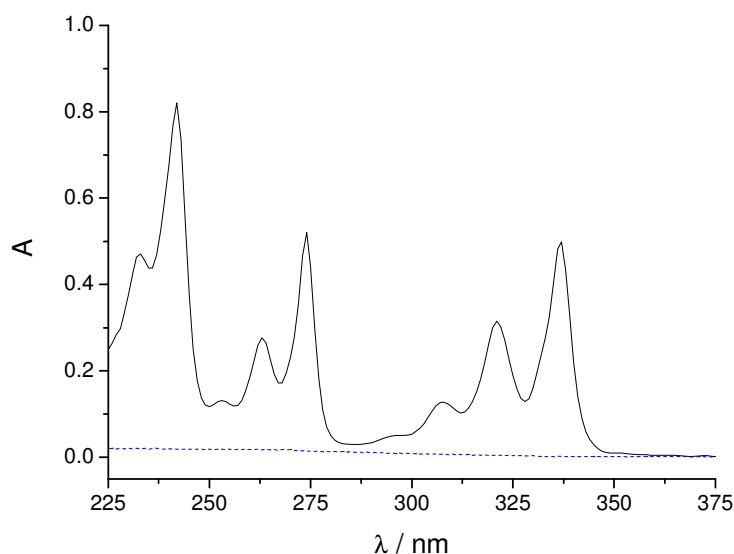
Figure 5.5. UV-Vis spectrum performed on a solution 10^{-5} M of pyrene in DCM before treatement with Pureblack 100 Carbon (black solid line) and on the exhaust solution (blue dashed line) after the treatment, in order to determinine the amount of pyrene adsorbed on carbon. Experimentally determined molar absorption coefficient: $\varepsilon^{336.5} = 4.29 \cdot 10^4$ $M^{-1}cm^{-1}$

The reproducibility of the analysis has been estimated from the data dispersion when irradiating different locations at the surface of several discs. The level of reproducibility has been estimated from the signal dispersion on the surface of the same sample disc, and from the signal dispersion when analysing different sample discs made from the same model soot powder.

Several sample discs have been made changing the critical parameter of the sample preparation. The considered parameters are: the size of the black carbon particles, the effect of the cooling during the pumping stage, and the pressure applied to the model soot powder in order to create the sample disc. The data dispersions are reported in Figure 5.6. The small dots represent the peak signal at different locations on the sample disc surface, while the large dots are the average on all the data measured on the same sample disc. Considering a normal distribution of the collected data, the error bars represent twice the standard deviation. The colours represent different sample discs. The standard deviation drops from above the 90% when using coarse Pureblack Carbon down to the 70% when using ground Pureblack, and 25% when using coarse Pureblack and cooling during the pumping.
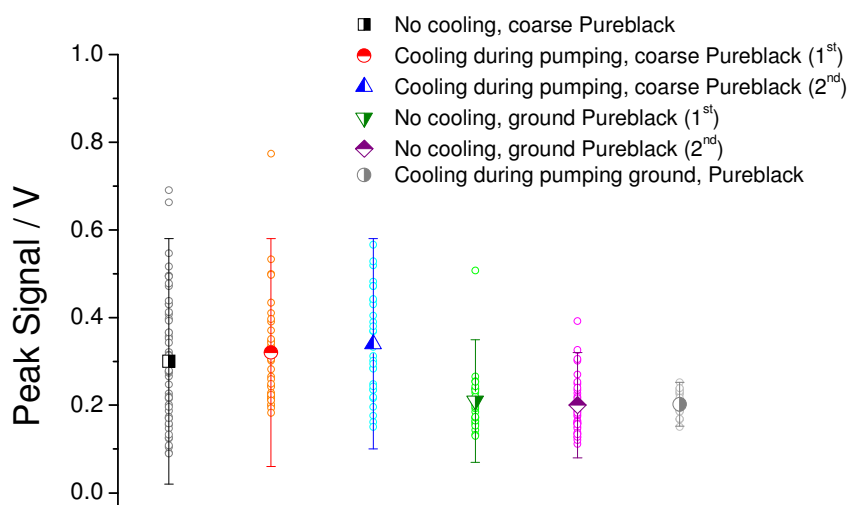
Figure 5.6. Peak signal dispersion obtained by changing the parameters of the sample preparation. The adopted model soot is a pyrene on Pureblack 100 Carbon at the concentration of 10^{-7} mol/g. I_{des} = 7.1 MW cm^{-2}, I_{ion} = 4.2 MW cm^{-2}. The colours represent different procedures. Each point is the average of 20 laser pulses on the same location.

The size of the particles of Pureblack Carbon is found to be the most important parameter affecting the data dispersion. When using ground carbon, even when simply grounding on a mortar before the treatment with the PAH solution, the absorption process seems much more homogeneous, and the standard deviation of the data gives a 25-30% narrower dispersion. The small reduction of peak signal occurring when using ground Pureblack is largely compensated by the smaller data dispersion.

The cooling of the sample with liquid nitrogen (~110 K) during the pumping stage has a moderate effect on the data dispersion, reducing the standard deviation of about 10-15%. However, it has been found crucially important when analysing high vapour pressure PAH like naphthalene. In absence of cooling, the most volatile PAH spontaneously desorbs during the pumping stage, and their signal peaks are reduced by more than one order of magnitude.

Different pressures in the range 1-3 bar have been tested when pressing the model soot powder into the sample-holder. No effect has been noted in terms of peak intensity or data dispersion.

In conclusion the measurements described in this Paragraph have to be considered when defining the analytical procedure for analysing for instance natural soot. For instance, in order to get the smallest data dispersion when analysing natural soot, the particle size of the adsorbing substrate has been chosen as small as possible (activated carbon rather than carbon black), while a cooling stage has always been performed during the pumping stage.

5.2.3. Effect of the irradiance

When analysing soot-like materials the presence of a carbonaceous matrix able to absorb radiation in a large spectral range allows a relatively high degree of freedom in the choice of the desorption wavelength. In this work the analysis of PAH adsorbed on soot has been performed

using 532 nm desorption wavelength for reasons analogous to those described in Paragraph 5.1.2 (high laser power available and enhanced signal for the low-mass PAH).

In Figure 5.7 the desorption yield of three different PAH adsorbed on black carbon is reported and compared to that of pure PAH. The desorption yield of PAH adsorbed on black carbon show a similar evolution to that of pure PAH in the low-desorption irradiance regime. The signal initially rises as a function of the desorption irradiance, comes to a maximum and then decreases. This behaviour has already been discussed in Section 5.2.1, and, briefly, it has been attributed to the competition between the desorption efficiency and the photo-dissociation through the increase of the internal energy of the desorbed species.

However, in the case of PAH adsorbed on carbon black two critical differences has been observed. First, the desorption yield rises again above the carbon black desorption threshold, indicating that the destruction of the carbon matrix is able to release additional PAH which were adsorbed in deeper layers.
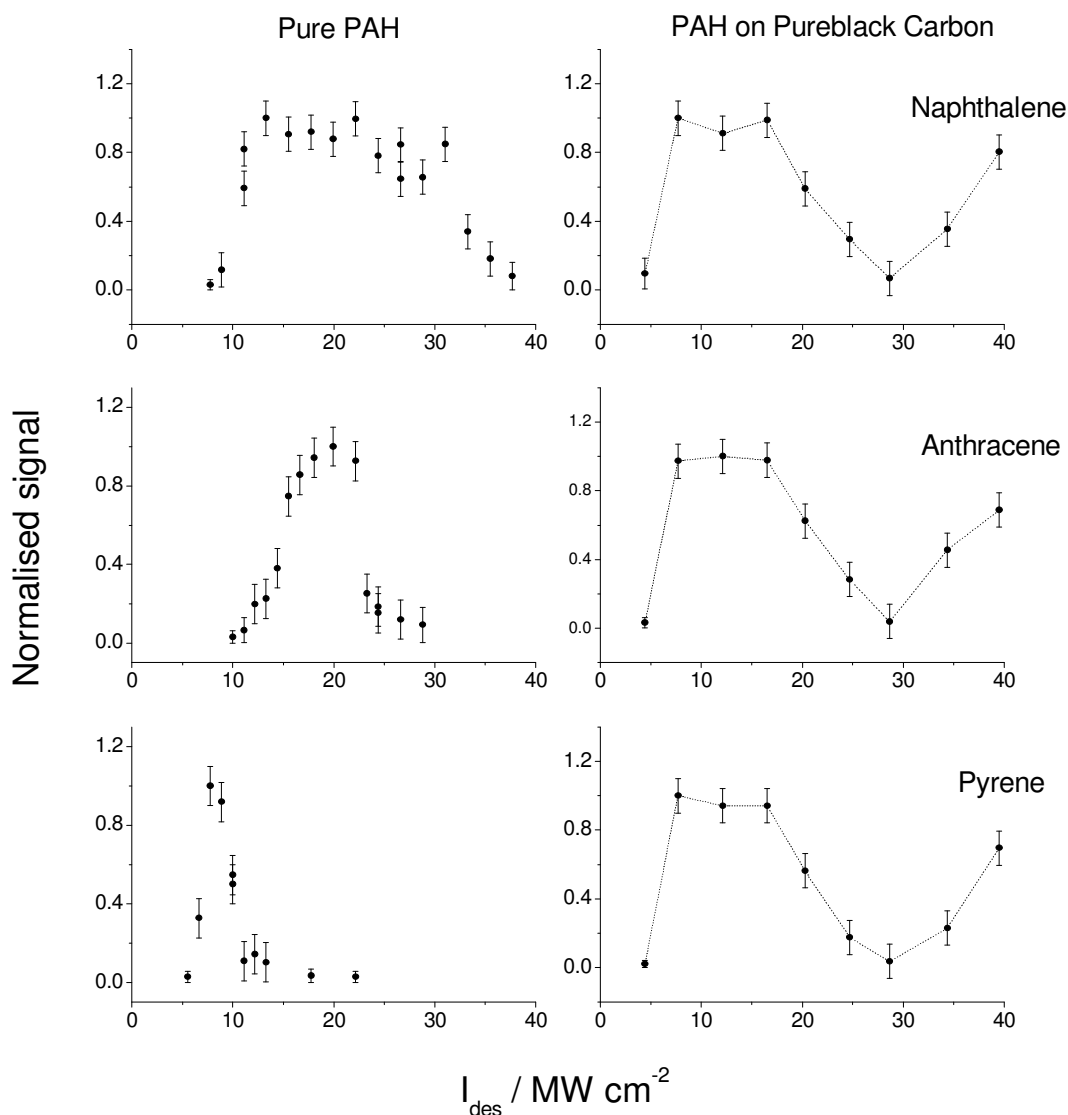
Figure 5.7. Comparison of the desorption yields of three low-mass pure PAH (on the left column) and the same PAH adsorbed on Pureblack Carbon (on the right column) at the concentration of 10^{-7} mol/g. $I_{ion} = 1.9$ MW cm^{-2}.

Second, while the desorption yield is very characteristic of pure PAH (Paragraph 5.1.2), the responses to the desorption irradiance of all the tested PAH adsorbed on carbon black are all very similar. In Figure 5.7 the comparison between the desorption yields of three pure PAH and the corresponding signal curves in carbon black are compared. To explain such behaviour the similarity of the PAH-substrate bonds has to be invoked. Particularly, for low-mass PAH the strength of the van der Waals interactions between the desorbed molecules and the substrate are close enough to guarantee a similar response to the desorption irradiance. From a practical point of view the selectivity of the technique is completely lost. However, as widely discussed by Zare and co-workers [71], in the LD/LI/TOF-MS diagnostic a number of parameters is able to affect the intensities of the measured signal peaks, but in the cases of both model soot and natural soot the role played by the desorption irradiance is strongly downsized. Being the desorption yields of PAH adsorbed on carbon virtually identical, the same desorption irradiance optimises the desorption yields of the PAH all together, thus there is no need of establishing different working points for each analysed PAH.

5.2.4. Signal decay as a function of the number of pulses

Each laser pulse delivered to the sample surface removes some matter from the total amount of adsorbed species in the irradiated volume. Therefore, when repeatedly irradiating the sample on the same location, the peak intensity decays as function of the number of the laser pulses. The signal stands until there is no more matter to be desorbed, and then the integral calculated on the overall decay function is proportional to the total amount of substance contained in the irradiated sample volume.
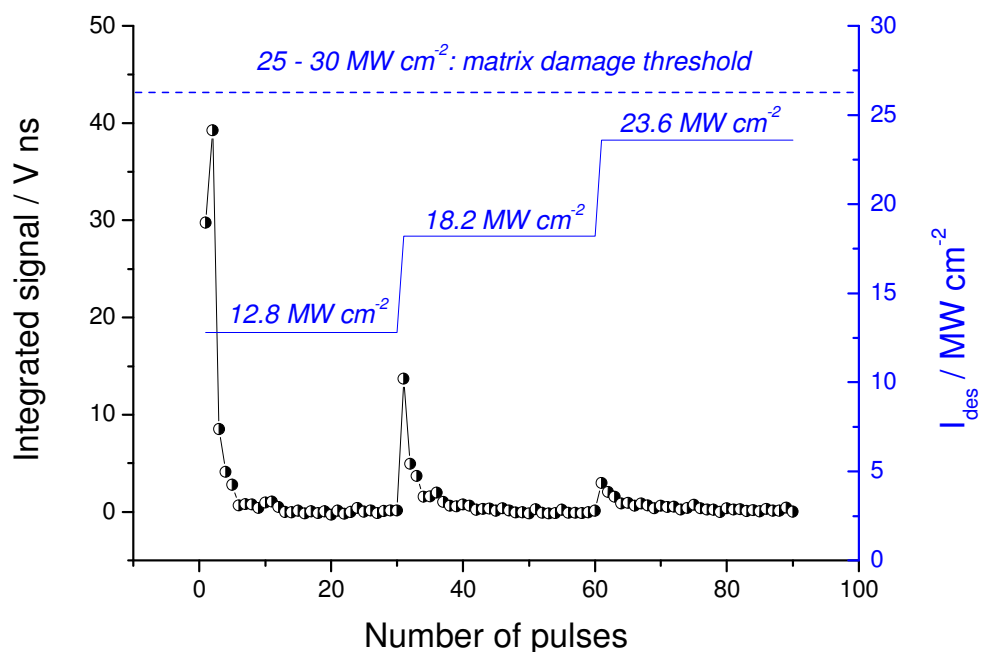
Figure 5.8. Signal decays (signal peak intensity versus number of laser pulses) obtained by rising the desorption irradiance during the analysis of a model soot containing pyrene in Pureblack Carbon at the concentration of $9.52 \cdot 10^{-8}$ mol/g. $I_{ion} = 2.1$ MW cm^{-2}. The represented curve is the average of three different decays.

The signal decay presented in Figure 5.8 has been obtained irradiating the same location on a model soot sample containing pyrene adsorbed in Pureblack 100 Carbon. The reported curve is the decay function of the mass 202 u vs. the number of laser pulses delivered to the sample surface.

The decay rate depends on the concentration of the adsorbed material on the substrate. In the typical range of concentrations of PAH adsorbed on model or real soot, the amount of desorbed substance by each laser pulse is comparable with the total amount of substance contained in the irradiated volume, and then the decays are usually fast (5-10 laser pulses).

The signal decay evolves as a function of the desorption energy, and as long as the heating affects deeper layers, a larger and larger amount of PAH is desorbed. In this work the desorption irradiance chosen for the routine analyses assures that the signal decays in a few laser pulses.

5.3. PAH photoionisation

The ionisation beam configuration strongly affects the type and magnitude of the detected LD/LI/TOF-MS signals. Both the irradiance and the transverse irradiance profile of the ionisation pulse are shown to affect the sequence of the detected masses (acting on the photo-dissociation) as well as the relative ratios of the PAH precursor peaks. The ionisation laser irradiance and alignment are the most difficult parameters to control, and thus provide the most practical limitations for quantitative analyses.

The dependence of the intensity of the peaks on the ionisation input is complex, and at least two different regimes can be identified. At low irradiance the signal increases with I_{ion} according to Equation (3.2), thus accounting for the two-photon absorption dynamic. However, at higher I_{ion} the signal levels off, reaches a maximum and finally decays. Simultaneously peak signals are detected for lower mass than the precursor ion, indicating that a third photon is absorbed, either by neutral molecules or by newborn ions, and this additional energy is inducing dissociation. This situation is illustrated in Figure 5.9, which contains the plot of the peak intensity of pyrene as a function of I_{ion} in the full explored irradiance range. The inserts give examples of the structure of the mass spectra detected under the specified irradiance conditions. These two limit situations require quite a different treatment. The low-I_{ion} regime is well known from the nonlinear optics, and a simple mathematic description is available [86]. On the other hand, the high-I_{ion} regime is still relatively unknown, and to the best of our knowledge no model exists. The behaviour of PAH under high-I_{ion} irradiation is detailed in Paragraph 5.3.4.

In mass spectrometry the knowledge of the dissociation pathways is a powerful tool to identify the molecular class the precursor ion belongs to [118], or to produce carbon/hydrogen clusters for special analytical purposes [119]. Conversely, when analysing mixtures of analytes all belonging to the same class (PAH in this work) no additional information is provided by the structure of the fragmented spectra. Rather the photo-dissociation phenomena remove precursor ions to produce fragment ions, worsen the signal-to-noise ratios and generate fragment ions which can be difficult to differentiate from the precursor ions. Therefore there is interest in limiting as far as possible photo-dissociation.
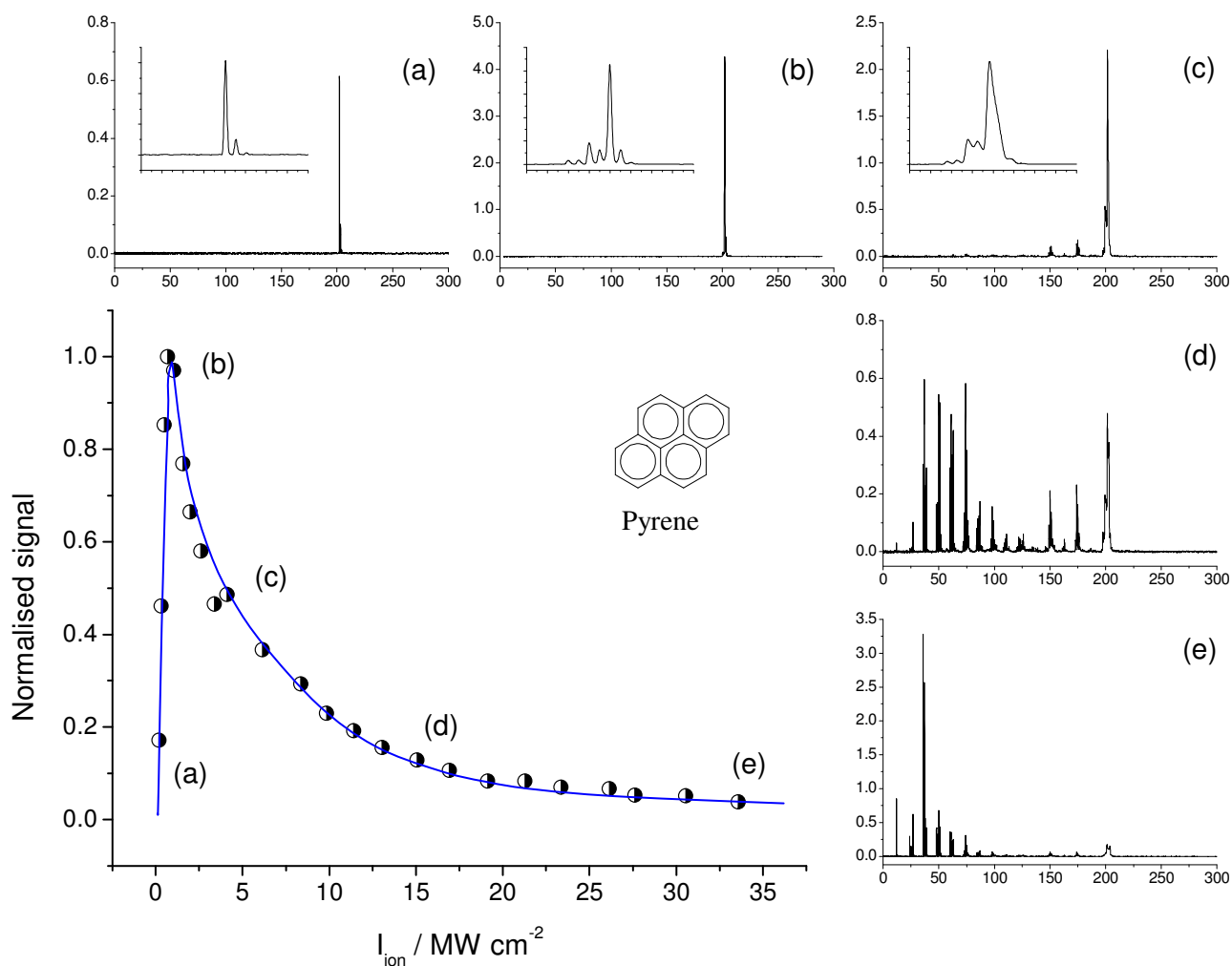
Figure 5.9. Pyrene ionisation curve and peak intensity (peak heigh / V) detected for the mass 202 u as a function of the ionisation irradiance (I_{des} = 11.4 MW cm^{-2}). In the insert the correspondent mass spectra are reported.

5.3.1. Influence of the beam transverse irradiance profile

The transverse irradiance profile of the ionisation beam has proven to be an important parameter in the determination of the LD/LI/TOF-MS response and particularly on the photo-dissociation of the analysed PAH. In this work several configurations of the ionisation optical path have been tested in order to obtain different transverse power profiles and study their effect on the photo-dissociation process. Those profiles are the unmodified Continuum laser output at 266 nm wavelength (roughly Gaussian) focused using a spherical and a cylindrical lens [100], and an unfocused beam imaging configurations leading to a Top-Hat profile. The procedure for calculating the peak irradiance in both cases is reported in Appendix A.

The beam diameter of the spot-focused Gaussian beam is small enough (~ 100 μm) that the resulting peak irradiance largely overcomes the dissociation threshold of the PAH in the plume even at the lowest pulse power measurable in this configuration (~ 102 MW cm^{-2}). As shown in Figure 5.9 this value is deeply located into the PAH dissociation region, i.e. it is not possible to get

fragment-free spectra whatever is the delivered pulse power. Although the relative intensities of the peaks associated to the fragment ions can be reduced with respect to the precursor ion, they cannot be completely removed from the spectrum. Despite the extremely high peak irradiance obtained in this configuration, the mass spectra are considerably rich in high-mass signal peaks, indicating that the PAH dissociation is not yet complete and a number of high-mass fragments still survive. Such behaviour can be explained invoking the Gaussian transverse irradiance distribution. Since the irradiance profile is not constant with respect to the transverse coordinate, different ionisation regimes take place in different locations. For instance, a typical mass spectrum obtained for a pure pyrene sample under those conditions is reported in Figure 5.10.
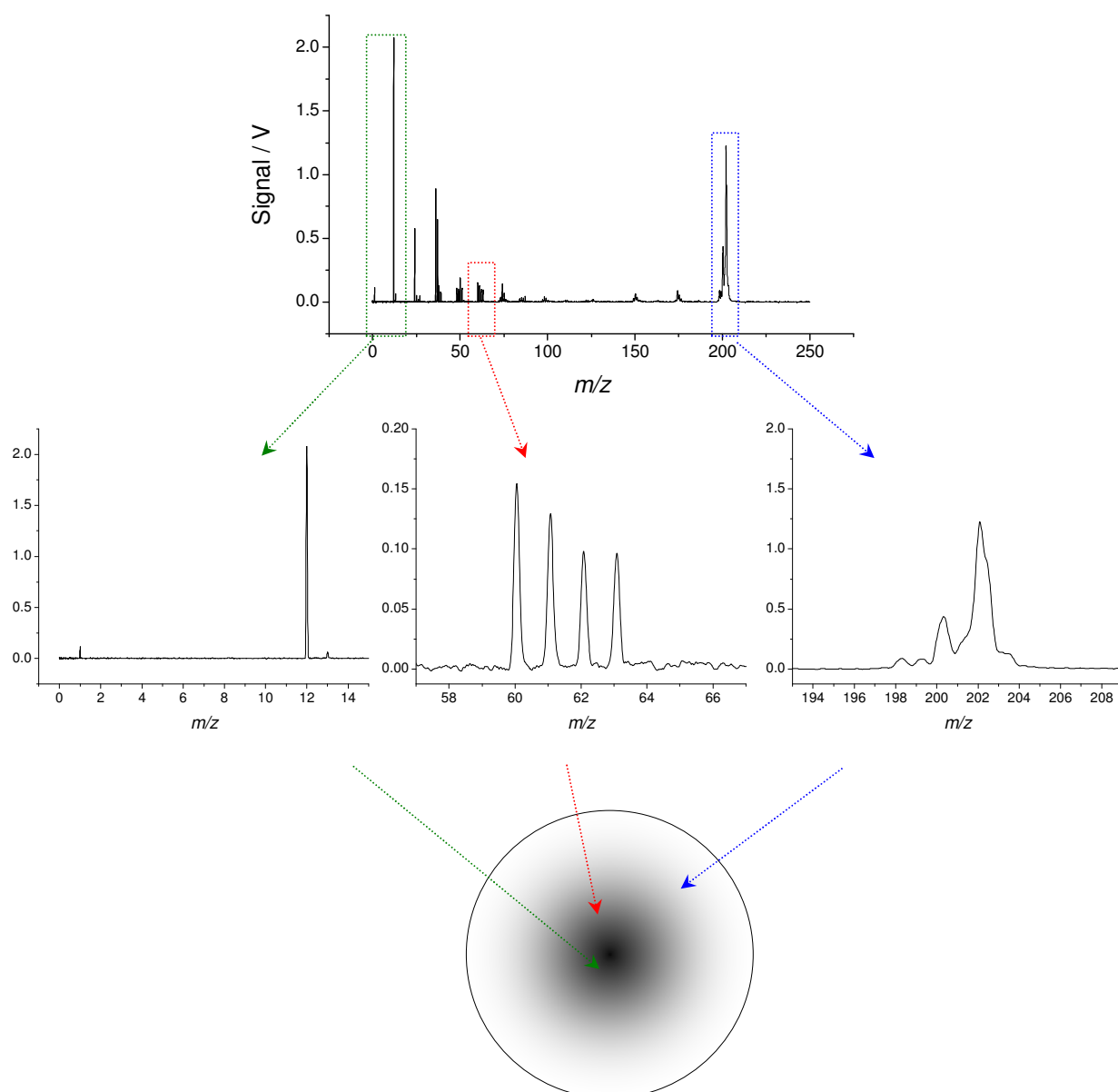
Figure 5.10. Mass spectrum obtained from pure pyrene, ionisation performed using a spot-focused beam by means of a spherical lens. The zooms on the spectrum highlight the light-mass fragments produced during the photo-dissociation process and the zones of the beam where they are produced (below). Figure reproduced from [100]. $I_{des} = 14.2$ MW cm^{-2}, $I_{ion} = 101.8$ MW cm^{-2}.

In addition to the precursor ion at 202 u, a large number of fragment ions is detected down to elemental carbon and hydrogen (the dissociation pathway of PAH will be discussed in Section 5.3.4). As depicted in Figure 5.10 in the centre of the beam, where the irradiance reaches its peak value, a deep dissociation occurs. Conversely, in the beam wings a softer ionisation occurs, and fragments having mass up to that of the precursor ion are still allowed to survive.

When using an unfocused beam under beam imaging configuration (see Paragraph 4.1.3 for the detailed description of the ionisation optical path), the obtained irradiance transverse profile is Top-Hat, i.e. constant with respect to the transverse coordinate. This configuration offers two critical advantages with respect to the focused Gaussian beam previously discussed. First, only one ionisation regime is possible. Second, the unfocused configuration produces a larger beam section, and thus it greatly decreases the peak irradiance. Under these conditions, power corresponding to peak irradiance down to 0.32 MW cm^{-2} has been measured, and this value is just slightly below the ionisation threshold of most of the analysed PAH. Furthermore, the resulting increase of the plume section irradiated by the ionisation beam, and consequently of the ionisation volume, increases the number density of the ions produced in the ion source, greatly improving the overall sensitivity.

Under the same measured pulse power, the wider fragment-free irradiance range and the best sensitivity have been obtained using the unfocused Top-Hat, and therefore this configuration has been adopted in all the following measurements.

5.3.2. The role of the absorption cross section

The measured signal peak depends not only on the amount of desorbed species, but also on its photoionisation cross section. Therefore it is not possible to use directly the ratio of two signal peaks as a measure of the ratio of the concentrations of two species [71]. A relatively common way to overcome this limitation is to use an internal standard to determine the relative LD/LI/TOF-MS response to different PAH, and then build up a calibration curve for each analyte [120-122].

The work presented in this Paragraph demonstrates that the ionisation cross sections account themselves for the largest deviation from the linearity in the signal vs. concentration data representation. This analysis has been performed on a soot model sample containing sixteen standard PAH. The adsorption process has been performed in solution, starting from a sixteen PAH standard solution (2 mg of each PAH in 2 mL of dichloromethane:benzene 1:1) purchased from Sigma Aldrich. This solution has been diluted and treated with Pureblack 100 Carbon (see Paragraph 5.2.2) to get the concentration of PAH on carbon down to 10^{-7} mol/g. UV-Vis-NIR absorption spectrometry on the exhaust solution allowed the quantification of the residual non-absorbed PAH. In the chosen concentration range the absorption efficiency of the benzene (present in the original standard) on Pureblack Carbon is too small to allow competition with others PAH.

In Table 5.1 the sixteen analysed PAH are listed together with their molecular and structural formulae and their concentrations in the model soot and the molar absorption coefficients [85]. The obtained mass spectra are reported in Figure 5.11.
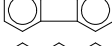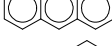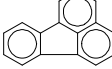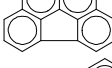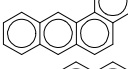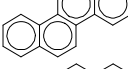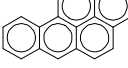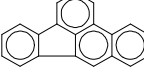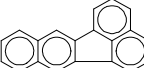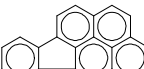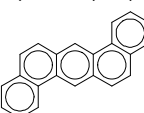
PAH	Molecular Formula	Structural Formula	m / u	c / mol g^{-1}	ε / 10^4 L cm^{-1} M^{-1}
Naphtalene	$C_{10}H_8$		128.063	1.56 ·10^{-7}	0.62
Acenaphthylene	$C_{12}H_8$		152.063	1.28 ·10^{-7}	0.36
Acenaphtene	$C_{12}H_{10}$		154.078	1.27 ·10^{-7}	0.5
Fluorene	$C_{13}H_{10}$		166.078	1.20 ·10^{-7}	1.95
Anthracene	$C_{14}H_{10}$		178.078	1.11 ·10^{-7}	0.2
Phenanthrene	$C_{14}H_{10}$		178.078	1.11 ·10^{-7}	4.8
Fluoranthene	$C_{16}H_{10}$		202.078	9.59 ·10^{-8}	0.96
Pyrene	$C_{16}H_{10}$		202.078	9.85 ·10^{-8}	1.8
Benzo(g,h,i)fluoranthene	$C_{18}H_{10}$		226.078	8.81 ·10^{-8}	1.9
Benzo(a)anthracene	$C_{18}H_{12}$		228.094	8.77 ·10^{-8}	3.2
Chrysene	$C_{18}H_{12}$		228.094	8.66 ·10^{-8}	9.6
Benzo(a)pyrene	$C_{20}H_{12}$		252.094	7.92 ·10^{-8}	4.91
Benzo(b)fluoranthene	$C_{20}H_{12}$		252.094	7.93 ·10^{-8}	2.5
Benzo(k)fluoranthene	$C_{20}H_{12}$		252.094	7.93 ·10^{-8}	1.7
Indeno(1,2,3-cd)pyrene	$C_{22}H_{12}$		276.094	7.21 ·10^{-8}	2.4
Dibenzo(a,h)anthracene	$C_{22}H_{14}$		278.107	7.09 ·10^{-8}	1.85

Table 5.1. List of the 16 PAH contained in the standard purchased from Sigma Aldrich. For each PAH the table reports: IUPAC name, molecular formula, structural formula, molecular mass calculated on the all-^{12}C molecule (M), final concentration on Pureblack 100 Carbon (c), and molar absorption coefficient (ε) measured in cyclohexane solution [85].

Figure 5.11. Mass spectrum obtained from the 16 PAH synthetic soot (concentration 10^{-7} mol/g). I_{des} = 5.3 MW cm^{-2}, I_{ion} = 1.9MW cm^{-2}. Average of the first five laser pulses. In the inserts zooms on all the peaks with signal attribution are reported.
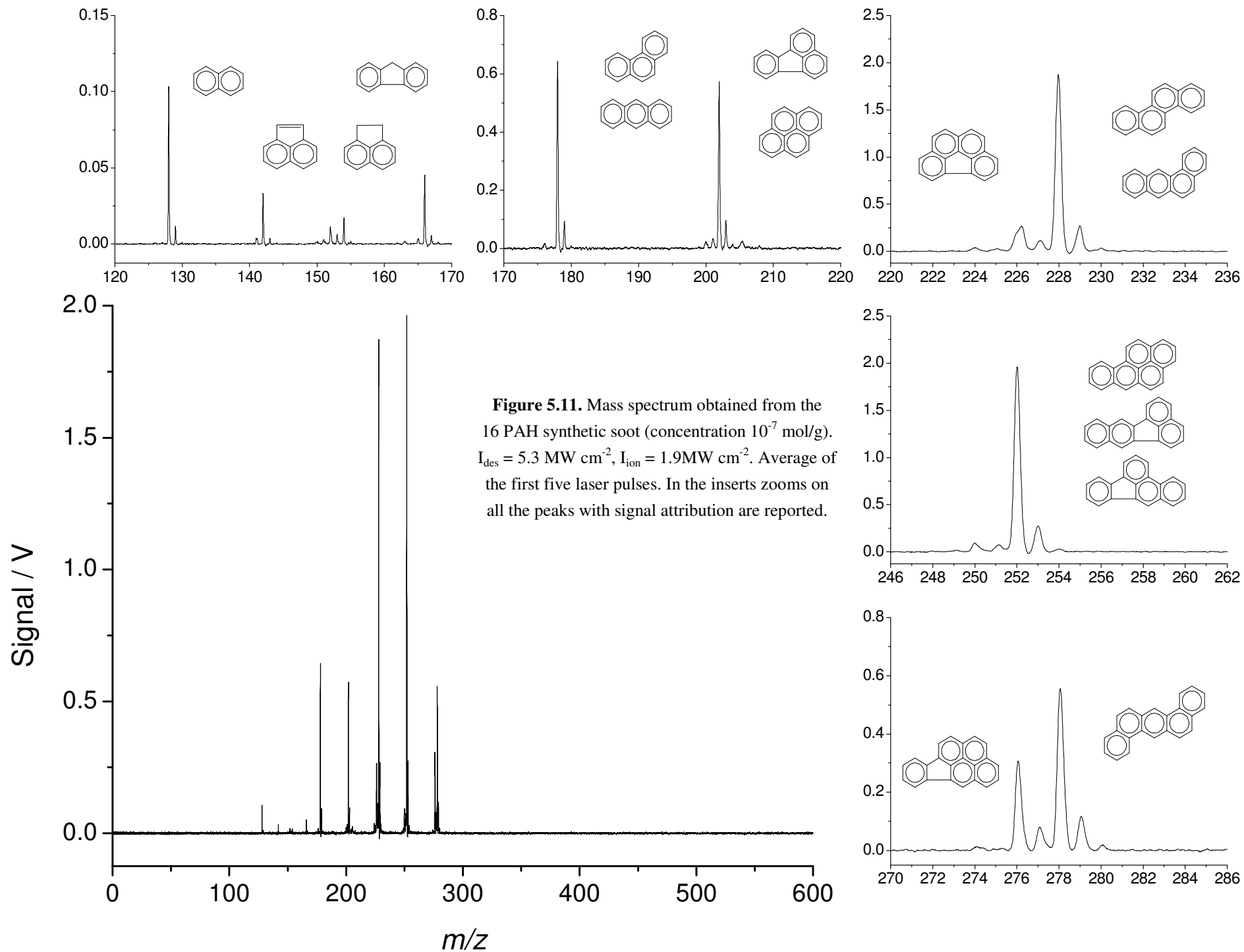
The covered mass range goes from 128 u (naphthalene) up to 278 u (dibenzo[a,h]anthracene). The standard contains sixteen PAH, but some of them are isomeric structures, and thus it is not possible to identify them only using the information provided by the mass spectrum. Twelve masses have been detected, and eleven of them correspond to PAH listed in the original standard. The mass 142 u is attributed to a residual already present in the original standard. No dissociation phenomena occur during the mass analysis, and the mass spectra are completely fragment-free. Each signal peak comes with a certain number of satellite peaks, attributed to isotopic homologues and to hydrogen elimination.

The following approach has been adopted to introduce a correction for the different efficiencies in the desorption-ionisation process. To a first approximation, the detected peak intensity as a function of the mass S(m) is estimated to follow equation:

$$S(m) = k \sum_j \varepsilon_j^{266nm} c_j \qquad (5.1)$$

where the index j runs over all the isomers having the same mass, ε_j^{266nm} are the molar absorption coefficients giving a correction based on the molecular cross section [85], and c_j are the PAH concentrations on carbon. The constant k depends on the overall system configuration, and must be determined experimentally. Since the LD/LI/TOF-MS analyses on adsorbed PAH is not isomer-selective, a priori it not possible to separate the contributions of each isomer to the final signal intensity. It is then only possible to correct the PAH concentrations on carbon and not the signals, predicting the signal intensity at each mass summing all the contributions from different isomers. The correlation between the corrected concentrations and the peak signals is reported in Figure 5.12.
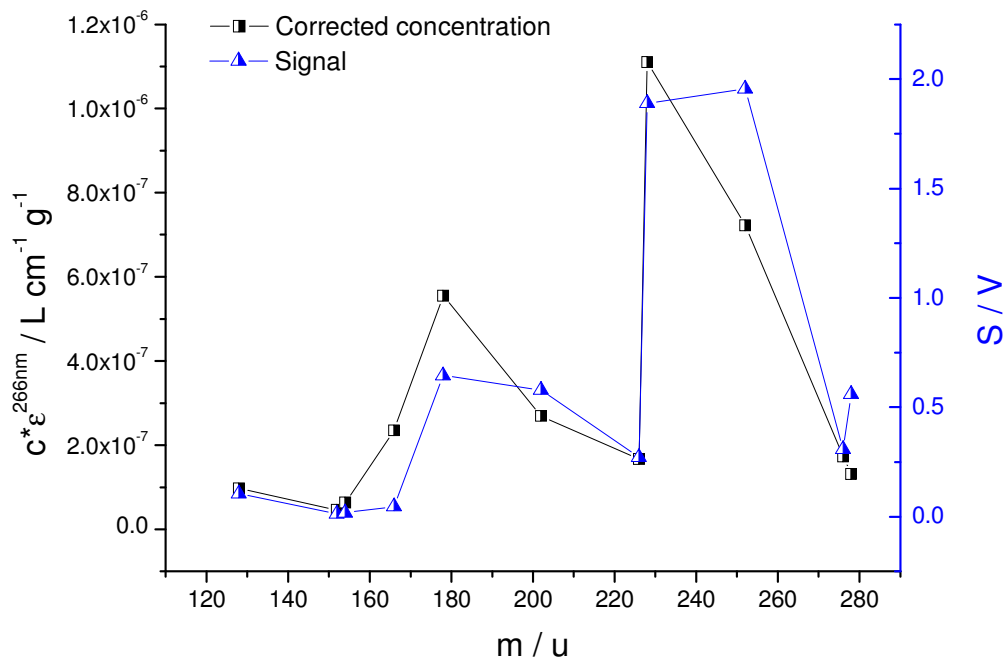

Figure 5.12. Corrected concentrations (black squares) and peak signals (blue triangles) vs. the detected masses. The concentrations here reported are calculated as the sum of the concentrations of all PAH having the same mass. The experimental uncertanties introduced with the dilution is not higher than 4% of the signal.

The good agreement between the corrected concentrations and the peak intensities leads to the following consequences. First, it indicates that the molar absorption coefficients involved in the ionisation process are the most important parameter accounting for the overall LD/LI/TOF-MS response of PAH adsorbed on carbon black and on activated carbon. Second, the good agreement between corrected concentrations and peak intensities indicates that in the analysed PAH (mass range 128<M<278) the two-photon ionisation is dominated by the first photon absorption (see also next Paragraph 5.3.3). Finally, the correction of the absorption cross sections accounting alone for the LD/LI/TOF-MS response confirms the loss of selectivity observed for PAH adsorbed on carbon (see Paragraph 5.2.3).

5.3.3. The low-I_{ion} regime: Two Photon Absorption

The ionisation energy of a large number of PAH is smaller than the energy of two photons at 266 nm wavelength (Section 3.1.3). Therefore at least two photons have to be absorbed in order to ionise a PAH molecular species. In Figure 5.13 the scheme of the one-colour, two-photon ionisation process for PAH proposed by Zimmermann and co-workers is reported [123]. The used terms are: S_0 ground state, S_1 first excited singlet state, S_n higher excited singlet state, IE ionisation energy. σ_1 and σ_2 denote the absorption cross sections of the first (absorption) and second (ionisation) step, respectively. On the left of the figure the correspondent UV-Vis-NIR absorption spectrum is depicted, while on the right the REMPI ionisation already discussed in Paragraph 3.1.3 is reported. In the nanosecond time regime and in the 248-266 nm range of excitation wavelength the ionisation occurs via an intermediate state of the broad rovibronic continuum of one of the excited electronic states (S_n).
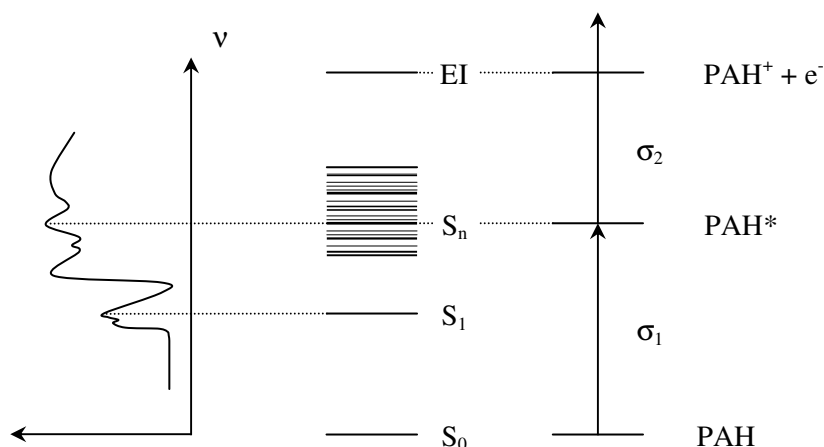

Figure 5.13. Photoionisation of PAH in the nanosecond regime using UV-Vis excitation wavelength [123]. In the middle of the figure the level structure is depicted, while on the sides the correspondent absorption spectrum (on the left) and REMPI scheme (on the right) are reported.

Indeed, most of the PAH having three or more condensed aromatic rings have broad absorption bands in this spectral region. Therefore, the difference of the laser wavelength in this spectral

region is more or less irrelevant for the efficiency of the overall REMPI process. Because of the huge number of rovibronic levels potentially involved, a small change in the ionisation wavelength would still get a resonance, so guaranteeing the REMPI response [89].

The ionisation order of the process has been measured for some standard PAH. As demonstrated by Johnson and Otis [124], if an unfocused UV beam is used and in absence of saturation of the absorption, the relationship between the peak signal S and the input ionisation irradiance I_{ion} follows the equation:

$$S = kI_{ion}^{x} \tag{5.2}$$

where the exponent x is the ionisation order of the process. Particularly for a two-photon process two limit situations can be identified. If the absorption cross sections for the ground state and for the excited state are very similar, i.e. $\sigma_1 \approx \sigma_2$ then x = 2. Otherwise, if one of the two cross sections is much larger than the other one, i.e. $\sigma_1 \gg \sigma_2$ or $\sigma_1 \ll \sigma_2$, then x = 1 [89]. In the general case $1 \leq x \leq 2$.
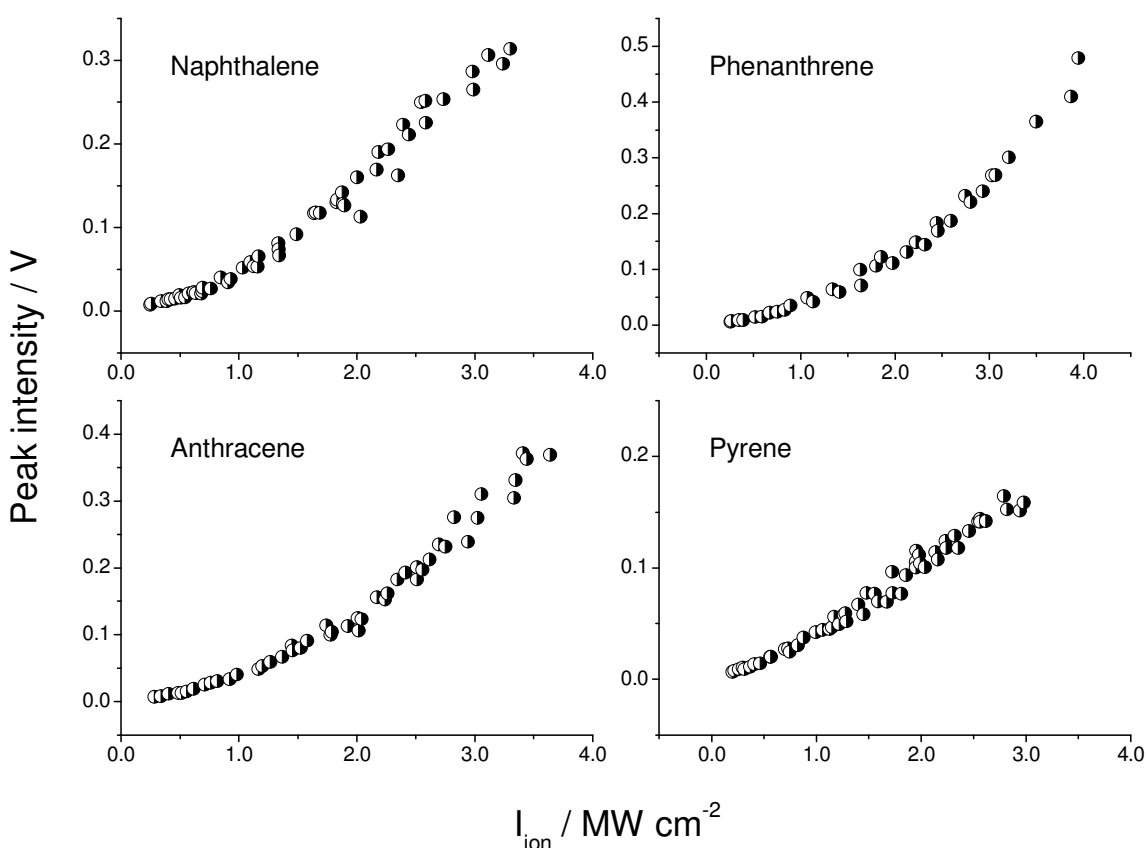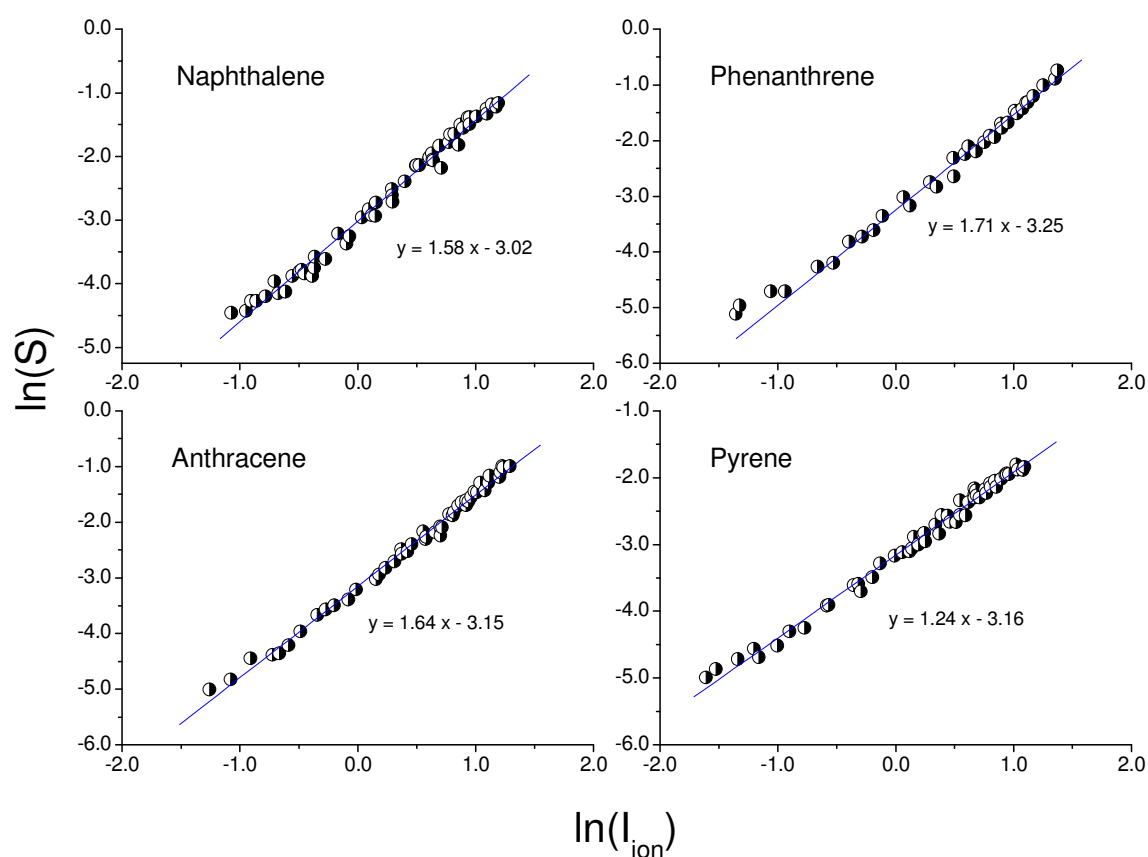

Figure 5.14. Signal dependence on the ionisation irradiance under low-irradiance conditions. The analytes have been brought in gas phase by thermal desorption.

The dependence of the LD/LI/TOF-MS signal on the ionisation irradiance has been measured at 266 nm wavelength with pulses of 6 ns for four PAH: naphthalene, phenanthrene, anthracene and pyrene. This measurement gives important information on the optimum ionisation irradiance needed for analytical determination. Particularly, it allows determining the range of irradiance in which the ionisation is more efficient (best signal-to-noise ratio) and the mass spectra are fragment-free.

Temperature and pressure in the ions source and ionisation irradiance have been initially stabilised in order to obtain 100 mV of peak intensity of the precursor ion. The measure has been then performed under conditions of stable pressure and temperature by changing the ionisation irradiance. The peak intensity vs. the ionisation irradiance for the analysed PAH is reported in Figure 5.14.

A convenient way to obtain the ionisation order of the absorption process is to represent the data in a double logarithmic plot. This way the exponential dependence shown in Figure 5.14 is reduced to a linear one, in which the ionisation order is given by the slope of the linear fit. This data representation is reported in Figure 5.15, together with the fitting parameters and the values of the correlation coefficients.

	Slope	Intercept	R^2
Naphthalene	1.58	-3.02	0.9884
Phenanthrene	1.71	-3.25	0.9908
Anthracene	1.64	-3.15	0.9940
Pyrene	1.24	-3.16	0.9914

Figure 5.15. Double logarithmic plot of the signal dependence on the ionisation irradiance. In the table the fit parameters (slope, intercept and correlation coefficient) have been reported.

Referring to Figure 5.14 two cases can be identified. Naphthalene, phenanthrene and anthracene show clearly nonlinear signal-irradiance dependences, while pyrene exhibits an almost linear relationship. Naphthalene data are consistent with Haefliger and co-workers LMMS [89] measurements, though the obtained exponent is not the same. On the other hand phenanthrene data do not agree with the same publication, where a linear S vs. I_{ion} dependence has been found. However in this second case the interpretation might be subject of discussion, since from the published data dissociation phenomena seem to occur, so changing the overall dynamic.

When switching to the double logarithmic plot the relationships are all linear, despite the experimental data are better fitted in the high ionisation irradiance limit. The linear fit of naphthalene, phenanthrene and anthracene all give an experimental value of the ionisation order around 1.6-1.7., while a value of 1.24 is obtained for pyrene.

The experimental ionisation orders are fairly lower than the value of 2.0 expected for a two-photon process (Paragraph 3.1.3). The experimentally obtained ionisation orders imply that for the analysed PAH one of the absorption cross sections at 266 nm is far larger than the other, and therefore one of the two photon-induced transitions is a rate limiting step. This observation is consistent with the UV-Vis-NIR absorption spectrum shown in Figure 5.3, in which the 266 nm ionisation wavelength corresponds to a spectral region dominated by a strong linear absorption. These arguments apply for all the analysed PAH except anthracene. Particularly, in the case of pyrene the 266 nm wavelength is very close to an optical resonance. This means that the first absorption occurs under resonance conditions, $\sigma_1 \gg \sigma_2$ and therefore the two-photon rate degenerates to a quasi-linear dependence. Further, the observed ionisation order is consistent with the measurements presented on Paragraph 5.3.2, in which the optical response of the low-mass analysed PAH is demonstrated to be controlled by the linear absorption.

The saturation of the absorption causes in the double logarithmic plots a deviation from linearity for high laser intensity [46]. In this analysis the double logarithmic plots always show signal-irradiance linear relationship except for a small deviation from the linearity occurring in the low-irradiance limit (0.2-0.4 MW cm$_{-2}$).

A quick note on the fit intercept. In the double logarithmic plot it accounts for all the experimental factors like the accelerating voltages, the response function of the ion detector, and so on. As already specified, the measure has been performed under thermal desorption conditions. Particularly the pressure of the PAH into the ion source has been set in order to get for all the PAH the same starting signal. Therefore the intercepts were actually expected to be numerically very similar, indeed this has ben experimentally observed (Figure 5.15).

5.3.4. The high-I_{ion} regime: photo-dissociation

The photo-dissociation is a complex process involving a number of different chemical species, both ionic and neutral-charged. The knowledge of the dissociation mechanisms has important analytical implications in addition to a mere spectroscopic interest. In fact in mass spectrometry-based techniques the dissociation pattern of organic molecules produces low-mass ions (fragment ions, or simply fragments) which are fingerprint of the molecule class of the precursor ions regardless the performed ionisation method (see also Figure 5.16). Thus, the identification of the fragment ions is usually the most straightforward way to get information on the structure of the precursor ion.

The dissociation process can be qualitatively explained invoking the Franck-Condon principle. Electronic transitions are processes much faster than the nuclear vibration period. Therefore the position and the relative velocity of the nuclear backbone do not change during an electronic transition, which can be represented with a vertical line in a potential energy diagram. The side scheme shows the potential energy curves as a function of the internuclear distance r for a two-atoms bond A-B, an excited bonding state A-B*, and a non-bonding state A+B$^+$. The curve relative to A-B* still has a minimum, thus the species A-B* would be stable enough to exist as a molecular species. This situation is very common when analysing PAH, whose π electrons create a molecular orbital able to compensate for the loss of one electron. On the other hand, the curve relative to A+B$^+$ does not have a minimum, thus the species A+B$^+$ would quickly dissociate once formed. The fragment ions and neutral molecules produced via dissociation can undergo structural rearrangement to produce more stable species. The whole set of fragment ions eventually detected constitute characteristic patterns for every class of molecules.
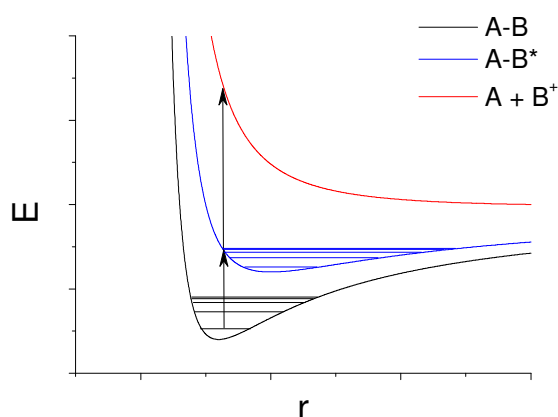
The most common dissociation reactions for organic molecules have been described by Biemann [118]. It is important to point out that the proposed structural formulae are only hypothetical. Since the structure of an ion can not be determined through classical methods, and a mass spectrometer only gives information on the elemental composition of ions, the real ion structure can only be obtained using isotope marking techniques or proposed on the basis of common sense.

This Paragraph proposes a study on the photo-dissociation process performed on four PAH, naphthalene, phenanthrene, anthracene and pyrene. The discussion considers the optical response of the PAH to the ionisation irradiance I_{ion} above the dissociation threshold, i.e. beyond the I_{ion} at which the first fragment ions are detected. It is important to point out that some critical features of the LD/LI/TOF-MS (for instance the width and the position of the maximum of the ionisation curves) are influenced by the desorption irradiance. This coupling between the desorption and ionisation processes will be discussed in the next Paragraph 5.4.

The data presented in this Section all refer to the analysis of pyrene. However, in this work it has been verified that the proposed arguments are valid for the other PAH too. Particularly, the detected fragment ions and their order of apparition as a function of the ionisation irradiance is the same (of course, according to the mass of the precursor ion).

The good agreement between the data experimentally obtained and the literature is shown in Figure 5.16, where one of the LD/LI/TOF-MS mass spectra is compared with that available in the NIST database [84].
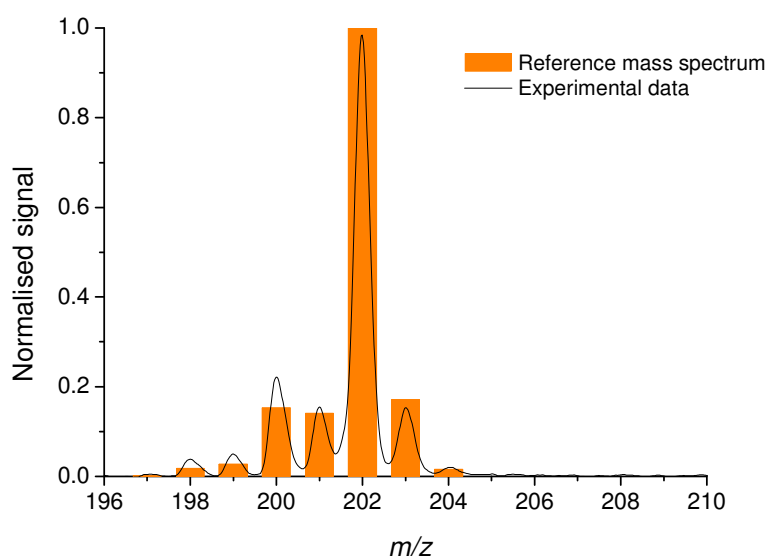
Figure 5.16. Comparison of the experimental data with the NIST reference mass spectrum of pyrene [84]. LD/LI/TOF-MS mass spectrum obtained at E_{des} = 9.2 MW cm^{-2} and E_{ion} = 1.8 MW cm^{-2}. The NIST mass spectrum has been obtained via electron impact ionisation.

As a very general consideration PAH have molecular formula $C_nH_m^+$ with n>m. Therefore in the dissociation pattern carbon-rich carbon/hydrogen fragment ions are expected to be the most characteristic species.

When increasing I_{ion} above the dissociation threshold, the peak intensity of the precursor ion comes to a maximum and then decays (see Figure 5.9). During the decay, the mass spectrum shows the progressive appearance of low-mass peak signals due to positively charged fragment ions, evolving as a function of I_{ion}. Figure 5.17 compares three mass spectra at different I_{ion}.

When I_{ion} is lower than the maximum of the ionisation curve, the only detected signal are those of the precursor and its isotopologue ions. In Figure 5.9 such a situation occurs when I_{ion} < 1.5 MW cm^{-2} , and the detected signals correspond to the ions: $C_{16}H_{10}^+$ (202 u), $^{13}CC_{15}H_{10}^+$ (203 u) and $^{13}C_2C_{14}H_{10}^+$ (204 u). The brackets contain the nominal masses of the ions. Because of the complete absence of fragment ions, such spectra are labelled fragment-free. For obvious reasons, this also represents the ideal analysis condition, i.e. one precursor ion generates the minimum number of signals in the mass spectrum, and thus the data interpretation is the easiest.

Increasing I_{ion} up to the maximum of the ionisation curve leads to the first visible change in the mass spectrum, i.e. the hydrogen atoms elimination from the precursor ion. This phenomenon occurs at low I_{ion} because the cleavage of a C-H bond is a less endothermic process than the dissociation of aromatic rings. Because of the elimination of one-to-four hydrogen atoms, a series of satellite peaks having nominal mass 198, 199, 200 and 201 u appear. This situation roughly corresponds to the maximum of signal in the ionisation curve, highlighted (b) in Figure 5.9.
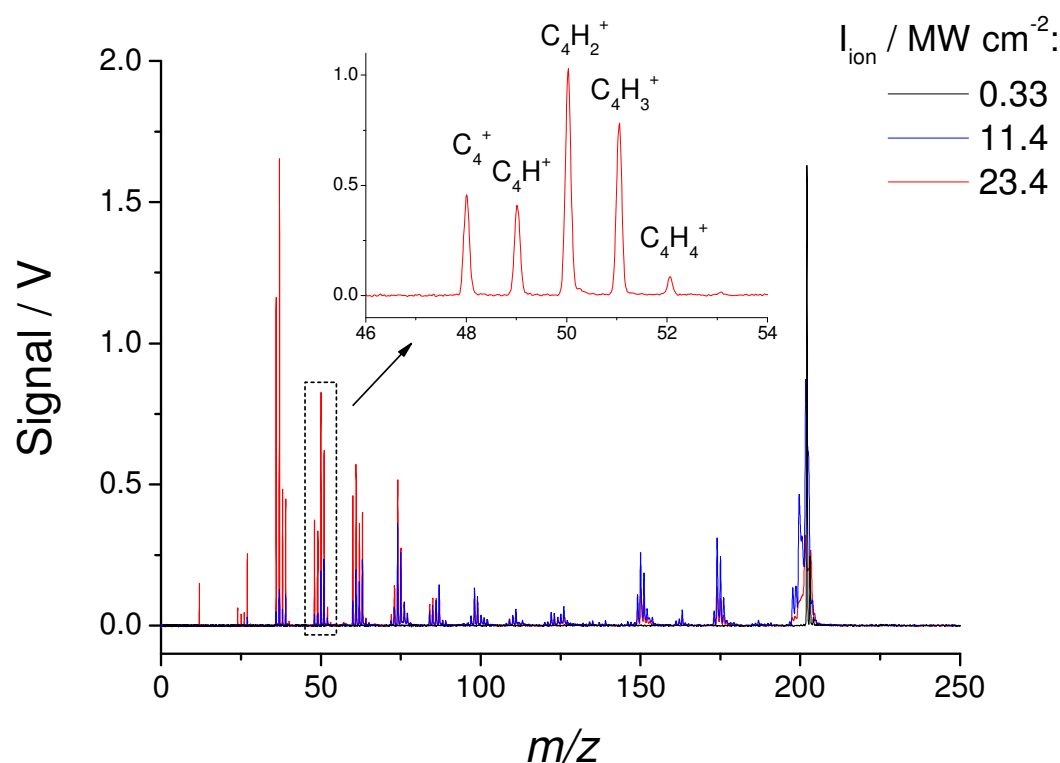
Figure 5.17. Pure pyrene mass spectra obtained under heavy dissociation conditions. $I_{des} = 11.4$ MW cm^{-2}.

The main signal peaks always occur together with more or less hydrogenated peaks, meaning that the hydrogen eliminations are common reactions both on the precursor ion and on the smaller fragments. When considering the precursor ion of pyrene, masses down to 198 u are detected even at low I_{ion}, indicating that up to four hydrogen atoms can be easily eliminated. The situation is analogous for the other analysed PAH, with the exception of anthracene and phenanthrene for which the elimination of only one hydrogen atom does not occur. In fact, the signal peak at 177 u has negligible intensity if compared with those at 178 u (precursor ion) and 176 u (double hydrogen elimination).

Increasing I_{ion} the signal peak of the precursor ion decays, and at the same time several weak peaks at low-mass appear. These low-mass peaks cover all the m/z range from zero up to the mass of the precursor ion, and their exact masses are consistent with those of hydrogen/carbon ionic aggregates having structural formula $C_nH_m^+$ (n and m being natural numbers). This is the situation represented at points (c) and (d) of Figure 5.9.

When I_{ion} is still relatively low, i.e. at the beginning of the decay of the ionisation curve (1.5-5.0 MW cm^{-2} for pyrene), the most intense signal peak correspond to fragment ions characterised by n which spans from 10 up to the carbon number of the precursor ion (n = 16 for pyrene, 14 for phenanthrene and anthracene, 10 for naphthalene). This observation suggests that the dissociation process mainly occurs via elimination of C_2H_m units. Conversely, m seems independent from the size of the fragment, always spanning from 5 up to 8. The three main groups of fragments are: $C_{10}H_5^+$, $C_{10}H_6^+$, $C_{10}H_7^+$ (125-126-127 u), $C_{12}H_6^+$, $C_{12}H_7^+$, $C_{12}H_8^+$ (150-151-152 u) and $C_{14}H_6^+$, $C_{14}H_7^+$, $C_{14}H_8^+$ (174-175-176 u). Those fragments most likely still contain aromatic ring(s). Very weak signal peaks corresponding to fragments containing an odd

number of carbon atoms are also present in the same mass range, implying that at least a secondary dissociation pathway, evolving via elimination of CH_m units, exists.

The presence of $C_{12}H_8^+$ (152 u) in the pyrene mass spectra is at least curious. This fragment ion gives a strong peak, and it appears early in the fragment sequence (see Figure 5.20). Evidently it can be only produced via C_2 elimination from a $C_{14}H_8^+$ (176 u), or via C_4H_m elimination from one of the ions belonging to the group of the precursor (202, 201 or 200 u). Both these hypotheses are consistent with the structure of the signal curves. However, C_4H_m elimination reaction from a precursor ion like pyrene would necessarily require the simultaneous dissociation of at least two aromatic rings, which is a very endothermic thus unlikely reaction. Therefore, an important role in the dissociation seems to be played by elimination reactions involving carbon clusters.

Under very high ionisation irradiance the peak intensities of the low-mass odd C-number fragments ($<C_{10}H_5^+$) become comparable to those of the even C-number fragments. The high I_{ion} mass spectra of PAH feature groups of strong peaks in correspondence of the entire set of masses corresponding to carbon clusters more or less hydrogenated. Eventually, a wide variety of small fragment ions ranging from the naked carbon clusters down to small ionic aggregates is produced, as already reported in Figure 5.9(d-f) and Figure 5.17. Besides the primary fragments discussed above, several groups of signal peaks spanning the range $0<m/z<112$ appear. In all the detected groups the lowest mass corresponds to a carbon cluster C_n^+, with n spanning from 1 up to 9. The carbon clusters occur together with more hydrogenated $C_nH_m^+$ fragments, where m varies from 1 up to 4. Each group contains four-five signal peaks.

Finally at extremely high ionisation irradiance the dominant peaks become those of the atomic species, C^+ and H^+.
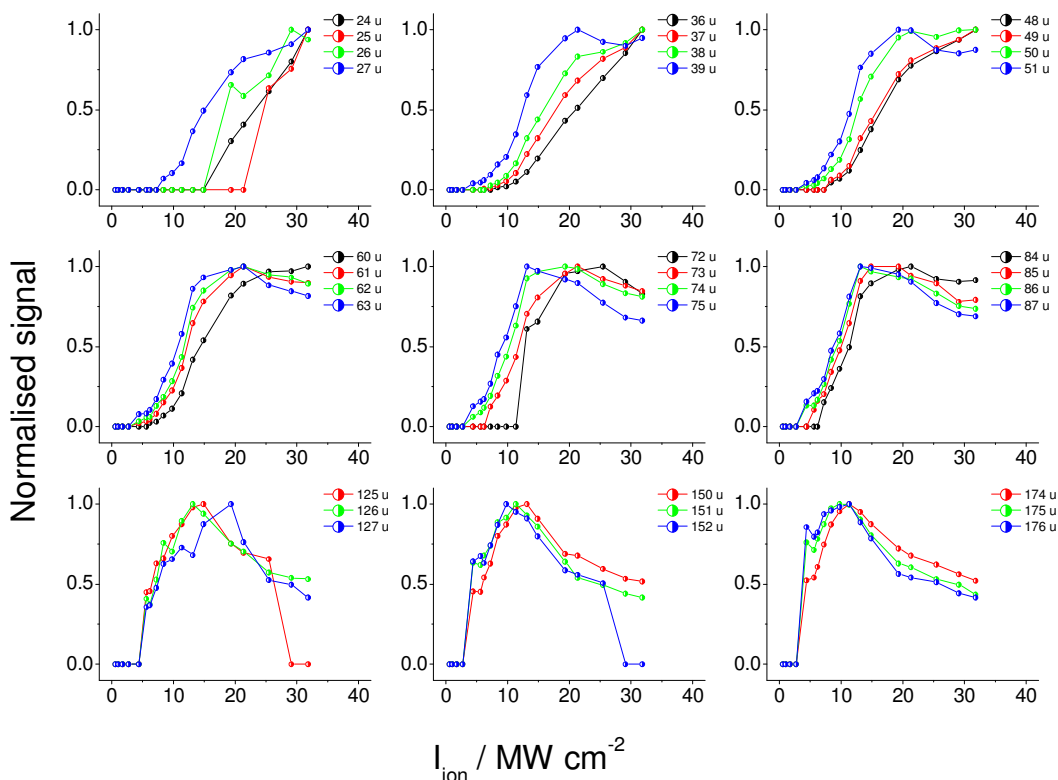

Figure 5.18. Pure pyrene fragment intensity evolution as a function of the ionisation irradiance. $I_{des} = 11.4$ MW cm^{-2}. For each group of fragments are reported: hydrogen-rich fragments (blue series), intermediate fragment (green series), hydrogen-poor fragment (red series) and carbon cluster (black series).

According to the ladder-switching dissociation mechanism developed by Boesl [125], the optical absorption of the fragments continues until the next dissociation channels switch over to a smaller fragment ion. In this model, the photo-dissociation dynamic evolves through a progressive dissociation of the precursor and of the high-mass fragment ions down to low-mass fragment ions, according to the intensity of the ionisation field.

The signal curves vs. I_{ion} for the low-mass pyrene fragments at constant $I_{des} = 11.4$ MW cm^{-2} are reported in Figure 5.18. The comparison between the signal curves of a few selected fragment ions and the ionisation curve of pyrene is reported in Figure 5.19. The maxima of the signal curves shift towards higher I_{ion} as the fragment mass decreases, implying the progressive stabilisation of lighter and lighter fragment ions under sustained irradiation.
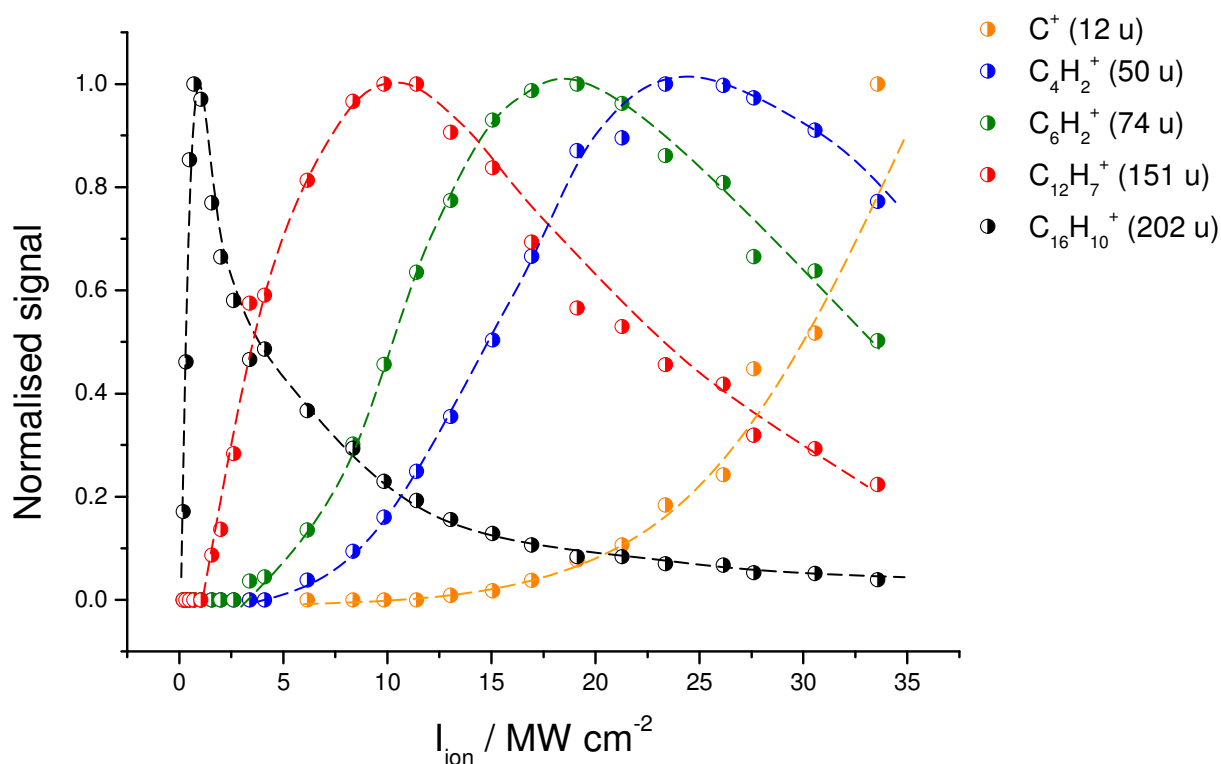

Figure 5.19. Ionisation curve of pyrene (black dots) and signal curves of some selected fragment ions reported as a function of Iion (coloured dots). The dashed lines are guidelines. $I_{des} = 11.4$ MW cm^{-2}.

It is important to point out that LD/LI/TOF-MS analyses performed in this configuration cannot provide information on the dissociation dynamic, but only on the stability range of the fragment ions with respect to the ionisation irradiance. Indeed, during the time of flight (~ 10 μs) structural rearrangements of the ions produced during the primary dissociation may generate further dissociation, resulting in very complex ion patterns in which the information on the early dissociations is lost. According to the discussion so far, the stability range of the detected fragment ions vs. the ionisation irradiance is reported in Figure 5.20. For instance, investigations leading to fragment free mass spectra performed on the maximum of pyrene's desorption yield ($I_{des} = 11.4$ MW cm^{-2}) require I_{ion} in the range 0.3-2.5 MW cm^{-2}.
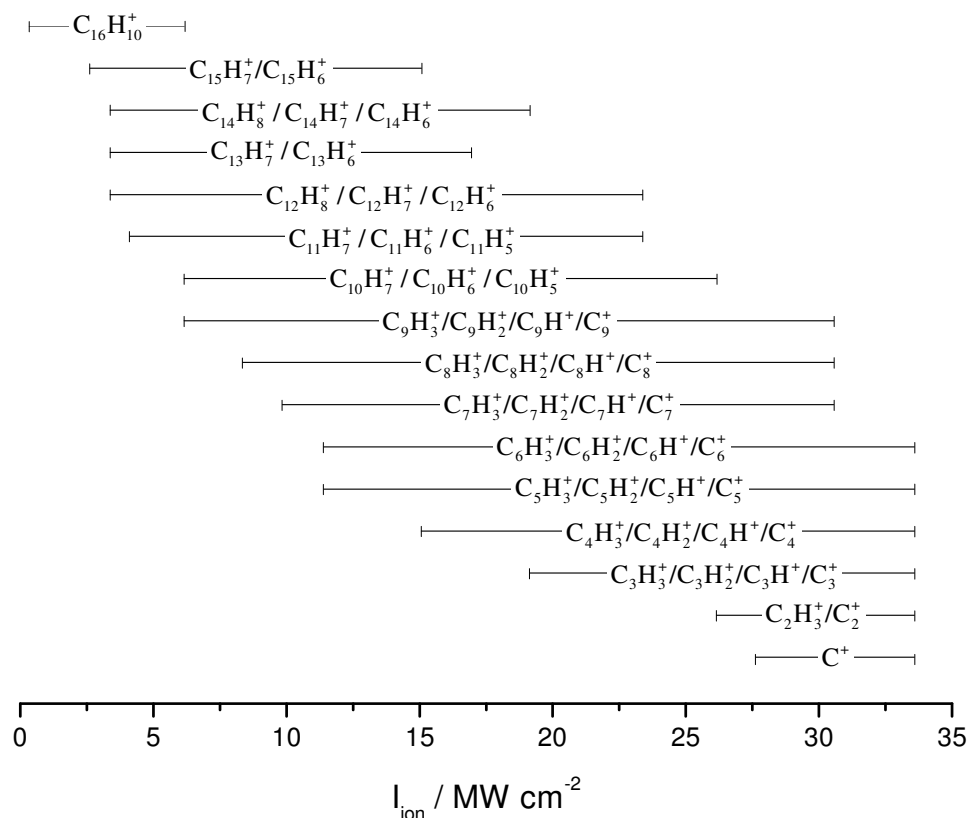
Figure 5.20. Stability range of the detected fragment ions in the dissociation pattern of pyrene. $I_{des} = 11.4$ MW cm^{-2}. $I_{ion} = 34$ MW cm^{-2} is the highest ionisation irradiance reachable in the adopted configuration of the ionisation path.

5.4. Coupling Desorption-Ionisation

The desorption and the ionisation steps in LD/LI/TOF-MS analyses are not totally independent processes. This Paragraph 5.4 proposes an early investigation on the relationship occurring between the two energy transfers (referred as coupling desorption-ionisation), performed by studying the evolution of the intensity of the precursor peaks of anthracene and pyrene in the desorption-ionisation irradiance plane. The coupling of desorption and ionisation is ultimately due to the increase of internal energy consequent to the desorption step, which shifts the molecular energy distribution to higher vibrational levels, and distributes the population on a broader set of rovibronic states.

The coupling desorption-ionisation has at least one important consequence, i.e. the desorption conditions play an important role in determining the overall ionisation efficiency. That is clear when looking Figure 5.21, in which the ionisation curves of pyrene under thermal and laser desorption are compared. The thermal desorption has been obtained heating the sample-holder in the ion source of the mass spectrometer in order to promote the sublimation of the sample without irradiating its surface. In the case of thermal desorption, the ionisation occurs at much higher ionisation irradiance, indicating that the energy contribution of the desorption to the total energy of the desorbed molecules is not negligible. Even if the desorption pulse itself is not sufficient to directly sublimate and ionise the analyte, it provides an extra energy content via vibrational excitation which eventually narrows the gap between the electronic ground and excited state.

Practically, under high desorption irradiance, the ionisation and the dissociation processes occur at significantly lower ionisation irradiance.
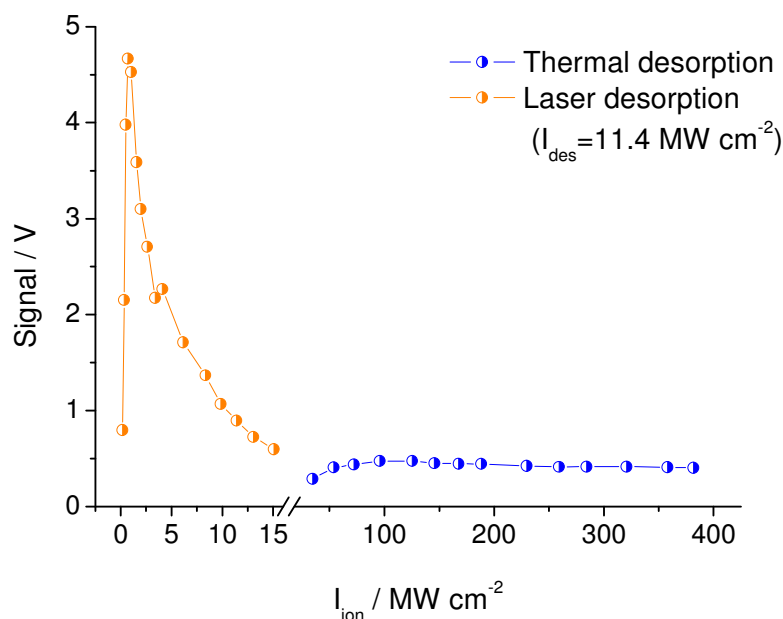

Figure 5.21. Comparison of the ionisation curves of pyrene under thermal (blue dots) and laser desorption (orange dots).

The optical response of anthracene and pyrene has been compared. Figure 5.22 shows the ionisation curves of anthracene and pyrene for different desorption irradiances.

Above the desorption threshold the ionisation curves are all characterized by a sudden rise at low ionisation irradiance, a signal maximum, and eventually a peak signal decay at higher ionisation irradiance. The position of the maximum and the width of the distribution are both depending on I_{des}. The existence of a signal maximum is due to the competition between the ionisation efficiency of the neutral PAH present in the desorbed plume and the dissociation induced under high intensity ionisation irradiance. The rate of the multi-photon ionisation increases as I_{ion} increases following Equation (3.2), but for high ionisation irradiance the dissociation phenomena play a more and more important role, removing precursor ions from the plume, and therefore accounting for the observed signal decay. As a result, the signal peak grows up to a maximum ionisation yield, and above this limit it decreases when further increasing I_{ion}. The experimental data locate the best ionisation efficiency when $10.0 \text{ MW cm}^{-2} < I_{des} < 13.5 \text{ MW cm}^{-2}$ for pyrene, and $42.8 \text{ MW cm}^{-2} < I_{des} < 57.1 \text{ MW cm}^{-2}$ for anthracene.

When considering the ionisation curves at different I_{des}, it is easy to note that when I_{des} rises the ionisation curves are simultaneously narrowed down and shifted to lower I_{ion}. This behaviour can be qualitatively attributed to the larger gain of internal energy of the ejecta consequent to the higher desorption irradiance, which ultimately leads to easier ionisation [126]. This effect explains the shift of the ionisation curves to lower values and also their sharper slope when increasing I_{des}. However, at even higher I_{des} the amount of internal energy is so important that the dissociation would eventually dominate even for low I_{ion}. In order to highlight this aspect and make the data interpretation easier, an alternative data representation is reported in Figure 5.23, in which the distributions have been shifted vertically up with increasing I_{des}, and the absolute intensity scale has not been reported.
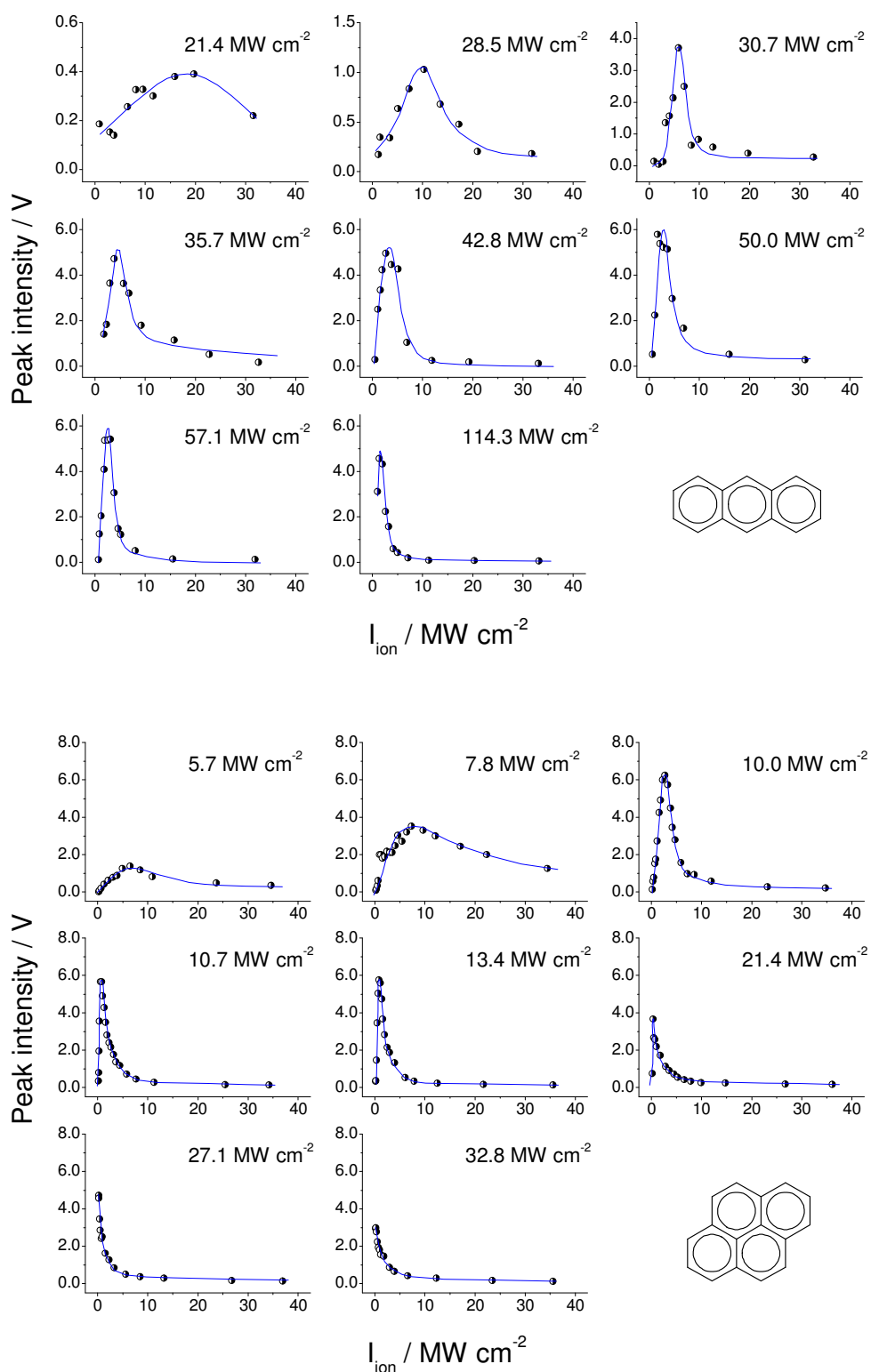
Figure 5.22. Ionisation curves of (a) anthracene and (b) pyrene. Peak intensity evolution as a function of the ionisation irradiance for different desorption irradiances (I_{des} values reported on the title of each graph). The blue lines are guidelines.
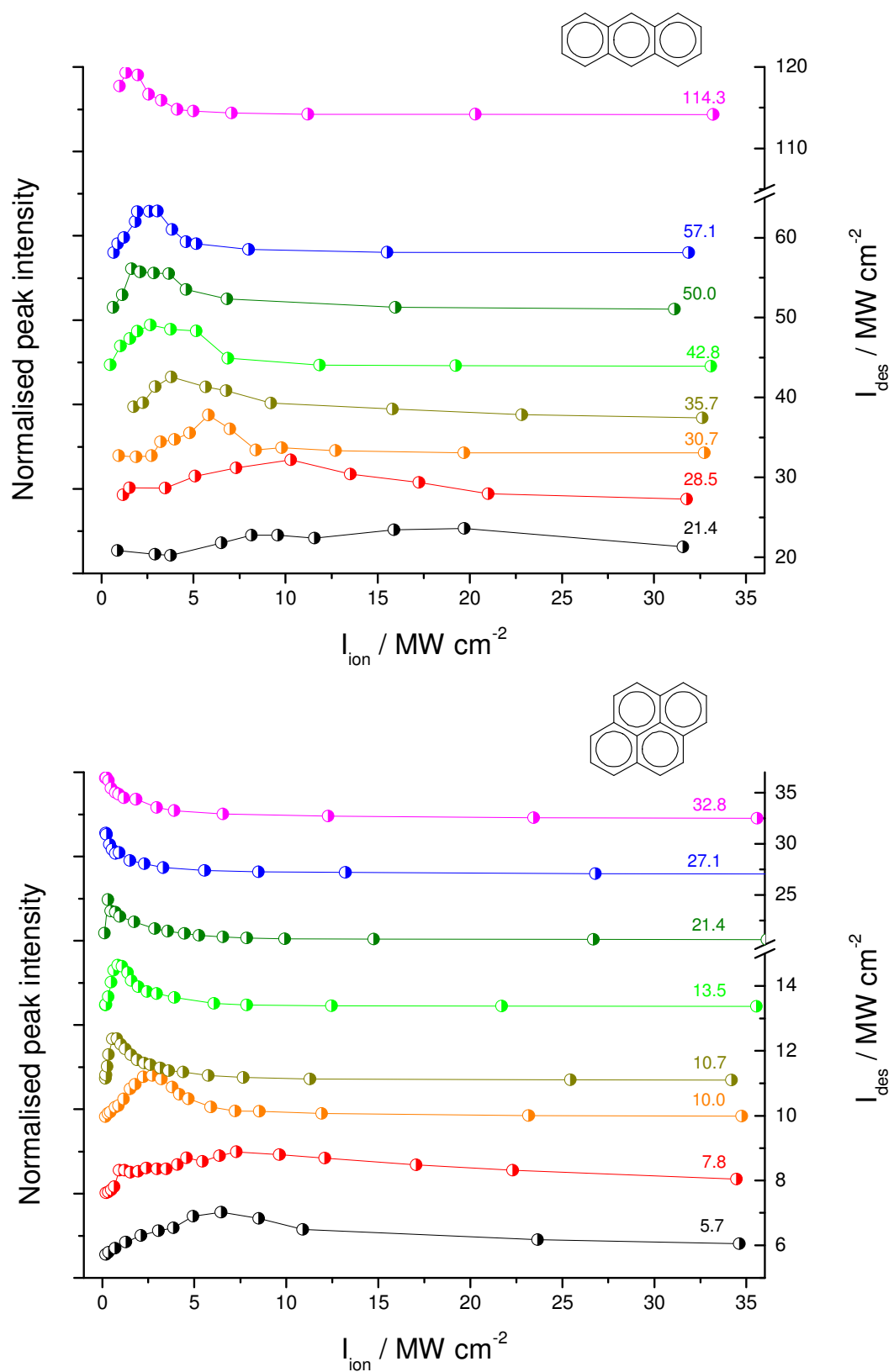
Figure 5.23. Evolution of anthracene (top figure) and pyrene (bottom figure) peak intensities as a function of I_{ion} for different I_{des}. The data series have been vertically translated in order to get an easier data comparison [126].

The mass spectra obtained under extreme desorption conditions are very rich of low-mass fragments even for low I_{ion}, the peak signals are broadened because of the larger and larger importance of the in-plume collisions, and eventually it is possible to recognise direct ionisation phenomena [126]. In Figure 5.24 mass spectra collected at different desorption irradiance are reported in order to show the effect of the collision broadening of the peak signals. The entity of the broadening is very dependent on the experimental conditions like the desorption efficiency of the analyte, but it can nevertheless reach 10-15 u when I_{des} is twice the desorption threshold.
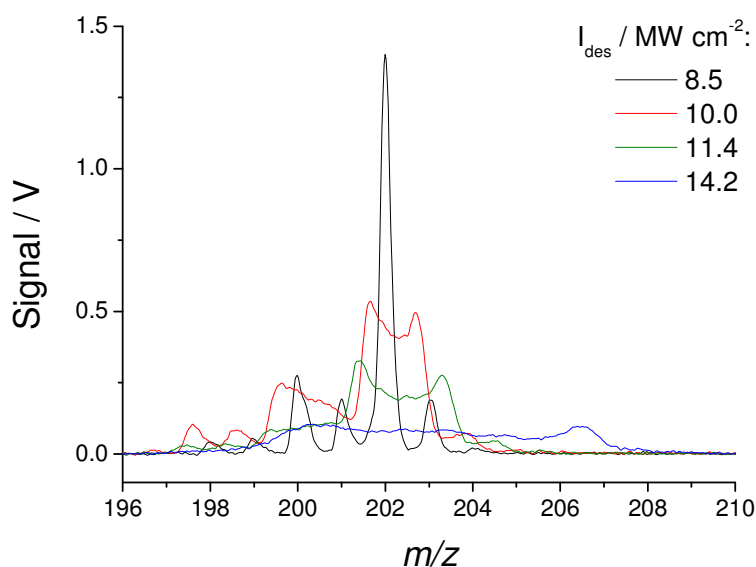

Figure 5.24. Pure pyrene mass spectra at different desorption irradiance. Progressive defocusing of the precursor ion packet due to the increasing desorption irradiance, $I_{ion} = 22.2$ MW cm^{-2}.

The above discussed arguments are supported by a symmetric study on the signal peak evolution as a function of the desorption irradiance. The resulting curves (desorption curves) have been built for different ionisation irradiances as shown in Figure 5.22. Particularly, the existence of a signal maximum for a given I_{ion} and the narrowing of the desorption curves at high I_{ion} highlights once again the relationship between desorption and ionisation through the increase of internal energy.

It is noteworthy that the appearance threshold and the maximum of the desorption curves are independent from the ionisation irradiance when $I_{ion} > 4.6$ MW cm^{-2} in the case of anthracene and $I_{ion} > 0.6$ MW cm^{-2} in the case of pyrene. Both these values are very close to the lowest measurable irradiance, and therefore investigation of even lower irradiance was not possible at the time of the present work. On the other hand the existence of a well-defined desorption threshold is related to the minimum energy needed to initiate the massive ejection of the analyte in the gas phase.

When comparing the desorption curves of pyrene and anthracene some differences can be observed about the profile width and the position of the maximum. First the I_{des} range in which the desorption yield is high is wider for anthracene than for pyrene, regardless of I_{ion}. This indicates a better efficiency for the laser energy transfer to solid pyrene (stronger absorption at 532 nm wavelength), leading to a higher internal energy for the ejecta, and furthermore to an improved ionisation yield as evidenced by Haefliger and co-workers [89].
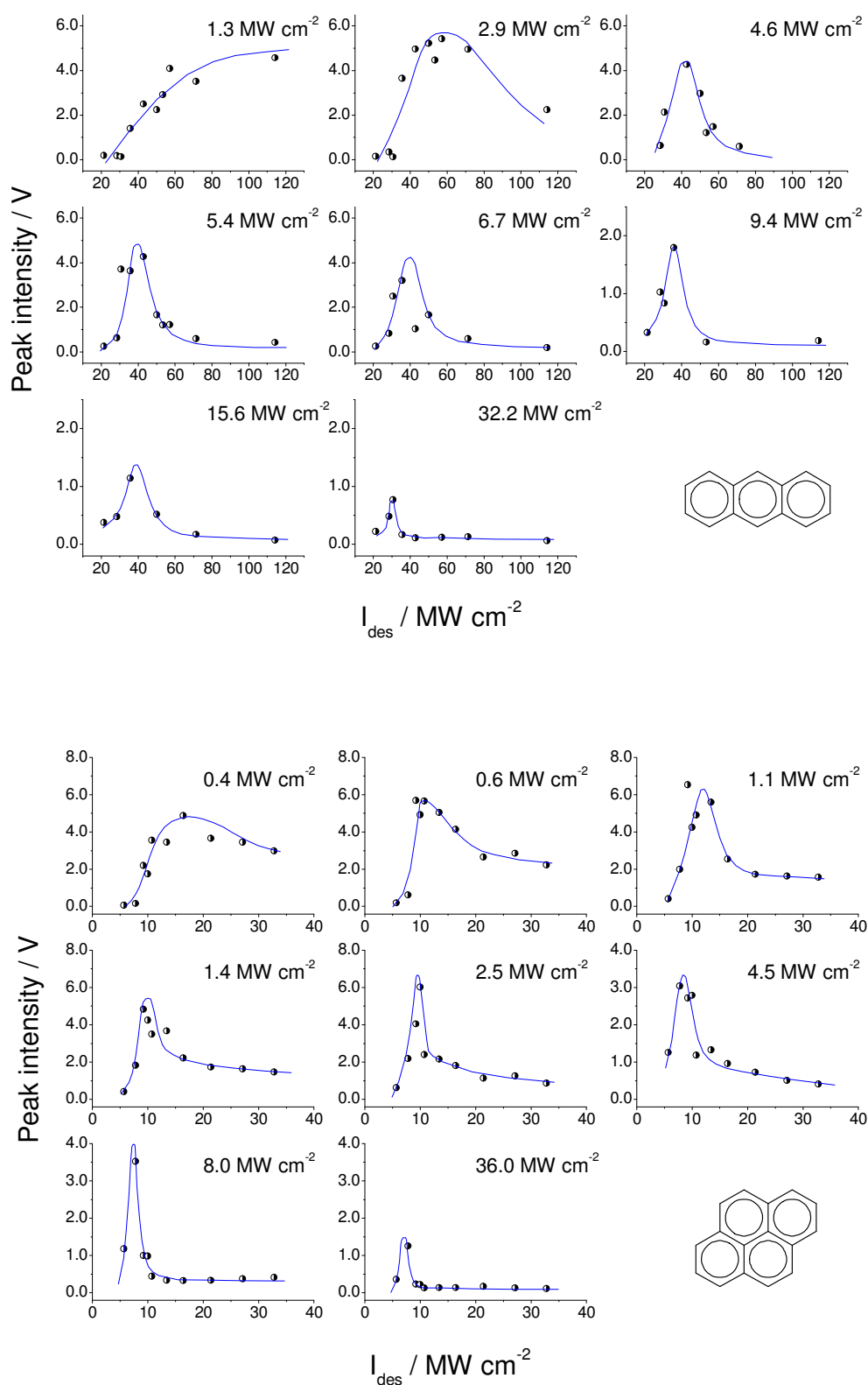
Figure 5.25. Desorption curves of (a) anthracene and (b) pyrene. Peak intensity evolution as a function of the desorption irradiance for different ionisation irradiances (I_{ion} values reported on the title of each graph). The blue lines are guidelines.

Clearly the signal curves of fragments are very dependent on the desorption energy as the ionisation curve of the precursor ion described in Figure 5.14. The extra energy coming from the desorption gives a contribution to the internal energy of the newborn fragments as well. The peak intensity of each fragment is strictly dependent on I_{ion}, and each signal curve has a maximum for very specific ionisation irradiance.

In the same group of fragments, at low I_{ion} the strongest peaks are always those of the most hydrogenated fragments (higher mass), while at high I_{ion} the strongest peaks are those of the less hydrogenated fragments, and eventually of carbon clusters (lower mass).

In conclusion the LD/LI/TOF-MS response of anthracene, pyrene and their dissociation products to the desorption and ionisation processes suggests that a complex relationship occurs between the peak intensities and the two laser irradiances. Rising the input irradiances, the mass spectra show a first fragment-free region where the signal rises according to the multi-photon ionisation described in Section 5.3. When the irradiance is too high the dissociation begins, the signal of the molecular decreases and the signals of the fragments rise each one with a specific profile. These results confirm the role of the desorbed molecules internal energy in the analysis process, and strengthen the idea that the choice of the desorption irradiance for analytical purposes must account for the effect of the dissociation as well as the broadening of the signal peaks.

The analyses performed in this Chapter allows a deeper understanding on the details of the desorption and ionisatio steps. Particularly, they lead to define a comprehensive and well controlled set of experimental parameters which will be used in the following Chapter 6 for the analyses of real soot sampled from flames.

Chapter 6.

Into the flames

This Section is dedicated to the LD/LI/TOF-MS analyses on soot samples collected from both model flames and real flames. Several measurements have been performed in order to get information on the influence of some flame properties, like the reaction time or the fuel composition, on the PAH content of soot. This Chapter mainly focuses on the analysis of two low-sooting flames, which are a low-pressure premixed methane flame ($f_{v,max} \sim 1$ ppb), and an atmospheric jet diesel flame ($f_{v,max} \sim 100$ ppb). An atmospheric premixed ethylene flame has been investigated as well to test the diagnostic and to compare the measurements with those already available in the specific literature.

The premixed flames are well suited for the study of the mechanisms of soot formation. Particularly, the LD/LI/TOF-MS analysis of the low-pressure methane flame complete other experimental investigations, performed via Laser Induced Incandescence (LII) and jet-cooled Laser Induced Fluorescence (LIF), for the selective detection and the determination of the role of PAH during the combustion process [109]. Furthermore the low-pressure flames are particularly suitable for the studies on kinetic modelling. Useful information is provided by the dependence of the chemical content of the collected soot on the reaction time and therefore on the Height Above the Burner (HAB) of the sampling on the overall growth process of the PAH. In order to study the chemical composition of the sampled gases and soot and its evolution during the combustion process, an original method has been tested. Information on the differences between the composition of the gas phase and the phase adsorbed on soot can be achieved by the comparison of the mass spectra obtained by depositing sampled gases and soot on adsorbing and non-adsorbing substrates (porous glass and activated carbon), as detailed in Section 6.3.

The main interest in studying the jet flame is that it is an actual and not a model flame which allows the investigations on practical liquid fuels. The LD/LI/TOF-MS analyses on such a flame give information on the dependence of the PAH adsorbed on soot on the composition of the liquid fuel burned. These analyses complete the in-situ measurements on the spatial distribution of soot and soot precursors performed via Laser Induced Incandescence and Laser Induced Fluorescence [112].

This Chapter is organised as follows. Since in this work the LD/LI/TOF-MS diagnostic is an ex-situ technique a sampling of the flame is required. The first part of this Chapter (Section 6.1) details the sampling procedure, while the following sections deal with the flame analyses. Three different flames have been analysed. Those are, in order, the atmospheric ethylene flame, (Section 6.2), the methane low-pressure flame (Section 6.3), and finally the turbulent jet flame (Section 6.4).

6.1. Sampling procedure

The soot sampling procedure has been proven to be an important step during the soot analyses. The produced samples have to be representative of the gases and soot collected from the flame and suitable for the LD/LI/TOF-MS analysis. The adopted configuration of the sampling line is detailed in Section 4.2 in the context of the description of the experimental setup. Briefly, it consists in the insertion of the extractive probe into the flame at the desired location. A pumping flow pulls gases and soot into the sampling line down to a sample-holder containing the porous borosilicate glass filter (if necessary covered by a layer of activated carbon) where gases and soot deposit.

The sampling procedure has been organised as follows. After the flame ignition a heating period of 30 min under lean flame conditions is required in order to thermally stabilise the burner (and the vessel in the case of the low-pressure flame). Further 10 min are spent to stabilise the temperature of the line pumping throughout the by-pass of the sample-holder (see Paragraph 4.2.6 for a description of the sampling line). After the pre-heating of the line, the sampling flow is switched from the by-pass to the sample-holder for the required sampling time, and switched back to the sample-holder in order to remove the now soot-covered borosilicate filter. The current configuration of the sample-holder (depicted in Figure 4.23) and particularly the couple of three-way valves allows changing the borosilicate filters with no need to stop the pumping, simply switching the flow in and out the by-pass. During the pumping stage required for operating the LD/LI/TOF-MS diagnostic, the filters are refrigerated down to -160 °C in order to avoid the spontaneous desorption of low-mass PAH.

The characterisation of the sampling procedure is long and complex, consisting in the analysis of many samples obtained by changing one sampling parameter at a time. At the end of this Section the effect on the mass spectra of the deposition on different substrates, of the dilution, of the line temperature, of the sampling time and of the probe aperture have been reported. All the changes in the sampling line configuration described below have been performed keeping the sampling flow constant.

6.1.1. Distinction of gaseous/adsorbed PAH

The PAH produced during the combustion are found both in the gas phase and adsorbed on soot particles. A hypothesis on the partition of PAH in the two phases can be made under specific experimental conditions.

The best case scenario is when the flame features a net separation of the reaction zones in which PAH and soot are formed. In this case positioning the probe into the two regions with sufficient spatial precision allows collecting only the gaseous PAH or soot. For instance in the Diesel jet-flames described in Section 6.4 and analysed via in-situ two-colour LII/LIF [111-112] a sharp evolution of the LIF signal (PAH fluorescence) and of the LII signal (soot volume fraction) occurs between 50 and 90 mm HAB, resulting in two separated reaction zones.

If such a separation does not occur, as in the case of the low-pressure flame described in Section 6.3, in principle it is not possible to separate the gas-phase PAH from those adsorbed on soot during the sampling. However, hypotheses on the partition of the PAH between the gas phase and soot can be deduced by comparing the deposits on adsorbing and non-adsorbing substrates. In this work the comparison between the matter collected on two different filters (neat borosilicate and activated carbon) has been performed. The borosilicate glass is chemically inert under the adopted

sampling conditions. On the other hand, the stronger interactions occurring between PAH and the graphitic-like structure of the activated carbon allow the collection of molecular species over a very large mass-range.

6.1.2. Effect of the dilution

The effect of the dilution with an inert gas during the sampling has been tested on the soot sampled from the Diesel jet flame presented in Section 6.4. Five samples have been collected at 92 mm HAB, the location of the maximum soot volume fraction. The obtained mass spectra are reported in Figure 6.1. The dilution gas is nitrogen, and the tested dilution factors vary from zero up to 92%. In this work higher dilutions were not possible because all the analysed flames are low-sooting flames, then the amount of collected soot is so little that even a small dilution factor requires hours-long sampling time.
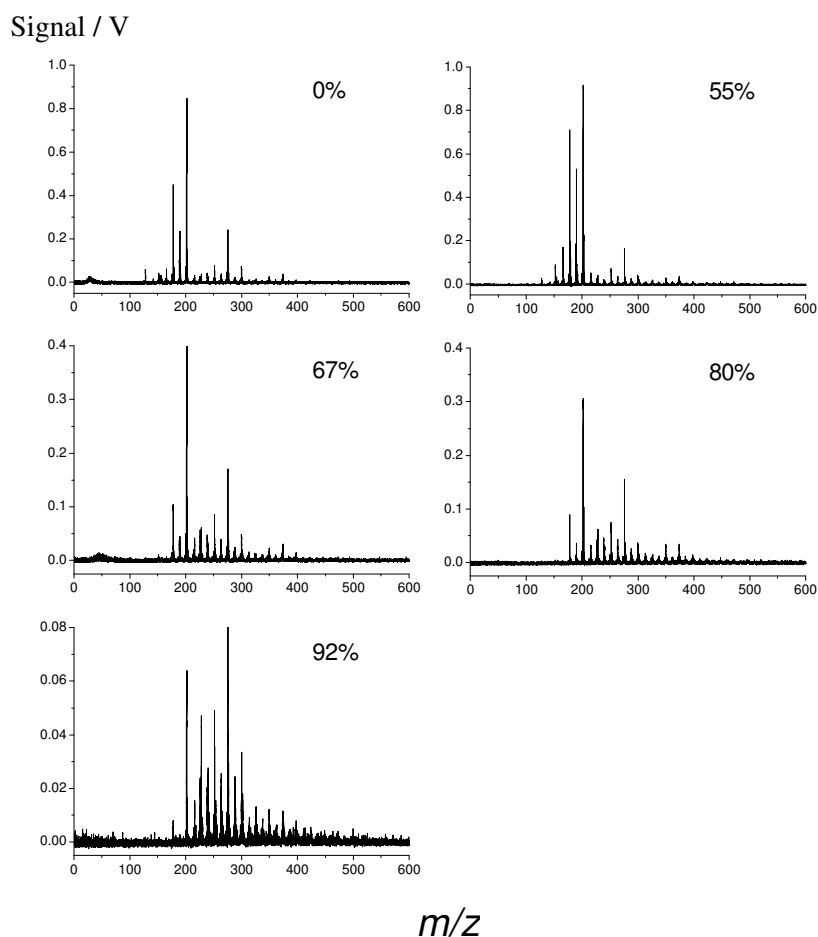
Figure 6.1. Effect of the dilution on the structure of the mass spectra. The analysed soot has been collected from the Diesel flame at 92 mm HAB and directly deposited on a neat filter, $I_{des} = 14.2$ MW cm^{-2}, $I_{ion} = 2.2$ MW cm^{-2}, 50 μs delay between pulses, average of the first five laser pulses.

The main mass sequence does not change when diluting, but the peak absolute and relative intensities all change. At least two different regimes are visible: the dilution strongly affects the light masses (128<m/z<202) while it leaves relatively untouched the heavier masses

(216<m/z<498). This difference in behaviour becomes particularly evident when comparing the peak intensities in a histogram plot (Figure 6.2).

The higher is the dilution factor, the lower are the signals detected on the light-mass side of the spectra. Particularly, the lightest masses (128<m/z<166) completely disappear, and the most intense peak signals (178, 190 and 202 u) are reduced by a factor 20 raising the dilution factor from 55% up to 92%. On the other hand, the behaviour of the heavy masses is far less influenced by the dilution factor. The order of magnitude of the signal is almost constant. The peak signal decreases only slightly when diluting, decreasing by a factor 3 in the worst case (mass 374 u) when raising the dilution factor from 55% up to 92%.
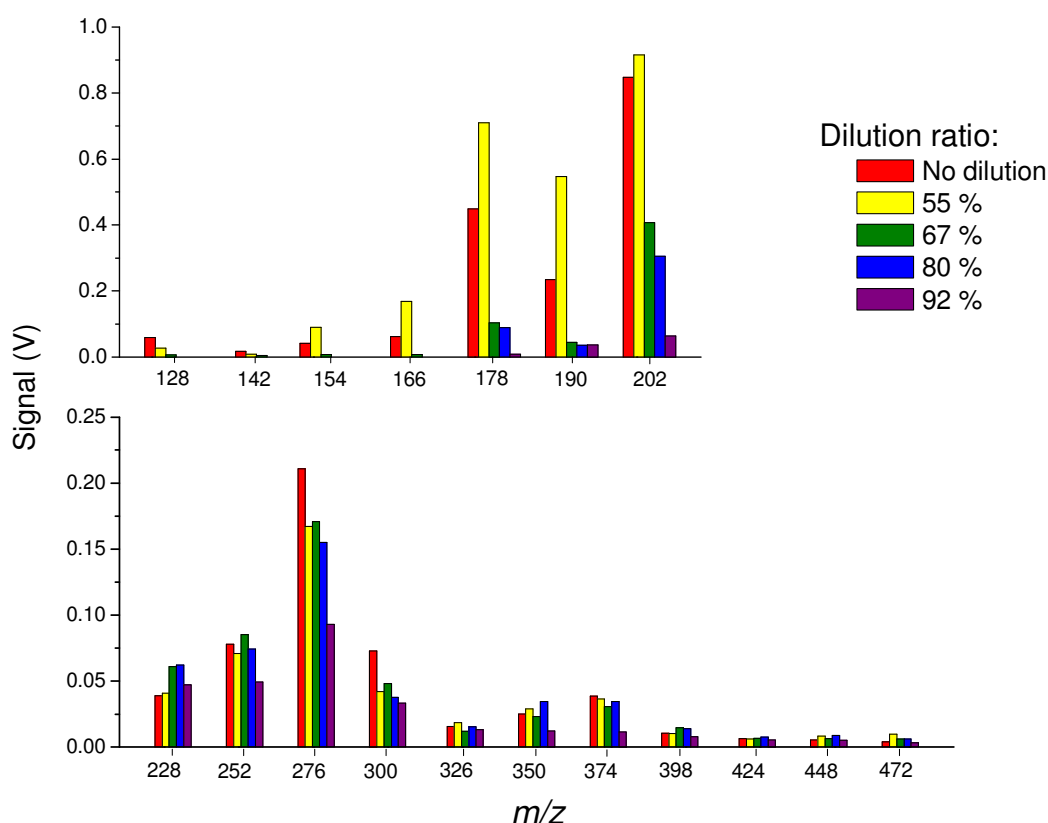
Figure 6.2. Histogram representing the change of the peak intensities of 18 selected masses as a function of the dilution. The top histogram contains the light and border-line PAH which are influenced by the dilution during the sampling, while the bottom plot gives information on the heavy PAH, whose detection is not influenced by the dilution.

Evidently two different phenomena occur. The important signal reduction observed for the lighter masses can be attributed to the very high vapour pressure of the PAH under the temperature and pressure condition of the sampling. Those PAH tend to accumulate in the gas phase and to condense only when the temperature drops down to or the pressure rises up to the environment values. Nevertheless, it is reasonable to believe that, considering heavier and heavier masses (i.e. less volatile species) a progressively higher amount of those PAH was present even in the adsorbed phase. This conjecture is supported by the experimental evidence that the signal peaks of the masses 178, 190 and 202 u does not completely disappear even under high dilution conditions (Figure 6.2). It is then possible to distinguish two classes of PAH on the basis of their response to

the dilution, which are the light PAH, whose properties are typically related to the gas phase, and the heavy PAH, which are typically associated to the adsorbed phase on soot. In this sense the three masses above mentioned define a border line between the two different behaviours.

6.1.3. Sampling line temperature

The temperature of the sampling line between the extractive probe and the sample holder is an important parameter to control in order to keep some PAH as long as possible into the gas phase, and therefore allowing them to reach the sample holder.

As shown in Figure 6.3, the temperature of the line affects both the detected mass sequence and the peak intensities. When heating the line up to 240 °C the signal intensities generally raise and a few new peaks appear. The masses most affected by the line heating are those in the range $128 \leq m/z \leq 202$.
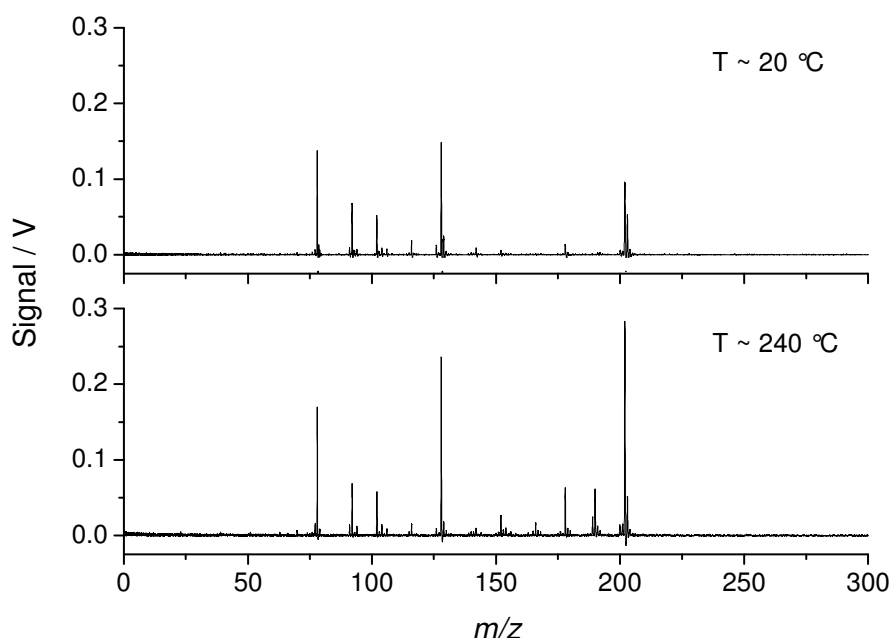

Figure 6.3. Comparison of the mass spectra obtained from soot collected keeping the sampling line at environment temperature (top mass spectrum) and heating up to 240°C (bottom mass spectrum. The sampled flame is the low-pressure methane described in the Section 6.3, sampling performed at 7.0 mm HAB, sampling time 30 min, probe aperture 0.3 mm, deposition of the combustion products on activated carbon. $I_{des} = 12.8$ MW cm^{-2}, $I_{ion} = 1.5$ MW cm^{-2}, 50 μs delay between pulses, average of the first five laser pulses.

The signal gain at high temperature largely differs depending on the volatility and concentration in the gas phase of each PAH. The most volatile PAH, like benzene (78 u) and naphthalene (128 u), are relatively unaffected by the change of temperature because they only exist in the gas phase at the environment temperature (20°C) and at the pressure of the line (2.67 kPa). On the other hand, some heavier PAH, like phenanthrene and anthracene (178 u), coexist in both the gas and the condensed phase, and thus the partitioning function may be significantly shifted towards the gas phase by raising the temperature.

6.1.4. Sampling time

This measure has been performed in order to establish the best compromise between the peak intensity and the sampling time.

The sampling time affects the amount of matter deposed on the filter or adsorbed on the activated carbon, and therefore the signal decay as a function of the number of laser pulses (Paragraph 5.2.4). When irradiating the same location on a sample surface, the signal progressively decreases down to the noise level because each laser shot removes PAH from the irradiated location. The decay rate has been estimated from the number of laser pulses required in order to get half of the maximum initial signal.

A series of measures to study the signal dependence on the sampling time has been performed. In Figure 6.4 the decay rate vs. the sampling time has been reported for a series of samples collected from the low-pressure flame described in Section 6.3. The decay rate rises at the beginning of the sampling and then reaches a plateau. This plateau occurs after a very short time for the atmospheric flames (~ 0.5 min), but after a rather long time for the low-pressure flame (~20 min).
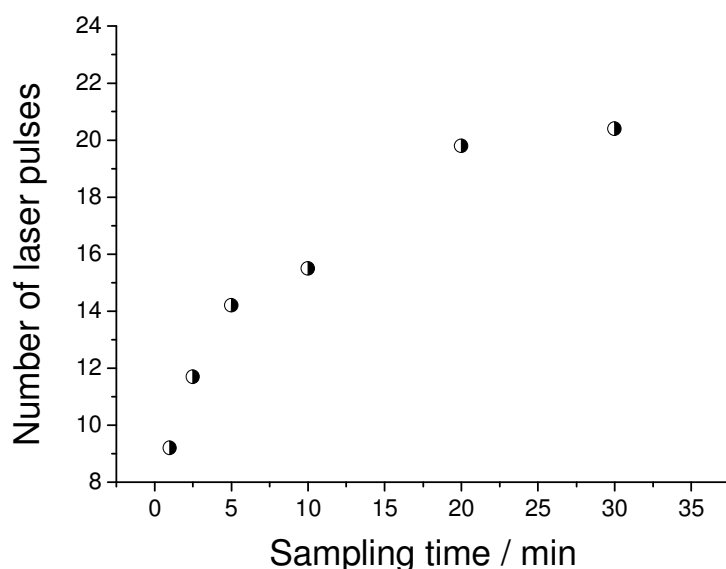

Figure 6.4. Decay rate (in number of laser pulses) of the mass 78 u for different sampling time. The sampled flame is the low-pressure methane described in Section 6.3, sampling performed at 7.0 mm HAB, probe aperture 0.3 mm, deposition of soot and gases on activated carbon, sampling line temperature 240°C. $I_{des} = 12.8$ MW cm^{-2}, $I_{ion} = 1.5$ MW cm^{-2}, 50 μs delay between pulses, average of the first five laser pulses.

The width of the signal decay rises (i.e. the signal decay curves become longer and longer) while the activated carbon is adsorbing substance from the gas phase, and then it reaches a plateau in correspondence of the saturation of the active sites of the activated carbon. It is convenient to work under saturation of the adsorption sites since the dynamic equilibrium established between the gas phase and the adsorbed/condensed species prevents further adsorption/condensation, and therefore the amount of deposed matter remains constant. On the basis of this interpretation, the sampling time has been set to 1 min for the atmospheric flames, and 30 min for the low-pressure flame.

6.1.5. Probe aperture

A curious effect due to the size of the probe aperture on the detected mass sequence has been observed. This influence has been verified during the study of both the low-pressure flame and the turbulent jet flames described in Section 6.3 and 6.4. Three different extractive probes having aperture diameter of 0.3, 0.8 and 1.0 mm have been tested on two different flames. In the mass spectra obtained from soot collected by means of 0.3 mm aperture probe no peak signals above 252 u have been detected.

While a thin aperture maximises the spatial resolution of the sampling, a large aperture reduces the sampling time and maximises the amount of collected substance. Particularly, the probe having 0.3 mm aperture seems effective in blocking the soot particles, to the point that the inner wall of the probe is still clean after sampling. However, no remarkable differences have been noted between the spectra collected with the probes having 0.8 and 1.0 mm aperture size. In this range the main mass sequence is not influenced by the aperture size and therefore 0.8 mm seems to be a reasonable choice in order to get the best compromise between spatial resolution and amount of collected substance.
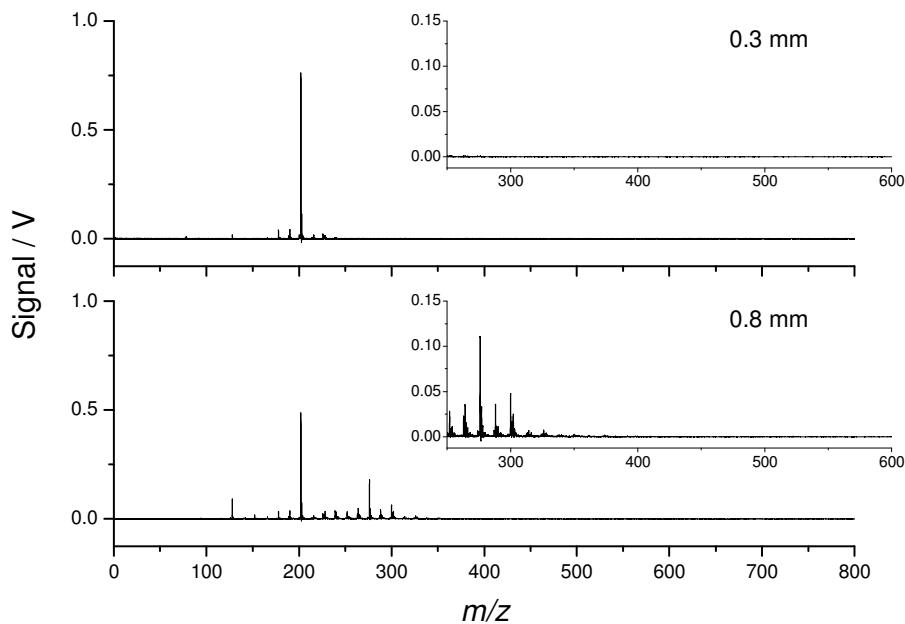

Figure 6.5. Comparison of the mass spectra obtained from soot collected with different probe apertures. The sampled flame is the low-pressure methane, sampling performed at 9.5 mm HAB, sampling time 30 min, temperature of the line 240°C, and deposition of the combustion products on activated carbon. $I_{des} = 12.8$ MW cm^{-2}, $I_{ion} = 1.5$ MW cm^{-2}, 50 μs delay between pulses, average of the first five laser pulses.

6.2. Reference atmospheric ethylene flame

The analyses performed in this section are intended to estimate the analytical capability of the LD/LI/TOF-MS diagnostic in comparison with other experimental setup. The goals are to compare the results with those already available in the literature on a well known flame, and then to establish an effective data representation to be used in the next analyses.

To this purpose the flame studied by Apicella and co-workers [76,77] described below has been reproduced. In their experimental setup, Apicella and co-workers stabilised a rich, laminar, premixed ethylene-oxygen flame, at atmospheric pressure. They adopted a bronze commercial McKenna burner, having internal diameter of 60 mm. The equivalence ratio is $\phi = 3.03$, the total unburned gases flow is $Q_T = 6.786$ slpm, and the velocity of the cold gases throughout the burner is kept constant at $v_0 = 40$ mm/s. The mole fractions are:

$$C_2H_4 : O_2 = 0.503 : 0.497$$
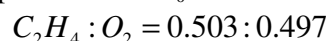
The flame is shielded with a nitrogen shroud, and stabilised by means of a stainless steel plate located 30 mm above the burner surface. The plate has 60 mm diameter and 5 mm thickness.

In the burner configuration, the stabilisation plate thickness is the only parameter different with respect to this work, in which the stabilisation plate is 10 mm thick. On the other hand the sampling procedure is a relevant difference with respect to the original Apicella's setup. It is useful to briefly review their sampling procedure from Paragraph 3.1.6. They used a stainless steel water-cooled probe having a 2 mm aperture introduced axially into the flame through the stabilisation plate. The soot collected from the probe walls, a Teflon filter and an ice-cooled trap placed downstream in the sampling line is recovered, extracted with dichloromethane, and the solution is used to prepare the LDI/TOF-MS sample.

In this work the soot has been extracted by means of a quartz probe having a 0.8 mm aperture axially introduced into the flame through the stabilisation plate (Paragraph 4.2.2). The sampling line temperature was set to 240 °C according to Paragraph 6.1.3. The collected soot is deposed on the surface of borosilicate filters which are LD/LI/TOF-MS analysed without further treatment except the cooling with liquid nitrogen down to -160°C. The flame is so sooty that after a few seconds sampling the filters are covered by a thick layer (about half a millimetre) of soot, and after less than 30 seconds sampling the probe blocks. The soot layer obtained this way is thick enough that does not make any sense to distinguish between soot directly deposed on a neat borosilicate surface and soot deposed on activated carbon. Soot has been collected without dilution during the sampling in order to match Apicella's conditions. For this reason, the detected PAH are expected to come from both the gas phase and the phase adsorbed on soot.

6.2.1. Collected mass spectra and literature reference

The mass spectra presented in this Section have been obtained from soot collected in the middle of the flame sooting region (14 mm HAB). The full range mass spectrum is presented in Figure 6.6 on the next page. It has been obtained averaging the data acquisitions of four different positions on the surface of the same sample, where each of them is the average of the first five laser pulses of the signal decay.
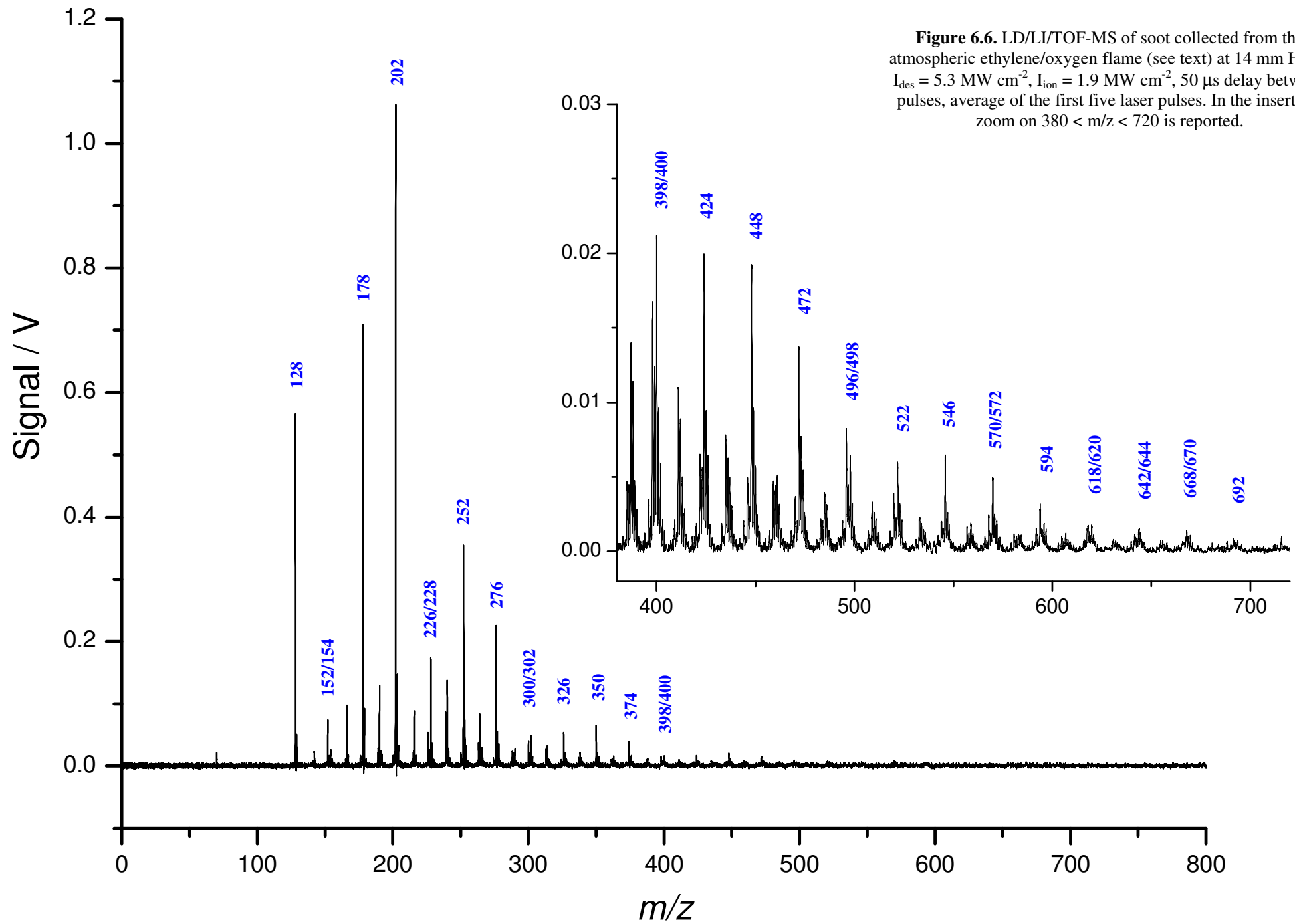
Figure 6.6. LD/LI/TOF-MS of soot collected from the atmospheric ethylene/oxygen flame (see text) at 14 mm HAB. I_{des} = 5.3 MW cm^{-2}, I_{ion} = 1.9 MW cm^{-2}, 50 μs delay between pulses, average of the first five laser pulses. In the insert the zoom on 380 < m/z < 720 is reported.

The mass analyses have been performed under constant experimental conditions of temperature (T = -160°C) and pressure (p = $6 \cdot 10^{-9}$ torr). The laser irradiances were set at: I_{des} = 5.3 MW cm^{-2} and I_{ion} = 1.9 MW cm^{-2}. The spectrum presented in the insert of Figure 6.6 is a second data acquisition, obtained in the same experimental conditions described above except the higher vertical sensitivity of the oscilloscope in order to get information on the high-mass side of the mass spectrum. For this vertical sensitivity the peaks in the range m/z < 276 are all saturated. The spectra obtained analysing different regions of the same sample are reproducible. The standard deviation of the peak intensity calculated from the average of four different acquisitions on the same sample goes from 8% for light masses (178 u) up to 20% for heavier masses (594 u) in the worst case. On the other hand the degree of reproducibility of different filters is lower, and the standard deviations rise up to the 40% of signal for light masses.

In Figure 6.7 the comparison between the mass spectra published by Apicella and co-workers, available for masses heavier than 300 u [76], and that obtained in this work is reported. The vertical scale of the former has been expanded in order to make the visual comparison easier.
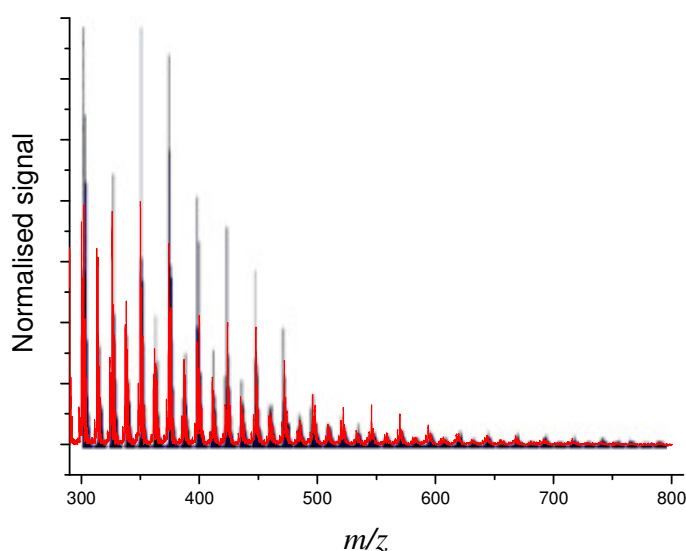

Figure 6.7. Mass spectra obtained from soot sampled from the ethylene-oxygen rich flame described in the text. Comparison of the mass spectra obtained in this work (red line) with those obtained by Apicella and co-workers (blue line).

The matching between the two spectra is satisfying. The mass sequence is the same, and the progressions of the relative peak intensities are very similar. On the other hand, caution must be paid when comparing the absolute peak intensities. As already discussed in Chapter 3, the analytical response of each photoionisation mass spectrometry setup is unique, and small variations in the experimental parameters potentially lead to very different mass spectra. However, in this specific analysis it is noteworthy that the mass spectra look this similar despite the different ionisation conditions and sampling procedure.

Apicella's and co-workers worked at the ionisation wavelength of 337 nm, while in this work a 266 nm has been chosen. Unfortunately the comparison for m/z < 300 was not possible because the published spectra focus on the high-mass side of the detected series of PAH. A second crucial conclusion is that the sampling procedure chosen in this work does not critically affect the mass sequence or the relative peak intensities.

6.2.2. Identification of the precursor ions: C-H diagrams

Several experimental evidences assure that the detected signals belong to PAH, thus it is possible to associate to each mass a C_nH_m molecular formula. Among those evidences, it is useful to remember the analyses performed by Dobbins and co-workers on deuterated fuels and the correspondence of the main mass sequence with Stein and Fahr's stabilomers (Paragraph 3.1.6), and the consistency with the pure PAH ionisation conditions and the observed dissociation pathways (Section 5.3).

A convenient way to represent the whole set of data is that formerly adopted by Homann and co-workers [4,11], in which all the detected masses are reported in a C-H diagram. In a C-H diagram each molecular formula C_nH_m is plotted as one point in the space (n, m). The totality of points represents the ensemble of PAH with different molecular formulae. Alternatively, it is possible to represent (m/n, n), i.e. to plot the H/C ratio in the y-axis instead of the H-number. Following these two representations, the mass sequence of the spectrum in Figure 6.6 is reported in Figure 6.8 below.
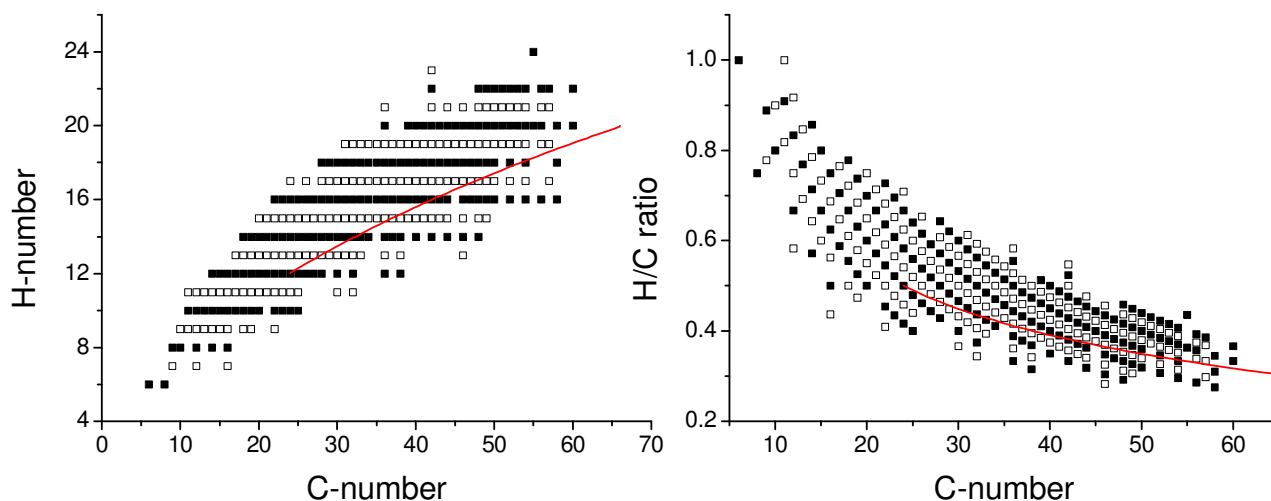

Figure 6.8. C-H diagrams representing the H-number (left) and the H/C ratio (right) versus the C-number in the ensemble of the molecular formulae observed. Full dots: even masses. Open dots: odd masses. The red line fits the peri-condensed 6-rings PAH (see Paragraph 6.2.3 for further details).

In the collected mass spectra the signal peaks always appear in groups, where each of them is characterised by a few strong peaks due to the PAH precursor ions occurring together with a number of satellites. These satellites are often measure artefact due to the isotopologue ions and to the very beginning of dissociation (Section 5.3). They occur at integer nominal mass, and they are spaced by an integer mass number from the main peaks as shown in Figure 6.9.

The critical interpretation of the mass spectra requires the distinction of the peaks due to the precursor ions from the satellite peaks due to the measure artifacts and the exclusion of the latter. Evidently the problem of recognising the measure artifacts rises when treating masses in the same group of signals. While it is easy to identify precursor ions having different C-number (their masses are at least 12 u-spaced), the situation is far less clear when precursor ions having the same C-number but different H-number are involved. In fact in this case the mass spacing due to different

H-number PAH is easily misled with the isotopologue ions or early dissociation phenomena. The identification of the precursor ion peaks is straightforward for the light masses, where only one H-number is allowed for the same group of signals, i.e. only one molecular formula exists. On the other hand the identification becomes difficult when high-mass PAH are involved, because of the large number of detected satellite peaks as well as the difficulty of finding out reference mass spectrum.

However, since the number of masses attributable to PAH for a well defined C-number is still reasonably small (1-3 H-number for each C-number up to 800 u), it is possible to invoke the natural occurrence of carbon as a strong argument to predict the shape of a group of signals. In a mass spectrum, the isotopologue ions appear as series of peaks whose relative surfaces (intensities) match the natural abundance of the isotopes. Carbon has only two stable isotopes, ^{12}C (98.93%) and ^{13}C (1.07%) and the contribution of hydrogen's isotopes is negligible, and therefore the expected peak intensities can be easily calculate using a binomial distribution. The probability $pr(k)$ to get k ^{13}C in a molecule containing n carbon atoms is given by:

$$\mathrm{pr}(k) = \binom{n}{k} p^k (1-p)^{n-k} \qquad (6.1)$$

where p is the natural occurrence of ^{13}C. Once known the C-number n, $pr(k)$ vs. k gives the predicted peak sequence. For instance, from Equation (6.1), a C_{50} PAH has ~60% of probability of containing only ^{12}C, ~30% of containing one ^{13}C, and ~10% of containing two ^{13}C. In a mass spectrum it would appear as a series of three peaks spaced by one unit mass having relative intensities 60-30-10. Whether the calculated and observed distributions do not match, a perturbation induced by another precursor ion having the same C-number but different H-number occurs. Therefore, it is possible to take advantage from the calculated isotopic distribution to identify the precursor ions having different masses but contained in the same group of signals.

An example is reported in Figure 6.9. The C_{10} group only admits PAH having molecular formula $C_{10}H_8$ (128 u), and there is no other existing PAH closer than 12 u to the mass 128 u. The expected intensity distribution of the detected peaks (green histogram) perfectly matches the observed one (black line) as shown in Figure 6.9 (a). On the other hand, when considering masses heavier than about 300 u the peak intensity distributions are often different than the calculated one.
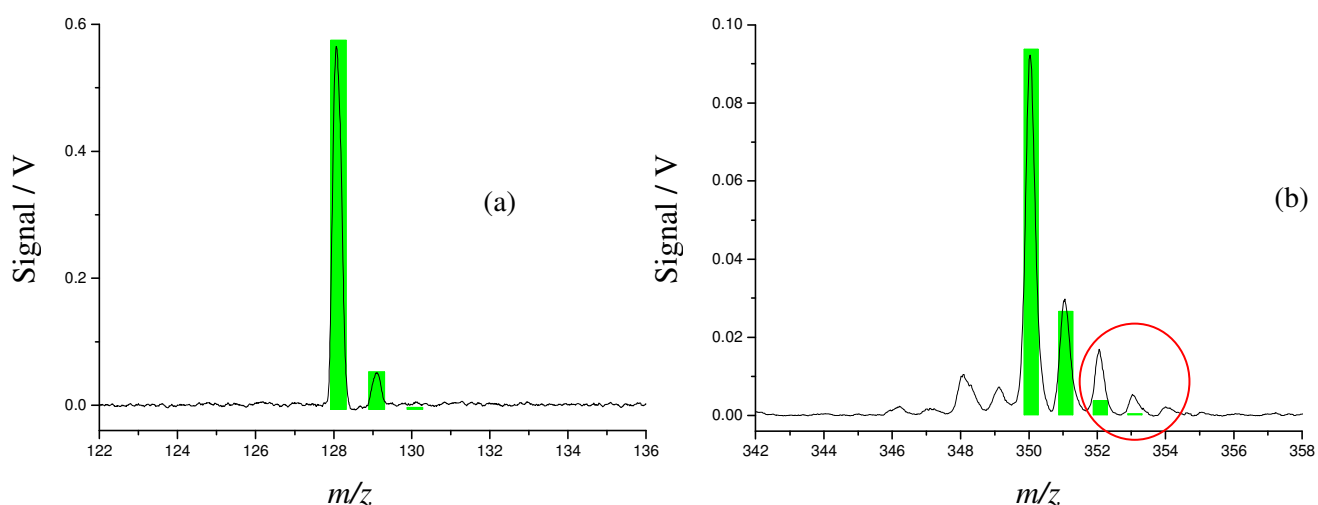

Figure 6.9. Zoom on the 128 u (a) and on the 350 u (b) signal peaks of the mass spectrum reported in Figure 6.6. Solid black line: experimental mass spectrum. Green histogram: expected peak intensities calculated using Equation (6.1).

For instance, the case of the mass 350 u is shown in Figure 6.9 (b): the highlighted M+2 and M+3 peaks are much stronger than predicted, indicating the mass 352 u as a probable candidate for a PAH precursor ion. A cross-comparison with the NIST database [84] confirms that 352 u is a possible mass for PAH, thus the presence of the 352 u as an independent mass must be accounted.

By the way, the presence of another molecular ion having 352 u mass would even give an explanation for the stronger than expected peak at 351 u. Its unusual intensity would be given by the sum of the M+1 of the 350 u (from ^{13}C), and the M-1 of the 352 u (from hydrogen elimination). Since the 352 u is far weaker than the 350 u, its contribution to the 351 is weaker as well.

Finally, it is easier to determine whether a mass comes from a precursor ion or is the product of hydrogen elimination. If a peak signal disappears when lowering the ionisation irradiance, it can be unambiguously attributed to hydrogen elimination phenomena. This is the case of the peak signals 346-349 u in Figure 6.9 (b).

6.2.3. Comment on the mass sequence

Once the artifact peaks have been identified and discarded, the remaining signal peaks are those representative of the mass sequence of the PAH detected in the sample. The representation of the data in a simplified C-H diagram is a very powerful tool to begin the discussion on the mass evolution. Indeed it allows a focus on the mass sequence regardless of the peak intensities which are subject to signal fluctuations. The simplified C-H diagrams representing the main masses sequence detected in the ethylene flame at 14 mm HAB is shown in Figure 6.10. As expected, it is considerably narrower than the complete mass sequence reported in Figure 6.8.
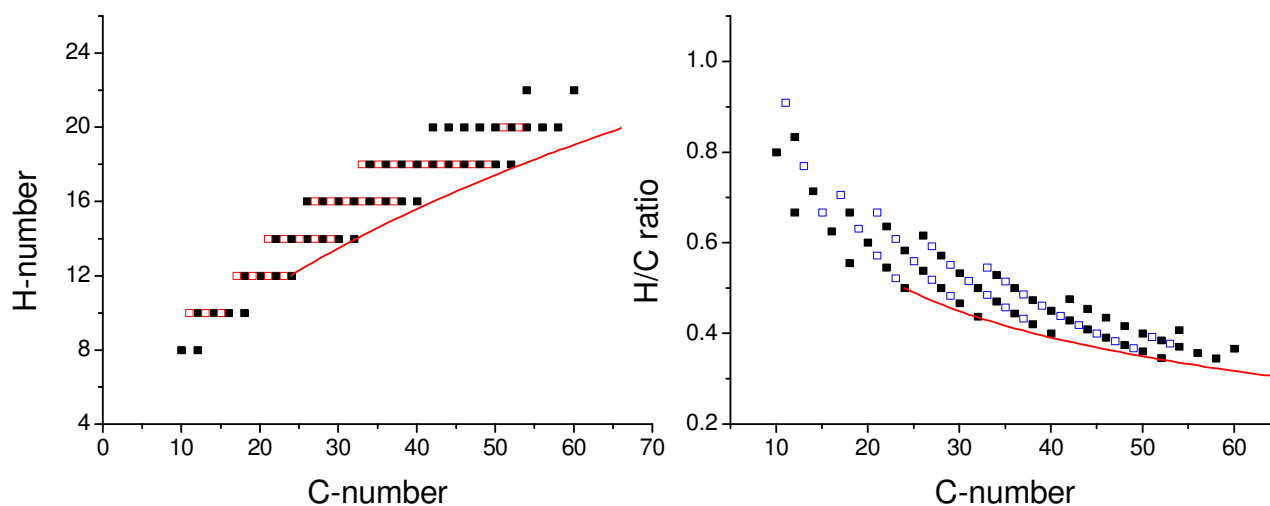

Figure 6.10. Simplified C-H diagrams, in which the satellite signals have been discarded. The graphs represent the H-number (on the left) and the H/C ratio (on the right) vs. the C-number in the ensemble of molecular formulae observed. Full black dots: even C-number PAH. Open blue dots: odd C-number PAH. The red line fits the peri-condensed 6-atom rings PAH (see text for further details).

Although the LD/LI/TOF-MS diagnostic is not isomer-selective when analysing PAH adsorbed on soot (Section 5.2), important information on the PAH growth are contained in the mass sequence regardless the isomeric composition.

The main mass sequence shows a considerable good agreement with other experimental data available in the literature [5,6,46,72,77]. The masses belonging to the main mass sequence and corresponding to even C-number molecular formulae are all consistent with those of Stein and Fahr's stabilomers discussed in Paragraph 2.1.2, as shown in Figure 6.11. Furthermore the largest part of the observed masses lies on the middle of the staircase curve, where the 6-atom rings PAH are located as well. Such a good agreement is not only found in the case of the ethylene flame, but in all the analysed flames, revealing a noteworthy little dependence of the masses constituting the main mass sequence to the flame conditions. The detected PAH lie on a staircase curve and constitute a very regular sequence from 78 u (benzene, C_6H_6) up to 742 u ($C_{60}H_{22}$). Each group of signals corresponds to a different C-number, and it is 10, 12 or 14 u spaced from its closest neighbours. In the main mass sequence the H-number increases slower than the C-number, evidencing the progressive enrichment in carbon of the high-mass flame-formed PAH.
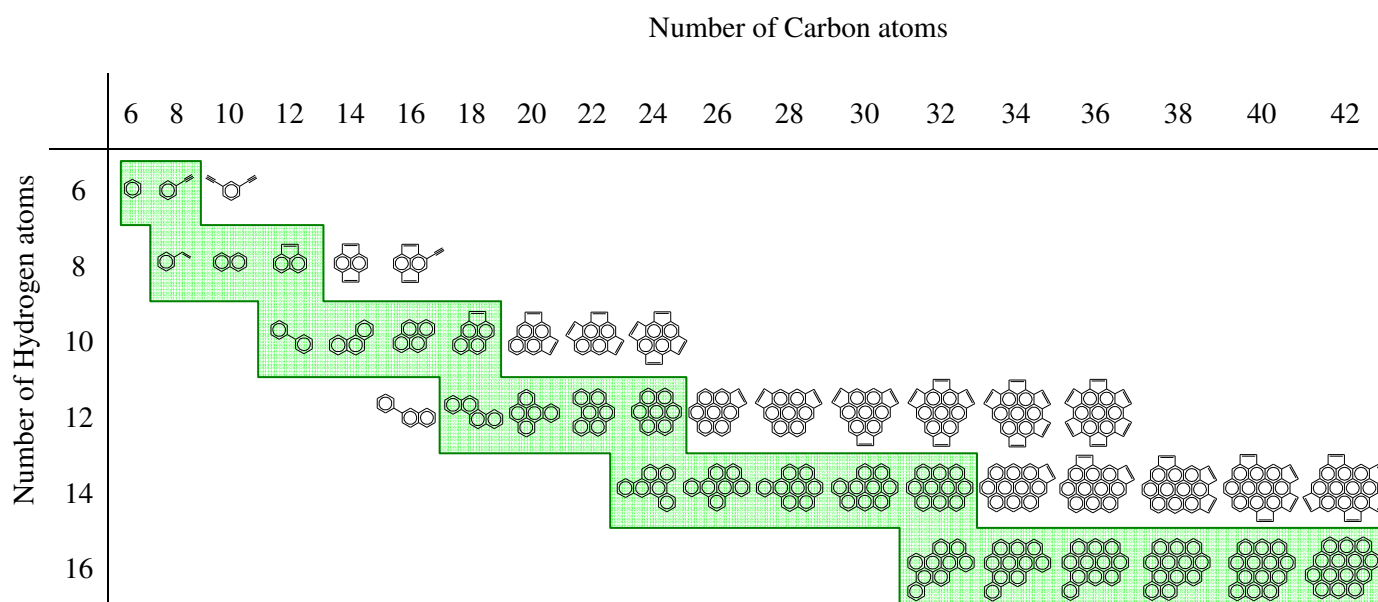

Figure 6.11. Stein and Fahr's stabilomer grid [28]. The green-highlighted PAH structural formulae have mass consistent with the experimentally observed main mass sequence.

The precursor peak intensities corresponding alternately to even and odd C-numbers have intensities of the same order of magnitude, while the odd C-number PAH show peaks clearly weaker than that of even C-number PAH.

A fairly important role in the growth of PAH is possibly played by the peri-condensed 6-atom rings PAH. As shown in the scheme below, these molecules contain only 6-atom rings and they are the most compact structures among all the PAH having the same C-number. In other words they possess the structure having the minimum H-number for a certain C-number, and for this reason they are expect to lie on the lower side of the PAH distribution. When looking Figure 6.10 (a) and Figure 6.10 (b), the 6-atom rings peri-condensed sequence (red solid line) seems to fit very well the lower limit of the experimental distribution when the C-number is bigger than twenty-four. This
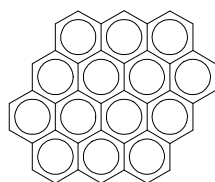
observation suggests that the growth process of PAH at a certain point switches from a low-mass regime dominated by open and side-substituted structures to a high-mass regime controlled by more compact and graphitic-like PAH.
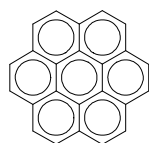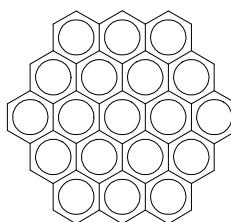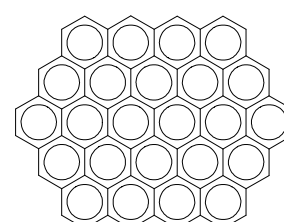
Coronene
$C_{24}H_{12}$ (300 u)
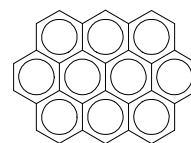
Ovalene
$C_{32}H_{14}$ (398 u)

Circumpyrene
$C_{42}H_{16}$ (520 u)

Circumcoronene
$C_{54}H_{18}$ (666 u)

Circumovalene
$C_{66}H_{20}$ (812 u)

6.3. Low pressure methane flame

In this Section the LD/LI/TOF-MS characterisation of a sooting methane low-pressure flame is presented. The low pressure flames are convenient system to study since all their reaction zones are expanded, thus it is easier to gain access to the different layers with considerably high spatial resolution. To the best of our knowledge LD/LI/TOF-MS analyses of the chemical phase adsorbed on soot have never been performed on low-pressure flames. Only Grotheer and co-workers performed similar analyses on 13.0 kPa a flame using a molecular beam-based technique.

The studied flame is a low pressure, premixed, laminar, methane/oxygen/nitrogen, having $\phi = 2.32$ and total flow $Q_T = 4.35$ slpm. The mole fractions are:

$$CH_4 : O_2 : N_2 = 0.462 : 0.398 : 0.140$$
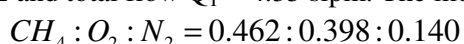
The flame is stabilised at 26.66 kPa in a stainless steel vessel. The adopted burner is a commercial McKenna, whose central area is a water-cooled sintered porous bronze plug fed with the premixed fuel/oxidiser mixture. The setup is detailed in Paragraph 4.2.3.

The LD/LI/TOF-MS characterisation of this flame is a complement to in-situ analyses performed via Laser Induced Incandescence (LII) for the determination of the soot volume fraction, and jet-cooled Laser Induced Fluorescence (LIF) for the determination of PAH mole fraction profiles (benzene and naphthalene were already available at the time of this work). Particularly, the knowledge of the soot volume fraction profile has proven to be a very useful tool for the choice of the Height Above the Burner (HAB) locations to be sampled. Nine different locations on the flame axis as a function of the HAB have been sampled, covering the transition from the PAH zone up to the beginning of the soot inception and to the soot oxidation zone. The C-H diagrams have then been used to compare the masses of the detected PAH.

Furthermore, the LD/LI/TOF-MS analyses of the combustion products deposed on adsorbing and non-adsorbing substrates (neat borosilicate filters and filters covered by activated carbon) have been compared. The interest in performing such a comparison lies in the complex interactions occurring between the species in the gas phase and those adsorbed on the soot particles (see Section 6.1).

The text is organised as follows. The first sections explain the flame sampling conditions, describing the LII preliminary measures performed in order to obtain the soot profile of the flame. The other sections contain the results obtained for each different kind of soot sampling/deposition (soot directly deposed on a blank filter and on activated carbon). The results are organised to emphasise any trend as a function of the sampling HAB and different deposition methods.

6.3.1. LII preliminary analysis and flame sampling

In order to handle the sampling the soot volume fraction profile of the flame is required. To this purpose LII analyses have been performed in this work: the obtained soot volume fraction profile is presented in Figure 6.12, while the LII theory is briefly described in Appendix B. Additionally, the mole fraction profile of naphthalene is also reported in Figure 6.12, in order to locate the beginning of the soot inception relatively to the gaseous soot precursors. Naphthalene profile was determined by jet-cooled LIF [129]. The flame temperature profile has been obtained by atomic fluorescence thermometry[4].
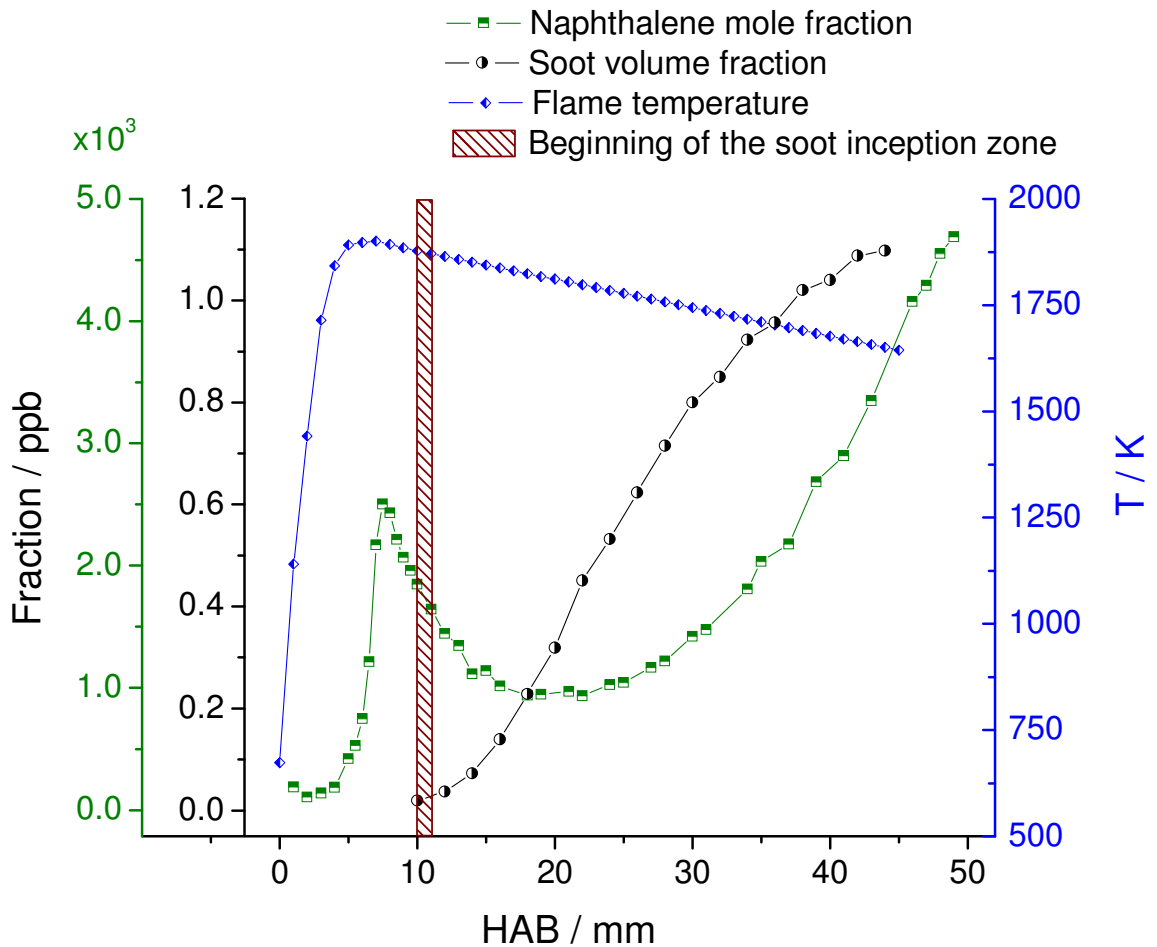

Figure 6.12. Soot volume fraction obtained from LII (black series), naphthalene mole fraction obtained from jet-cooled LIF (gren series) and termperature obtained via atomic fluorescence thermometry (blue series) vs. sampling HAB of the low-pressure methane flame. The beginning of the soot inception zone at 10-11 mm HAB is highlighted in the brown box. In the underlying image the corresponding flame region has been reported.

The beginning of the soot inception zone, corresponding to the very first detected LII signal, is located in the region 10-11 mm HAB. After the beginning of the soot inception, the soot volume fraction sharply rises from the noise level, passes through an inflection point at 22 mm HAB, and eventually flattens and comes to a plateau at 40-50 mm HAB. The presence of the plateau is due to the reduction of the soot growth rate occurring high in the flame.

The profile of naphthalene (128 u) obtained via jet-cooled LIF suddenly rises at 5 mm HAB, passes through a local maximum at 7.5 mm HAB, decreases to a local minimum located around 20 mm HAB and finally rises again in the highest regions of the flame. At the time of those measurements the mole fraction profile of benzene was available as well, but it has not been reported in Figure 6.12 for clarity of interpretation, being very similar to that of naphthalene.

The sampling has been performed at several different HAB, to cover both the regions before and after the beginning of the soot inception. 5, 7, 9.5, 10, 11, 12, 15, 20, 40 and 60 mm HAB have been sampled. The probe whose aperture is 0.8 mm has been introduced axially into the flame to minimise any flow perturbation. The sampling line temperature was set to 240 °C according to Paragraph 6.1.3. Soot has been collected during a time period of 30 min, and deposed on the surface of both neat borosilicate filters and filters covered with a layer of activated carbon, in order to trap both the solid and gaseous matter. Each HAB has been doubled or tripled to give a reproducibility measure. The reproducibility is always good when analysing the surface of the same filter, but it is slightly worse when analysing different samples. Standard deviations are around 50% of the peak signal in the worst case.

Before concluding this discussion it is important to notice that the spatial resolution of the extractive sampling and the LII measurement is not necessarily the same. Though the positioning uncertainty of the probe in the flame is less than 0.1 mm, the sampling volume is estimated as twice the diameter of the probe aperture [113], i.e. 1.6 mm in all the measurements performed on the low-pressure flame (Paragraph 4.2.5).

6.3.2. LD/LI/TOF-MS analysis

This section contains the set of mass spectra obtained by analysing gases and soot condensed and deposed on the surface of neat filters and in parallel on a layer of activated carbon. The full range mass spectra are presented in Figure 6.14 (deposition on a neat filter) and in Figure 6.15 (deposition on activated carbon) at pages 138 and 139. The inserts contain the zooms on the high-mass region of the spectra.

The mass analyses have all been performed under constant experimental conditions of temperature (T = -160°C) and pressure (p = $6^.10^{-9}$ torr). The laser irradiances were set at: I_{des} = 5.3 MW cm^{-2} and I_{ion} = 1.9 MW cm^{-2}. All the mass spectra reported in this work are the average calculated on four mass spectra obtained from different locations on each filter surface. Each of these points is the average calculated on the first five laser pulses of the signal decay.

The main mass sequence shows a good agreement with other experimental data available in the literature [5,6,46,72,77], and the even C-number masses are all consistent with Stein's stabilomers where the calculations are available (Paragraph 6.2.3). The detected PAH constitute a regular sequence from 78 u (benzene, C_6H_6) up to 642 u ($C_{52}H_{18}$) when depositing on a neat filter, and up to 792 u ($C_{64}H_{24}$) when depositing on activated carbon. The structure of the mass spectra is much close to that of the ethylene flame discussed in the previous Section 6.2. The peaks recur to groups

10, 12 or 14 u spaced from its closest neighbours, and each of them corresponds to PAH having different C-number. In the main mass sequence the H-number increases slower than the C-number.

The mass spectra obtained from sampling on non-adsorbing substrate (neat filter) are reported in Figure 6.14. Below the beginning of the soot inception (5 and 7 mm HAB), the gases do not condense on the filters, which are still blank after the sampling, and no LD/LI/TOF-MS signal is detected. The mass spectra obtained from samples collected at 9.5 and 10 mm HAB look very similar, with all the masses except 202 u almost at noise level (SNR~3). Nevertheless, it is possible to recognise some PAH peak signals in the range 200<m/z<300, and up to 15 mm HAB they only increase in intensity without giving rise to any detectable heavier mass. The filters appear pale yellow-coloured. The spectra collected at 12, 15 and 20 mm HAB are critical since striking differences exist between the two deposition modes. When depositing on neat filters, no peak signals are detected for m/z>300 at 12 and 15 mm HAB, and at 20 mm HAB weak signal peaks (~2 mV, SNR~10) appear for 300<m/z<522. The filters collected at 12 mm HAB are pale gray/yellow coloured, but they turn gray at 15 and 20 mm HAB. The mass spectra obtained from samples collected higher in the flame (40 and 60 mm HAB) are always dominated by the masses in the range 78<m/z<300, but the peak signals for m/z>300 become more and more intense with respect to the low-mass side of the mass spectra. The filters collected at both 40 and 60 mm HAB are dark grey. In this range the heaviest detected mass gently approaches its final value of 642 u.

The mass spectra obtained from sampling on adsorbing substrate (activated carbon) are reported in Figure 6.15. Below the beginning of the soot inception (5 and 7 mm HAB) strong peak signals in the range 78<m/z<300 are detected, indicating the presence of PAH in the gas phase which have been adsorbed on the carbon. The strongest signals correspond to the masses 128 u and 202 u. At 9.5 and 10 mm HAB peak signals in the range 78<m/z<300 are detected once again, and the mass spectra are dominated by the masses 128, 202 and 276 u. The spectra collected at 12, 15 and 20 mm HAB show the most important deviation with respect to the deposition on non-adsorbing substrate. At 12 mm HAB a series of signal peaks in the range 300<m/z<792 suddenly appears. These heavy masses are very characteristic of samples collected high in the flame, well above the beginning of the soot inception zone. The peak intensities are well above the noise level (~20 mV, SNR~100). At 15 and 20 mm HAB this series is still present but it evolves backward, with the heaviest mass of the series decreasing as a function of the HAB. Finally, the mass spectra collected very high in the flame (40 and 60 mm HAB) look quite similar in the two deposition modes. They are dominated by the mass range 78<m/z<300, the peak signals for m/z>300 become more and more intense with respect to the low-mass side of the mass spectra. The heaviest detected mass approaches its final value of 792 u.

6.3.3. Experimental evidences of the PAH growth

An important but sensitive aspect of the measure is the evolution of the peak intensities as a function of the sampling HAB. The direct comparison of the peak intensities has proven to be a very useful way to get information on the PAH growth process occurring into the flame. However, differently than the mass sequence, the peak intensities are subject to fluctuations which can reach up to the 40% of the measured value. Therefore, the direct comparisons are only possible when a high level of reproducibility of the peak intensities is reached. If this condition was not fulfilled (for instance whenever much different amounts of soot are deposed on the filters) a normalisation with respect to a reference mass is required.

Figure 6.13. (Side) Six samples collected at different HAB from the low-pressure methane flame. Picture taken after the LD/LI/TOF-MS analyses.
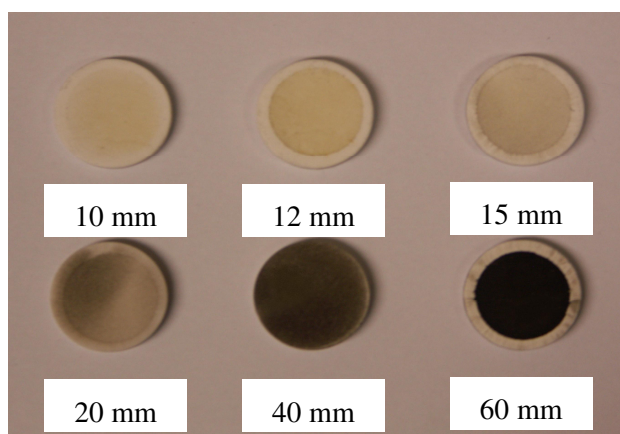
Figure 6.14. (Below) Mass spectra obtained from soot sampled at different HAB and deposed on the neat surface of borosilicate glass filters. In the inserts zooms of the range 300<m/z<600 are reported. I_{des} = 5.3 MW cm^{-2}, I_{ion} = 1.9 MW cm^{-2}, 50 μs delay between pulses. Each mass spectrum is the average of the first five laser pulses of the signal decay. A picture of the samples taken after the mass analyses is reported as well.
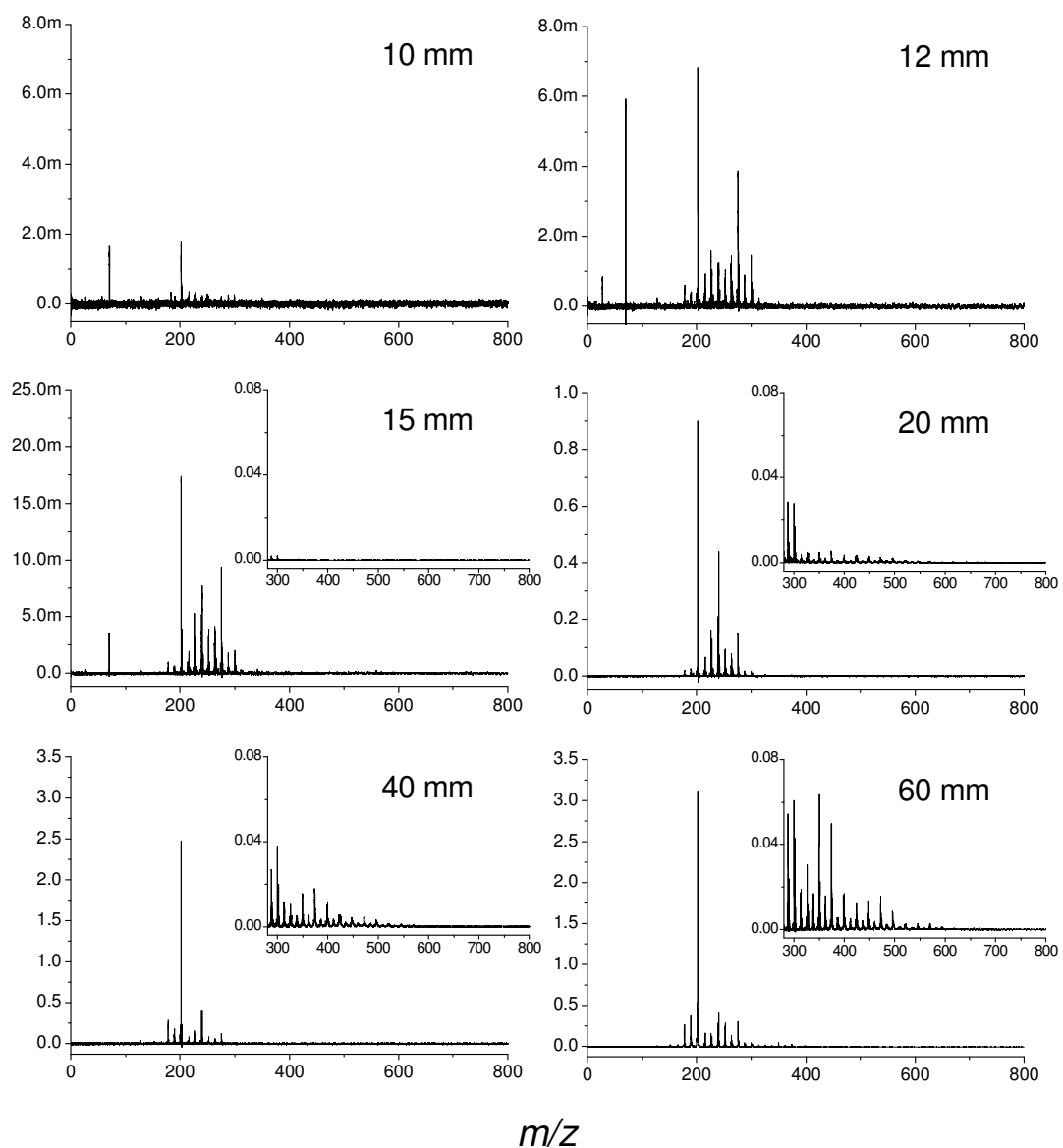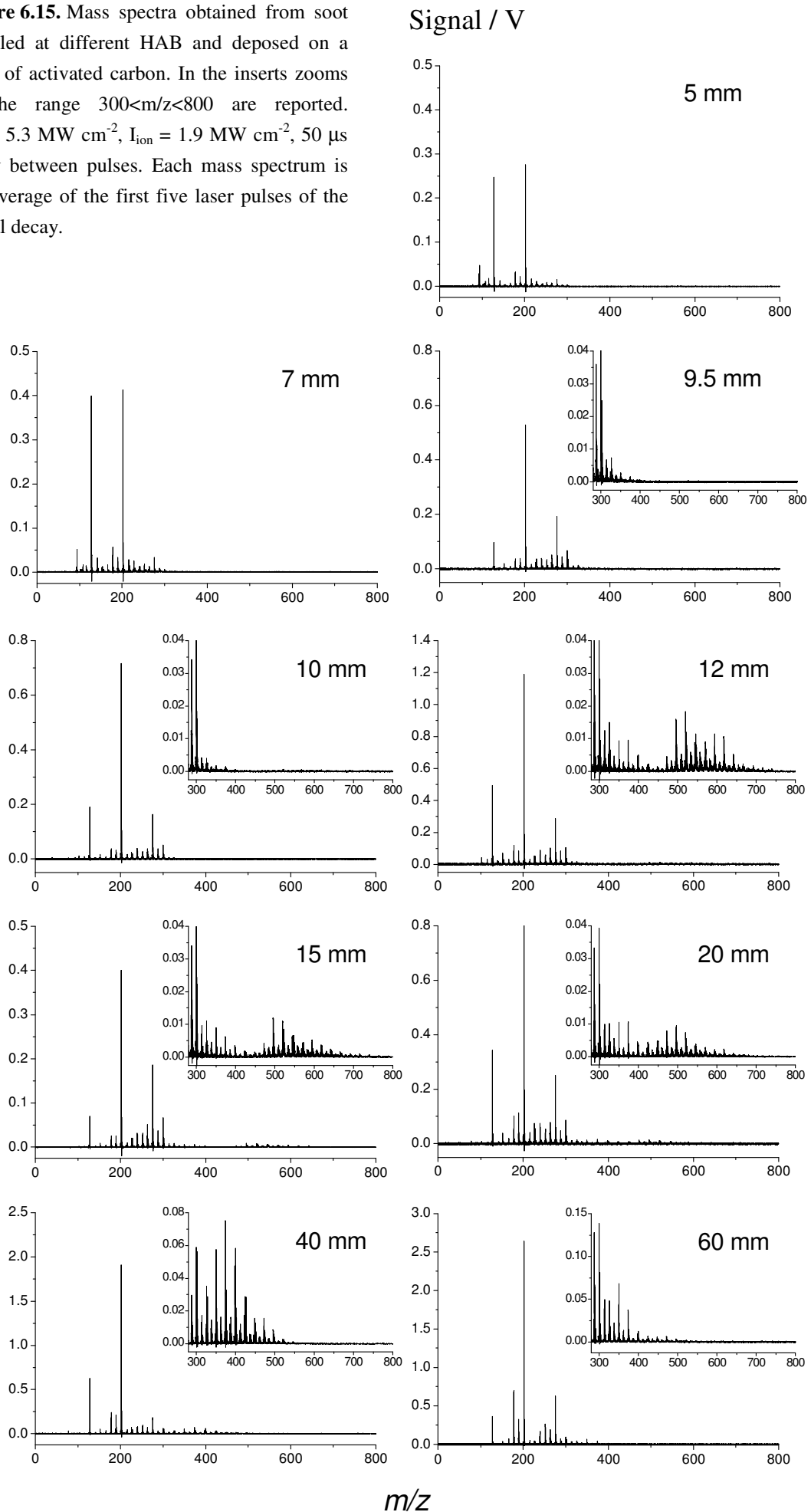

Signal / V

m/z

Figure 6.15. Mass spectra obtained from soot sampled at different HAB and deposed on a layer of activated carbon. In the inserts zooms of the range 300<m/z<800 are reported. I_{des} = 5.3 MW cm^{-2}, I_{ion} = 1.9 MW cm^{-2}, 50 μs delay between pulses. Each mass spectrum is the average of the first five laser pulses of the signal decay.

Deposition on non-adsorbing substrate

In Figure 6.16 and Figure 6.17 the mass spectra obtained from the depositions on neat filters at different HAB are compared. Figure 6.16 focuses on the very beginning of the detected signal at 10, 12 and 15 mm HAB, in the closest region to the beginning of the soot inception (10-11 mm HAB). Figure 6.17 focuses on the soot-rich region of the flame, comparing the mass spectra obtained at 15, 20, 40 and 60 mm HAB.

The rough mass spectra reported in Figure 6.16 all show the same mass sequence (178<m/z<302) and the peak intensities rise proportionally to the HAB. No changes in the mass sequence were observed below 15 mm HAB. In addition (not shown here) the mass spectra have been normalised with respect to the strongest peak (202 u). The intensities of the normalised peaks of different mass spectra well overlap (the intensities are randomly distributed 1.04±0.49), suggesting that the three mass spectra only differ for the amount of substance deposed on the filter.
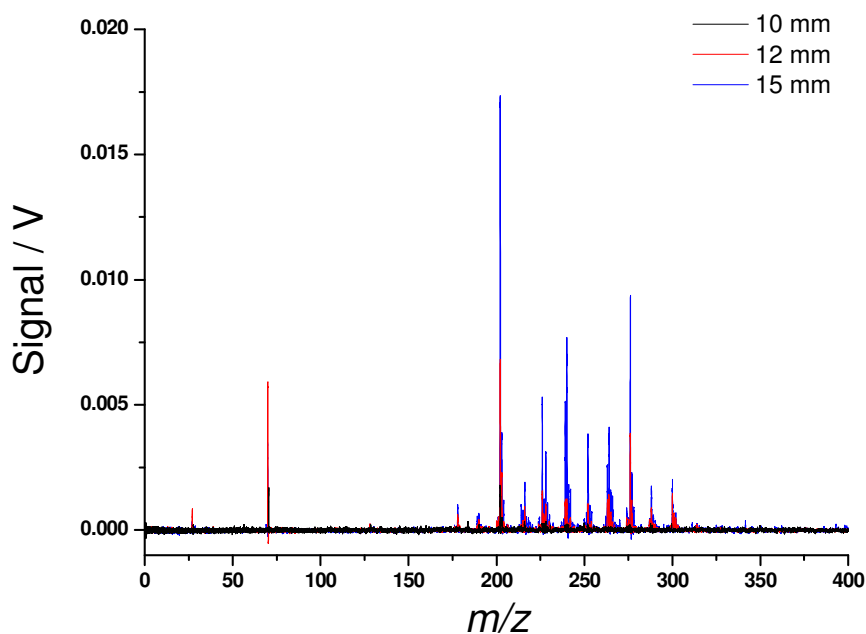

Figure 6.16. Evolution of the peak intensities in the HAB range including the beginning of the soot inception region. Deposition on neat filters. Mass spectra obtained from soot sampled from 10 to 15 mm, zoom on the region of light masses (m/z<300). The peaks at 27 u and 70 u have been attributed to Al$^+$ and Al$_2$O$^+$ from the borosilicate glass.

The mass spectra obtained from samples collected higher in the flame (20, 40 and 60 mm HAB) are compared in Figure 6.17. Two different behaviours have to be distinguished. In the low-mass side of the spectra the mass sequence is identical for all the spectra and it spans the range 78<m/z<300. In the high mass side of the spectra the heaviest detected mass increases as a function of the HAB, evolving from 400 u (C$_{32}$H$_{16}$) at 15 mm HAB up to 642 u (C$_{52}$H$_{18}$) at 60 mm HAB. Furthermore, the peak intensities progressively rise as a function of the HAB, evolving from the noise level at 20 mm HAB up to 60 mV at 60 mm HAB. These observations suggest that the higher is the sampling zone, the heavier are the PAH able to accumulate above the detection threshold of the LD/LI/TOF-MS.

In the mass spectra reported in Figure 6.17 it is particularly evident the alternate succession of strong and weak group of peaks. The stronger peaks always correspond to precursor ions having even C-number and consistent with Stein's stabilomers. The weaker peaks are those of precursor ions having odd C-number.
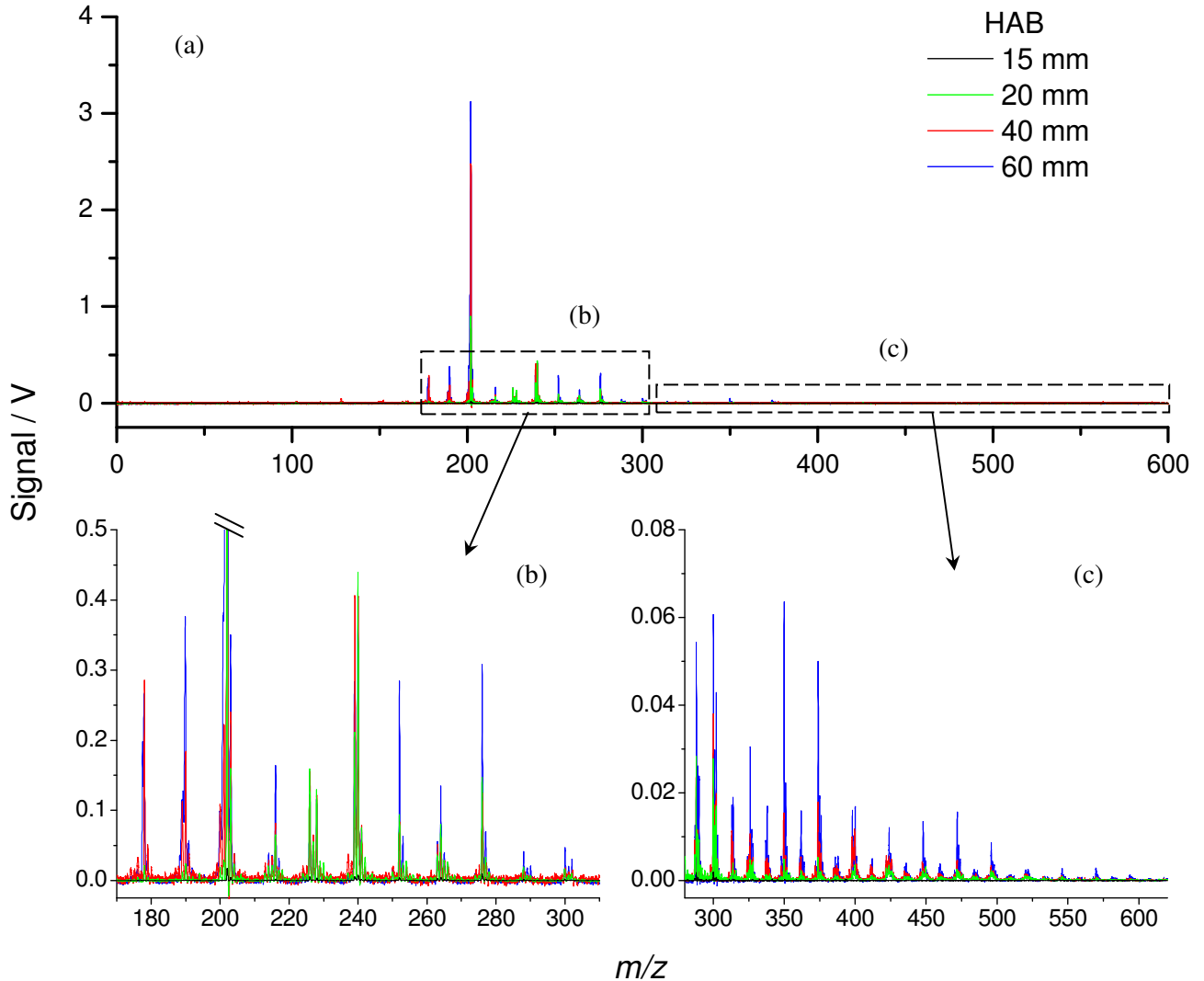

Figure 6.17. Evolution of the peak intensities after the beginning of soot inception region. (a) Full range, (b) zoom on the low-mass side and (c) zoom on the high-mass side. Mass spectra obtained from soot sampled from 15 to 60 mm HAB, zoom on the region of heavy masses (m/z>300). Deposition on neat filters.

Deposition on adsorbing substrate

In Figure 6.18 and Figure 6.19 in the next pages the mass spectra obtained from the depositions on activated carbon at different HAB are compared. In Figure 6.18 the gas-phase spectra at 5, 7, 9.5 and 10 mm HAB are reported, while in Figure 6.19 the soot-rich region of the flame are reported, and the mass spectra obtained at 12, 15, 20, 40 and 60 mm HAB are compared.

Figure 6.18 focuses on the region before the beginning of the soot inception zone, and therefore the masses detected there necessarily come from the gas phase. In those spectra the main mass

sequence is the same except for its low-mass side, which undergoes a gentle evolution from a hydrogen-rich sequence at 5 mm HAB to a hydrogen-poor sequence at 9.5-10 mm HAB. A detailed discussion of this evolution requires the use of C-H diagrams, and therefore it will be postponed to Paragraph 6.3.5. On the other hand, the evolution of the peak intensities is particularly evident. As depicted in Figure 6.18, the superposition of the lower-HAB mass spectra clearly shows the progression from a mass spectra dominated by very light masses (green spectrum) to another one where the contribution of 200<m/z<300 becomes more and more important (red and blue spectra). Only a very few masses above 300 u are visible at 9.5 and 10 mm HAB.
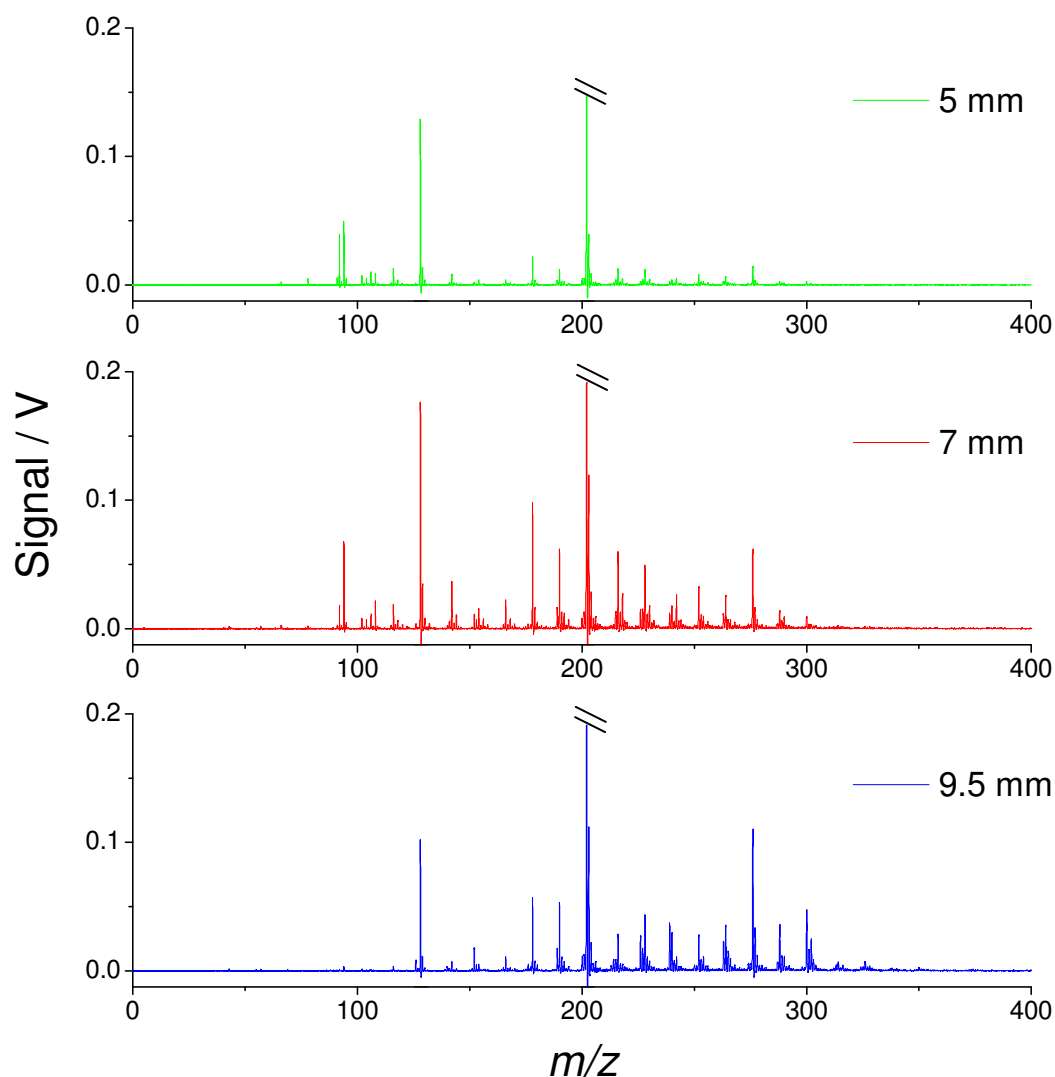

Figure 6.18. Growth of light masses in the HAB range. Mass spectra obtained from soot sampled from 5 to 9.5 mm, zoomed on the region of light masses (50<m/z<350). Deposition on activated carbon.

When directly comparing the high-mass side of the mass spectra at 12, 15, 20, 40 and 60 mm HAB the evolution of the main mass sequence occurring after 12 mm HAB becomes particularly evident. The mass spectra collected at 12, 15 and 20 mm HAB feature two main groups of masses, that are a low-mass sequence spanning the range 78<m/z<398, and a high-mass sequence spanning the range 398<m/z<792. As shown in Figure 6.19 the heaviest mass is detected in the middle of the flame (15 mm HAB) instead of the far end of the flame (60 mm HAB) as in the direct deposition on neat filters. The mass spectra collected higher in the flame show a regression of the main mass sequence from 792 u ($C_{64}H_{24}$) at 15 mm HAB down to 642 u ($C_{52}H_{18}$) at 60 mm HAB. By the way, this second value corresponds to the heaviest detected mass in the deposition on neat filter discussed just above.
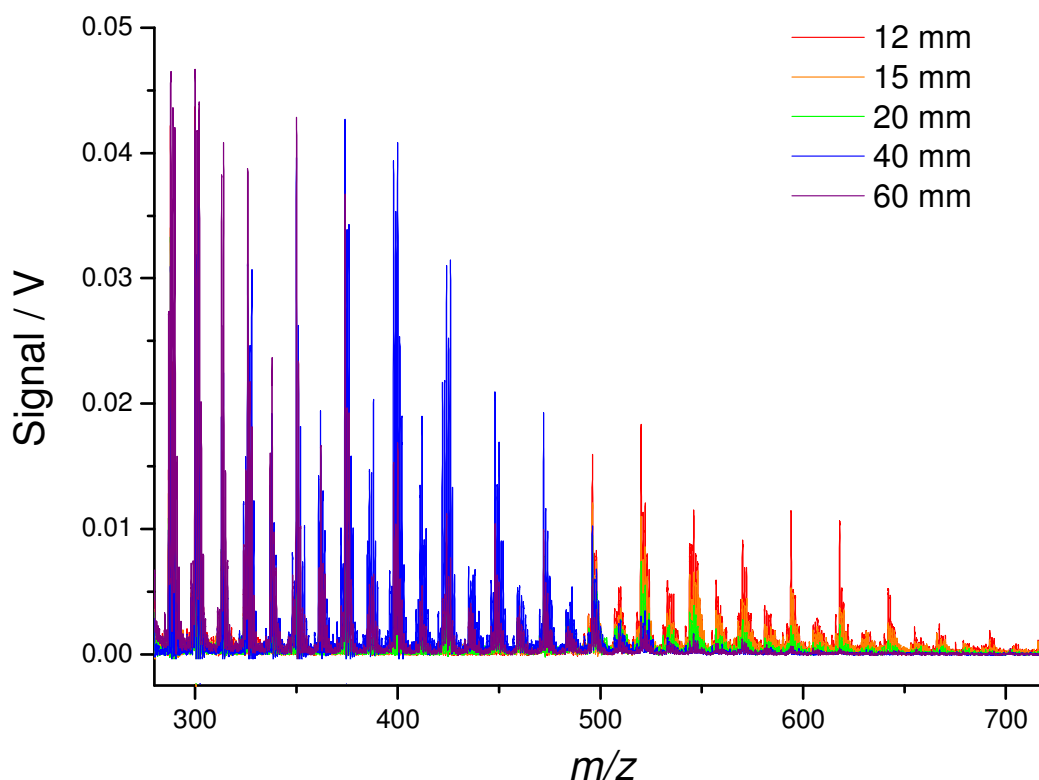

Figure 6.19. Growth of heavy masses from 12 to 60 mm HAB. Mass spectra obtained from soot sampled at different HAB after the beginning of the soot inception zone. Zoom on 480<m/z<750. Deposition on activated carbon.

Figure 6.20 below contains the plots of the peak intensities as a function of the HAB for fifteen selected masses for both depositions. When considering the deposition on a neat filter, the signals generally grow as a function of the HAB. However the trend can be very different, sometimes the signal reaches a plateau after 40 mm HAB or it slightly decreases, and other times the growth looks almost linear.

When considering the deposition on activated carbon, it was not possible to find any regularity. The signal does not clearly grow as in the previous case, and the plateau almost disappeared. The heaviest masses (496, 546 and 618 u) show a signal decrease vs. HAB, accordingly with the backward evolution of the main mass sequence discussed in Paragraph 6.3.5.
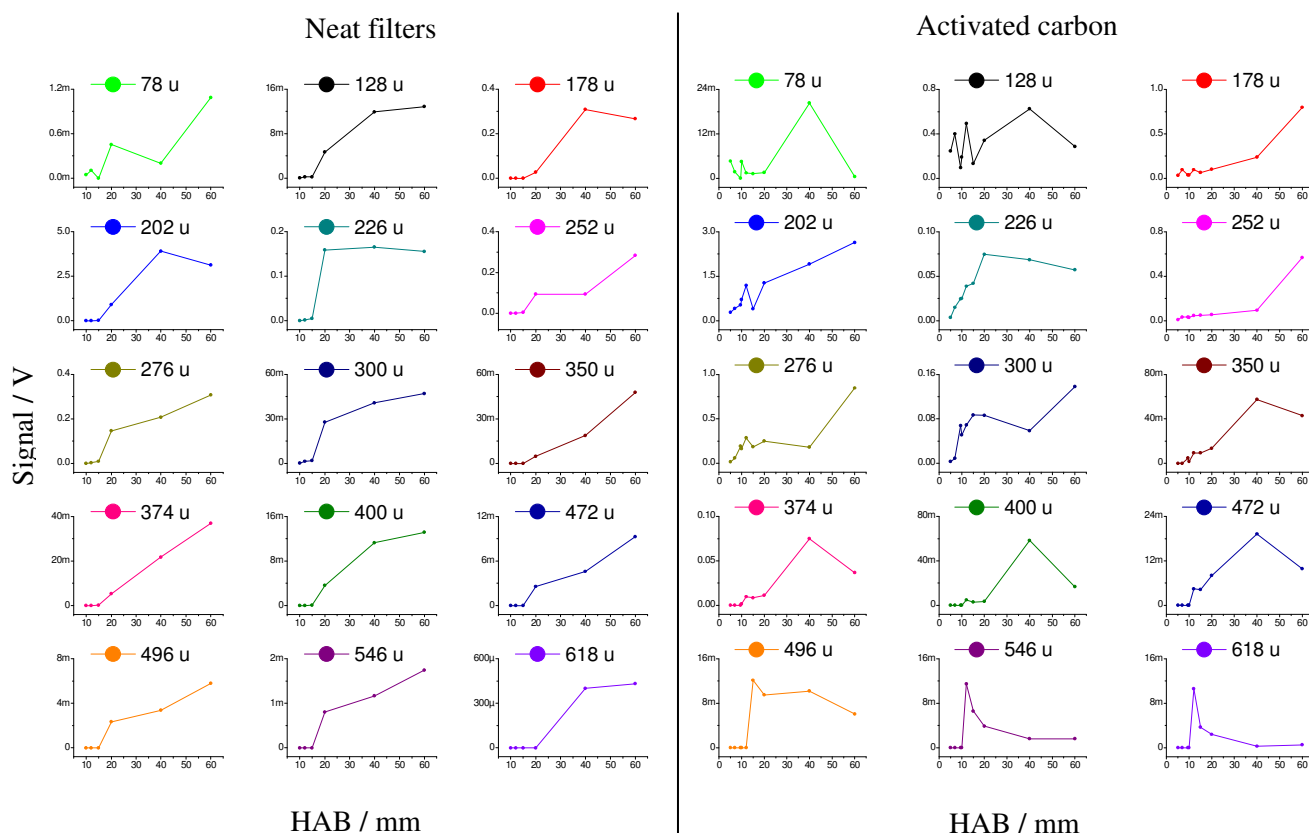
Figure 6.20. Growth of the rough peak intensities as a function of HAB for fifteen selected masses, going from 78 u up to 618 u. Deposition of the combustion products on a neat borosilicate filter (on the left), and on activated carbon (on the right).

To reduce the fluctuations affecting the evolution of the peak intensities, the sum of all the intensities over a certain m/z range has been performed. Six m/z ranges has been chosen: 78-190, 202-302, 314-400, 412-498, 508-594, and 606-742. The obtained series of data have been normalised with respect to 60 mm HAB, plotted as a function of the HAB and compared with the LII profile. The comparison of the six series of data obtained this way for the deposition on a neat filter is reported in Figure 6.21. About the deposition on activated carbon, the trends are far too different to allow any kind of normalisation.

Figure 6.20 confirms that the investigation on the intensity of the signal peaks is difficult particularly when analysing the sample deposition on adsorbing substrate. About the deposition on a non-adsorbing substrate, as shown in Figure 6.21, the signal peak intensities sharply rise as a function of the sampling HAB up to 20 mm, and then they tend to level at 40-60 mm, following the general trend already observed in the soot volume fraction evolution (Section 6.3.1). In this second case the high-masses tend to form later in the flame.
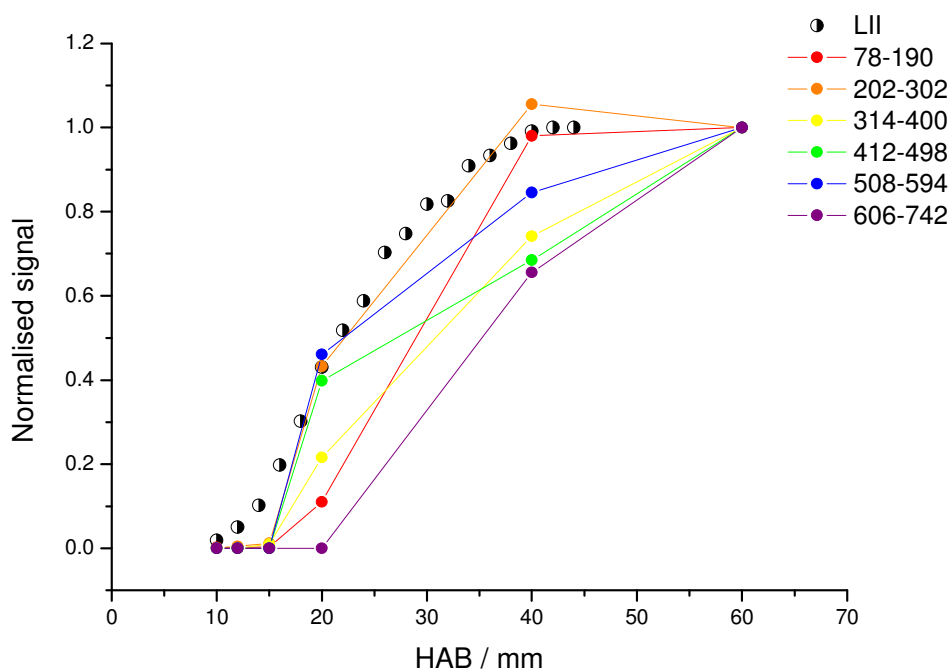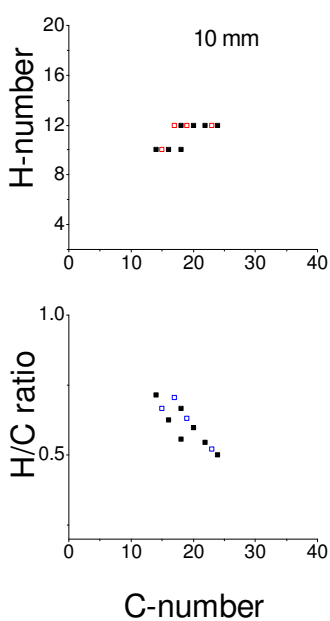
Figure 6.21. Comparison of the normalised LII profile with the normalised sum of peak intensities over six different m/z ranges. Data obtained from a deposition on a neat filter.

6.3.4. Comment on the mass sequence

Once the main mass sequence has been identified as discussed in Paragraph 6.2.2, it is possible to attribute a molecular formula C_nH_m to each detected mass, and build up the C-H diagrams as a function of the HAB.

Figure 6.22 and Figure 6.23 show the C-H diagrams of the samples collected below the sooting inception zone, from 5 up to 10 mm HAB. Figure 6.22 contains the data on the deposition on a neat filter, while Figure 6.23 contains the data collected from deposition on activated carbon.

Figure 6.22. C-H diagrams of the gases collected on a neat filter at 10 mm HAB. Full black dots represent even C-numbers, while empty coloured dots represent odd C-numbers.
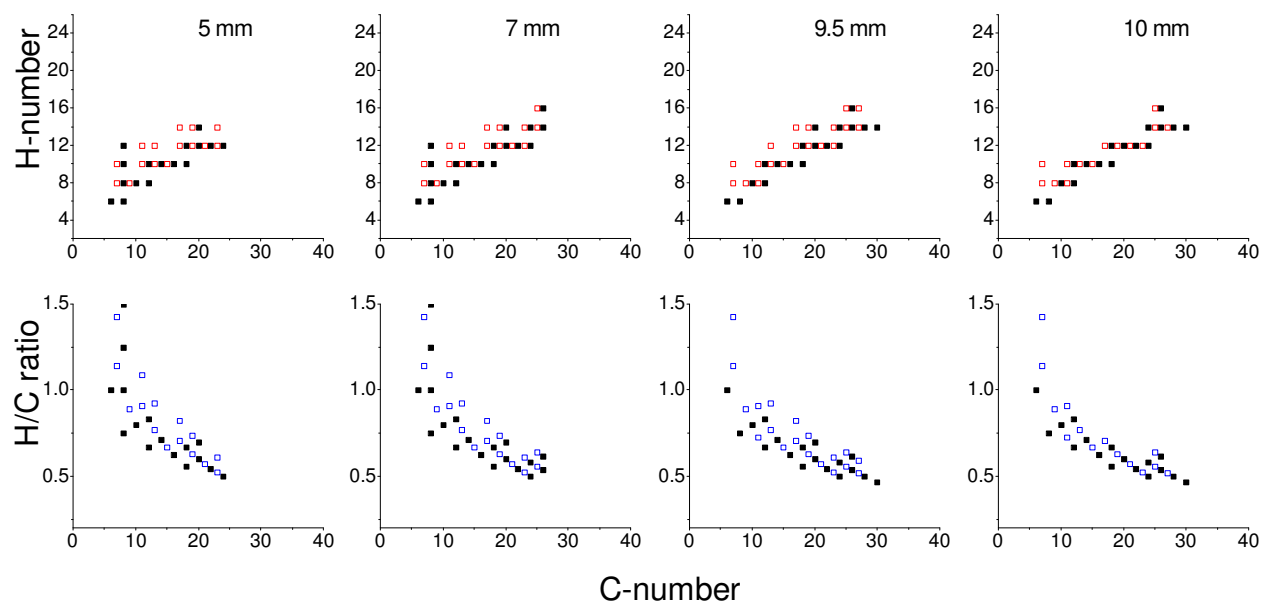
Figure 6.23. C-H diagrams of the combustion products collected on activated carbon for 5<HAB<10 mm. Full black dots represent even C-numbers, while empty coloured dots represent odd C-numbers.

A first interesting observation concerns the structure of the mass spectra of the combustion products collected at 5, 7, 9.5 and 10 mm HAB obtained via deposition on activated carbon (Figure 6.23). Only a slight increase of the heaviest detected mass has been observed, which rises from C_{24} at 5 mm HAB up to C_{30} at 10 mm HAB. In comparison, the C-H diagrams of the deposition on a neat filter (Figure 6.22) are far less rich in light masses than the corresponding on activated carbon (Figure 6.23). The reason is to be sought in the high specific surface of the activated carbon which leads it to efficiently trap low-mass molecules from the gas phase.

Though the C-H diagrams reproduced in Figure 6.23 look quite similar, the low-HAB diagram appears richer in hydrogen-rich species. This fact is particularly evident in the dot distributions presented in Figure 6.23, which is progressively thinner when increasing the HAB. The higher is the HAB, the lesser are the dots on the left side of the data distribution, which correspond to the hydrogen-rich species. On the other hand, the number of dots on the right side of the distribution, which correspond to the carbon rich species, remains unchanged. This observation can be attributed to the progressive reaction of the hydrogen-rich and substituted PAH initially formed, and it can be considered as an evidence of the progressive elimination of hydrogen occurring in parallel with the growth of the flame-formed PAH.

A direct comparison of the mass spectra collected before and after the beginning of the soot inception region reveals a few signal peaks detected at 5 and 7 mm HAB but absent at 10 mm HAB and higher in the flame. Those masses are always right-shifted with respect to those belonging to the main mass sequence, and therefore their corresponding molecular formulae always contain a larger H-number than the precursor ions belonging to the main mass sequence. They span the whole range 90<m/z<240, and each group of signals contains 1-3 of these masses. As example, a comparison of the two mass spectra obtained at 7 and 15 mm HAB in the range 85<m/z<125 has been reported in Figure 6.24.
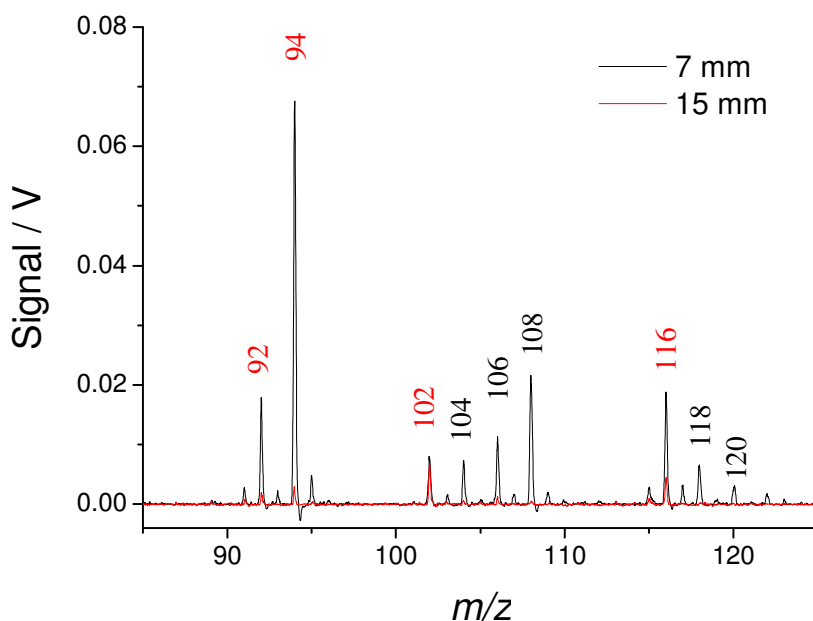
Figure 6.24. Mass spectra obtained at 7 mm (black line) and 15 mm (red line) HAB, soot deposed on activated carbon. Red-labeled masses have been detected in both mass spectra, while black-labelled masses have been detected only at 7 mm HAB.

The detected masses 92, 102, 104, 106, 116 and 118 u are all consistent with structural formulae constituted by aromatics side-substituted by aliphatic chains. On the other hand, the hypotheses on structure of the masses 94, 108 and 120 u involve partially saturated rings or open structures.
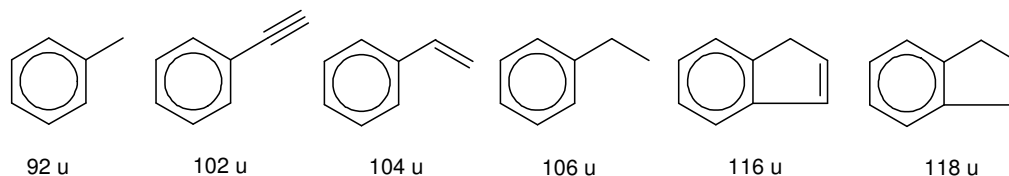
In a number of signal groups, all corresponding to odd C-number PAH, a couple of strong peaks only spaced one unit mass has been observed. Most evident are the low-mass couples 115/116 u and 239/240 u, where 116 and 240 u are masses of precursor ions. Since PAH masses are necessarily even, strong peaks corresponding to odd masses represent an unexpected result. A possible explanation is based on hydrogen elimination reactions leading to ions stabilised by means of an extended resonance with the next aromatic ring. This mechanism works since all the structures for which this phenomenon has been observed correspond to odd C-numbered PAH, whose structure is consistent with the presence of at least one non-aromatic carbon (for instance one $-CH_2-$ group). That kind of structure can easily give hydrogen elimination reactions because the ion obtained from the elimination of one hydrogen atom from a $-CH_2-$ group is stabilised by resonance, as detailed below for the case of indene:

Figure 6.25. C-H diagrams (H-number vs. C-number) of the combustion products collected at different HAB. On the left the deposition on neat filters, and on the right deposition on activated carbon are reported. Full black dots represent even C-numbers, while empty red dots represent odd C-numbers.
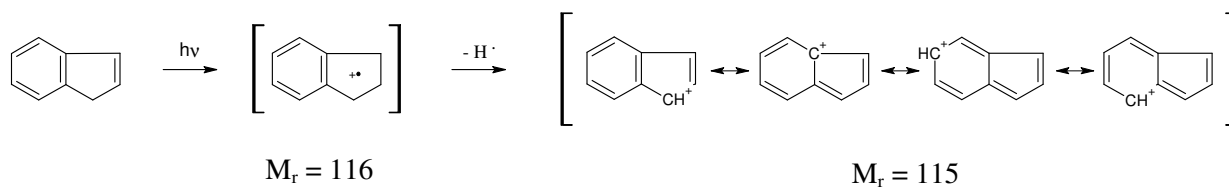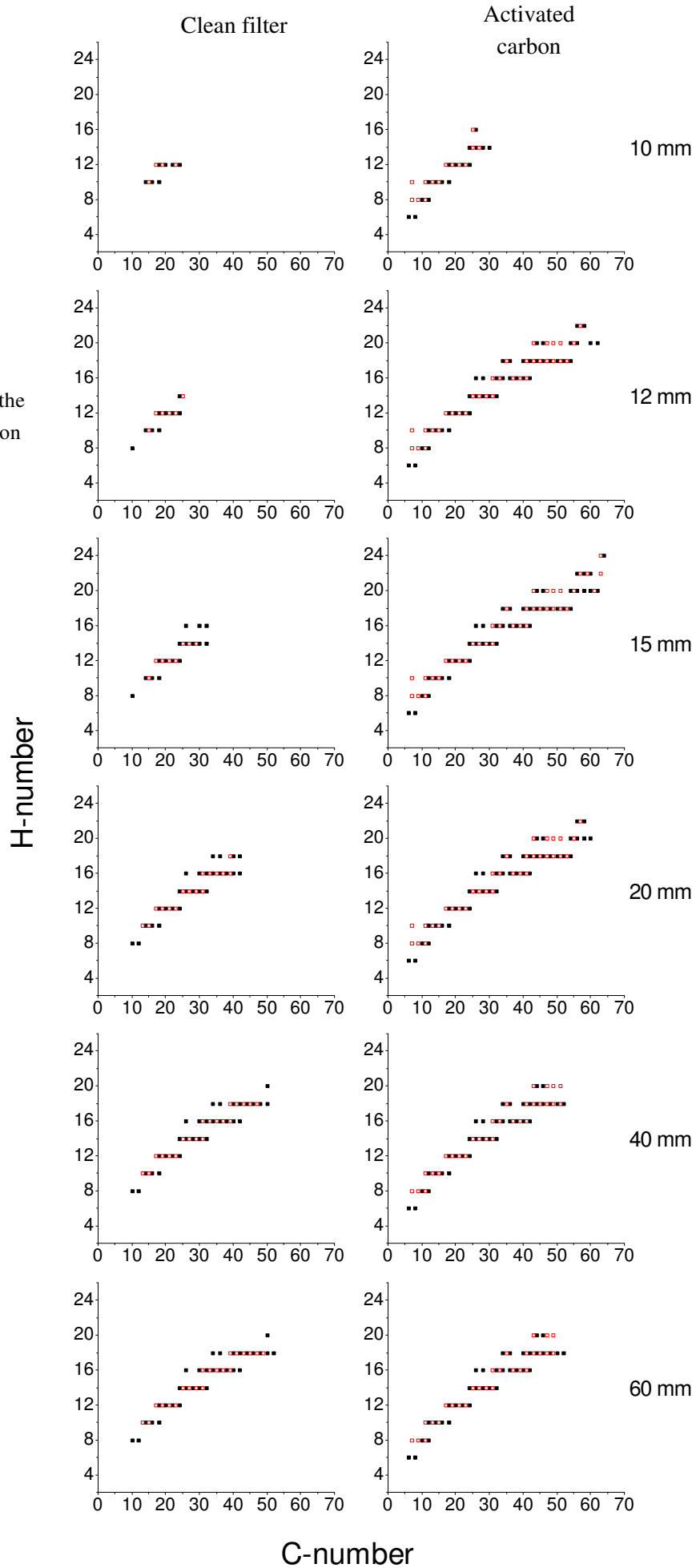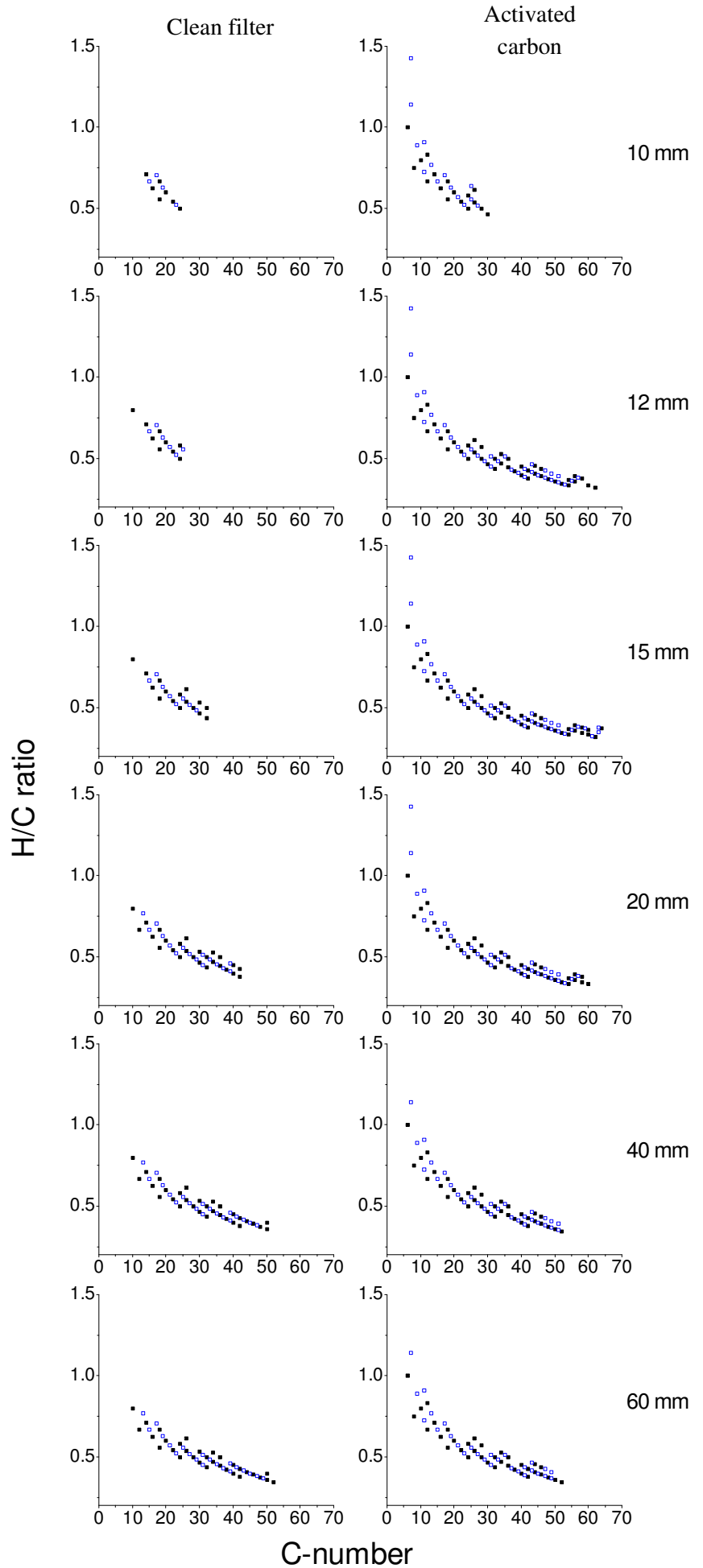
Figure 6.26. C-H diagrams (H/C ratio vs. C-number) of the combustion products collected at different HAB. On the left the deposition on neat filters, and on the right deposition on activated carbon are reported. Full black dots represent even C-numbers, while empty blue dots represent odd C-numbers.

In Figure 6.25 and Figure 6.26 above the C-H diagrams of the combustion products sampled at various HAB and deposed on both neat filters and activated carbon are reported. They are organised to emphasise the evolution of the main mass sequence as a function of the HAB and the differences between the two depositions.

From the comparison of the C-H diagrams a few interesting conclusions can be done. The C-H ratios of the diagrams reported in Figure 6.26 converge around 0.1 in the limit of high carbon numbers [134,135]. The C-H diagrams are very similar high in the flame, well above the beginning of the soot inception region (40-60 mm HAB), but a striking difference occurs at 10, 12, 15 and 20 mm HAB. These sampling HAB are particularly important because they are located in correspondence of and immediately after the beginning of the soot inception zone, and therefore this is the region where the changes due to the formation of the first soot particles are expected.

Particularly, when analysing the combustion products on activated carbon (see also Figure 6.14 and Figure 6.15), suddenly at 12 mm HAB a large group of masses which were absent at 10 mm HAB appears. These masses cover the range 374<m/z<764, which correspond to PAH having C-number from C_{30} up to C_{62}. In comparison, the masses detected on the neat filter show a progressive evolution as a function of the HAB, gently rising from 302 u (C_{24}) at 12 mm HAB up to the same value of the previous series at 40 mm HAB. This difference is particularly evident when representing the heavier detected mass as a function of the sampling HAB, as shown in Figure 6.27.
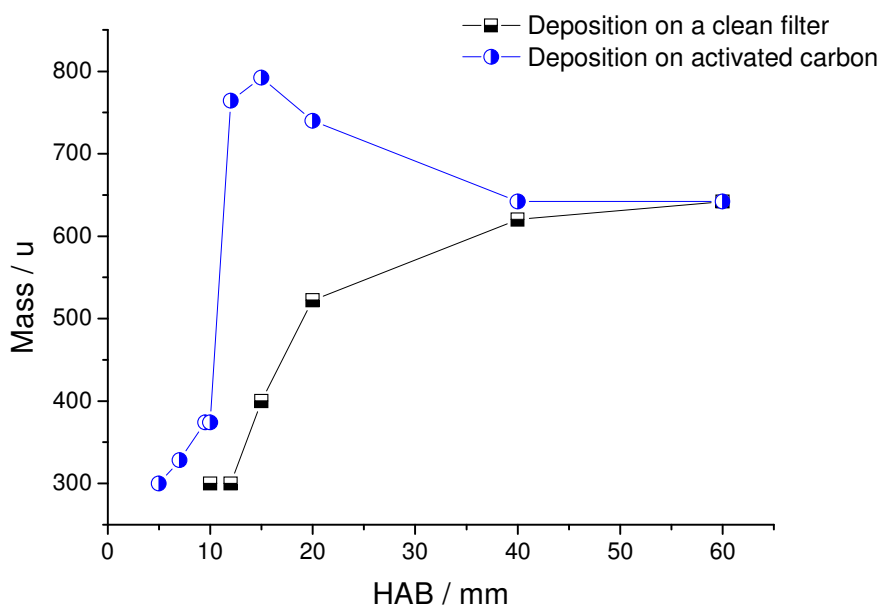
Figure 6.27. Heaviest detected mass vs. HAB obtained for a soot deposition on activated carbon (blue dots) compared with the same distribution obtained for a soot deposition on a neat filter (black dots).

Once again the growth of PAH seems to approach a plateau around 40 mm HAB, but there is a clear difference in behaviour. When depositing on a neat filter the heaviest detected mass directly reaches a plateau after 40 mm HAB. When depositing on activated carbon the heaviest detected mass pass through a maximum a 15 mm HAB, and then decreases down to the same value already observed for the deposition on neat filters. Looking at the main mass sequence obtained in the C-H diagrams, the H-number always increases slower than the C-number, and hence the H/C ratio decreases as a function of the C-number. The detected PAH grow richer and richer in carbon, and

therefore the pathway leading from low-mass up to high-mass PAH/soot precursors evolve via progressive hydrogen elimination (sometimes called "soot graphitisation"). In all cases, the HACA mechanism is evidently not the only one working. The presence of odd C-number PAH demonstrates that molecular species containing 5-atom rings are present in the soot extracted from flame, and the signal they provide in LD/LI/TOF-MS analyses is on the same order of magnitude of that provided by benzenoid PAH. Since there is no reason for believing that the absorption cross sections are much different in the two cases, the concentration of those species cannot differ by more than one order of magnitude.

The H/C ratio diagrams reported in Figure 6.26 highlight very effectively the behaviour of the light masses, particularly of those having C-number < 15. From the diagrams it is straightforward to see the difference between the two depositions, i.e. in the combustion products deposited on a neat filter the light masses having C-number < 12 are almost completely absent. This indicates that low-mass PAH are not visible on soot, i.e. their concentration is below the diagnostic detection limit. However, in presence of activated carbon they are able to accumulate on the carbon surface beyond the detection limit of the LD/LI/TOF-MS diagnostic. Among those, particularly important is the naphthalene (128 u), which accumulates at high concentration in the flame environment. Looking at the mass spectra in Figure 6.14 and in Figure 6.15, naphthalene is evidently one of the most important peaks in the analyses of the combustion products deposed on activated carbon, but it is almost absent in the direct deposition on neat filters.

6.3.5. Origin of the high-mass sequence

The comparison between the mass spectra obtained from different depositions on neat filters and activated carbon highlights an important difference in the mass sequence occurring between 10 and 20 mm HAB. In this HAB range, including the beginning of the soot inception and the region immediately after it, a series of high-masses (going from 450 up to 792) u suddenly appears. This high-mass sequence is only visible on activated carbon and not on neat filters, and therefore it can be attributed to gaseous species adsorbed on the activated carbon having C-number going from C_{30} up to C_{62} and first formed between 10 and 12 mm HAB, consistently with the position of the beginning of the soot inception zone (10-11 mm) located by the LII analysis. Of course, this does not prevent the fact that gaseous PAH can also condense on neat filters with a much lower efficiency. The sudden appearance of the high-mass series at the same time with the beginning of the soot inception suggests that the two processes are correlated, thus the soot particles are somehow involved in the formation of such masses. Furthermore it is possible to argue that only the young soot actively participates to the phenomenon, because higher in the flame (40-60 mm HAB) the mass sequences detected on both neat filter and activated carbon converge. At the same time, it is known from jet-cooled LIF measurements that small gaseous PAH exist in this region of the flame. This observation is consistent with the reduction of the number of active sites occurring during the soot aging as discussed in Paragraph 2.2.6.

The origin of the high-mass sequence in the beginning of the soot inception region is not yet fully understood, and at least two different hypotheses can be made in order to explain its nature. The effect of the temperature decrease (from 1870 K at 11 mm to 1670 K at 40 mm HAB, see Figure 6.12) along the flame has not been considered for the data interpretation. The mass sequence can originate from high-mass PAH formed via growth reaction involving small molecules and radicals like the HACA mechanism discussed in Paragraph 2.1.3, or from the clustering of low-

mass PAH in which the nascent soot particles act as intermediary. In every instance the existence of the high-mass sequence only in the beginning of the soot inception region and immediately after it is interpreted as an evidence of the capability of the nascent soot to play an active role in the growth process of PAH. The hypothesis of clustering formation during the sampling, i.e. when depositing soot and gases on the activated carbon, has been excluded. Since low-mass PAH have been detected all along the flame axial profile, if the formation of the high-mass sequence had been caused by the activated carbon on the filter, the same high-mass sequence would have been visible at different HAB than 10-20 mm. Conversely, the high-mass sequence is only visible in the HAB range 10-20 mm.

In the following of this Paragraph two mechanisms are tentatively proposed to explain the formation of the high-mass PAH series in the methane low-pressure flame.

Heterogeneous reactions

In this hypothesis the PAH synthesis takes place on the surface of the early soot particles. Such surface reactions are much more efficient and more likely for planar molecules compared to the formation in the gas phase by random collisions [136]. The early and active site-rich soot might promote the growth reactions of PAH via heterogeneous reactions, as depicted in Figure 6.28, catalysing the formation of high-mass structures among which the stabilomers are the thermodynamically most likely to prevail (see Paragraph 2.1.2). It is noteworthy that at this level this hypothesis works regardless the considered growth pathway of the PAH. Indeed they can be formed both via progressive addition of low mass species, following for instance the HACA mechanism, or even by contributions of high-mass species formed and/or activated later in the flame environment.
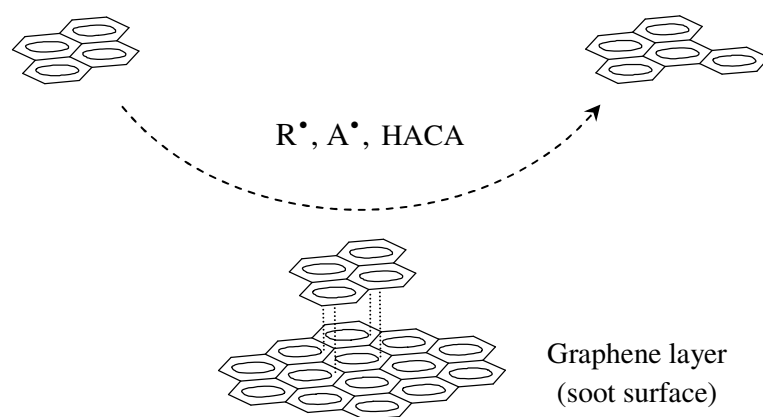
Figure 6.28. Heterogeneous reaction of PAH at the soot surface leading to higher-mass stabilomers.

A similar behaviour has already been observed by Siegmann and co-workers, who investigated a co-flow laminar methane/air diffusion flame and detected the PAH formed on the flame axis via REMPI/TOF-MS after extraction using a thin microprobe [136]. They found that soot particles are formed in the flame before the concentration peak of PAH: *"It is found that particles are formed before large PAH appear. As opposed to previous models where the flat PAH were generated in homogeneous gas phase reactions, we conclude that PAH are synthesised on the particles using their surface as templates and evaporate into the gas phase when synthesis is completed"*. According to the Authors, the response of the photoelectric yield measurements in their work is

promoted by the presence of PAH adsorbed on the soot surface. Therefore they conclude that the formation of PAH occurs on the particle surface, and then the PAH evaporate into the gas-phase. Authors propose their own soot formation model explaining the formation of high-mass PAH through heterogeneous reactivity on soot surface.

PAH clustering

In this hypothesis the clustering of low-mass PAH in 3D structures is examined. This process is believed to be one of the leading mechanisms of formation of the first nanostructures able to evolve in soot primary particles [54]. The PAH clustering is possible because of the stacking van der Waals interactions occurring between neighbouring molecules. At some point in the growth of large aromatic structures the magnitude of the attractive van der Waals forces is sufficiently large to allow the formation of clusters. The stacked PAH dispose plane-parallel, as illustrate in Figure 6.29, and depending on the PAH the ring systems may substantially overlap or barely at all. The distance between two different planes reflects the size of the carbon atomic orbital involved in the aromatic system (p_z), and it is on the order of 0.35 nm [54].

It must be pointed out that, while the formation of PAH clusters can be hypothetised on the basis of the collected experimental data, the stability of the cluster ions during the time-of-flight is unknown.
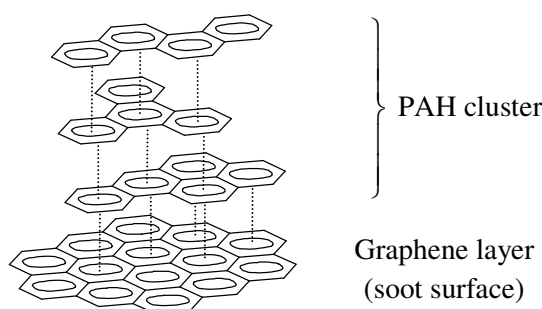

Figure 6.29. PAH clustering at the soot surface

Analysis of the detected masses

All the masses detected in the high-mass series are consistent with those of stabilomers. However, considering a clustering process, we have tried to calculate the high-mass series as linear combinations of the low-mass PAH detected all along the flame profile. It turns out that all the masses belonging to the high-mass series detected on activated carbon can be calculated summing three low masses. In other words, it appears that the terms belonging to the high-mass series are consistent with both PAH trimers or large stabilomeric planar structures.

In conclusion, the detected LD/LI/TOF-MD diagnostic only gives access to the masses of the combustion-formed species, and the masses of the high-mass series those are consistent with both stabilomers and three-PAH clusters. However, in all the considered hypotheses the early soot particles play an active role in the growth process of PAH, catalysing the growth of the graphene layer via larger and larger PAH, or supporting the formation of 3D structures. This implies that the growth of high-mass PAH involves not only gas-phase chemistry, but surface reactions during which the early soot particles act as intermediary agent.

6.4. Turbulent jet flames

In this Section the analysis of the phase adsorbed on Diesel and surrogates Diesel soot sampled from jet flames is presented. The flames were stabilized on the modified McKenna burner, equipped with the nebuliser for the atomisation of the liquid fuels described in Paragraph 4.2.4. This original set-up allowed the standardisation of various hydrocarbon flames by imposing identical hydrodynamic conditions resulting in similar sooting flame patterns [137].

Diesel and Diesel surrogate flames have been studied. The interest of performing such investigation lies in the complexity of the composition of practical fuels, which contain hundreds of compounds included aliphatics, aromatics among which PAH and oxygenated species [130]. On the other hand, the far simpler model fuels (surrogates) are used in numerical simulations. Particularly, the composition of the surrogate has to fulfil some specific requirements described in [130,131].

Using a burner already available at PC2A laboratory, the effectiveness of the surrogate to reproduce the sooting behaviour of the parent Diesel fuel has been achieved by comparing the soot volume fraction mappings as detailed in [111,112]. In the same works it has been found that the mixture 80% n-decane and 20% α-methyl naphthalene leads to very similar soot and PAH profiles as shown in next Paragraph 6.4.1, thus this composition has been retained in this work.

The objective of the LD/LI/TOF-MS analysis performed in this work is then to complete the previous study to compare the composition of soot particles sampled either in the Diesel flame or in its surrogate. This has been achieved taking advantage on in-situ laser diagnostic based on the coupling of Laser Induced Incandescence (LII) and Laser Induced Fluorescence (LIF) techniques described in the next Paragraph in order to handle the sampling. Particularly, five different locations on the flame axis as a function of the HAB have been sampled, covering the transition from the PAH zone up to the soot inception and to the soot oxidation zone. The C-H diagrams have then been used to compare the masses of the detected PAH. The presented data have been organised to emphasise any difference between the two fuels trend as a function of the HAB.

Before proceeding in the discussion it is important to point out that in this work the analyses presented in this Section were the first performed on real soot. The goal aimed to was not only the investigation of the behaviour of different fuels, but even a testing ground for the LD/LI-TOF-MS diagnostic on real soot samples. Therefore, the analyses suffer of all the common issues of a starting setup, i.e. the reproducibility level is not good enough to allow any quantitative conclusion
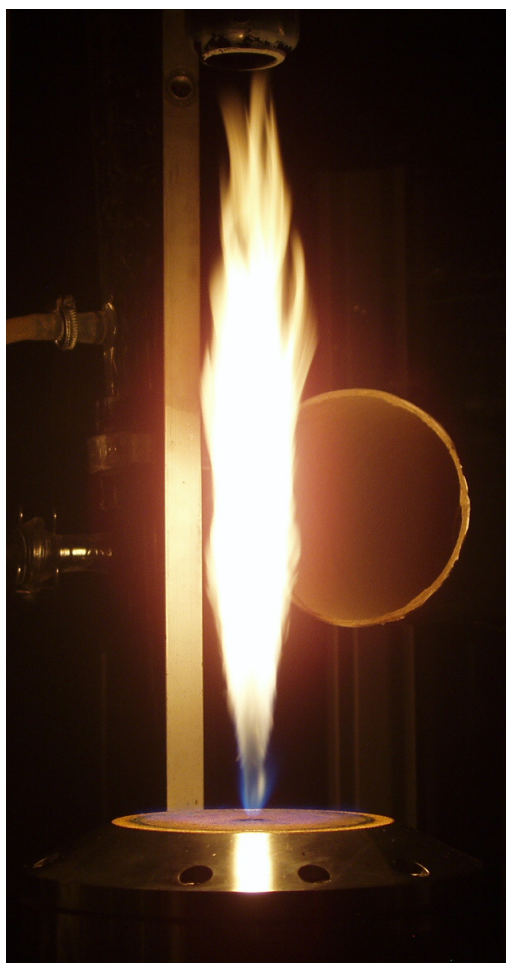
on the peak intensity evolution. Nevertheless, the qualitative information provided by the main mass sequence (those obtained from the C-H diagrams) remain valuable data, and they are all consistent with the other diagnostic performed on the same flames.

6.4.1. LII/LIF preliminary analyses and flame sampling

In order to handle the sampling, preliminary LII/LIF analyses on flames fed by both fuels have been performed.

The measure of the soot volume fraction and LIF profiles of turbulent flames fed by different fuels has been one of the subjects of the Ph.D. thesis of Lemaire [111]. The soot volume fraction and the LIF profiles have been measured along the entire length of the flames using a two-colour LII/LIF technique [112]. Briefly, the principle of the two-colour LII/LIF [132] is that the measured radiation emission from 1064 nm heated soot is only assignable to soot (LII signal) while the emission from 532 nm irradiation originates from both LII signal and fluorescent species. As demonstrated in [132] the radial LIF profile can be deduced from the difference between the radial profiles obtained at 532 and 1064 nm while the soot profile is that obtained at 1064 nm.

In Figure 6.30 and Figure 6.31 the axial and the radial profiles of the PAH fluorescence and soot volume fraction measurements of the Diesel flame have been reported. The surrogate Diesel flame profiles are not reported since they are very similar to those of the Diesel flame. Figure 6.31 reports the adopted sampling scheme as well.
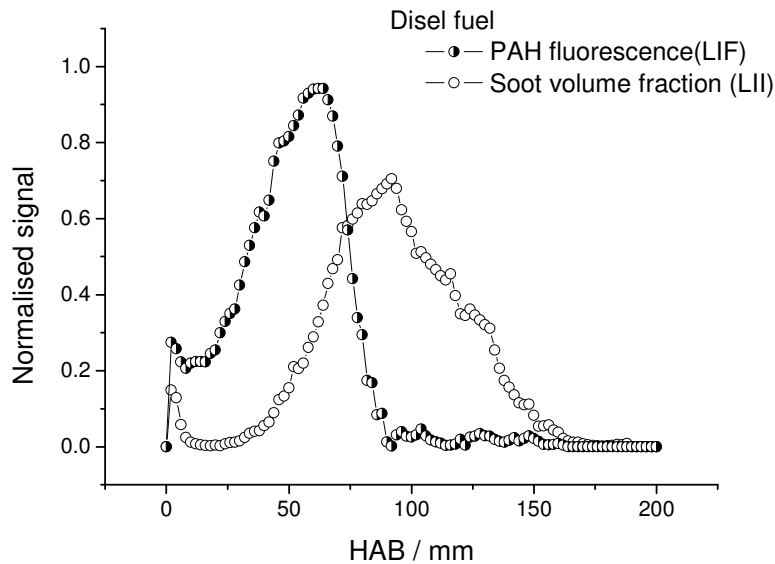

Figure 6.30. PAH fluorescence and soot volume fraction profiles obtained respectively via LIF and LII measurements on the Diesel flame.
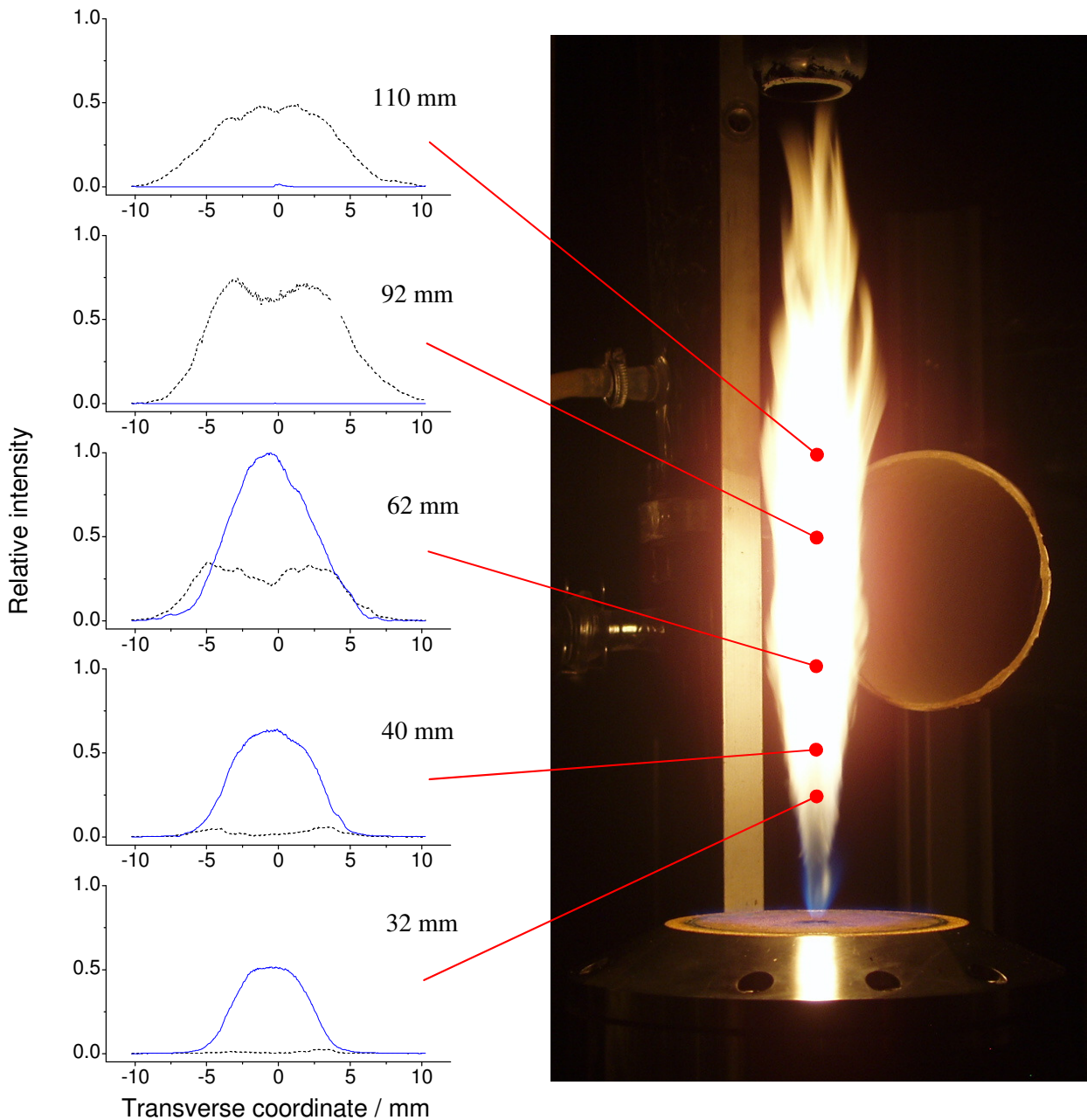
Figure 6.31. PAH fluorescence (LIF, blue solid line) and soot volume fraction (LII, black dotted line) radial profiles of the jet turbulent diffusion Diesel flame Red arrows indicate the sampling locations.

At low HAB (32 mm), a strong LIF signal indicates that PAH in gas phase are present while soot particles are not yet formed. Then the intensity of the LIF signal increases up to a maximum at 62 mm HAB. After this height, the LIF signal quickly decreases while the soot formation is progressing up to a maximum at 92 mm HAB. One of the main interests in studying this kind of flames is that the LIF/LII analyses reveal two sharply separated regions for the PAH and soot, which could allow the sampling of the PAH-rich phase with little interference by the nascent soot, and vice versa. Soot particles then enter in an oxidation zone and the LII signal decreases. It is

interesting to underline that soot particles are formed at low heights in the outer edges of a core containing fluorescent soot precursors (among which PAH) while they join the flame axis at higher heights. The same behaviour is observed for both the tested fuels.

The sampling has been performed at five different HAB, in order to cover the most important regions identified via the LII/LIF analyses described above. The probe has been introduced radially down to the axis of the flame, to avoid any interference from the outer shell of soot. 32 and 40 mm HAB are very low in the flame, at the very beginning of the axial soot inception, and therefore only gaseous PAH are present in these locations. 62 mm HAB corresponds to the maximum of the LIF signal and to the rising of the LII signal, then both gaseous PAH and soot particles are present. 92 mm HAB is in the maximum of the LII signal, i.e. it corresponds to the maximum soot volume fractions. Finally, 110 mm HAB is located in the soot oxidation zone. At 92 and 110 mm HAB the LIF analysis does not reveal gaseous PAH.

Soot has been collected during a time period of 1 min, and deposed on non-adsorbing substrates (neat borosilicate filters). At the time of these first analyses, the dilution system was not yet operational, and therefore the amount of soot collected even for very short sampling time was large enough that it did not make any sense to distinguish between soot directly deposed on a neat borosilicate surface and soot deposed on activated carbon.

Measurements at each HAB has been doubled or tripled to give a reproducibility measure. Although the reproducibility is always good when analysing different location on the surface of the same filter, reproducibility issues have been found when analysing different samples obtained nominally in the same experimental conditions. In this case the main mass sequence remains constant, but the absolute peak intensities are spread upon one order of magnitude, and even the relative peak intensities sometimes are not reproducible.

6.4.2. LD/LI/TOF-MS analysis

This section contains the mass spectra obtained by analysing the combustion products sampled from both the flames (Diesel and Diesel surrogate), which have been deposed on the surface of neat filters. Some pictures of the borosilicate filters taken after the mass analyses are reported in Figure 6.32. Three samples from each flame HAB and thirty positions on each sample surface have been analysed. The mass spectra obtained by LD/LI/TOF-MS are reported in Figure 6.33 and Figure 6.34, and are at least qualitatively reproducible.

The mass analyses have been performed under constant experimental conditions of temperature (T = -160°C) and pressure (p = $6 \cdot 10^{-9}$ torr). The laser irradiances were set at: I_{des} = 7.1 MW cm^{-2} and I_{ion} = 2.2 MW cm^{-2}.
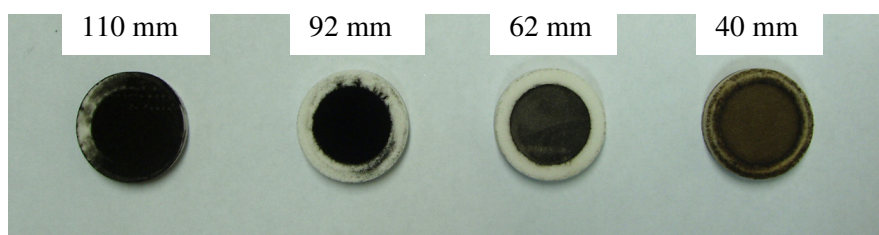
Figure 6.32. Picture of the Diesel soot samples taken after the mass analysis.
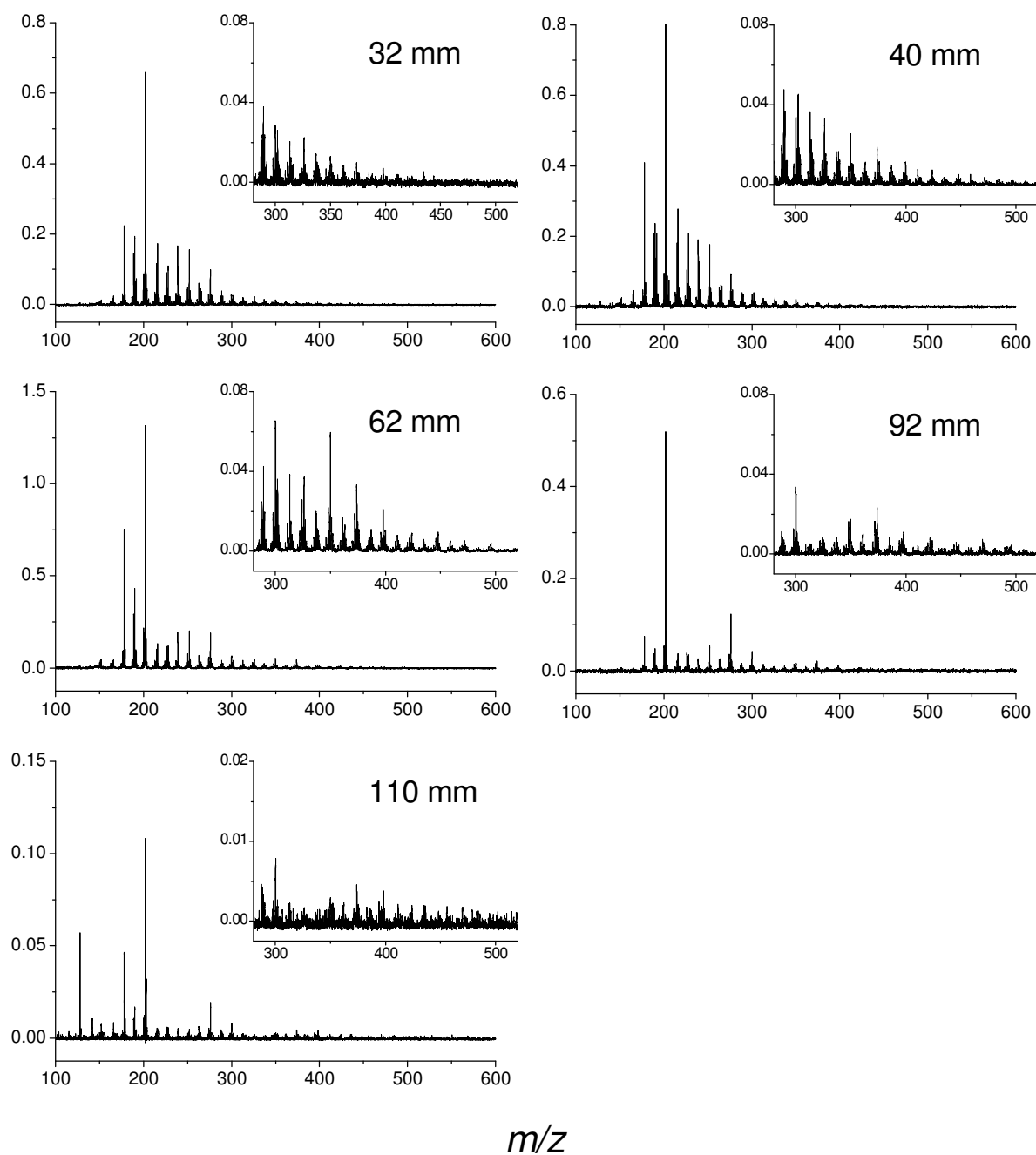
Figure 6.33. Diesel soot. Mass spectra obtained from soot sampled at different HAB and deposed on the neat surface of borosilicate glass filters. In the inserts zooms of the range 300<m/z<500 are reported. I_{des} = 7.1 MW cm^{-2}, I_{ion} = 2.2 MW cm^{-2}, 50 μs delay between pulses.
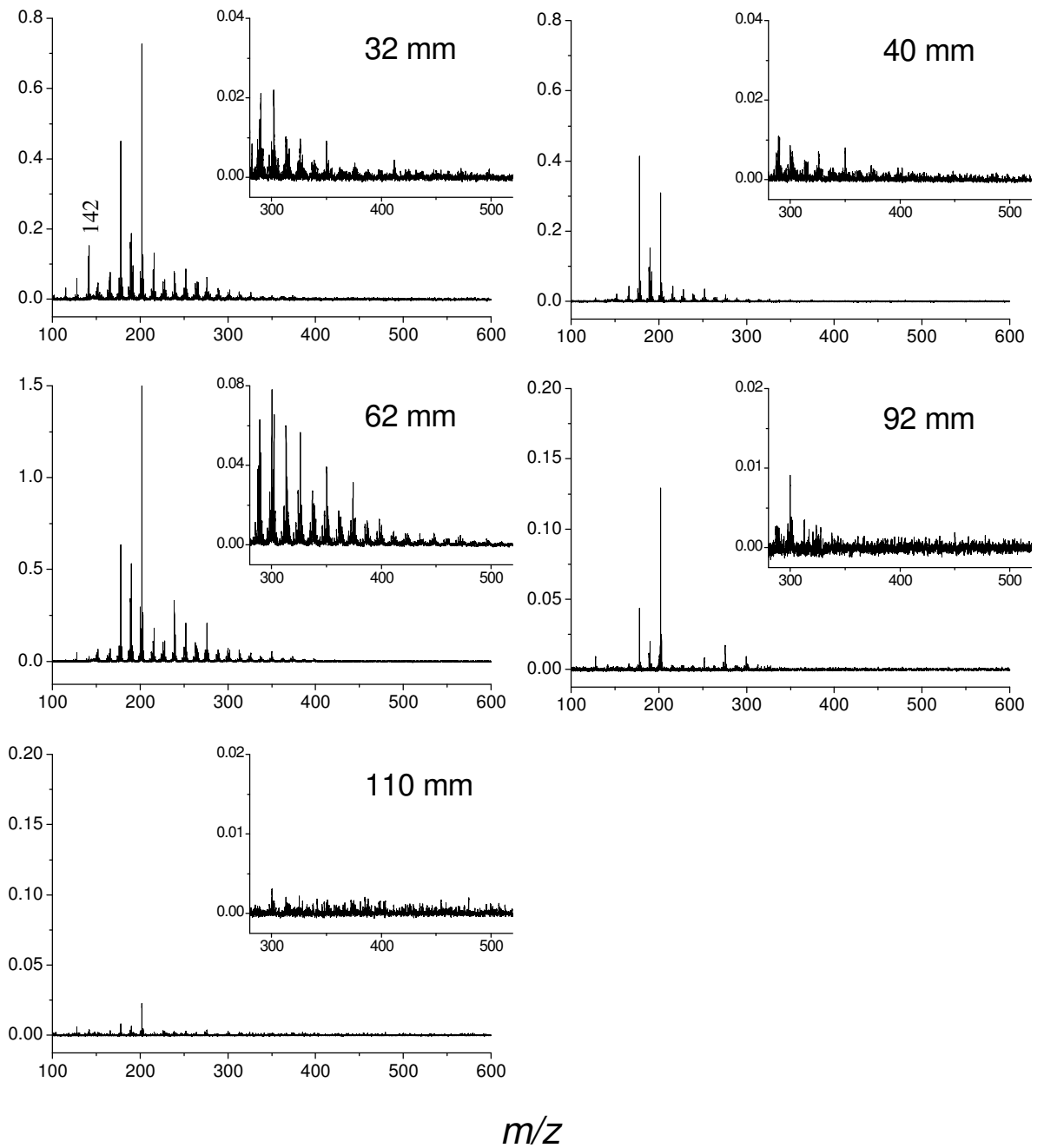
Figure 6.34. Surrogate Diesel soot. Mass spectra obtained from soot sampled at different HAB and deposed on the neat surface of borosilicate glass filters. In the inserts zooms of the range 300<m/z<500 are reported. I_{des} = 7.1 MW cm^{-2}, I_{ion} = 2.2 MW cm^{-2}, 50 μs delay between pulses.

The mass spectra of the Diesel and Diesel surrogate samples are very similar at 32, 40 and 62 mm HAB. At 32 and 40 mm HAB the sampled substance is liquid-like, and tends to form droplets at the probe aperture and to stick into the inner wall of the probe. The filters after sampling are dark yellow-orange coloured at 32 mm HAB, and turn dark yellow-gray at 40 mm HAB. The LD/LI/TOF-MS spectra are generally very rich of high-mass signals, and dominated by the masses in the range $178<m/z<300$. The peak at 142 u (α-methylnaphthalene) only present in the surrogate Diesel at 32 mm HAB most likely comes from fuel droplets or fuel vapours (petrogenic origin) and not from the combustion process (pyrogenic origin). Indeed this peak is not present in the mass spectra of Diesel soot at the same HAB. 62 mm is in the transition region where the maximum of the fluorescence signal due to gaseous PAH occurs together with a sharp rise of the soot volume fraction. The samples in this region are gray-yellow coloured, and the mass spectra are still very rich in masses. The heaviest detected mass in is located there. As for the spectra at 32 and 40 mm HAB, the most intense peaks correspond to the masses in the range $178<m/z<300$.

The mass spectra collected at 92 and 100 mm HAB are qualitatively very similar. In this region, shifting from the maximum of the soot volume fraction to the beginning of the oxidation zone, the collected soot is dry and form very thick and homogeneous layers when compacted on the filter surface. The filters are coloured. The LD/LI/TOF-MS signals are less intense than at lower HAB, as well as the highest detected mass is lighter. A few masses are still visible. The range $178<m/z<300$ still contains the most intense peaks, with the mass 202 u as the most intense peak in both the Diesel than the Diesel surrogate soot. In this HAB range a noteworthy difference between the two fuels appears. At 92 and 110 mm HAB the PAH signal from the Diesel surrogate almost completely disappear, while in the Diesel soot a clear progression of masses is still visible up to 500 u.

The flames are smokeless, at 180 mm HAB no signals have been detected in both cases.

As a complement to the LD/LI/TOF-MS, a Gas Chromatography - Mass Spectrometry (GC-MS) analysis has been performed on Diesel soot sampled at 92 mm HAB[5]. The corresponding LD/LI/TOF-MS analysis is reported in Figure 6.33. GC-MS allows the identification of the isomeric structures and their quantification using series of internal standards. On the other hand, the GC-MS analysis potential is limited in the $m/z<300$ range, then the comparison with the mass spectra is only possible below this limit. Nineteen different PAH in the mass range $128<M<300$ have been identified via GC-MS, and for some of them the amount contained in the analysed sample has been determined. The identified PAH are reported in Table 6.1.

The most abundant masses detected by chromatography are acenaphthylene (152 u), phenanthrene (178 u), pyrene (202 u), benzo(ghi)perylene (276 u) and coronene (300 u). All these PAH are stabilomers, and they are associated to the most intense signal peaks in the LD/LI/TOF-MS spectra collected at 92 mm HAB as well. The mass 190 u gives a strong LD/LI/TOF-MS signal, but unfortunately none of the two isomers existing at this mass has been considered for the chromatographic analysis. Seven further signal peaks attributed to PAH in the mass range $178<m<300$ u have been detected but not identified.
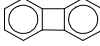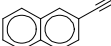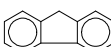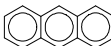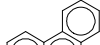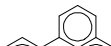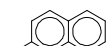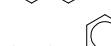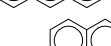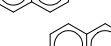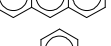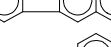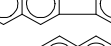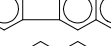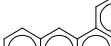
PAH	Moleculr Formula	Structural Formula	M / g mol-1	m (µg)
Naphtalene	$C_{10}H_8$		128.1705	0.0799
Biphenylene	$C_{12}H_8$		152.1919	0.0349
Ethynylnaphthalene*	$C_{12}H_8$		152.1919	0.0506
Acenaphthylene	$C_{12}H_8$		152.1919	0.2366
Acenaphtene	$C_{12}H_{10}$		154.2078	/
Fluorene	$C_{13}H_{10}$		166.2185	0.0663
Anthracene	$C_{14}H_{10}$		178.2292	0.0889
Phenanthrene	$C_{14}H_{10}$		178.2292	0.2629
Fluoranthene	$C_{16}H_{10}$		202.2505	0.2899
Pyrene	$C_{16}H_{10}$		202.2505	0.6866
Benzo(a)anthracene	$C_{18}H_{12}$		228.2879	/
Chrysene	$C_{18}H_{12}$		228.2879	/
Benzo(a)pyrene	$C_{20}H_{12}$		252.3093	0.0300
Benzo(b)fluoranthene	$C_{20}H_{12}$		252.3093	/
Benzo(k)fluoranthene	$C_{20}H_{12}$		252.3093	/
Indeno(1,2,3-cd)pyrene	$C_{22}H_{12}$		276.3307	0.0475
Benzo(ghi)perylene	$C_{22}H_{12}$		276.3307	0.1797
Dibenzo(ah)anthracene	$C_{22}H_{14}$		278.3466	/
Coronene	$C_{24}H_{12}$		300.3521	0.2315

Table 6.1. PAH detected via GC-MS on a soot sample collected at 92 mm HAB on the Diesel flame. * The GC-MS could not separate 1- and 2- ethynylnaphthalene.

Following the approach presented in Paragraph 5.3.2, the amount of each PAH isomer detected on soot by GC-MS has been corrected for the absorption cross section at 266 nm and compared with the LD/LI/TOF-MS signal as illustrated in Figure 6.35. Once again the agreement between the two series of data is generally good, the only important deviation being the mass 178 u. This result further supports the crucial role of the ionisation step, and especially confirms the possibility of performing semi-quantitative LD/LI/TOF-MS analyses on real soot only accounting for the absorption cross sections. The PAH isomers having a small absorption cross section at 266 nm wavelength, typically those on the low-mass side going from naphthalene up to acenaphthene in Table 6.1, result in very small LD/LI/TOF-MS peak signals even when their concentration in the sample is large (see also Paragraph 5.3.2). On the other hand, the most intense LD/LI/TOF-MS signals come from the PAH isomers having the higher concentrations and the larger adsorption cross sections, typically those in the mass range 200<M<300.
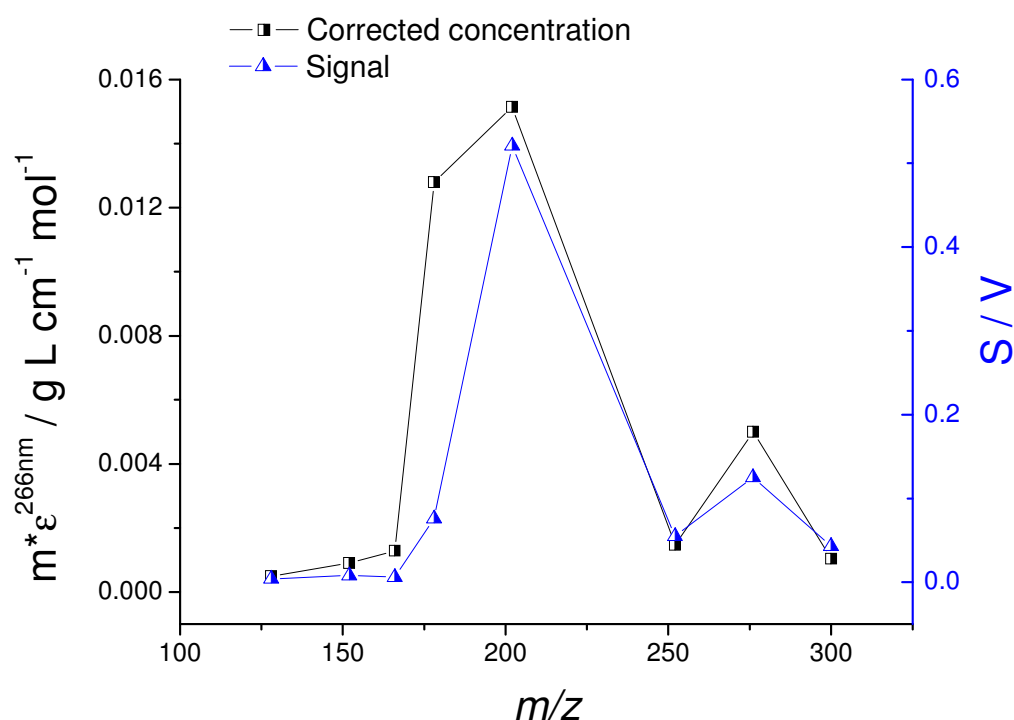
Figure 6.35. Corrected masses (black squares) and peak signals (blue triangles) vs. the detected masses.

When the GC-MS analyses give quantitative information on the amounts of all the existing pyrogenic isomers molecular mass, it is possible to establish some semi-quantitative correlations between their amounts contained into the sample. For instance, at 152 u only four isomers exist, and three of them are stabilomers (1- and 2-ethynylnaphthalene and acenaphthylene). The amounts of all of them have been quantified by GC-MS. In this case, it is then possible to assert that their relative mass percentages are: biphenylene (11%), 1- and 2-ethynylnaphthalene (16%) and acenaphthylene (73%). It is noteworthy that, repeating the calculation only for the three stabilomers gives: 1- and 2-ethynylnaphthalene (18%) and acenaphthylene (82%), which are values reasonably close to the "real" percentages calculated accounting for all the isomers. This can be interpreted as a further evidence of the fundamental role of the stabilomers with respect to the less thermodynamically stable isomers. Analogously, at 178 u only two stabilomers are possible, anthracene (20%) and phenanthrene (80%).

6.4.3. Comment on the mass sequence

According to the discussion so far, molecular formulae C_nH_m have been attributed to the detected mass, and the C-H diagrams as a function of the HAB have been built up and reported in Figure 6.36 and Figure 6.37.

The main mass sequence is the same in all the samples analysed in the two flames. As in the case of the ethylene reference flame described in Section 6.2, and of the low-pressure flame described in Section 6.3, different peak signals appear depending on the HAB. The agreement of the detected masses with other experimental data available in the literature is very good [5,6,46,72,77], and the even masses are all consistent with Stein's stabilomers where the calculations are available (Paragraph 6.2.3).

The detected PAH constitute a regular sequence from 128 u (naphthalene, $C_{10}H_8$) up to 594 u ($C_{48}H_{18}$) in the Diesel soot, and up to 498 u ($C_{40}H_{18}$) in the surrogate Diesel soot. The peak signals recur in groups 10, 12 or 14 u spaced from they closest neighbours, and each of them contains all the PAH having the same C-number. In the main mass sequence the H-number increases slower than the C-number.

The quantitative analysis on the evolution on the peak intensities was not possible because of the lack of reproducibility of the peak intensities at the time of these measurements. However, some general trends already observed in the other flames are confirmed there. Most notably, the mass spectra are characterised by intense signal peaks in the range 128<m/z<400 and progressively decreasing signals up to the heaviest detected mass. Furthermore, the PAH intensities corresponding alternately to an odd or an even carbon number have the same order of magnitude. The peak intensities associated to even carbon numbers are generally much more intense than those associated to odd carbon numbers.

Figure 6.36. C-H diagrams (H-number vs. C-number on the left and H/C ratio vs. C-number on the right) of the combustion products collected at different HAB from the Diesel flame. Full black dots represent even C-numbers, while empty coloured dots represent odd C-numbers.
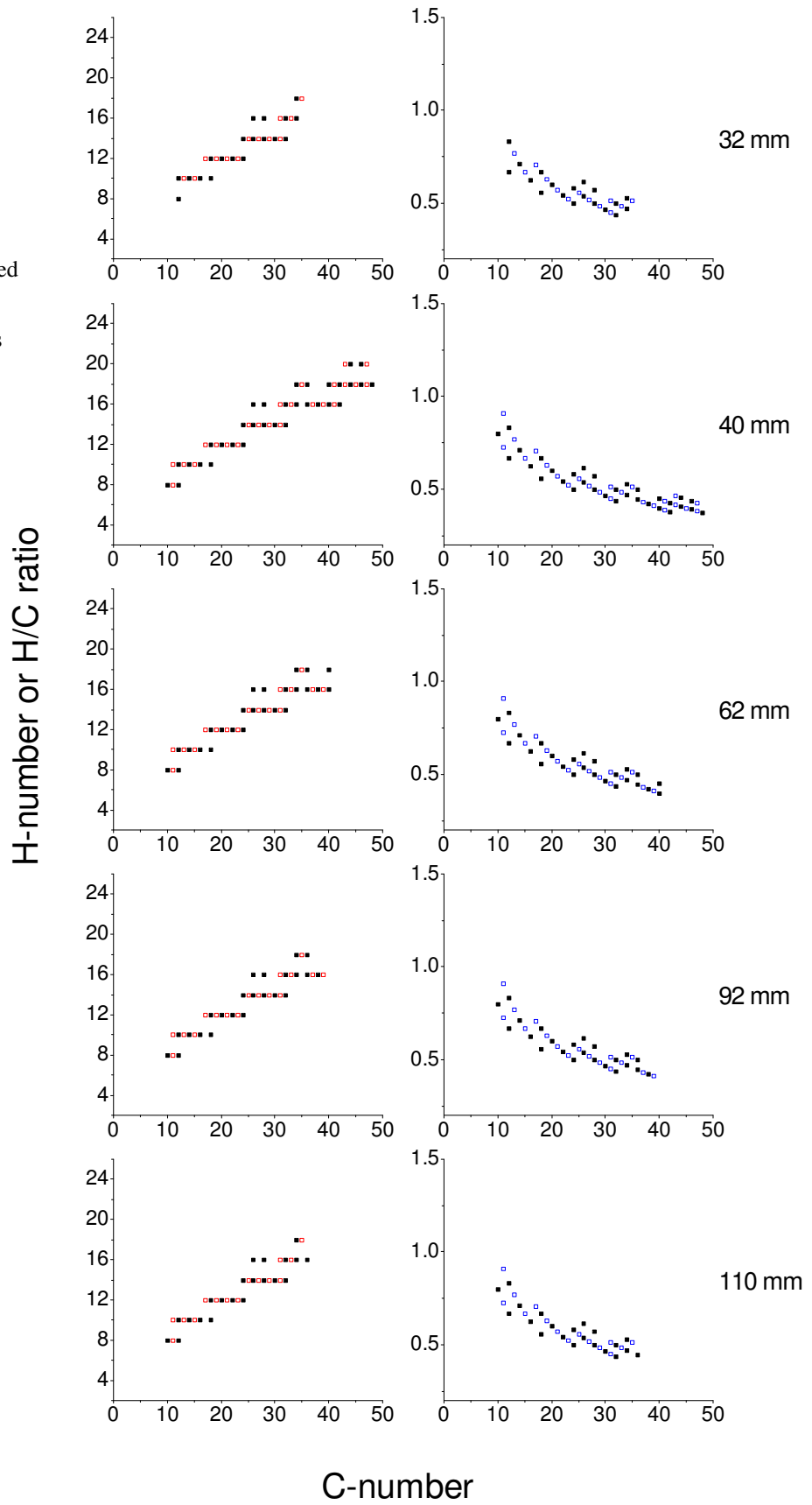
Figure 6.37. C-H diagrams (H-number vs. C-number on the left and H/C ratio vs. C-number on the right) of the combustion products collected at different HAB from the Diesel surrogate flame. Full black dots represent even C-numbers, while empty coloured dots represent odd C-numbers.
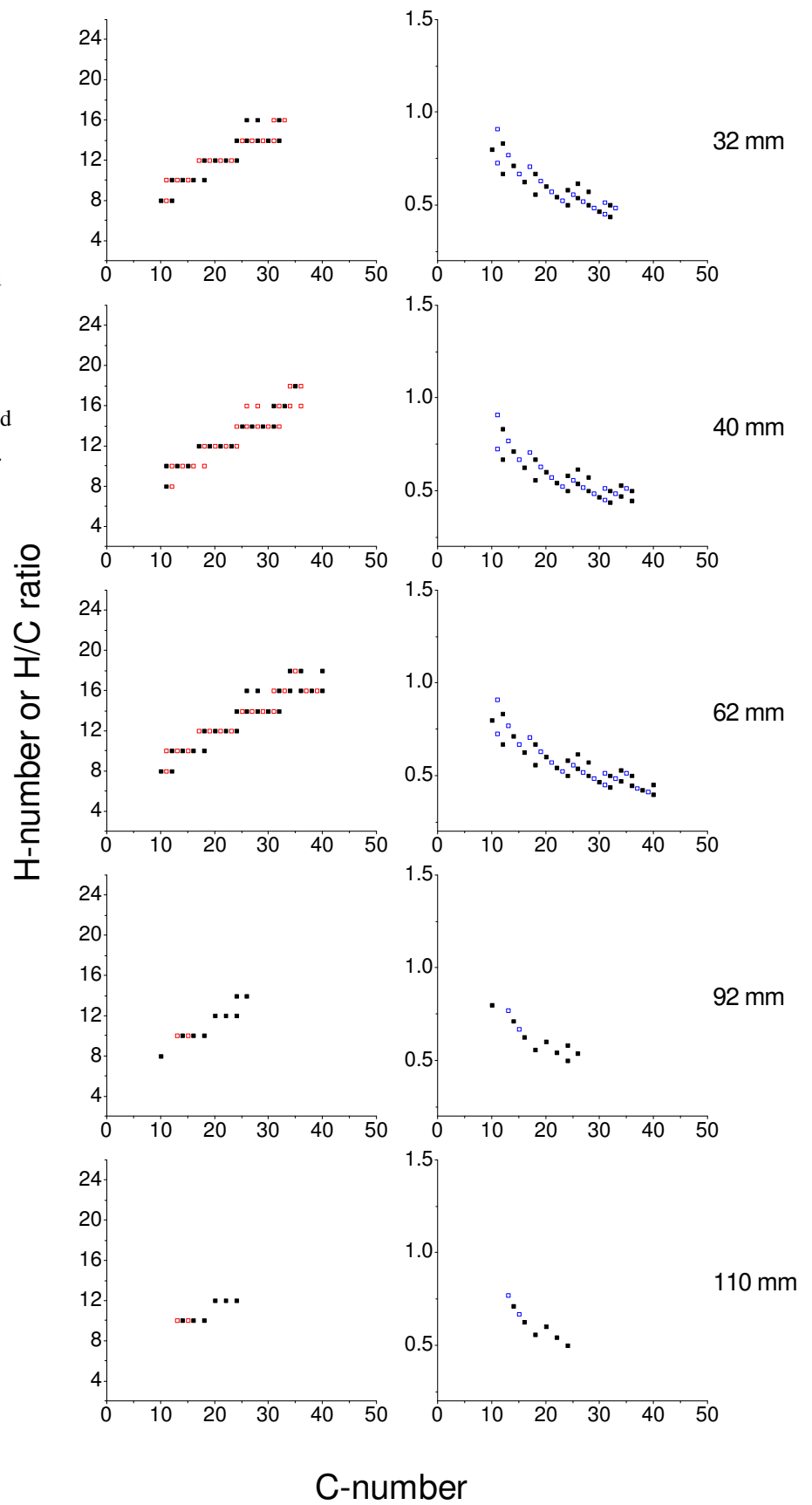
In Figure 6.38 the heaviest detected mass as a function of the sampling HAB has been reported for the two flames. Generally the detected PAH mass sequences are broader in the case of the Diesel flame, as already remarked in Section 6.4.2. The heaviest detected mass is indeed always lighter for the Diesel surrogate soot with respect to the Diesel soot. The heaviest detected masses have been detected in both flames at 62 mm HAB. Simultaneously, 62 mm is also the HAB in which the most intense peak signals have been found in both flames. This observation is consistent with the maximum concentration of gaseous PAH detected via LIF, suggesting that an important role on the detected masses in possibly played by gas-phase PAH condensed on soot.
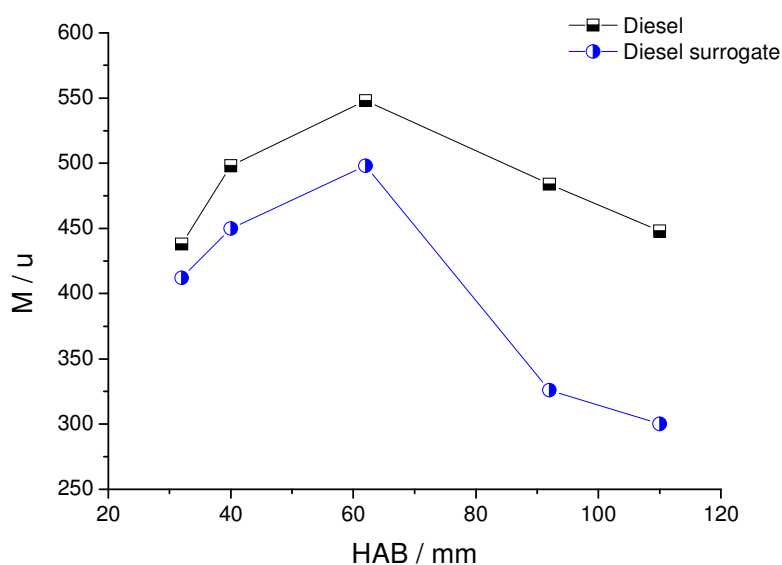
Figure 6.38. Heaviest detected mass vs. HAB obtained from soot sampled on the Diesel flame (black dots) compared with the same distribution obtained from soot sampled on the Diesel surrogate flame (blue dots).

The mass spectra collected very high in the flame (92 and 110 mm HAB) look differently in the two flames, in a way which surprisingly could not be suspected from the previous spatially resolved laser measurements performed via in-situ LIF and LII and showing a perfect agreement between the flames. In the case of the Diesel flame, the mass sequence is still very rich and characterised by strong signal peaks in the region 128<m/z<300. On the other hand, in the surrogate diesel flame only few masses survive. These are 178, 190 and 202 u (strong peaks), and 128, 252, 276 and 300 u (much weaker peaks). These three masses also correspond to the most intense signals found in the Diesel soot. In other words the soot sampled high in the surrogate Diesel flame appears cleaned out of its PAH content. This result suggests that the fuel composition influences the PAH content of the soot particles. A hypothesis which has been formulated attributes the difference between the mass spectra to the PAH originally contained in Diesel fuel (petrogenic PAH, [72,73]). For instance, in the surrogate Diesel flame the mass at 142 u detected at 32 mm HAB indicates that a detectable amount of unburned fuel can survive to the early combustion stage. However it is not yet clear how they influence the pyrogenic PAH formation. Nevertheless, for identical soot volume fraction and particle diameter, as determined by time-resolved LII, soot particles issued from the Diesel surrogate seem to present a slightly faster oxidation [112] which

could be linked to the surface composition determined by LDI TOF-MS. The presence of larger adsorbed PAH on Diesel soot probably induces a longer oxidation process.

Chapter 7.

Conclusions

This PhD work concerns the study of the chemical composition of soot particulates sampled in several flames in view of improving the understanding of soot formation process in those flames. The analysis method is the Laser Desorption/Laser Ionisation/Time-Of-Flight Mass Spectrometry (LD/LI/TOF-MS) applied to soot particulates deposed on a filter after probe extraction from the flame. The experiment was set-up in a previous thesis [116] and the method feasibility was demonstrated mainly by performing analysis of mixtures of pure PAH or model soot (known concentrations of selected PAH adsorbed on black carbon).

This work at first focused on the method improvement in terms of selectivity, sensitivity and reproducibility. To this purpose, each step of the process has been thoroughly examined by using home-made calibrated model soot samples. Fragment-free mass spectra have been obtained selecting the laser irradiances below a given threshold and imposing a top-hat transverse irradiance profile of the ionisation laser beam. The analysis of the desorption dynamic allows to select the most appropriate number of laser pulses to apply at a given location of the sample. The photodissociation turned out to be very sensitive to the ionisation step, especially in terms of local irradiance. This has been the source of an extended study leading to the characterisation of the series of fragment ions resulting from pyrene analysis as function of the laser irradiance. It has been shown that both the ionisation and desorption irradiances influence the response of the PAH in terms of peak signal intensity. Particularly, the ionisation curves are found narrowed down and shifted towards lower irradiance upon higher and higher laser desorption irradiance. This has been attributed to the larger gain of internal energy from the desorption step which ultimately leads to easier ionisation. This extra energy coming from desorption has an important impact on the overall ionisation process which have to be taken into account if analytical purposes are sought, since it strongly affects both the number and the intensity of the detected signal peaks.

While the use of LD/LI/TOF-MS as an analytical method for the soot content determination necessitates working in the low-irradiance regime, the previous study was necessary to properly select the ensemble of the experiment parameters. In the low-ionisation irradiance regime (< 3 MW cm^{-2}), the photon order of the ionisation process has been determined from the log-log plot of the signal intensity vs. laser irradiance for four PAH (naphthalene, phenanthrene, anthracene and pyrene). For most low-mass PAH (< 300 u) at the excitation wavelength of 266 nm, the process involves two photons, the first one bringing the molecule to an excited state and the second one to the ionisation continuum. The photon order was found to be around 1.6 for the three first PAH and 1.2 for pyrene, indicating that the process is dominated by one of the two steps. Using a mixture of 16 PAH adsorbed on black carbon, a good correspondence could be obtained between the peak intensity of the precursor ions and the initial concentration of each PAH at the condition to correct

the signal for the molar absorption coefficient at the ionisation wavelength. That indicates that the two-photon ionisation process is dominated by the absorption step (resonant condition) which is correctly represented through its molar absorption coefficient.

The second part of the thesis has been devoted to sooting flame investigations. Three flames have been selected. (1) An ethylene/oxygen premixed flat flame, studied at CNR of Naples has been reproduced in view of comparing our overall method performances to the reported literature. (2) A low-pressure methane/oxygen/nitrogen premixed flat flame selected for its appropriateness for further kinetics study about PAH and soot formation and in which the complementary determination of gaseous PAH is undertaken in the group. (3) A turbulent jet flame of liquid fuels for testing the possibility of the method in a context of a more realistic flame.

One crucial issue of the method dedicated to the analyses of the chemical composition of the soot surface lies in the quality of the soot sampling procedure. In this work soot particles have been deposed on a porous borosilicate filter after they have been extracted from the flame using a microprobe. Despite many precautions, for example prevention of condensation in the sampling line, the reproducibility of the mass signal intensities between samples was not as good as with model soot. Typically a standard deviation of 10-20% depending on the mass range was achieved on a same sample while the reproducibility drops down to 40 % when comparing different filters. However the structure of the mass spectra in terms of mass peak identification was quite reproducible.

By contrast to model soot, mass spectra collected from real soot analyses exhibit up to 200 different peaks, some of them are artifacts due to early dissociation phenomena or to the isotopic abundance of carbon. The identification and exclusion of those artifacts leads to decrease the number of peaks down to the 60% of their initial number. All the masses can be represented by a molecular formula C_nH_m. In each investigated flame, the peak intensities correspond alternately to even and odd C-numbers having intensities of the same order of magnitude and the odd C-number PAH show peaks clearly weaker than that of even C-number PAH. Even C-number masses are all consistent with those of Stein and Farr's stabilomers, while odd C-number suggests that during growth process of PAH in flame an important role is played by 5-atoms rings.

The analysis of soot sampled 14 mm HAB in the reference atmospheric flame has shown a very good correspondence of our mass spectra with those obtained by Apicella and co-workers, although the sampling procedure in the flame, the sample preparation and the ionisation scheme are different.

Then we have switched to the low-pressure methane flame. To the best of our knowledge, the composition of the soot particles in such a low-sooting flame (peak soot volume fraction is 1 ppb) has been investigated for the first time in this work. The low-pressure flame offers an extended and easy-to-access reaction zone, thus it is expected to spatially-resolve the soot nucleation zone. Interestingly, this flame is investigated at the laboratory using the combined approaches of different laser techniques (Laser Induced Incandescence, jet-cooled Laser Induced Fluorescence). In this flame, samples have been taken in the gaseous zone before soot inception and at several positions along the soot profile. The data reduction is made easier using H number vs. C number or H/C vs. C number representations of the molecular formulae attributed to the detected masses as function of the height of the sampling in the flame. Two kinds of sampling filters have been taken: clean filters aiming to collect mainly soot particles, and adsorbing filters on which both particles and gaseous PAH are trapped. Using this approach, the comparative analysis of the H/C diagrams as function of the height in the flame and thus of the reaction time exhibits important variations.

Two important conclusions follow from the analysis of the collected spectra. (1) Gaseous PAH collected on activated carbon before soot inception present masses extending towards C-number equal to 30. (2) Once in the soot inception zone, mass spectra collected on activated carbon exhibit very high masses up to C-number equal to 70, value which then reduces down to 55 higher in the flame. Conversely the soot content observed on clean filters shows a regular progression towards the higher masses (C-number equal to 55), consistent with the increase of the soot volume fraction along HAB. Thanks to the comparative analysis, the heavier masses observed on activated carbon in the region of the soot inception from 10 to 20 mm have been attributed to large gaseous PAH masses.

Two hypotheses have been addressed to explain the existence of the high-mass series. The mass sequence can originate from high-mass PAH (stabilomers) formed via growth reaction involving small molecules and radicals like the HACA mechanism, or from the clustering of low-mass PAH in which the nascent soot particles act as intermediary. In every instance the existence of the high-mass sequence only in the soot inception region and immediately after it is interpreted as an evidence of the capability of the nascent soot to play an active role in the growth process of PAH, catalysing heterogeneous reactions at its surface. The absence of high masses just upstream the soot inception region suggests that the nucleation process is lead by relatively small PAH i.e. those identified below 10 mm HAB. This is consistent with the nucleation process currently proposed in the literature which considers dimmers constituted by two stacking pyrene molecules as primary soot particles. This study suggests that slightly higher PAH could also be involved up to C-number equal to 30.

The third studied flame is a turbulent jet flame burning liquid fuel droplets. The ability of the method to bring reliable data in terms of soot mass spectra in this non-stationary flame was one motivation. In this context, the sampling has been performed radially in several zones previously identified by in-situ LIF/LII methods as containing soot particles, gaseous PAH or both. The reproducibility of the peak signals intensities is worst than in the case of two above discusses flames, however the structure of the mass spectra is highly reproducible. Two flames have been investigated, the first one burning Diesel fuel and the second one burning a Diesel surrogate (80 % n-decane and 20 % α-methylnaphthalene). The detected PAH constitute a regular sequence from 128 u up to 594 u in the Diesel soot and 498 u in the Diesel surrogate soot, i.e. the detected PAH mass sequence is broader in the case of the Diesel flame. The heaviest mass is indeed always lighter for the Diesel surrogate soot with respect to the Diesel soot suggesting that the fuel composition influences the PAH content of the soot particles (pyrogenic role). The presence of larger adsorbed PAH on Diesel soot probably induces a longer oxidation process. Finally the turbulent flame is sufficiently sooting to collect a significant soot quantity to process Gas Chromatography-Mass Spectrometry analysis which could provide quantitative determination of nineteen PAH in the mass range 128<M<300. The comparison of GC-MS measurements with LD/LI/TOF-MS spectra corrected for the molar absorption coefficient is globally satisfying confirming the potentiality of the last method to perform semi-quantitative measurements.

In conclusion the LD/LI/TOF-MS technique has proven to be a reliable method to provide new insights on the PAH growth and soot formation processes in flames, providing information in terms of PAH content which are not easily available using other techniques. Particularly, its high

sensitivity and the capability of gaining information on a large *m/z* range allowed the investigation of the transition between the gaseous phase and the soot inception zone in low-pressure flames.

This work has been performed as a part of an ensemble of experimental investigations of selected laboratory flames. The objective is to gather a sufficient large range of sensitive data (among them the PAH adsorbed on soot and the large gaseous PAH obtained using LD/LI/TOF-MS) in view of improving the PAH and soot modelling. Our findings suggest to consider a wider range of PAH and more sooting pathways in the current detailed chemical mechanisms.

The most attractive experimental improvement is currently the possibility of making on-line analyses, directly coupling the extractive probe with the mass spectrometer, in order to eliminate the process of soot deposition and giving access to faster and less intrusive measurements.

Appendix A.

Peak irradiance calculation

In this work the calculated laser irradiance is always the peak irradiance I_0, corresponding to the the maximum irradiance value reached during the laser pulse life. The pulse power is measured using a power-meter, and the peak irradiance is calculated knowing the transverse intensity profile of the beam, which has been investigated using a beam profiler.

A detailed description of the propagation properties of TEM_{00} beams are beyond the purpose of this work. Brifely, the irradiance spatial profiles of Gaussian and Top-Hat beams are compared below [133]:

- Gaussian transverse profile: $I(r) = I_0 \, e^{-\frac{2r^2}{w^2}}$

- Top-Hat transverse profile: $I(r) = I_0$

where $I(r)$ is the space-dependent irradiance, r is the transverse spatial coordinate and w is the beam radius. In the scheme below the two transverse dependences are compared.
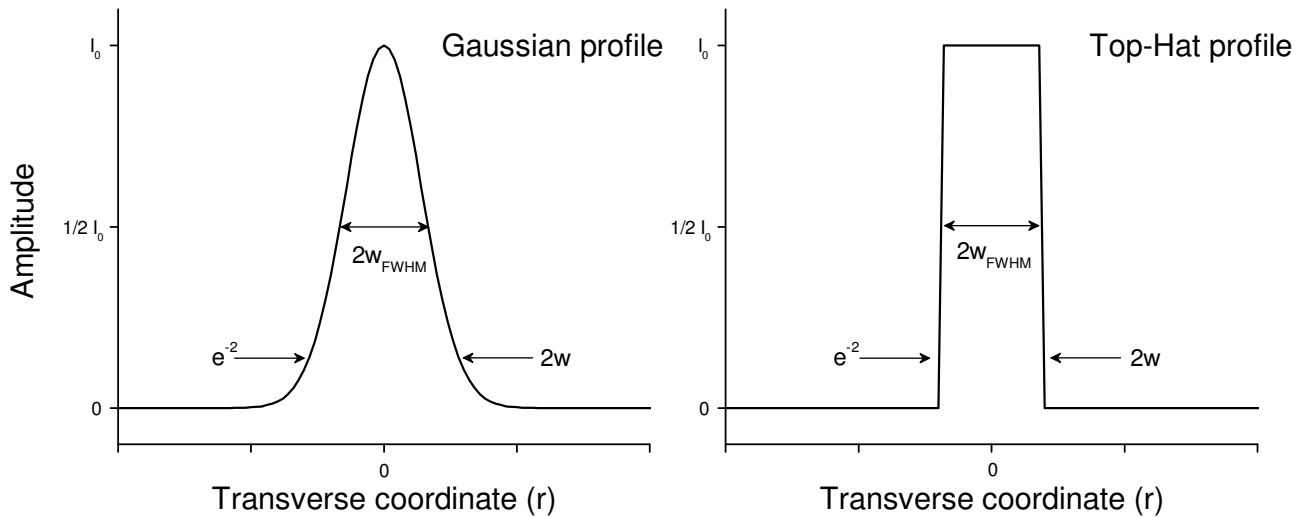
The power delivered by each laser pulse can be obtained by integrating the irradiance dependence with respect to the spatial coordinates and resolving for the peak irradiance:

- Gaussian transverse profile: $I_0 = \dfrac{2P}{\pi w^2}$

- Top-Hat transverse profile: $I_0 = \dfrac{P}{\pi w^2}$

The beam radius is usually measured where the irradiance is reduced down to a factor e^{-2} of its peak value (w), or down to half of its peak value (Full Width Half Maximum radius, w_{FWHM}).

The temporal profile of the laser beams are assumed to be constant, and the time durations of the pulses used for the calculations are those given by the laser manufacturers. If a Gaussian temporal profile was considered, a further factor $\pi^{-1/2}$ would multiply the two equations for the peak irradiance reported above.

Appendix B.

Laser Induced Incandescence

Laser Induced Incandescence (LII) is a sensitive technique giving high resolution spatial profiles of the soot volume fraction and on the size of the soot particles directly into the flame environment [138]. The LII diagnostic is based on the controlled heating of the soot particles well above the flame temperature (up to 4000-4500 K) by means of a laser pulse. The incandescence signal re-emitted from the heated particles gives information on the soot volume fraction (signal vs. power density) and on the particle size (signal vs. de-excitement time).

The LII signal is quantified as the blackbody emission following the Plank's law, into which the density and optical properties of the primary particles are considered:

$$LII\left(\Delta\lambda_{exc},T\right)=48\pi^2hc^2\int_{\Delta\lambda}\frac{E\left(m\right)}{\lambda_{exc}^6}\left[e^{\frac{hc}{\lambda_{exc}k_BT}}-1\right]^{-1}f_v d\lambda$$

$$f_v = N_p\frac{4}{3}\pi r^3$$

where f_v is the soot volume fraction, $T = T(t)$ and $r = r(t)$ are the time-dependent temperature and radius of the soot primary particles. They can be both obtained from the energy balance calculated on a soot particle in the flame environment under sustained laser irradiance once the border and initial conditions are known. These conditions are: the temporal profile of the laser excitation pulse $I(t)$, the excitation wavelength λ_{exc}, the flame temperature T_0 and the initial particle diameter, a_0.

Figure B1. Schematic representation of the terms participating to the energy balance of an irradiated soot primary particle in the flame environment.

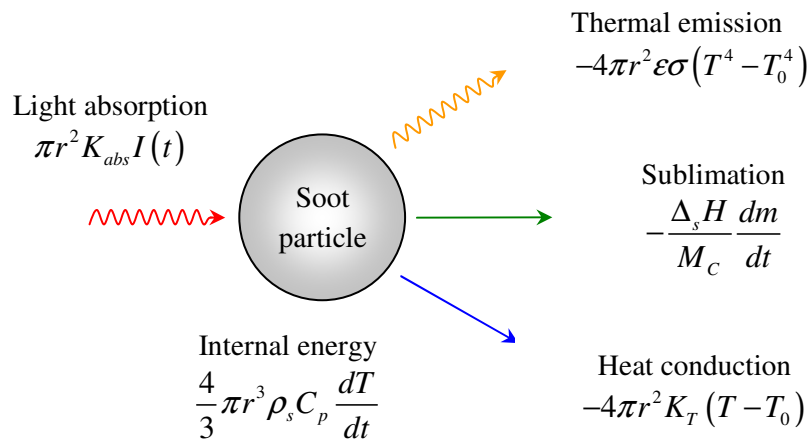In his original work Melton [139] proposed the following energy balance for a spherical particle of radius r:

$$\pi r^2 K_{abs} I(t) - 4\pi r^2 K_T (T - T_0) - \frac{\Delta_s H}{M_C} \frac{dm}{dt} - 4\pi r^2 \varepsilon \sigma (T^4 - T_0^4) + \frac{4}{3}\pi r^3 \rho_s C_p \frac{dT}{dt} = 0$$

As depicted in Figure B1, each one of the five rate terms represents a different phenomenon to which the primary soot particles are subject into the flame environment.

The first term accounts for the absorption of the laser power, taking into account the absorption cross section of the soot particles. I(t) is the time-dependent irradiance of the excitation pulse. In the Rayleigh regime ($2\pi r / \lambda \ll 1$), the light absorption coefficient K_{abs} is only dependent on the particle radius, the excitation wavelength and the complex refraction index:

$$K_{abs} = \frac{8\pi r E(m)}{\lambda}$$

where E(m) is the refractive index function [140].

The second term is the heat transfer for conduction. This is a sensitive term to be considered, because meaningful differences may occur as a function of the size particles. Nevertheless the reported expression is one of the most common used, where K_T is the thermal conductivity in the gas and $T - T_0$ is the temperature difference between the heated soot particle and the flame environment.

The third term is the energy expended in the sublimation process, expressed as a function of the heat of vaporization ($\Delta_s H$), the molecular weight of solid carbon (M_c), and the rate of mass vaporization (dm/dt).

The fourth term is the energy loss by blackbody radiation, which is simply given by the Stefan-Boltzmann's law, where σ and ε are respectively the Stefan-Boltzmann constant and the soot emissivity. Remember that soot particles behave like a grey body, i.e. they absorb and re-emit only a fraction of the exciting radiation. According to Kirchoff's law, the soot emissivity is taken equal to the absorption coefficient K_{abs}.

Finally, the internal energy expressed by the fifth term can be easily calculated knowing the specific heat of carbon (C_p) and the soot density (ρ_s).

LII analyses are allowed on a wide excitation wavelength range. The LII emission constitutes wide-band signals, going from ~300 nm up to the IR, to which the emission of other component in the flame is overlapped. Particularly, the emission of C_2 represents an important interference to the measure. However the infrared laser light, typically the 1064 nm, is a convenient choice because some of the emission bands interfering with the measure (Swan's bands of C_2) are strongly reduced in intensity.

A scheme of the experimental setup used for the LII analyses on the methane low-pressure flame (Section 6.3) is reported in Figure B2 [109]. A slightly modified setup has been used for the measurements on the turbulent jet flame (Section 6.4), which has been detailed in [111,112]. The unfocused excitation laser beam at 1064 nm wavelength is set parallel to the burner surface. The LII signal is collected at right angle using a combination of two plano-convex lenses (200 mm focal length) and a head-on photomultiplier (PMT Philips XP 2237).
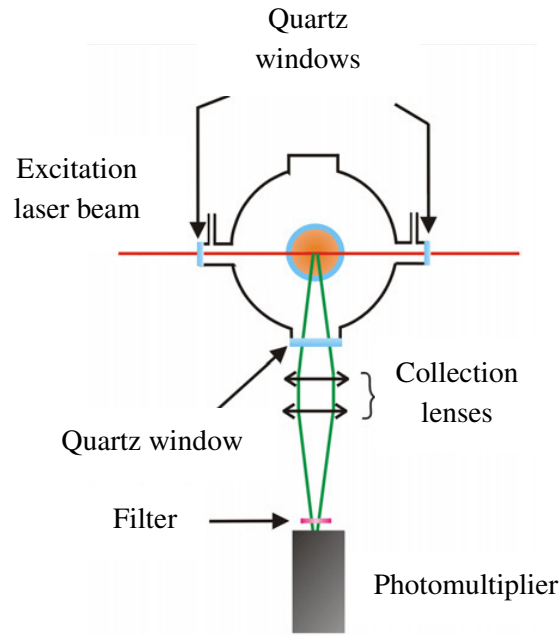
Figure B2. Experimental setup of the LII measurements [109].

Because of the very low signal typical of the low-pressure flames it is necessary to probe a large collection volume while obtaining a good spatial resolution in the vertical direction representative of the reaction time axis. This has been achieved by using a narrow (0.2 mm wide) horizontal slit parallel to the laser beam and placed in front of the photomultiplier, which images the central part of the beam as shown in Figure B2. Thus the collection volume can be approximated by a slab of volume: $w \cdot h \cdot d = 12$ mm^3 being h the height of the slit (10 mm) and d the depth of field limited by the laser beam diameter (6 mm). The soot volume fraction is considered nearly uniform in the selected horizontal slab [109].

The vertical resolution of 0.2 mm is well suited to the investigated low-pressure flames. Measurements are performed by collecting the entire visible range, in order to get a good enough signal/noise ratio within the working pressure range. The soot volume fraction profile obtained this way is presented in Section 6.3.1.

Appendix C.

Estimation of the amount of desorbed

matter

The amount of substance desorbed from soot during a standard LD/LI/TOF-MS analysis has been estimated as follows. Each laser pulse delivered to the sample surface removes some matter from the pool of absorbed species contained in the irradiated region. Thus, when keep irradiating a sample on the same location the peak signal decays as function of the number of laser pulses (Figure 5.8). The signal stands until there is no more matter to be desorbed, and therefore the integral S_{tot} calculated on the overall decay function and the amount of PAH contained in the irradiated volume n_{tot} are proportional:

$$\frac{S_i}{S_{tot}} = \frac{n_i}{n_{tot}} \tag{C1}$$

where S_i and n_i are the integral of the decay curve and the amount substance desorbed up to the ith laser pulse. The variable to find is n_i with $i = 1$, i.e. the amount of substance desorbed with the first laser pulse. The integrals S_i and S_{tot} are given from the desorption curve, while the total amount of substance contained on the irradiated volume n_{tot} is given by:

$$n_{tot} = c_b m_{irr} = c_b V_{irr} \rho_b \tag{C2}$$

where c_b is the bulk concentration of PAH in the sample, m_{irr} is the irradiated mass, V_{irr} is the irradiated volume and $\rho_b = 2.1 \text{ g cm}^{-1}$ the bulk density of the carbon black. In other words, the problem is moved to the evaluation of the parameters c_b and V_{irr}. The former is known from the preparation of the model soot, while the latter can be evaluated from the optical properties of the carbon matrix.

Model soot: c_b

A model soot containing pyrene adsorbed on black carbon has been chosen for the analysis. The model soot sample has been thought to match as well as possible the analysis response of natural soot, i.e. signal peak around 100 mV, and signal decay no longer than 4-5 laser pulses. For the preparation procedure, see Paragraph 5.2.2. The treated model soot contains $c_b = 9.52 \cdot 10^{-8} \; mol/g$ of pyrene on Pureblack 100 black carbon.

Irradiated volume: V_{irr}

The order of magnitude of the irradiated volume can be provided from the linear optical absorption of the carbonaceous matrix (made equal to graphite in this calculation). Since in the desorption optical path the sample is far away from the focus and the absorption coefficient of soot is large, the irradiated volume can be approximated with a cylinder thin with respect to its diameter:

$$V_{irr} = AL \qquad (C3)$$

where A is the impact section of the beam on the sample surface ($A = 2.64 \cdot 10^{-6}\, m^2$, see also Section 4.1.2), and L is the depth of penetration of the beam in graphite. The depth of penetration corresponding to an arbitrary reduction of the beam intensity can be evaluated from the absorption coefficient of pure graphite $k_{abs} = 5 \cdot 10^5$ cm^{-1} [141] using Beer-Lambert's law. For example when:

$$L_{10^{-2}} = \frac{2}{k_{abs}} \approx 40 \text{ nm} \qquad (C4)$$

the beam intensity drops of two orders of magnitude, i.e. the 99% of the beam energy is absorbed. Such a choice for the penetration depth is totally arbitrary. However, while the light attenuation is exponential, the corresponding variation of the penetration depth is only linear (for instance $L_{10^{-6}} \approx 120$ nm), thus this approximation is suitable to get the order of magnitude of the depth of penetration. Substituting Equation (C4) into Equation (C3) with $L = L_{10^{-2}}$:

$$V_{irr} = \frac{2A}{k_{abs}} \qquad (C5)$$

then $V_{irr} \approx 1.1 \cdot 10^{-13}\, m^3$.

Integration: S_i and S_{tot}

Figure C1 reports the integral function calculated on the decays presented in Figure 5.8. Since the penetration depth of the beam on soot depends on I_{des} only the first decay has been considered in order to calculate S_{tot}.
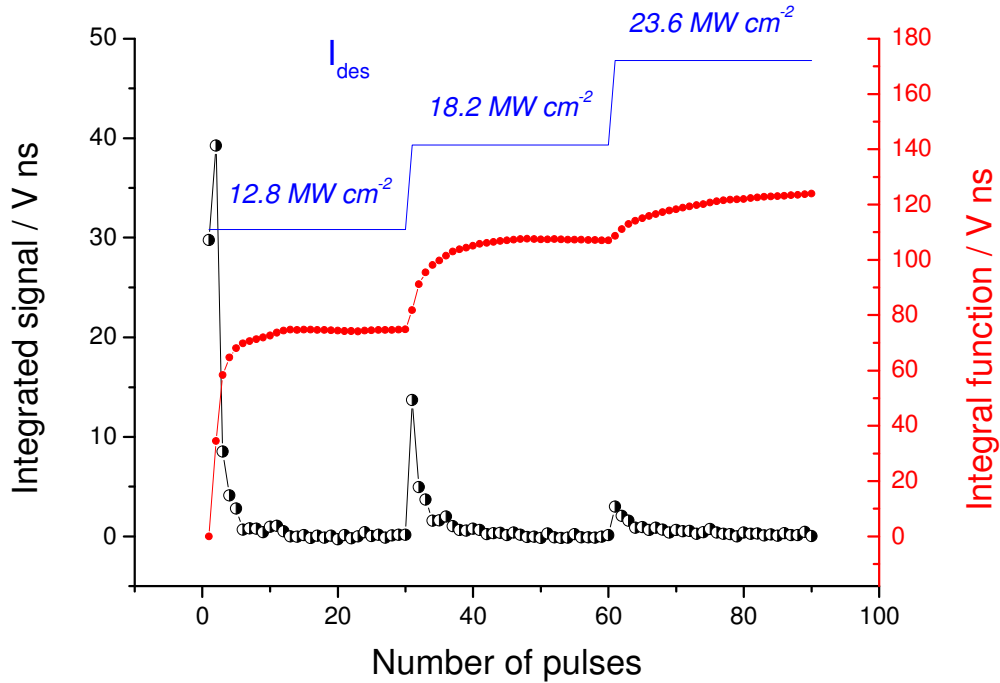
Figure C1. Signal decay (black large dots) and its integral function (red small dots) for different desorption irradiances (blue line) obtained from model soot $9.52 \cdot 10^{-8}$ mol g^{-1} of pyrene in Pureblack 100 Carbon. While the desorption irradiance have been progressively raised up to the carbon breaking threshold, the ionisation irradiance have been kept constant at $I_{ion} = 2.1$ MW cm^{-2}, 50 μs delay between pulses.

The desorption irradiance in this case is I_{des} = 12.8 MW cm^{-2}, about twice that one adopted during routine soot analysis. This choice was needed in order to obtain a signal decay long enough to perform a fit.

The values of the integrals obtained this way are:

$S_1 = 34.5 \; V \cdot ns \cdot shot \; number$

$S_{tot} = 74.9 \; V \cdot ns \cdot shot \; number$

Substituting Equation C2 into Equation C1 and rearranging:

$$n_1 = \frac{S_1}{S_{tot}} c_b V_{irr} \rho_b \qquad\qquad (C6)$$

from which it is possible to get the order of magnitude of the amount of matter desorbed with the first laser pulse, i.e. $n_1 \approx 10 \; fmol$.

Appendix D.

List of the detected masses

Nominal mass	Molecular formula	Nominal mass	Molecular formula	Nominal mass	Molecular formula
78	C_6H_6	350	$C_{28}H_{14}$	570	$C_{46}H_{18}$
92	C_7H_8	352	$C_{28}H_{16}$	572	$C_{46}H_{20}$
94	C_7H_{10}	362	$C_{29}H_{14}$	582	$C_{47}H_{18}$
102	C_8H_6	374	$C_{30}H_{14}$	584	$C_{47}H_{20}$
116	C_9H_8	386	$C_{31}H_{14}$	594	$C_{48}H_{18}$
128	$C_{10}H_8$	388	$C_{31}H_{16}$	606	$C_{49}H_{18}$
140	$C_{11}H_8$	398	$C_{32}H_{14}$	608	$C_{49}H_{20}$
142	$C_{11}H_{10}$	400	$C_{32}H_{16}$	618	$C_{50}H_{18}$
152	$C_{12}H_8$	412	$C_{33}H_{16}$	630	$C_{51}H_{18}$
154	$C_{12}H_{10}$	424	$C_{34}H_{16}$	632	$C_{51}H_{20}$
166	$C_{13}H_{10}$	426	$C_{34}H_{18}$	642	$C_{52}H_{18}$
178	$C_{14}H_{10}$	438	$C_{35}H_{18}$	654	$C_{53}H_{18}$
190	$C_{15}H_{10}$	448	$C_{36}H_{16}$	666	$C_{54}H_{18}$
202	$C_{16}H_{10}$	450	$C_{36}H_{18}$	668	$C_{54}H_{20}$
216	$C_{17}H_{12}$	460	$C_{37}H_{16}$	680	$C_{55}H_{20}$
226	$C_{18}H_{10}$	472	$C_{38}H_{16}$	692	$C_{56}H_{20}$
228	$C_{18}H_{12}$	484	$C_{39}H_{16}$	694	$C_{56}H_{22}$
240	$C_{19}H_{12}$	496	$C_{40}H_{16}$	706	$C_{57}H_{20}$
252	$C_{20}H_{12}$	498	$C_{40}H_{18}$	716	$C_{58}H_{20}$
264	$C_{21}H_{12}$	508	$C_{41}H_{16}$	718	$C_{58}H_{22}$
276	$C_{22}H_{12}$	510	$C_{41}H_{18}$	730	$C_{59}H_{22}$
288	$C_{23}H_{12}$	520	$C_{42}H_{16}$	740	$C_{60}H_{20}$
300	$C_{24}H_{12}$	522	$C_{42}H_{18}$	742	$C_{60}H_{22}$
302	$C_{24}H_{14}$	534	$C_{43}H_{18}$	752	$C_{61}H_{20}$
314	$C_{25}H_{14}$	536	$C_{43}H_{20}$	764	$C_{62}H_{20}$
326	$C_{26}H_{14}$	546	$C_{44}H_{18}$	778	$C_{63}H_{22}$
328	$C_{26}H_{16}$	548	$C_{44}H_{20}$	780	$C_{63}H_{24}$
338	$C_{27}H_{14}$	558	$C_{45}H_{18}$	792	$C_{64}H_{24}$

Figure D1. Full list of the *nominal* masses attributed to PAH and detected on the soot collected from the methane low pressure flame at 15 mm HAB (Section 6.3).

Acknowledgements

And there we go, at the end of this three years long journey… Before concluding – and this time once and for all, I promise! – I just would like to mention and to thanks all the people which have made possible this work.

First of all I would like to thanks my parents Rita and Ivan for the constant encouragement and support provided during every crazy adventure that I begin (and sometimes that I finish too!), especially this last one abroad…

This work would not have been possible without the dedication of Dr. Pascale Desgroux and Dr. Michael Ziskind and the support from Prof. Cristian Focsa. Particularly warm thanks are devoted to Dr. Desgroux for the hours-long scientific discussions as well as the nights just before the deadline passed revising this manuscript.

Thanks to Kevin, for the great time spent together during the first year of my PhD learning the fundamentals of the experimental technique, as well as for his pumpkin cake recepi! Hang in there Kevin, even if your coke won't be any longer as fresh as you were used to!

And many thanks to Marc and Thierry for the irreplaceable help provided during the lab move and to Marc (the *other* Marc, now in Strasbourg!) for the days spent in lab trying to obtain a decent Top-Hat laser profile…

Special thanks are also due to Eric, Natalie and Xavier for their precious advises concerning the data interpretation, and to Béatrice for her unfailing French lessons and especially for having dealt with the huge mess of papers which actually was the first version of this dissertation!

A bit less scientific but still fundamental support came from all the old and new friends met in Lille. First of all from Sara and Oliver, the couple of *adventurers* I started this journey with!

And again thanks to Romain and Claudia & Claudio first met as my lab neighbours, to Iain the Scottish and The Maxime. Particularly huge thanks to Adriana, the fellow student I shared the lab with, who had to stand me during all the measurement campaign… Not an easy task indeed!

Last but not least, how to forget Alex, Tanguy, the *Trois Brasseurs* and the Unreal amount of beer drunk together?!?

Bibliography

[1] K.H. Homann, H.G. Wagner, *Some new aspects of the mechanism of carbon formation in premixed flames*, Proc Combust Inst 11 (1967) 371

[2] H.F. Calcote, *Mechanisms of soot nucleation in flames – A critical review*, Combust Flame 42 (1981) 215

[3] B.S. Haynes, H.G. Wagner, *Soot formation*, Prog Energy Combust Sci 7 (1981) 229

[4] A. Keller, R. Kovacs, K.H. Homann, *Large molecules, ions, radicals and small soot particles in fuel-rich hydrocarbon flames. Part IV: large polycyclic aromatic hydrocarbons and their radicals in a fuel-rich benzene/oxygen flame*, Phys Chem Chem Phys 2 (2000) 1667

[5] B. Öktem, M.P. Tolocka, B. Zhao, H. Wang, M.V. Johnston, *Chemical species associated with the early stage of soot growth in a laminar premixed ethylene/oxygen/argon flame*, Combust Flame 142 (2005) 364

[6] O. Mathieu, G. Frache, N. Djebaili-Chaumeix, C.E. Paillard, G. Krier, J.F. Muller, F. Douce, P. Manuelli, *Characterization of adsorbed species on soot formed behind reflected shock waves*, Proc Comb Inst 31 (2007) 511

[7] J. Griesheimer, K.H. Homann, *Large molecules, radicals, ions, and small soot particles in fuel-rich hydrocarbon flames. Part II: aromatic radicals and intermediate PAH in a premixed low-pressure naphthalene/oxygen/argon flame*, Proc Comb Inst 27 (1998) 1753

[8] H. Richter, S. Granata, W.H. Green, J.B. Howard, *Detailed modeling of PAH and soot formation in a laminar premixed benzene/oxygen/argon low-pressure flame*, Proc Comb Inst 30 (2005) 1397

[9] H. Wang, M. Frenklach, *Transport properties of polycyclic aromatic hydrocarbons for flame modelling*, Combust Flame 96 (1994) 163

[10] H. Böhm, H. Jander, *PAH formation in acetylene-benzene pyrolysis*, Phys Chem Chem Phys 1 (1999) 3775

[11] P. Weilmünster, A. Keller, K.H. Homann, Large molecules, radicals, ions, and small soot particles in fuel-rich hydrocarbon flames. Part I: positive ions of polycyclic aromatic hydrocarbons (PAH) in low-pressure premixed flames of acetylene and oxygen, Combust Flame 116 (1999) 62

[12] H. Wang, M. Frenklach, *A detailed kinetic modeling study of aromatics formation in laminar premixed acetylene and ethylene flames*, Combust Flame 110 (1997) 173

[13] C.F. Melius, J.A. Miller, E.M. Evleth, *Unimolecular reaction mechanisms involving C_3H_4, C_4H_4 and C_6H_6 hydrocarbon species*, Proc Combust Inst 24 (1992) 621

[14] C.F. Melius, M.E. Colvin, N.M. Marinov, W.J. Pitz, S.M. Senkan, *Reaction mechanisms in aromatic hydrocarbon formation involving the C_5H_5 cyclopentadienyl moiety*, Proc Combust Inst 26 (1996) 685

[15] P.R. Westmoreland, A.M. Dean, J.B. Howard, J.P. Longwell, *Forming benzene in flames by chemically activated isomerisation*, J Phys Chem 93 (1989) 8171

[16] R.D. Kern, K. Xie, *Shock tube studies of gas phase reactions preceding the soot formation process*, Prog Energy Combust Sci 17 (1991) 191

[17] M. Frenklach, D.W. Clary, W.C. Gardiner, S.E. Stein, *Detailed kinetic modelling of soot formation in shock-tube pyrolysis of acetylene*, Proc Comb Inst 20 (1985) 887

[18] M. Frenklach, J. Warnatz, Detailed modeling of PAH profiles in a sooting low-pressure acetylene flame, Combust Sci Tech 51 (1987) 265

[19] M. Weissman, S. Benson, *Pyrolysis of methyl chloride, a pathway in the chlorine-catalyzed polymerization of methane*, Int J Chem Kinet, 16 (1984) 307

[20] J.A. Cole, J.D Bittner, J.P. Longwell, J.B. Howard, *Formation mechanisms of aromatic compounds in aliphatic flames*, Combust Flame 56 (1984) 51

[21] J.A. Miller, C.F. Melius, *Kinetic and thermodynamic issues in the formation of aromatic compounds in flames of aliphatic fuels*, Combust Flame 91 (1992) 21

[22] M. Frenklach, T. Yuan, M.K. Ramachandra, *Soot formation in binary hydrocarbon mixtures*, Energy Fuels 2 (1988) 462

[23] N.M. Marinov, M.J. Castaldi, C.F. Melius, W. Tsang, *Aromatic and polycyclic aromatic hydrocarbon formation in a premixed propane flame*, Combust Sci Technol 128 (1997) 295

[24] M. Frenklach, S. Taki, M.B. Durgaprasad, R.A. Matula, *Soot formation in shock-tube pyrolysis of acetylene, allene, and 1,3-butadiene*, Combust Flame 54 (1983) 81

[25] C.S. McEnally, L.D. Pfefferle, B. Atakan, K. Kohse-Höinghaus, *Studies of aromatic hydrocarbon formation mechanisms in flames: progress towards closing the fuel gap*, Prog Energy Combust Sci 32 (2006) 247

[26] M. Frenklach, *Reaction mechanism of soot formation in flames*, Phys Chem Chem Phys 4 (2002) 2028

[27] J.A. Miller, M.J. Pilling, J. Troe, *Unravelling combustion mechanism through a quantitative understanding of elementary reactions*, Proc Comb Inst 30 (2005) 43

[28] S.E. Stein, A. Fahr, *High- temperature stabilities of hydrocarbons*, J Phys Chem A 89 (1985) 3714

[29] A.M. Cowperswaite, S.H.J. Bauer, *Estimation of molecular parameters of C/H fragments*, J Chem Phys 36 (1962) 1743

[30] R.E. Duff, S.H. Bauer, *Equilibrium composition of the C/H system at elevated temperatures*, J Chem Phys 36 (1962) 1754

[31] M. Frenklach, H. Wang, *Detailed modelling of soot particle nucleation and growth*, Proc Combust Inst 23 (1991) 1559

[32] J. Appel, H. Bockhorn, M. Frenklach, *Kinetic modeling of soot formation with detailed chemistry and physics: laminar premixed flames of C_2 hydrocarbons*, Combust Flame 121 (2000) 122

[33] M. Frenklach, D.W. Clary, W.C. Gardiner, S.E. Stein, *Effect of fuel structure on pathways to soot*, Proc Comb Inst 21 (1987) 1067

[34] M. Frenklach, N.M. Moriarty, N.J. Brown, *Hydrogen migration in polyaromatic growth*, Proc Comb Inst 27 (1998) 1655

[35] R. Whitesides, A.C. Kollias, D. Domin, W.A. Lester, M. Frenklach, *Graphene layer growth: collision of migrating five-member rings*, Proc Combust Inst 31 (2007) 539

[36] M. Frenklach, C.A. Schuetz, J. Ping, *Migration mechanism of aromatic-edge growth*, Proc Comb Inst 30 (2005) 1389

[37] C.P. Leusden, N. Peters, *Experimental and numerical analysis of the influence of oxygen on soot formation in laminar counterflow flames of acetylene*, Proc Combust Inst 28 (2000) 2619

[38] D.K. Hahn, S.J. Klippenstein, J.A. Miller, *A theoretical analysis of the reaction between propargyl and molecular oxygen*, Faraday Discuss 119 (2002) 79

[39] T. Ishiguro, Y. Takatori, K. Akihama, *Microstructure of diesel soot particles probed by electron microscopy: first observation of inner core and outer shell*, Combust Flame 108 (1997) 231

[40] O.I. Smith, *Fundamentals of soot formation in flames with application to Diesel engine particulate emissions*, Prog Energy Combust Sci 7 (1981) 275

[41] R.L. Vander Wal, A.J. Tomasek, T.M. Ticich, *Synthesis, laser processing, and flame purification of nanostructured carbon*, Nano Letters 3 (2003) 223

[42] M.M Maricq, *A comparison of soot size and charge distributions from ethane, ethylene, acetylene and benzene/ethylene premixed flames*, Combust Flame 144 (2006) 730

[43] D. Cecere, L.A. Sgro, G. Basile, A. D'Alessio, A. D'Anna, P. Minutolo, *Evidence and characterization of nanoparticles produced in nonsooting premixed flames*, Combust Sci Technol 174 (2002) 377

[44] L.A. Sgro, G. Basile, A.C. Barone, A. D'Anna, P. Minutolo, A. Borghese, A. D'Alessio, *Detection of combustion formed nanoparticles*, Chemosphere 51 (2003) 1079

[45] L.A. Sgro, P. Minutolo, G. Basile, A. D'Alessio, *UV-visible spectroscopy of organic carbon particulate sampled from ethylene/air flames*, Chemosphere 42 (2001) 671

[46] J. Happold, H.H. Grotheer, M. Aigner, *Distinction of gaseous soot precursor molecules and soot precursor particles through photoionisation mass spectrometry*, Rapid Commun Mass Spectrom 21 (2007) 1247

[47] M. Frenklach, L.B. Ebert, *Comment on the proposed role of spheroidal carbon clusters in soot formation*, J Phys Chem 92 (1988) 561

[48] J.H. Miller, *The kinetics of polynuclear aromatic hydrocarbon agglomeration in flames*, Proc Comb Inst 23 (1990) 91

[49] P. Minutolo, G. Gambi, A. D'Alessio, A. D'Anna, *Optical and spectroscopic characterization of rich premixed flames across the soot formation threshold*, Combust Sci Tech 101 (1994) 311

[50] A. D'Anna, A. Violi, *A kinetic model for the formation of aromatic hydrocarbons in premixed laminar flames*, Proc Combust Inst 27 (1998) 425

[51] A. D'Anna, A. Violi, A. D'Alessio, A.F. Sarofim, *A reaction pathway for nanoparticle formation in rich premixed flames*, Combust Flame 127 (2001) 1995

[52] A. Violi, A.F. Sarofim, T.N. Truong, *Quantum mechanical study of molecular weight growth process by combination of aromatic molecules*, Combust Flame 126 (2001) 1506

[53] S.J. Harris, I.M. Kennedy, *The coagulation of soot particles with van der Waals Forces*, Combust Sci and Technol 59 (1988) 443

[54] J.H. Miller, *Aromatic excimers: evidence for polynuclear aromatic hydrocarbon condensation in flames*, Proc Combust Inst 30 (2005) 1381

[55] J.Z. Wen, M.J. Thomson, M.F. Lightstone, S.N. Rogak, *Detailed kinetic modeling of carbonaceous nanoparticle inception and surface growth during the pyrolysis of C_6H_6 behind shock waves*, Energy Fuels 20 (2006) 547

[56] Q.L. Zhang, S.C. O'Brien, J.R. Heath, Y. Liu, R.F. Curl, H.W. Kroto, R.E. Smalley, *Reactivity of large carbon clusters: spheroidal carbon shells and their possible relevance to the formation and morphology of soot*, J Phys Chem 90 (1986) 525

[57] K.H. Homann, *Carbon formation in premixed flames*, Combust Flame 11 (1967) 265

[58] P. Mitchell, M. Frenklach, Monte Carlo simulation of soot aggregation with simultaneous surface growth - why primary particles appear spherical, Proc Combust Inst 27 (1998) 1507

[59] H. Bockhorn, *Soot formation in combustion – Mechanism and models*, Springer-Verlag, Berlin (1994)

[60] S.J. Harris, A.M. Weiner, Surface growth of soot particles in premixed ethylene/air flames, Combust Sci Tech 31 (1983) 155

[61] T.G. Benish, A.L. Lafleur, K. Tghizadeh, J.B. Howard, *C_2H_2 and PAH as soot growth reactants in premixed C_2H_4-air flames*, Proc Comb Inst 26 (1997) 2319

[62] K.G. Neoh, J.B. Howard, A.F. Sarofim, *Effect of oxidation on the physical structure of soot*, Proc Comb Inst 20 (1985) 951

[63] R.P. Lucht, D.W. Sweeney, N.M. Laurendeau, *Laser-saturated fluorescence measurements of OH in atmospheric pressure $CH_4/O_2/N_2$ flames under sooting and non-sooting conditions*, Comb Sci Technol 42 (1985) 259

[64] S.J Harris, A.M. Weimer, *Determination of the rate constant for soot surface growth*, Combust Sci Technol 32 (1983) 267

[65] S.J. Harris, A.M. Weimer, *Chemical kinetics of soot particle growth*, Annu Rev Phys Chem 36 (1985) 31

[66] I.M. Kennedy, *Models of soot formation and oxidation*, Prog Energy Combust Sci 23 (1997) 95

[67] A. Ciajolo, B. Apicella, R. Barbella, A. Tregrossi, F. Beretta, C. Allouis, *Depletion of fuel aromatic components and formation of aromatic species in a spray flame as characterized by fluorescence spectroscopy*, Energy Fuel 15 (2001) 987

[68] A. Tregrossi, A. Ciajolo, R. Barbella, *The combustion of benzene in rich premixed flames at atmospheric pressure*, Combust Flame 117 (1999) 553

[69] R. Zimmermann, L. Van Vaeck, M. Davidovic, M. Beckmann, F. Adams, *Analysis of polycyclic aromatic hydrocarbons (PAH) adsorbed on soot particles by fourier transform laser microprobe mass spectrometry (FT LMMS): variation of the pah patterns at different positions in the combustion chamber of an incineration plant*, Environ Sci Technol 34 (2000) 4780

[70] R. Zenobi, R.N. Zare, *Advances in multiphoton spectroscopy and processes*, S.H. Lin Ed, World Scientific: Singapore Vol 7 (1991)

[71] J.E. Elsila, N.P. de Leon, R.N. Zare, *Factors affecting quantitative analysis in laser desorption/laser ionisation mass spectrometry*, Anal Chem 76 (2004) 2430

[72] R.A. Dobbins, R.A. Fletcher, H.C. Chang, *The evolution of soot precursor particles in a diffusion flame*, Combust Flame 115 (1998) 285

[73] R.A. Dobbins, R.A. Fletcher, W. Lu, *Laser microprobe analysis of soot precursor particles and carbonaceous soot*, Combust Flame 100 (1995) 301

[74] I. Goldhirsch, D. Ronis, *Theory of thermophoresis – I General considerations and mode-coupling analysis*, Phys Rev A 27 (1983) 1616

[75] I. Goldhirsch, D. Ronis, *Theory of thermophoresis – II Low-density behavior*, Phys Rev A 27 (1983) 1635

[76] B. Apicella, A. Carpentieri, M. Alfè, R. Barbella, A. Tregrossi, P. Pucci, A. Ciajolo, *Mass spectrometric analysis of large PAH in a fuel-rich ethylene flame*, Proc Combust Inst 31 (2007) 547

[77] B. Apicella, M. Millan, A.A. Herod, A. Carpentieri, P. Pucci, A. Ciajolo, *Separation and measurement of flame-formed high molecular weight polycyclic aromatic hydrocarbons by size-exclusion chromatography and laser desorption/ionisation time-of-flight mass spectrometry*, Rapid Commun Mass Spectrom 20 (2006) 1104

[78] B. Öktem, M.P. Tolocka, M.V. Johnston, *On-line analysis of organic components in fine and ultrafine particles by photoionisation aerosol mass spectrometry*, Anal Chem 76 (2004) 253

[79] O. Mathieu, G. Frache, N. Djebaïli-Chaumeix, C.E. Paillard, G. Krier, J.F. Muller, F. Douce, P. Manuelli, *Laser desorption-ionisation time-of-flight mass spectrometry for analyses of heavy hydrocarbons adsorbed on soot formed behind reflected shock waves*, Proc Combust Inst 32 (2009) 971

[80] L.V. Zhigilei, E. Leveugle, B.J. Garrison, Y.G. Yingling, M.I. Zeifman, *Computer simulations of laser ablation of molecular substrates*, Chem Rev 103 (2003) 321

[81] R. Kelly, A. Miotello, *Comments on explosive mechanisms of laser sputtering*, Appl Surf Sci 96-98 (1996) 205

[82] M. Karas, D. Bachman, F. Hillenkamp, *Influence of the wavelength in high-irradiance ultraviolet laser desorption mass spectrometry of organic molecules*, Anal Chem 57 (1985) 2935

[83] L.V. Zhigilei, B.J. Garrison, *Microscopic mechanisms of laser ablation of organic solids in the thermal and stress confinement irradiation regimes*, J Appl Phys 88 (2000) 1281

[84] National Institute of Standards and Technology (NIST) database, available online at www.nist.gov

[85] F. Cignoli, G. Zizak, S. Benecchi, D. Tencalla, *Atlas of fluorescence spectra of aromatic hydrocarbons*, Editorial group & Graphic design: S. De Iuliis, D. Ferretti (1992)

[86] R. Boyd, *Nonlinear Optics*, 2nd Edition, Academic Press (2003)

[87] H.H. Grotheer, H. Pokorny, K.L. Barth, M. Thierley, M. Aigner, *Mass spectrometry up to 1 million mass units for the simultaneous detection of primary soot and of soot precursors (nanoparticles) in flames*, Chemosphere 57 (2004) 1335

[88] U. Boesl, *Laser mass spectrometry for environmental and industrial chemical trace analysis*, J Mass Spectrom 35 (2000) 289

[89] O.P. Haefliger, R. Zenobi, *Laser mass spectrometric analysis of polycyclic aromatic hydrocarbons with wide wavelength range laser multiphoton ionisation spectroscopy*, Anal Chem 70 (1998) 2660

[90] U. Boesl, *Multiphoton excitation and mass-selective ion detection for neutral and ion spectroscopy*, J Phys Chem 95 (1991) 2949

[91] M. Guilhaus, V. Mlynski, D. Selby, *Perfect timing: Time-Of-Flight Mass Spectrometry*, Rapid Commun Mass Spectrom 11 (1997) 951

[92] M. Guilhaus, J Mass Spectrom, *Principles and instrumentation in Time-Of-Fight Mass Spectrometry*, 30 (1995) 1519

[93] B.A. Mamyrin, *Time-Of-Flight mass spectrometry (concepts, achievements, and prospects)*, Int J Mass Spectrom 206 (2001) 251

[94] R.A. Fletcher, R.A Dobbins, H.C. Chang, *Mass spectrometry of particles formed in a deuterated ethene diffusion flame*, Anal Chem 70 (1998) 2745

[95] J.R. Dias, *Handbook of Polycyclic Hydrocarbons*, Elsevier, Amsterdam (1987), data available on NIST online database at www.nist.gov

[96] B. Apicella, R. Barbella, Ciajolo, A. Tregrossi, *Formation of low- and high-molecular weight hydrocarbon species in sooting ethylene flames*, Combust Sci Technol 174 (2002) 309

[97] H.H. Grotheer, K. Hoffmann, K. Wolf, S. Kanjarkar, C. Wahl, M. Aigner, *Study of carbonaceous nanoparticles in premixed C_2H_4–air flames and behind a spark ignition engine*, Combust Flame 156 (2009) 791

[98] K.H. Homann, H. Wolf, *Charged soot in low-pressure acetylene/oxygen flames*, Proc Combust Inst 21 (1988) 1013

[99] K. Siegmann, H.C. Siegmann, *The formation of carbon in combustion and how to quantify the impact on human health*, Europhysics News 28 (1997) 50

[100] K. Thomson, M. Ziskind, C. Mihesan, E. Therssen, P. Desgroux, C. Focsa, *Influence of the photoionisation process on the fragmentation of laser desorbed polycyclic aromatic hydrocarbons*, Appl Surf Sci 253 (2007) 6435

[101] C. Mihesan, M. Ziskind, E. Therssen, P. Desgroux, C. Focsa, *IR laser resonant desorption of polycyclic aromatic hydrocarbons*, Chem Phys Lett, 423 (2006) 407

[102] C. Mihesan, M. Ziskind, B. Chazallon, E. Therssen, P. Desgroux, S. Gurlui, C. Focsa, *IR wavelength-selective laser desorption via OH and CH stretching modes*, Appl Surf Sci, 253 (2006) 1090

[103] Y. Bouvier, C. Mihesan, M. Ziskind, E. Therssen, C. Focsa, J.F. Pauwels, P. Desgroux, *Molecular species adsorbed on soot particles issued from low sooting methane and acetylene laminar flames: a laser-based experiment*, Proc Combust Inst 31 (2007) 841

[104] S.M. Hankin, P. John, *Laser Time-of-Flight Mass Analysis of PAHs on Single Diesel Particulates*, Anal Chem 71 (1999) 1100

[105] R.J. Cotter, S. Iltchenko, D. Wang, *The curved-field reflectron: PSD and CID without scanning, stepping or lifting*, Int J Mass Spectrom 240 (2005) 169

[106] W.H. Aberth Rev Sci Instrum, *Construction of an einzel lens capable of high voltage operation*, 45 (1974) 1289

[107] T.I. Wang, C.W. Chu, H.M. Hung, G.S. Kuo, C.C. Han, *Design parameters of dual-stage ion reflectrons*, Rev Sci Instrum 65 (1994) 1585

[108] G. Westmacott, M. Frank, S.E. Labov, W.H. Benner, *Using a superconducting tunnel junction detector to measure the secondary electron emission efficiency for a microchannel plate detector bombarded by large molecular ions*, Rapid Commun Mass Spectrom, 14 (2000) 1854

[109] P. Desgroux, X. Mercier, B. Lefort, R. Lemaire, E. Therssen, J.F. Pauwels, *Soot volume fraction measurement in low-pressure methane flames by combining laser-induced incandescence and cavity ring-down spectroscopy: Effect of pressure on soot formation*, Combust Flame 155 (2008) 289

[110] X. Mercier, M. Wartel, J.F. Pauwels, P. Desgroux, *Implementation of a new spectroscopic method to quantify aromatic species involved in the formation of soot particles in flames*, Appl Phys B 91 (2008) 387

[111] R. Lemaire, *Etude de l'impact de la combustion de différents types de carburants sur les caractéristiques physico-chimiques des particules de suie par couplage de l'Incandescence et de la Fluorescence Induite par Laser*, PhD thesis (2008) University of Lille 1 (in French)

[112] R. Lemaire, A. Faccinetto, E. Therssen, M. Ziskind, C. Focsa, P. Desgroux, *Experimental comparison of soot formation in turbulent flames of Diesel and surrogate Diesel fuels*, Proc Combust Inst 32 (2009) 737

[113] J.C. Biordi, C.P. Lazzara, J.F. Papp, *Molecular beam mass spectrometry applied to determining the kinetics of reactions in flames, I. Empirical characterization of flame perturbation by molecular beam sampling probes,* Combust Flame 21 (1973) 371

[114] C. Focsa, C. Mihesan, M. Ziskind, B. Chazallon, E. Therssen, P. Desgroux, J.L. Destombes, *Wavelength-selective vibrationally excited photodesorption with tunable IR sources*, J Phys Condens Mat 18 (2006) S1357

[115] C. Mihesan, M. Ziskind, E. Therssen, P. Desgroux, C. Focsa, *Parametric study of polycyclic aromatic hydrocarbon laser desorption*, J Phys Condens Matter 20 (2008) 025221

[116] C. Mihesan, *Mise en œuvre et caractérisation d'une technique de désorption laser couplée à la spctrometrie de masse pour l'analyse d'hydrocarbures aromatiques polycycliques adsorbés à la surface de particules de suies*, PhD thesis (2007) University of Lille 1 (in French)

[117] W. Karcher, R.J. Fordham, J.J. Dubois, J.M. Glaude, J.A.M. Ligthart, D.Reidel, *Spectral atlas of polycyclic aromatic compounds*, Kulwer Academic Publisher Group, Dordrecht-Boston-Lancaster (1983)

[118] K. Bieman, *Mass spectroscopy: organic chemical applications* (1962) McGraw-Hill

[119] X. Guo, H.L. Sievers, H.F. Grützmacher, *Hydrogen atom elimination from polycyclic aromatic hydrocarbons with sustained off-resonance irradiation: a new approach to produce carbon/hydrogen cluster cations $C_nH_x^+$*, Int J Mass Spectrom 185-187 (1999) 1

[120] S. M. Hankin, P. John, A.W. Simpson, G.P. Smith, *spatially resolved time-of-flight mass spectrometry of polycyclic aromatic hydrocarbons: quantification studies*, Anal Chem 68 (1996) 3238

[121] M. Kalberer, B.D. Morrical, M. Sax, R. Zenobi, *Picogram quantitation of polycyclic aromatic hydrocarbons adsorbed on aerosol particles by two-step laser mass spectrometry*, Anal Chem 74 (2002) 3492

[122] C. Weickhardt, K. Tonnies, D. Globig, *Detection and quantification of aromatic contaminants in water and soil samples by means of laser desorption laser mass spectrometry*, Anal Chem 74 (2002) 4861

[123] R. Zimmermann, M. Blumenstock, H.J. Heger, K.W. Schramm, A. Kettrup, *Emission of nonchlorinated and chlorinated aromatics in the flue gas of incineration plants during and after transient disturbances of combustion conditions: delayed emission effects*, Environ Sci Technol 35 (2001) 1019

[124] P.M. Johnson, C.E. Otis, *Molecular multiphoton spectroscopy with ionisation detection*, Annu Rev Phys Chem 32 (1981) 139

[125] U. Boesl, *Multiphoton excitation and mass-selective ion detection for neutral and ion spectroscopy*, J Phys Chem 95 (1991) 2949

[126] A. Faccinetto, K. Thomson, M. Ziskind, C. Focsa, *Coupling of desorption and photoionisation processes in two-step laser mass spectrometry of polycyclic aromatic hydrocarbons*, Appl Phys A 92 (2008) 969

[127] B. Apicella, M. Alfè, R. Barbella, A. Tregrossi, A. Ciajolo, *Aromatic structures of carbonaceous materials and soot inferred by spectroscopic analysis*, Carbon 42 (2004) 1583

[128] A. Ciajolo, R. Ragucci, B. Apicella, R. Barbella, M. de Joannon, A. Tregrossi, *Fluorescence spectroscopy of aromatic species produced in rich premixed ethylene flames*, Chemosphere 42 (2001) 835

[129] M. Wartel, ongoing PhD thesis (2009) University of Science and Technology of Lille (in French)

[130] P. Dagaut, M. Cathonnet, *The ignition, oxidation, and combustion of kerosene: a review of experimental and kinetic modeling*, Prog Energy Combust Sci 32 (2006) 48

[131] J.T. Farrell, H. Pitsch, N.P. Cernansky, F.L. Dryer, D.Friend, C.A. Hergart, C.K. Law, R.M. McDavid, C.J. Mueller, A. Patel, *Development of an Experimental Database and Kinetic Models for Surrogate Diesel Fuels*, SAE Paper (2007) 2007-01-0201

[132] E. Therssen, Y. Bouvier, C. Schoemaecker-Moreau, X. Mercier, P. Desgroux, M. Ziskind, C. Focsa, *Determination of the ratio of soot refractive index function E(m) at the two wavelengths 532 and 1064 nm by laser induced incandescence*, Appl Phys B 89 (2007) 417

[133] H. Kogelnik, T. Li, *Laser beams and resonators*, Appl Optics 5 (1966), 1550

[134] N. El Mejdoub, B. Calaminus, G. Trouvé, P. Gilot, L. Delfosse, *Reactivity of the soot produced during pyrolysis of hexachlorobenzene. Influence of the presence of chlorine*, Carbon 33 (1995) 1593

[135] A. Smekens, M. Knupfer, P. Berghmans, R. Van Grieken, *The elemental composition and microstructure of soot emitted by different sources*, J Aerosol Sci 31 (2000) S917

[136] K. Siegmann, K. Sattler, H.C. Siegmann, *Clustering at high temperatures: carbon formation in combustion*, J Electron Spectrosc Relat Phenom 126 (2002) 191

[137] R. Lemaire, M. Maugendre, T. Schuller, E. Therssen, J. Yon, *Original use of a direct injection high efficiency nebulizer for the standardization of liquid fuels spray flames*, Rev Sci Instrum 80 (2009) 105105

[138] C.R. Shaddix, K.C. Smyth, *Laser-Induced Incandescence measurements of soot production in steady and flickering methane, propane, and ethylene diffusion flames*, Comb Flame 107 (1996) 418

[139] L.A. Melton, *Soot diagnostics based on laser heating*, Applied Optics, 23 (1984) 2201

[140] K.C. Smyth, C.R. Shaddix, *The elusive history of $\tilde{m} = 1.57 - 0.56i$ for the refractive index of soot*, Combust Flame 107 (1996) 314

[141] M. Khaleeq-ur-Rahman, M.S. Rafique, K. Siraj, S. Shahid, M.S. Anwar, H. Faiz, *Theoretical and experimental comparison of splashing in different materials*, 31st EPS Conference on Plasma Physics, London, ECA 28G, (2004) 2049

Abstract

Polycyclic Aromatic Hydrocarbons (PAH) are important precursors of carbonaceous soot particles, thus influence the quantity and morphology of particulate emission of combustion processes. Furthermore the PAH adsorbed on the surface of the soot particles contribute to the carcinogenicity of the particles, so there is scientific interest in characterising and quantifying those species to provide key information on the mechanism of soot formation and to understand their impact on environment and human health.

An original setup based on the coupling of Laser Desorption, Laser Ionisation and Time-Of-Flight Mass Spectrometry techniques has been dedicated to the analysis of PAH desorbed from soot. Briefly, soot is sampled from flames using an extractive vacuum probe and deposed on porous filters. The samples are irradiated with a 532 nm laser beam to promote the desorption of neutral molecules. The ejecta are then ionised with a 266 nm laser beam, and the positive ions produced this way are mass analysed in a TOF-MS.

The complete characterisation of the desorption and ionisation process has been the first goal of this work. The acquired expertise allowed investigations on different flames in which the PAH have been identified and studied at different level of their formation. Particularly, relevant differences in the mass spectra have been detected in the soot inception region. A new method based on the deposition of soot on different substrates is proposed in order to distinguish the PAH belonging to the gas-phase during the sampling from those adsorbed on soot particles, hence the role of the heterogeneous reactions between gaseous PAH and soot particles has been highlighted.

Résumé

Présent dès les premiers instants de la combustion, les Hydrocarbures Aromatiques Polycycliques (HAP) jouent un rôle prépondérant dans la formation des suies avant d'être adsorbés par les particules ainsi formées. Les HAP influencent ainsi la quantité, la composition et la morphologie des suies émises pendant la combustion. L'étude de l'évolution de la phase adsorbée de ces particules au sein de la flamme doit permettre de mieux comprendre leur mécanisme de formation ainsi que leur impact sur la santé et l'environnement.

Une expérience originale dédiée à une telle étude et basée sur le couplage des techniques de Désorption Laser, Ionisation Laser et Spectrométrie de Masse a été développée pendant cette thèse. Des suies collectées dans des flammes sont irradiées par un laser à 532 nm permettant ainsi la libération des HAP adsorbés. Les HAP sont ionisés par un deuxième laser à 266 nm avant d'être finalement analysés dans un spectromètre de masse à temps de vol. L'interprétation des spectres ainsi obtenus a fait l'objet d'une analyse très approfondie afin de caractériser les étapes de désorption et d'ionisation.

Les analyses, réalisées dans différents types de flammes permettent d'identifier les HAP présents à la surface des suies à différents stades de leur formation, l'étendue des spectres variant fortement dans la zone de nucléation des suies. Afin de distinguer les HAP gazeux de ceux adsorbés, une nouvelle méthode de collecte basée sur le dépôt des suies et des HAP gazeux sur des substrats différents a été développée. Par ce biais, l'implication de réactions hétérogènes entre les HAP gazeux et les suies dans la croissance de ces dernières a pu être mise en évidence.